



ADDRESS OF PUBLISHER
& EDITOR'S OFFICE:

GDAŃSK UNIVERSITY
OF TECHNOLOGY

Institute
of Naval Architecture
G. Narutowicza 11/12
80-233 Gdańsk, POLAND

EDITORIAL STAFF:

Wiesław Tarełko
| Editor in Chief
Janusz Kozak
| Deputy Editors-in-Chief
Wojciech Litwin
| Deputy Editors-in-Chief

Price:
single issue: 25 PLN

Prices for abroad
single issue:
- in Europe EURO 15
- overseas USD 20

WEB:
pg.edu.pl/pmr

e-mail : pmr@pg.edu.pl

ISSN 1233-2585

CONTENTS

- | | |
|-----|--|
| 4 | Sang-Do Lee, Sam-Sang You, Hwan-Seong Kim, Jeong-Hum Yeon, Bui Duc Hong Phuc
<i>ROLL PREDICTION AND PARAMETER IDENTIFICATION OF MARINE VESSELS UNDER UNKNOWN OCEAN DISTURBANCES</i> |
| 16 | Jinglei Yang, Han-bing Sun, Xiao-wen Li, Xin Liu
<i>ANALYTICAL AND EXPERIMENTAL INVESTIGATION OF ASYMMETRIC FLOATING PHENOMENA OF UNIFORM BODIES</i> |
| 24 | Thomas Mazarakos, Theodosios Tsaousis
<i>HYDRODYNAMIC LOADS ON A SEMI-SUBMERSIBLE PLATFORM SUPPORTING A WIND TURBINE UNDER A MOORING SYSTEM WITH BUOYS</i> |
| 35 | Hongyuan Xu, Wei Wang, Yonghe Xie
<i>STUDY OF THE HYDRODYNAMIC CHARACTERISTICS OF ANTI-HEAVE DEVICES OF WIND TURBINE PLATFORMS AT DIFFERENT WATER DEPTHS</i> |
| 43 | Janusz Mindykowski, Łukasz Wierzbicki, Mariusz Górniak, Andrzej Piłat
<i>ANALYSIS AND EXPERIMENTAL VERIFICATION OF IMPROVING THE EEDI OF A SHIP USING A THRUSTER SUPPLIED BY A HYBRID POWER SYSTEM</i> |
| 55 | Michał Drężek, Marek Augustyniak
<i>UNIVERSAL SEA/FEM BASED METHOD FOR ESTIMATION OF VIBROACOUSTIC COUPLING LOSS FACTORS IN REALISTIC SHIP STRUCTURES</i> |
| 64 | Sudipta Roy, Dipak Kumar Jana, Nguyen Long
<i>RE-IDENTIFYING NAVAL VESSELS USING NOVEL CONVOLUTIONAL DYNAMIC ALIGNMENT NETWORKS ALGORITHM</i> |
| 77 | Norbert Sigiel, Marcin Chodnicki, Paweł Socik, Rafał Kot
<i>AUTOMATIC CLASSIFICATION OF UNEXPLODED ORDNANCE (UXO) BASED ON DEEP LEARNING NEURAL NETWORKS (DLNNS)</i> |
| 85 | Hossein Ghaemi, Hamid Zeraatgar, Mojtaba Barjasteh
<i>INVESTIGATING FUEL INJECTION STRATEGIES TO ENHANCE SHIP ENERGY EFFICIENCY IN WAVE CONDITIONS</i> |
| 94 | Cunfeng Wei, Guohe Jiang, Gang Wu, Yu Zhou, Yuanyuan Liu
<i>EFFECTS ON OF BLENDED BIODIESEL AND HEAVY OIL ON ENGINE COMBUSTION AND BLACK CARBON EMISSIONS OF A LOW-SPEED TWO-STROKE ENGINE</i> |
| 102 | Fayou Liu, Weijia Li, Yaozhong Wu, Yuhang He, Tianyun Li
<i>FAULT DIAGNOSIS OF IMBALANCE AND MISALIGNMENT IN ROTOR-BEARING SYSTEMS USING DEEP LEARNING</i> |

**ADDRESS OF PUBLISHER
& EDITOR'S OFFICE:**

**GDAŃSK UNIVERSITY
OF TECHNOLOGY**

**Institute
of Naval Architecture
G. Narutowicza 11/12
80-233 Gdańsk, POLAND**

- 114 Liping Chen, Minghua Sun, Wang Li**
*PRACTICAL FINITE-TIME EVENT-TRIGGERED CONTROL OF UNDERACTUATED
SURFACE VESSELS IN PRESENCE OF FALSE DATA INJECTION ATTACKS*
- 127 Selin Barış Çamlı, Gokdeniz Naser, Ayberk Sözen**
*ENVIRONMENTAL MARINE DEGRADATION
OF PLA/WOOD COMPOSITE
AS AN ALTERNATIVE SUSTAINABLE BOATBUILDING MATERIAL*
- 135 Chandra Priya J, Krzysztof Rudzki, Thanh Tuan Le, Hoang Phuong Nguyen,
Naruphun Chotechuang, Nguyen Dang Khoa Pham**
*BLOCKCHAIN-ENABLED TRANSFER LEARNING FOR VULNERABILITY
DETECTION AND MITIGATION IN MARITIME LOGISTICS*
- 146 Yusuf Genç, FMustafa Kafali, Uğur Buğra Çelebi**
*APPROXIMATE ESTIMATION OF MAN-DAY IN SHIP BLOCK PRODUCTION:
A TWO-STAGE STOCHASTIC PROGRAM*

Editorial

POLISH MARITIME RESEARCH is the scientific journal with a worldwide circulation. This journal is published quarterly (four times a year) by Gdansk University of Technology (GUT). On September, 1994, the first issue of POLISH MARITIME RESEARCH was published. The main objective of this journal is to present original research, innovative scientific ideas, and significant findings and application in the field of :

Naval Architecture, Ocean Engineering and Underwater Technology,

The scope of the journal covers selected issues related to all phases of product lifecycle and corresponding technologies for offshore floating and fixed structures and their components.

All researchers are invited to submit their original papers for peer review and publications related to methods of the design; production and manufacturing; maintenance and operational processes of such technical items as:

- all types of vessels and their equipment,
- fixed and floating offshore units and their components,
- autonomous underwater vehicle (AUV) and remotely operated vehicle (ROV).

We welcome submissions from these fields in the following technical topics:

- ship hydrodynamics: buoyancy and stability; ship resistance and propulsion, etc.,
 - structural integrity of ship and offshore unit structures: materials; welding; fatigue and fracture, etc.,
 - marine equipment: ship and offshore unit power plants: overboarding equipment; etc.
-

Scientific Board

Chairman : Prof. JERZY GIRTLER - Gdańsk University of Technology, Poland


Vice-chairman : Prof. CARLOS GUEDES SOARES, Universidade de Lisboa, Lisbon, Portugal

Prof. POUL ANDERSEN Technical University of Denmark Kongens Lyngby Denmark	Prof. YORDAN GARBATOV Universidade de Lisboa, Lisbon Portugal	Prof. JERZY MERKISZ Poznan University of Technology Poznan Poland
Prof. JIAHN-HORNG CHEN National Taiwan Ocean University Keelung Taiwan	Prof. STANISLAW GUCMA Maritime University of Szczecin Szczecin Poland	Prof. VALERI NIEKRASOV Admiral Makarov National University of Shipbuilding Mikolaiv Ukraine
Prof. VINCENZO CRUPI University of Messina Messina Italy	Prof. JIAHN-HORNG CHEN National Taiwan Ocean University Keelung Taiwan	Prof. SERHIY SERBIN Admiral Makarov National University of Shipbuilding Mikolaiv Ukraine
Prof. MAREK DZIDA Gdansk University of Technology Gdansk Poland	Prof. ANTONI ISKRA Poznan University of Technology Poznan Poland	Prof. JOZEF SZALA UTP University of Science and Technology Bydgoszcz Poland
Dr. KATRIEN ELOOT, Flanders Hydraulics Research, Antwerpen Belgium	Prof. JAN KICINSKI Institute of Fluid-Flow Machinery - Polish Academy of Sciences Gdansk Poland	Prof. HOANG ANH TUAN Ho Chi Minh City University of Technology (HUTECH) Ho Chi Minh Vietnam
Prof. ODD MAGNUS FALTINSEN Norwegian University of Science and Technology Trondheim Norway	Prof. ZBIGNIEW KORCZEWSKI Gdansk University of Technology Gdansk Poland	Prof. TADEUSZ SZELANGIEWICZ Maritime University of Szczecin Szczecin Poland
Prof. MASSIMO FIGARI University of Genova Genova Italy	Prof. JOZEF LISOWSKI Gdynia Maritime University Gdynia Poland	Prof. DRACOS VASSALOS University of Strathclyde Glasgow United Kingdom
Prof. HASSAN GHASSEMI Amirkabir University of Technology Tehran Iran	Prof. JERZY EDWARD MATUSIAK Aalto University Espoo Finland	


ROLL PREDICTION AND PARAMETER IDENTIFICATION OF MARINE VESSELS UNDER UNKNOWN OCEAN DISTURBANCES

Sang-Do Lee

Division of Navigation & Information System, Mokpo National Maritime University, Republic of Korea

Hwan-Seong Kim* 

Division of Logistics, Korea Maritime and Ocean University, Republic of Korea

Sam-Sang You 

Northeast-Asia Shipping and Port Logistics Research Center, Korea Maritime and Ocean University, Republic of Korea

Jeong-Hum Yeon

R&D Department, Busan Port Authority, Republic of Korea

Bui Duc Hong Phuc 

Department of Engineering Technology, Gadowski School of Engineering, Christian Brothers University, United States

* Corresponding author: kimhsyskmou@gmail.com (Hwan-Seong Kim)

ABSTRACT

This paper deals with two topics: roll predictions of marine vessels with machine-learning methods and parameter estimation of unknown ocean disturbances when the amplitude, frequency, offset, and phase are difficult to estimate. This paper aims to prevent the risky roll motions of marine vessels exposed to harsh circumstances. First of all, this study demonstrates complex dynamic phenomena by utilising a bifurcation diagram, Lyapunov exponents, and a Poincare section. Without any observers, an adaptive identification applies these four parameters to the globally exponential convergence using linear second-order filters and parameter estimation errors. Then, a backstepping controller is employed to make an exponential convergence of the state variables to zero. Finally, this work presents the prediction of roll motion using reservoir computing (RC). As a result, the RC process shows good performance for chaotic time series prediction in future states. Thus, the poor predictability of Lyapunov exponents may be overcome to a certain extent, with the help of machine learning. Numerical simulations validate the dynamic behaviour and the efficacy of the proposed scheme.

Keywords: Non-periodic roll motions, dynamic analysis, reservoir-computing, parameter estimation, periodic disturbances, backstepping

INTRODUCTION

Marine vessels frequently encounter roll behaviour. Non-periodic patterns appear at the end of stable responses, despite regular waves. This phenomenon is hard to predict and control by the officers on the bridge. Chaos is an aperiodic, long-term motion that exhibits sensitive dependence on initial conditions in a deterministic system. Even slight changes

in initial conditions (IC) result in various outcomes. The sensitivity of a chaotic dynamic system has merit because it shows a different periodic orbit by using a light adjustment of parameters without the whole reconstruction of the system [1]. However, controlling the non-periodic behaviour of a chaotic system is not a trivial issue in the marine environment.

First of all, this paper attempts to predict non-periodic roll motions through machine learning (ML) techniques,

before their manipulation. Simple and complex systems were recently studied under a veil of chaos, using ML, to contribute to predicting dynamic behaviour [2]. Notably, echo state networks (ESN), which are termed ‘reservoir computing’ (RC), are efficient and easy to apply to the black box modelling of dynamic systems [3]. The RC is a recurrent neural network (RNN)-based framework that enables the readout to extract the desired output by using linear mapping [4, 5]. The sensitivity of a chaotic system challenges prediction, which only works if the initial uncertainty is not quickly multiplied by the evolution law [6]. However, this skill is preferable for chaotic time series forecasts because it remembers past values and handles external disturbances, where all of the past elements are implicitly contained in a state vector [4].

As mentioned, the non-periodic roll motions are revealed at the end of stable responses, despite regular excitations [7]. However, estimating the frequencies of unknown external disturbances is difficult because the waves acting on a ship can not be known in advance [8]. Under manoeuvring conditions, it is difficult to measure the exact amounts of time-varying disturbances for a ship, such as waves, winds, currents, ice-covered waters, green waters, etc. Also, estimating the sinusoidal signal is a significant problem for the control system. It is essential to identify the parameters of unknown periodical excitations in tracking and rejection control [9]. In order to realise the safe voyage of marine vessels under severe sea situations, this paper investigates the parameter estimation of unknown periodic disturbances and the suppression of non-periodic roll motions.

It is known that a periodic excitation consists of the sum of its frequency, amplitude, bias (offset), and phase (randomness). As for the real-time processing of chaotic motion in nonlinear systems, a potential solution, based on Fourier analysis, is deemed to be an unwelcome method, owing to the maximisation of the periodogram [10]. A similar work [10] identified the full parameters by using a fifth-order estimator, showing the complexity and computational costs. The frequency and other parameter estimation techniques are separated in the present paper. Other parameter estimations of amplitude, bias, and phase are treated using the simple update law without any observers [9, 11]. In order to design the disturbance rejection control, precise frequency estimation is guaranteed with finite-time convergence [8]. To achieve the stability and robustness of a nonlinear system, this paper implements linear second-order filters and parameter estimation errors, to converge the global parameter estimation without a higher-order estimator. Such a filtering operation overcomes the infinitely increasing auxiliary vector [12]. Then, a backstepping control is designed to suppress the non-periodic roll motions of the marine vessels under unknown periodic disturbances.

The remainder of the paper is organised as follows. A ship rolling model and control synthesis for non-periodic roll stabilisation, using backstepping and roll prediction with RC, are explained in Section 2. The parametric estimation of amplitude, frequency, offset, phase, and adaptive mechanisms is expressed. Numerical simulations verify the proposed

schemes in Section 3. The dynamic theory is used to explore the uncontrolled roll responses using the bifurcation diagram, Poincare map, and Lyapunov exponents (LEs). Final remarks and recommended future research directions are given in Section 4.

MATHEMATICAL FORMULATION

SHIP ROLLING MODEL

The rolling motion of a ship, in transverse directions, can be modelled as follows [7]:

$$[I_{44} + A_{44}] \ddot{\phi} + B_{44} \dot{\phi} + \Delta \overline{GZ}(\phi) = F_{sea}(t) \quad (1)$$

where ϕ (rad), $\dot{\phi}$ (rad/s), and $\ddot{\phi}$ (rad/s²) are the roll angle, rate, and acceleration; I_{44} , and A_{44} (kg·m²) are the moment of inertia and the added mass coefficients; and B_{44} (kg·m²/s) is the damping coefficient. It should be noted that both the added mass and hydrodynamic damping coefficients are a function of the wave frequency; Δ is the ship's displacement; \overline{GZ} is the righting lever; and F_{sea} is the wave-exciting moment. As for periodic roll excitation, the external wave F_{sea} is given as:

$$F_{sea}(t) = HF_{roll}(\omega) \cos(\omega t) \quad (2)$$

where F_{roll} (N·m) is the rolling moment; and ω and H are the angular frequency and the wave amplitude. Generally, Eq. (1) can be rewritten with a quadratic damping, as follows:

$$[I_{44} + A_{44}] \ddot{\phi}(t) + B_{44} \dot{\phi}(t) + B_{44q} \dot{\phi}(t) |\dot{\phi}(t)| - C_1 \Delta \phi(t) + C_3 \Delta \phi^3(t) = HF_{roll}(\omega) \cos(\omega t) \quad (3)$$

where B_{44q} is the quadratic damping coefficient. Eq. (3) can be scaled into a non-dimensional equation, thus:

$$\frac{\omega_n^2 (I_{44} + A_{44})}{C_1 \Delta} \ddot{x}(\tau) + \frac{\omega_n B_{44}}{C_1 \Delta} \dot{x}(\tau) + \frac{\omega_n^2 B_{44q}}{C_1 \Delta} \dot{x}(\tau) |\dot{x}(\tau)| - x(\tau) + \frac{C_3}{C_1} x^3(\tau) = \frac{HF_{roll}(\omega)}{C_1 \Delta} \cos(\Omega \tau) \quad (4)$$

with $x(\tau) = \phi(t)$, $\tau = \omega_n t$, and $\Omega = \omega / \omega_n$; where Ω is the ratio of excitation (ω) to a natural angular frequency (ω_n). Then, the simplified form is derived as:

$$\ddot{x}(\tau) + b_1 \dot{x}(\tau) + b_2 \dot{x}(\tau) |\dot{x}(\tau)| - x(\tau) + kx^3(\tau) = F \cos(\Omega \tau) \quad (5)$$

with

$$b_1 = \frac{B_{44}}{\omega_n (I_{44} + A_{44})} = \frac{\omega_n B_{44}}{C_1 \Delta}, \quad \omega_n = \sqrt{\frac{C_1 \Delta}{I_{44} + A_{44}}}$$

$$b_2 = \frac{B_{44q}}{I_{44} + A_{44}}, \quad k = \frac{C_3}{C_1}, \quad F = \frac{HF_{roll}}{\omega_n^2 (I_{44} + A_{44})} = \frac{HF_{roll}}{C_1 \Delta}$$

where b_1 and b_2 are the linear and nonlinear damping and k is the restoring part of a duffing type roll motion.

CONTROL SYNTHESIS OF BACKSTEPPING

The idea of backstepping is to recursively design a controller by considering some of the state variables as being ‘virtual controls’ and creating intermediate control laws for them [13]. This method is one of the proper nonlinear controllers for regulating the desired ship motions. By adding the actuation (u) in Eq. (5), the complete control system represents a forced rolling system with an active control input:

$$\ddot{x} + b_1 \dot{x} + b_2 \dot{x} | \dot{x} | - x + kx^3 = F \cos(\Omega \tau) + u \quad (6)$$

where the periodic excitation $F \cos(\Omega \tau)$ is given as a time-varying disturbance. In fact, an active controller is vital, to achieve a satisfactory anti-rolling effect. By selecting the state variables as $x = x_1$ and $\dot{x} = x_2$, the governing Eq. (6) can be rewritten into the state-space representation, as follows:

$$\dot{x} = Ax + f(x, \tau) + Bu + B_1 d \quad (7)$$

In Eq. (7), d represents the time-varying disturbance input ($F \cos(\Omega \tau)$), while the state vector (x), system matrices (A , B , B_1), and nonlinear term (f) are described by:

$$x = \begin{bmatrix} x_1 \\ x_2 \end{bmatrix}, A = \begin{bmatrix} 0 & 1 \\ 1 & -b_1 \end{bmatrix},$$

$$B = B_1 = \begin{bmatrix} 0 \\ 1 \end{bmatrix}, f(x, \tau) = \begin{bmatrix} 0 \\ -b_2 x_2 |x_2| - kx_1^3 \end{bmatrix} \quad (8)$$

In the dynamic model, there are two types of inputs: the control (u), which can be manipulated by the control actuator, and the disturbance (d), which represents external influences on ship motion. The two state variables are rewritten in the state-space representation form,

$$\begin{cases} \dot{x}_1 = x_2 \\ \dot{x}_2 = x_1 - b_1 x_2 - b_2 x_2 |x_2| - kx_1^3 + d + u \end{cases} \quad (9)$$

From Eq. (9), x_2 is considered to be a virtual control input for x_1 . To make x_1 exponentially converge to zero, the desired value for x_2 is chosen at $x_{2d} = -\gamma_1 x_1$, where γ_1 is a positive constant. Consequently, $x_2 \rightarrow x_{2d}$ would yield the solution $x_1 \rightarrow x_{1d} = x_1(0)e^{-\gamma_1 t}$. We declare $z_2 = x_2 - x_{2d} = x_2 + \gamma_1 x_1$ as the tracking error of state x_2 and define a positive definite (P.D.) The Lyapunov function is as follows:

$$V_1 = \frac{1}{2} x_1^2 + \frac{1}{2} z_2^2 \quad (10)$$

Then the derivative of V_1 is given as:

$$\dot{V}_1 = x_1 \dot{x}_1 + z_2 \dot{z}_2 = -\gamma_1 x_1^2 + z_2 (2x_1 + \gamma_1 x_2 - b_1 x_2 - b_2 x_2 |x_2| - kx_1^3 + d + u) \quad (11)$$

As z_2 should be asymptotically stable, \dot{V}_1 is expected to be a negative definite (N.D.) function. If the disturbance is well-defined, the control input can be given as follows:

$$u(t) = -2x_1 - \gamma_1 x_2 + b_1 x_2 + b_2 x_2 |x_2| + kx_1^3 - d - \gamma_2 z_2 \quad (12)$$

where γ_2 is a positive constant, resulting in a P.D. function $\dot{V}_1 = -\gamma_1 x_1^2 - \gamma_2 z_2^2$. However, since the amplitude and frequency of disturbance are hardly recognised, the control input cannot be defined as Eq. (12). In fact, the control input is dependent on the estimated value \hat{d} instead of d , so the controller in Eq. (12) should be rewritten as:

$$u(t) = -2x_1 - \gamma_1 x_2 + b_1 x_2 + b_2 x_2 |x_2| + kx_1^3 - \hat{d} - \gamma_2 z_2 \quad (13)$$

which would yield

$$\dot{V}_1 = -\gamma_1 x_1^2 - \gamma_2 z_2^2 + z_2 (d - \hat{d}) \quad (14)$$

The problem is to make an estimation \hat{d} that eliminates the term $z_2 (d - \hat{d})$. In general, four critical features should be determined, to define a sinusoidal signal completely, in terms of offset, amplitude, frequency, and phase. Assuming that $\hat{d}(\tau) = \hat{F}_o + \hat{a} \cos(\Omega \tau) + \hat{b} \sin(\Omega \tau)$, where \hat{F}_o is the estimated offset, $\hat{\Omega}$ is the estimated frequency, $\hat{F} = \sqrt{\hat{a}^2 + \hat{b}^2}$ is the estimated amplitude, and $\hat{\psi} = \arctan(\hat{b}/\hat{a})$ is the estimated phase. The following subsections will present an adaptive mechanism to update those components.

ESTIMATION FOR FREQUENCY

Let us introduce a second-order filter for the disturbance, as shown in Eq. (15),

$$\xi(s) = \frac{\lambda_0}{s^2 + \lambda_1 s + \lambda_2} d(s) \quad (15)$$

where λ_0, λ_1 , and λ_2 are positive constants that make $\Lambda(s) = s^2 + \lambda_1 s + \lambda_2$ a Hurwitz polynomial. Neglecting the initial conditions, it is simple to obtain the relation as follows:

$$\ddot{\xi}(t) = -\Omega^2 \xi(t) = \Theta \xi(t) + \varepsilon_\xi(t) \quad (16)$$

where $\dot{\xi}(t)$ and $\ddot{\xi}(t)$ are derivatives of the output variable of the filter (15). Triple differentiation of $\xi(t)$ gives $-\Omega^2 \dot{\xi}(t) + \Omega^2 \dot{\xi}(t) + \ddot{\xi}(t)$, in which $\varepsilon_\xi(t) = \Omega^2 \dot{\xi}(t) + \ddot{\xi}(t)$ is the exponential damped function with exponential damped derivatives defined by non-zero initial conditions [14]; $\Theta = -\Omega^2$ is a constant parameter. The updated law for the identification of Θ , including the frequency Ω [8], is as follows:

$$\begin{cases} \hat{\Omega} = \sqrt{|\Theta|} \\ \hat{\Theta} = \chi + \gamma \xi \ddot{\xi} \\ \chi = -\gamma_3 \xi^2 \hat{\Theta} - \gamma_3 \ddot{\xi}^2 \end{cases} \quad (17)$$

where $\hat{\Omega}$ is an estimated frequency Ω and $\hat{\Theta}$ is an estimated unknown parameter Θ . The estimated error $\tilde{\Omega} = \Omega - \hat{\Omega}$ is guaranteed to converge to zero and is bounded by a decaying exponent $|\tilde{\Omega}(t)| \leq \sqrt{|\tilde{\Theta}(t)|} \leq \rho_0 e^{-\beta_0 t}$, where ρ_0 and β_0 are positive numbers [14]. The derivative of the estimated error $\dot{\tilde{\Theta}} = \dot{\Theta} - \dot{\hat{\Theta}}$ can be proved with a positive constant γ_3 as follows:

$$\begin{aligned} \dot{\tilde{\Theta}}(t) &= \dot{\Theta} - \dot{\hat{\Theta}}(t) \\ &= -\dot{\chi}(t) - \gamma_3 \ddot{\xi}^2(t) - \gamma_3 \dot{\xi}(t) \ddot{\xi}(t) \\ &= -(-\gamma_3 \dot{\xi}^2(t) \hat{\Theta}(t) - \gamma_3 \ddot{\xi}^2(t)) - \gamma_3 \ddot{\xi}^2(t) - \gamma_3 \dot{\xi}(t) \ddot{\xi}(t) \\ &= \gamma_3 \dot{\xi}^2(t) \hat{\Theta}(t) - \gamma_3 \dot{\xi}^2(t) \Theta - \gamma_3 \dot{\xi}(t) \varepsilon_\xi(t) \\ &= -\gamma_3 \dot{\xi}^2(t) \tilde{\Theta}(t) - \gamma_3 \dot{\xi}(t) \varepsilon_\xi(t) \end{aligned} \quad (18)$$

The P.D. Lyapunov function is $V_2 = \frac{1}{2} \tilde{\Theta}^T \Gamma_1 \tilde{\Theta}$, where Γ_1 is a symmetric P.D. matrix. Using the result in Eq. (18), the following can be obtained:

$$\begin{aligned} \dot{V}_2 &= \tilde{\Theta}^T \Gamma_1 \dot{\tilde{\Theta}} = \tilde{\Theta}^T \Gamma_1 (-\gamma_3 \dot{\xi}^2 \tilde{\Theta}) - \gamma_3 \Gamma_1 \dot{\xi} \tilde{\Theta} \varepsilon_\xi \\ &= -\gamma_3 \dot{\xi}^2 V_2 + \frac{1}{2} \gamma_3 \Gamma_1 \varepsilon_\xi^2 \leq 0 \end{aligned} \quad (19)$$

It is clear from Eq. (19) that \dot{V}_2 is a non-increasing function and, hence, V_2 is bounded. According to Barbalat's Lemma, $V_2 \rightarrow 0$ as $t \rightarrow \infty$, which also leads to $\tilde{\Omega} \rightarrow 0$. Consequently, the updated law in Eq. (17) is proven to estimate the frequency $\hat{\Omega} \rightarrow \Omega$ of the sinusoidal signal.

ESTIMATION FOR OFFSET, AMPLITUDE, AND PHASE

To estimate the rest of the parameters, the disturbance is calculated as follows:

$$d(t) = \theta^T \varphi(t) \quad (20)$$

where $\theta = [F_o \quad a \quad b]^T$ is a vector of unknown constants and $\varphi(t) = [1 \quad \cos(\Omega t) \quad \sin(\Omega t)]^T$ is the regression vector [9]. Replacing into Eq. (14) gives

$$\dot{V}_1 = -\gamma_1 x_1^2 - \gamma_2 z_2^2 + z_2 (\theta^T \varphi - \hat{\theta}^T \varphi) = -\gamma_1 x_1^2 - \gamma_2 z_2^2 + z_2 \tilde{\theta}^T \varphi \quad (21)$$

where $\tilde{\theta} = \theta - \hat{\theta}$ is the estimated error. With a P.D Lyapunov function $V_3 = V_1 + \frac{1}{2} \tilde{\theta}^T \Gamma_2^{-1} \tilde{\theta}$, where Γ_2 is a symmetric P.D matrix, the derivative \dot{V}_3 is given as:

$$\begin{aligned} \dot{V}_3 &= \dot{V}_1 + \tilde{\theta}^T \Gamma_2^{-1} \dot{\tilde{\theta}} = -\gamma_1 x_1^2 - \gamma_2 z_2^2 + z_2 \tilde{\theta}^T \varphi - \tilde{\theta}^T \Gamma_2^{-1} \dot{\tilde{\theta}} \\ &= -\gamma_1 x_1^2 - \gamma_2 z_2^2 + \tilde{\theta}^T (\varphi z_2 - \Gamma_2^{-1} \dot{\tilde{\theta}}) \end{aligned} \quad (22)$$

To make \dot{V}_3 an N.D. function, the update law should be chosen as follows:

$$\dot{\tilde{\theta}} = \Gamma_2 \varphi z_2 \quad (23)$$

Finally, with the chosen update law, $\dot{V}_3 = -\gamma_1 x_1^2 - \gamma_2 z_2^2$ is a non-increasing function and V_3 and V_1 are bounded, hence $x_1 \rightarrow 0$ and $\hat{\theta} \rightarrow \theta$ as $t \rightarrow \infty$. To sum up, the necessary parameters for estimating sinusoidal disturbance and controller have been explained. In the next section, simulation results illustrate the system's dynamic behaviour under backstepping control with an adaptive mechanism, as well as the estimation process, to formulate the external disturbance.

NON-PERIODIC ROLL PREDICTION USING RC

In contrast to conventional RNN, only the readout weight is trained. The input weight (W_{in}), feedback weight (W_{fb}), and adjacency matrix (W_{res}) are fixed and chosen randomly. In some simple applications, where feedback response is not required, W_{fb} can be omitted. Based on similar effects on reservoirs, W_{in} and W_{fb} are primarily constructed in the same way. Both input and feedback responses can be used to generate output [15]. For a reservoir with N neurons, the structure of a general ESN, having N reservoir states, is illustrated in Fig. 1. The linear mapping input-output at a perceptron is presented in Fig. 1.

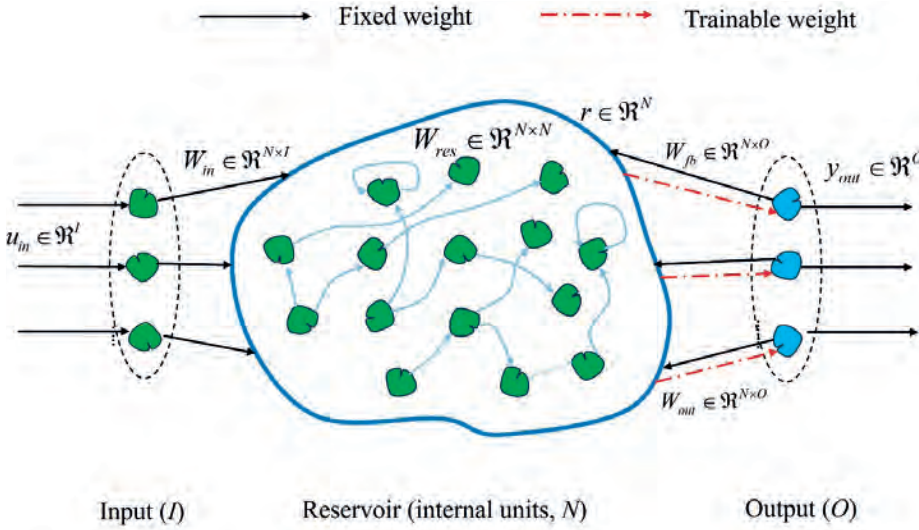


Fig. 1. Generic sketch of the RC framework

According to [15], the complete form of the updated equation for the reservoir state vector $r(n)$ is defined as follows:

$$\tilde{r}(n) = \tanh \left(W_{in} \begin{bmatrix} b_{in} \\ u_{in}(n) \end{bmatrix} + W_{res} r(n) + W_{fb} y_{out}(n-1) \right) \quad (24)$$

$$r(n) = (1 - \alpha) r(n-1) + \alpha \tilde{r}(n) \quad (25)$$

where $u_{in}(n) \in \mathbb{R}^I$ is the input fed to the reservoir at time step n ($n = 1, \dots, T$); T is a data point in the training dataset; b_{in} is the bias of the reservoir's input; $r(n) \in \mathbb{R}^N$ is a vector of a reservoir neuron; $\tilde{r}(n)$ is its updated value; and $y_{out}(n) \in \mathbb{R}^O$ is a vector of network outputs [13]. Weight matrices W_{in} , W_{res} , and W_{fb} are defined as the input weight matrix, the adjacency matrix describing the connection of the nodes in the reservoir, and the feedback weight matrix from the output back to the reservoir, respectively. α is the leaking rate ($0 \leq \alpha \leq 1$). Without the leaking term, $\tilde{r}(n) \equiv r(n)$

for the case where $\alpha = 1$, $f(x) = \tanh(x)$ is the activation function. The weighted sum of the input states is then fed through an activation function to give the final output. The most basic activation function is the step function. However, smooth (sigmoid) functions are mostly preferred, such as the hyperbolic tangent function $\tanh(x)$. Eqs. (24) and (25) indicate that the reservoir state $r(n)$ will be updated based on the current input $u_{in}(n)$ and the feedback from the previous sample $y_{out}(n-1)$. The feedback term can be omitted in some tasks, where the feedback state is unnecessary. The output state $y_{out}(n)$ of the reservoir at the sampling point can be calculated from the linear combination between the reservoir state and input state, as below [15]:

$$y_{out}(n) = W_{out} \begin{bmatrix} b_{out} \\ u_{in}(n) \\ r(n) \end{bmatrix} \quad (26)$$

where W_{out} is the weight matrix from the reservoir to the output and b_{out} is the bias of the reservoir's output. In the training procedure, the input data is the reference data (teacher data) and the actual output of the reservoir is replaced by the desired output [15]. Within a training duration of T samples, all input and output data are

collected into matrices $Y^{(N \times T)}$ and $X^{(N \times T)}$, by concatenating T columns. Regarding Eq. (26), the linear relation between Y and X can be written in matrix form, as follows:

$$Y = W_{out} X \quad (27)$$

At the end of the training phase, the trained weight matrix W_{out} can be analytically computed using ridge regression.

$$W_{out} = YX^T (XX^T + \nu I)^{-1} \quad (28)$$

where ν is the regularisation constant added to avoid overfitting and I is the identity matrix. After the training phase, the output weight W_{out} is computed and can be used for continuous computation. The actual output of the iteration can be reapplied as input for the next iteration. The teacher data is now unnecessary because the reservoir computer can generate prediction data. As presented in Eq. (26), the actual output of the reservoir can be obtained.

SIMULATION RESULTS

DYNAMIC ANALYSIS OF NON-PERIODIC ROLL MOTIONS

In this section, finding the chaos using dynamic theory, stabilisation, and the parametric identification of unknown periodic disturbances are discussed in sequence. Numerical simulations are performed to reveal the effectiveness of the proposed mechanism. The main parameters of the chosen model, from a marine vessel, [7] show strong nonlinear characteristics such as chaos, limit cycles, and resonance under periodic disturbances [16]. For the numerical simulation, the initial condition (IC) of the roll dynamics is $= [0.5 \text{ (rad)} \ 0.2 \text{ (rad/s)}]$.

First, we analysed the non-periodic roll motions before parametric estimation and stabilisation. The bifurcation diagram easily recognises this phenomenon, representing the qualitatively sudden change as a varied parameter. When a small perturbation causes the qualitative responses in the system, it is regarded as unstable, whereas the opposite case is stable. This roll model shows rich dynamic behaviours, depending on the initial conditions. For example, a strange attractor exhibits sensitivity to initial conditions.

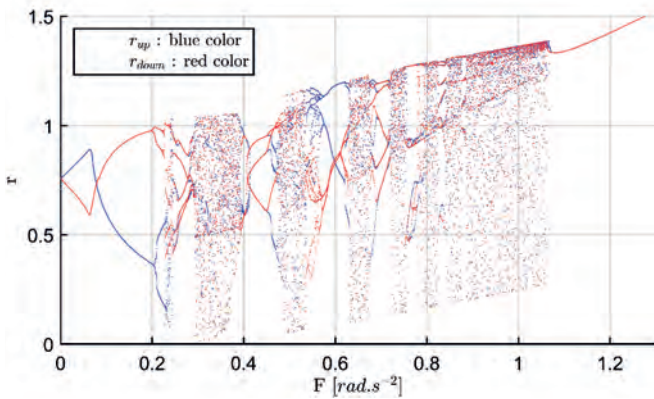
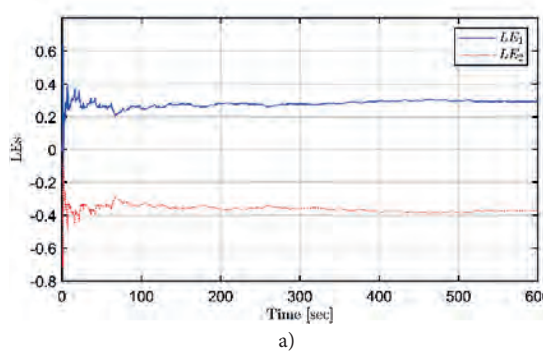


Fig. 2. Bifurcation diagram using the second iterative method



The ramp-up and ramp-down parts of the graph are necessary for observing the bistable region [17]. Fig. 2 shows the stable and unstable rolling motions, based on the second iterative method, where $r = (\sqrt{x_1^2 + x_2^2})$ is the distance from the origin in the Poincare map [18]. The ramp-up (r_{up} , in blue) and ramp-down (r_{down} , in red) parts enable checking of the bistable region. \bar{F} is the forcing amplitude of wave excitations, with respect to roll mode after dividing inertia terms. A ship's motion is stable, with periodic responses, until \bar{F} reaches a value of 0.2. However, the branches in the diagram start to split (bifurcate) into two new branches from the point $\bar{F} = 0.2$, and the ship becomes unstable. Such unstable regions are more dominant, as the forcing amplitude reaches 1. Period-doubling routes to chaos and period-undoubling routes to single branches are clearly observed when the \bar{F} increases. With a slight rise in forcing amplitude, the periodic windows, which are stable regions, can be seen among the chaotic clouds of dots.

Fig. 3(a) illustrates the Lyapunov exponents (LEs) of the uncontrolled systems, demonstrating a chaos system. It is a measure of predictability and sensitivity for controlling parameter changes. The exponential growth in LE_i can be estimated as follows:

$$\|\Delta_i(t)\|_2 \approx \|\Delta_i(0)\|_2 e^{LE_i t}, \quad 1 \leq i \leq n \quad (29)$$

where $\|\Delta_i(0)\|_2$ denotes the initial separation, with a chaotic motion of $LE_i > 0$ making behaviour *unpredictable*, whereas $LE_i \leq 0$ for regular motion. The stretching and contracting of attractors can be defined with LEs, whose positive values signify chaos [19]. The LE measures the mean rate of exponential divergence of nearby trajectories, which gives information on the growth rate of IC. The positive LEs (LE_1 , blue line) show that the system is sensitive to IC and their trajectories diverge with time, while negative LEs (LE_2 , red line) indicate a tendency for convergence. A positive LE usually indicates that the system is chaotic. The larger the exponent, the more unstable the system. The negative LEs mean that the system is stable. The negative LEs are characteristic of dissipative systems, such that the roll system exhibits asymptotic stability; the more negative the exponent, the greater the stability [17].

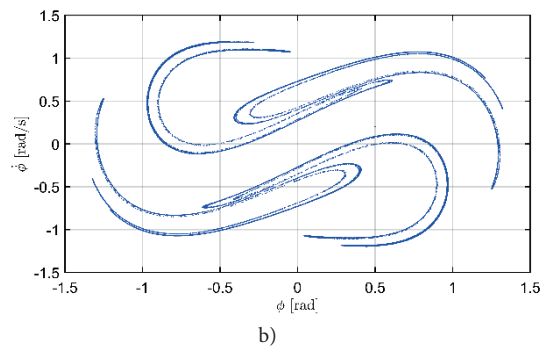


Fig. 3. Dynamic analysis of the uncontrolled system in the case of IC $[0.5 \text{ (rad)} \ 0.2 \text{ (rad/s)}]$: (a) Lyapunov exponents; (b) Poincare section

Fig. 3(b) shows where the Poincare section shows a deterministic system's uncontrolled roll, with no random or noisy inputs; it appears to be non-periodic. The main parameters are adopted in a marine model [7]. The Poincare map reduces the n -dimensional flow to a $n-1$ dimensional map. All trajectories of an n -dimensional system start on the $n-1$ dimensional surface of a section flowing through it. Such reduced dimensionality makes it possible to preserve periodic and quasi-periodic orbits. To make an autonomous flow in a torus, a third value $\theta = \Omega t$ can be considered from Eq. (6) without control. A trajectory flowing around a torus with a period ($T = 2\pi / \Omega$) leads to the Poincare mapping of a $\theta = \theta_0$ plane. Picking up a cross-section of roll angle and rate, the Poincare map is mainly varied according to the strength of the forcing function. The manifolds become tangential and intersect transversely when F increases. If a trajectory in the phase plane intersects itself repeatedly, then a strange attractor and fractals may be observed in the roll dynamics [20-22].

PARAMETRIC IDENTIFICATION OF PERIODIC DISTURBANCES

Next, the simulations for the proposed backstepping control are conducted. The filter and controller design parameters are set as $(\lambda_0, \lambda_1, \lambda_2, \gamma_1, \gamma_2, \gamma_3) = (0.15, 2, 8, 5, 5, 2.5)$. The updated rate matrix is chosen as $\Gamma_2 = \text{diag}(2, 1.2, 1.2)$ and the IC is $(\hat{F}_0(0), a(0), b(0), \Omega(0)) = (0.2, 0.3, 0.1, 0)$. Figs. 4 and 5 demonstrate the estimation process for the frequency, offset, amplitude, and phase, respectively. In contrast, Fig. 5 (a) verifies a combination of the above results to form a complete estimation for the sinusoidal disturbance. All parameters of periodic disturbances can be precisely estimated. Suppression of the roll angle and rate is achieved using the backstepping control, as seen in Figs. 5(b) and 5(c). Finally, filtered signals are illustrated in Fig. 5(d), according to the updated law in Eq. (17).

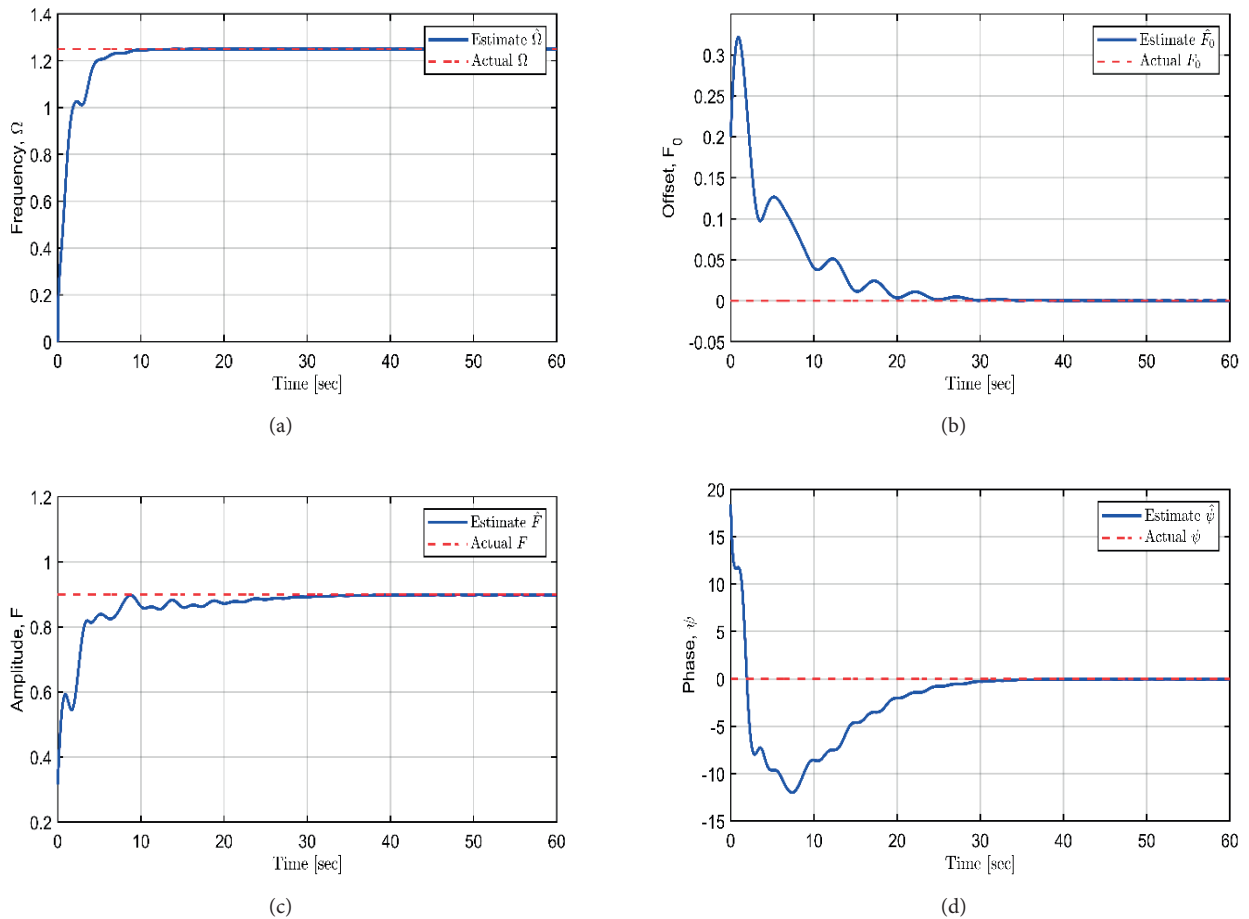


Fig. 4. Test results of estimation (1): (a) frequency; (b) offset; (c) amplitude; (d) phase

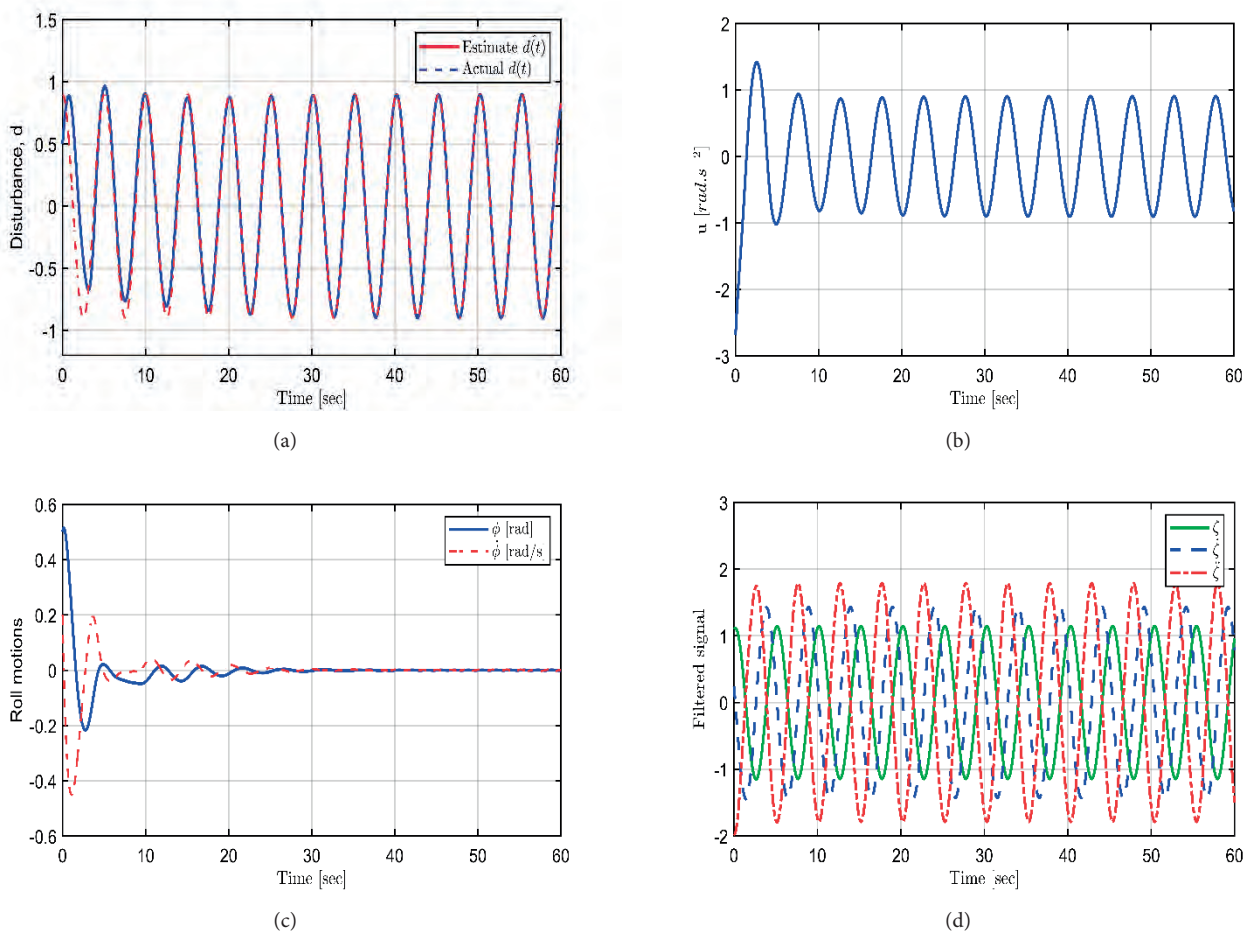


Fig. 5. Test results of estimation (2): (a) periodic disturbances; (b) control inputs; (c) suppression of two states; (d) filtered signals

SHIP ROLL PREDICTION USING RC

Finally, the non-periodic rolling motions are predicted via RC. Such an ESN algorithm is used to forecast the reference data of roll angle and roll rate for the training and prediction processes of the reservoir. After the initial input weight (W_{in}) and feedback weight (W_{fb}) are fixed, the predicted process is performed from the computation of the trained reservoir. In fact, the prediction performance strongly depends on the parameter values, as listed in Table 1. A reservoir size (N), related to the memory capacity, is selected as $N = 600$, where σ is a hyper-parameter for adjusting the performance. The input range $[-\sigma, \sigma]$ indicates the dispersion level of components in the weight matrices (W_{in} , W_{fb}). The adjustment of the leaking rate (α) indicates the level of dependence of the network on past information. The lower the α value, the more dependent it is on past information. The spectral radius (ρ) is related to the magnitude of the largest eigenvalue of internal weight (W_{res}) and performance. As α increases, the wider it spreads on the weight matrices. The author decided that α should not be too low because it will inflict an amplitude value on input and feedback responses.

Tab. 1. Main parameter values for the prediction model

Reservoir size (N)	Hyper-parameter (σ)	Leaking rate (α)	Regularisation coefficient (V)	Spectral radius (ρ)
600	0.5	0.1	10^{-8}	0.75

The prediction performance of *quantitative* and *qualitative* measures, such as error criteria and non-periodic orbits in future states, is presented. At first, the mean squared error (MSE) is employed to evaluate the prediction performance, which measures the average of the squares of the errors. It shows a positive value that decreases, as the error approaches zero, and is defined as follows:

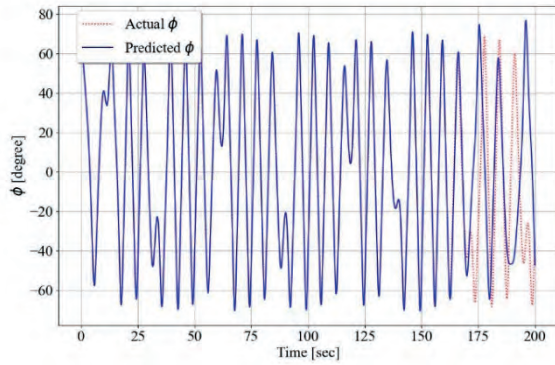
$$MSE = \frac{1}{n} \sum_{n=1}^n (Y_T - \hat{Y}_T)^2 \quad (30)$$

where Y_T and \hat{Y}_T describe the actual and predicted values of roll responses in the time period, respectively.

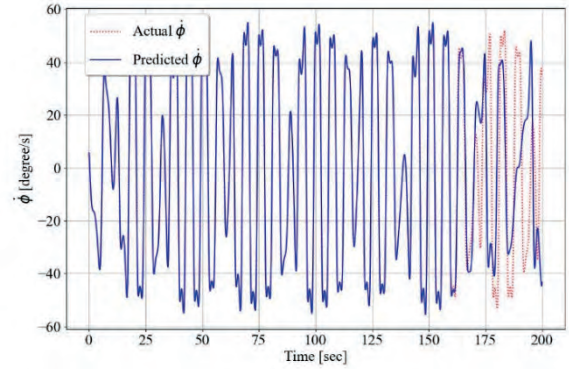
The numerical tests were conducted based on several scenarios: Case 1 ($T_T = 160$, $P_T = 40$), Case 2 ($T_T = 200$, $T_p = 400$), Case 3 ($T_T = 200$, $P_T = 800$), and Case 4 ($T_T = 400$, $P_T = 800$), where T_T and P_T mean the times of training and prediction, as listed in Table 2. The indices show that the results of Case 1, Case 2, and Case 4 are better than Case 3. When T_p increases, the values of MSE increase as well, and prediction performance is degraded over time. Then, a proper T_p should be adjusted accordingly. The ratio value of $T_T / P_T = 0.5$ is necessary for this simulation. Interestingly, the results of RC slightly vary at every simulation. The test results of each case are changeable, according to the reservoir size or the other parameters in Table 1.

Tab. 2. Prediction accuracies using performance index (MSE)

States	Case 1 ($T_T / P_T = 4$)		Case 2 ($T_T / P_T = 0.5$)		Case 3 ($T_T / P_T = 0.25$)		Case 4 ($T_T / P_T = 0.5$)	
	T_T	P_T	T_T	P_T	T_T	P_T	T_T	P_T
	160 s	40 s	200 s	400 s	200 s	800 s	400 s	800 s
$x_1(\phi)$	0.3336		0.8659		1.0768		0.8912	
$x_2(\dot{\phi})$	0.2342		0.6809		0.8946		0.6383	

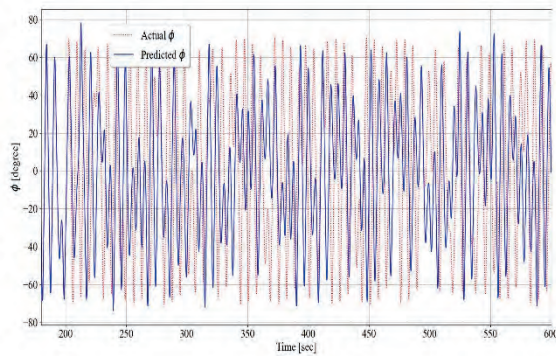


(a)

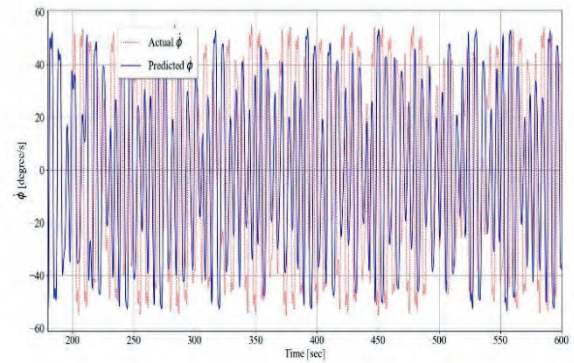


(b)

Fig. 6. Prediction results (Case 1): (a) roll angle; (b) roll rate

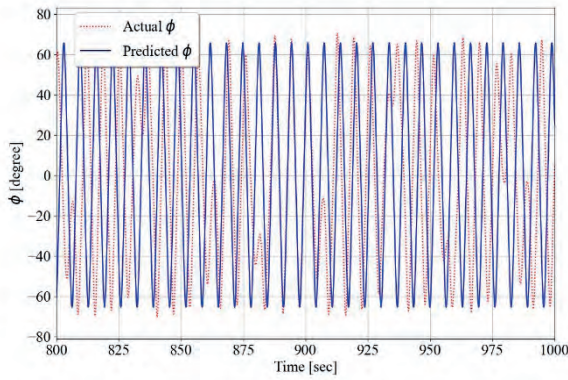


(a)

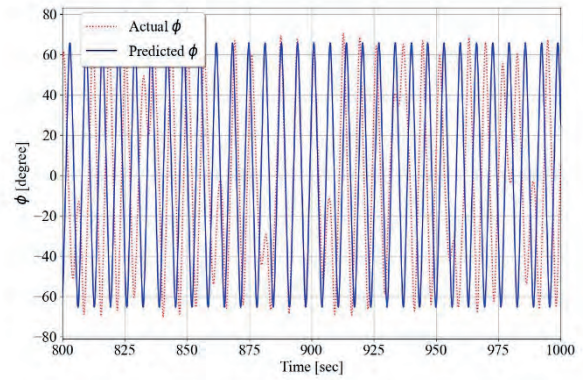


(b)

Fig. 7. Prediction results (Case 2): (a) roll angle; (b) roll rate

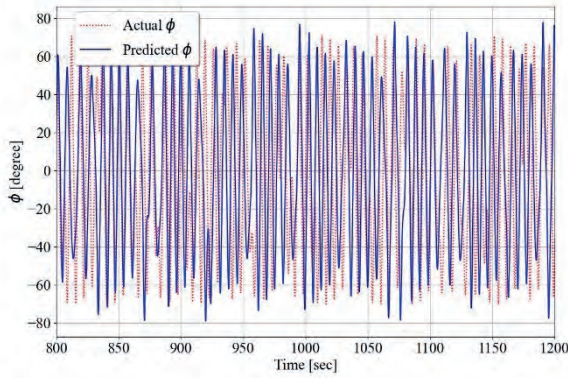


(a)

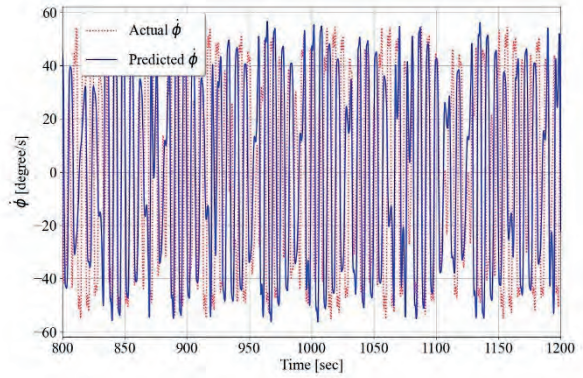


(b)

Fig. 8. Prediction results (Case 3): (a) roll angle; (b) roll rate



(a)



(b)

Fig. 9. Prediction results (Case 4): (a) roll angle; (b) roll rate

The main purpose of the RC is to predict chaotic time series behaviours. Figs. 6 to 9 depict the qualitative features of prediction results based on the training time T_T of 160-400 seconds. Then, the model performance is demonstrated by increasing the prediction time P_T by 40-800 seconds. Figs. 6, 7, and 9 show that the non-periodic pattern is clear for cases where $T_T > P_T$ and $T_T < P_T$. However, chaotic time series prediction is obscure, due to the insufficient T_T , as seen in Fig. 8. Chaotic features become evident in Fig. 9, by increasing T_T . Thus, prediction performance can be secured in the case of $T_T / P_T \geq 0.5$, by adjusting the corresponding T_T and P_T . As a result, the RC process shows good performance, even for chaotic time series prediction in future states, although it lacks predictability [6].

CONCLUSIONS

One can easily imagine that the marine environment is not easy for humans and marine vessels to deal with. This paper has investigated two topics: how to estimate the parameters of unknown ocean disturbances and how to control a ship's dynamic behaviour in future states. The rolling behaviour of marine vessels shows non-periodic responses, as well as regular responses. Sometimes, the complicated rolling motions are demonstrated by strong nonlinearities or forcing amplitudes of extreme wave excitation. Specifically, the complex behaviours of a rolling system are investigated by nonlinear analyses, such as bifurcation diagrams, the Lyapunov exponent (LE), and Poincaré maps. The chaos is not a casual phenomenon but, rather, it yields particular responses. It is an aperiodic, long-term motion that exhibits sensitive dependence on the initial conditions in a deterministic system. The nonlinear rolling motion shows a strange attractor, depending on the initial conditions. The

second iterative method of the bifurcation diagram displays the unstable qualitative responses in the ship's roll due to slight changes in the parameters, such as the initial conditions or forcing amplitudes. Based on the magnitude of the wave excitations, rich dynamic responses can be observed, such as periodic (stable, regular) routes to chaos (reverse doubling), and chaos at the end. In fact, a ship under excessive rolling motions may result in a capsized state with no other recovery oscillations until it is in an upright position. Since there is no response amplitude operator (RAO), including wave height, in this paper, it is a limitation that marine vessels do not recognise the precise timing of chaos or capsize in sea states. It is difficult for ships' crews to deal with the abrupt changes in the rolling motions.

Therefore, this paper has investigated rolling motion predictions for marine vessels with machine-learning methods and parameter estimation of unknown disturbances. All parameters, such as frequency, offset, amplitude, and phase, are precisely estimated based on the adaptive mechanism without any observers. The linear second-order filters and parameter estimation errors are employed to achieve global exponential convergence. Also, the backstepping method is realised, to regulate the roll angle and rate, in the case of severe disturbances to marine vessels. Moreover, the RC process revealed its predictive performance in terms of the future states' chaotic time series behaviours. This may help to support the lack of predictability by LEs [6]. Unfortunately, prediction performance is highly dependent on the parameter values selected by the designer's empirical trials. Interestingly, the results of RC vary slightly in every simulation. According to the reservoir size, practitioners might find the optimum values of parameters. However, the method presented may help them obtain a satisfactory conclusion. Insufficient training time causes the obscure prediction of chaotic orbits. Thus, prediction criteria and the prediction and training time ratio are necessary. This paper suggests a ratio value of greater than 0.5 but it has a limitation of slow convergence in transient performance; however, it shows less oscillation due to the second-order filtered signals [9]. Finding the proper values to adjust to fast convergence speed and transient performance is necessary. To make a safe and robust system of marine vessels under severe sea environments, an adversarial attack might be considered, based on adaptive control with machine learning skills or quantum RC in future research.

ACKNOWLEDGEMENT

This research was supported by the 'Regional Innovation Strategy (RIS)' through the National Research Foundation of Korea (NRF), funded by the Ministry of Education (MOE) (2023RIS-007).

REFERENCES

1. E. Ott, C. Grebogi, J.A. Yorke, 'Controlling chaos', *Phys. Rev. Lett.* 1990, 64, 1196–1199, DOI: 10.1103/PhysRevLett.64.1196.
2. Y. Tang, J. Kurths, W. Lin, E. Ott, and L. Kocarev, 'Introduction to Focus Issue: When machine learning meets complex systems: Networks, chaos, and nonlinear dynamics', *Chaos* 2020, 30 (6), 063151, DOI: [10.1063/5.0016505](https://doi.org/10.1063/5.0016505).
3. H. Jaeger and H. Haas, 'Harnessing nonlinearity: Predicting chaotic systems and saving energy in wireless communication', *Science* 2004, 304 (5667), 78–80, DOI: [10.1126/science.109127](https://doi.org/10.1126/science.109127).
4. Y. LeCun, Y. Bengio, and G. Hinton, 'Deep learning', *Nature* 2015, 521, 436–444. <https://doi.org/10.1038/nature14539>.
5. A.A. Ferreira, T.B. Ludermit, and R.R.B. De Aquino, 'An approach to reservoir computing design and training', *Expert Syst. Appl.* 2013, 40(10), 4172–4182, DOI: 10.1016/j.eswa.2013.01.029.
6. G. Boffetta, M. Cencini, M. Falcioni, and A. Vulpiani, 'Predictability: A way to characterize complexity', *Phys. Rep.* 2002, 356, 367–474, DOI: 10.1016/S0370-1573(01)00025-4.
7. S.D. Lee, B.D.H. Phuc, X. Xu, and S.S. You, 'Roll suppression of marine vessels using adaptive super-twisting sliding mode control synthesis', *Ocean. Eng.* 2020, 195, 106724, DOI: 10.1016/j.oceaneng.2019.106724.
8. A.A. Pyrkin, A.A. Bobtsov, S.A. Kolyubin and A.A. Vedyakov, 'Precise frequency estimator for noised periodical signals', 2012 IEEE International Conference on Control Applications. 2012, 92–97, DOI: 10.1109/CCA.2012.6402392.
9. N. Jing, Y. Juan, W. Jing and G. Yu, 'Adaptive parameter identification of sinusoidal signals', 2013 IFAC Conference on Intelligent Control and Automation Science ICONS, 2013, 624–629, DOI: 10.3182/20130902-3-CN-3020.00096.
10. M. Hou, 'Parameter identification of sinusoids', *IEEE Transactions on Automatic Control*. 2012, 57(2), 467–472, DOI: [10.1109/TAC.2011.2164736](https://doi.org/10.1109/TAC.2011.2164736).
11. J. Na, J. Yang, X. Wu, and Y. Guo, 'Robust adaptive parameter estimation of sinusoidal signals', *Automatica*. 2015, 53, 376–384, DOI:10.1016/j.automatica.2015.01.019.

12. V. Adetola and M. Guay, 'Performance Improvement in Adaptive Control of Linearly Parameterized Nonlinear Systems', *IEEE Transactions on Automatic Control*. 2010, 55(9), 2182-2186, DOI: [10.1109/TAC.2010.2052149](https://doi.org/10.1109/TAC.2010.2052149).
13. S.D. Lee, Y.S. Song, D.H. Kim, and M.R. Kang, 'Path following control of an underactuated catamaran for recovery maneuvers', *Sensors*. 2022, 22, 2233, doi.org/10.3390/s22062233.
14. A.A. Pyrkin, 'Adaptive algorithm to compensate parametrically uncertain biased disturbance of a linear plant with delay in the control channel', *Autom Remote Control*. 2010, 71, 1562-1577.
15. M. Lukoševičius, 'A Practical Guide to Applying Echo State Networks. In: Montavon, G., Orr, G.B., Müller, K.R. (eds) *Neural Networks: Tricks of the Trade. Lecture Notes in Computer Science*', 2012, vol 7700. Springer, Berlin, Heidelberg. https://doi.org/10.1007/978-3-642-35289-8_36.
16. S.D. Lee, S.S. You, X. Xu, and T.N. Cuong, 'Active control synthesis of nonlinear pitch-roll motions for marine vessels'. *Ocean Eng.* 2021, 221, 108537, DOI: 10.1016/j.oceaneng.2020.108537.
17. S. Lynch, 'Poincaré Maps and Nonautonomous Systems in the Plane. In: *Dynamical Systems with Applications using MATLAB**', 2014, Birkhäuser, Cham, DOI: 10.1007/978-3-319-06820-6_15.
18. E. Ott, 'Chaos in Dynamical Systems (2nd ed.)', Cambridge: Cambridge University Press. 2002. DOI: 10.1017/CBO9780511803260.
19. S. Lynch, 'Electromagnetic Waves and Optical Resonators. In: *Dynamical Systems with Applications using MATLAB**', 2014, Birkhäuser, Cham, DOI: 10.1007/978-3-319-06820-6_5.
20. K.K. Dey and G.A. Sekh, 'Effects of Random Excitations on the Dynamical Response of Duffing Systems', *J Stat Phys.* 2021, 182, 18, DOI: [10.1007/s10955-020-02694-x](https://doi.org/10.1007/s10955-020-02694-x).
21. B.S. Ahmed, 'A practical test for noisy chaotic dynamics', *SoftwareX*. 2015, 3-4, 1-5, DOI: 10.1016/j.softx.2015.08.002.
22. J.J. Bramburger and J. Nathan Kutz, 'Poincaré maps for multiscale physics discovery and nonlinear Floquet theory', *Physica D: Nonlinear Phenomena*. 2020, 408, 132479, DOI: [10.1016/j.physd.2020.132479](https://doi.org/10.1016/j.physd.2020.132479).

ANALYTICAL AND EXPERIMENTAL INVESTIGATION OF ASYMMETRIC FLOATING PHENOMENA OF UNIFORM BODIES

Jinglei Yang ¹

Han-bing Sun^{2*}

Xiao-wen Li¹

Xin Liu¹

¹ Jimei University, School of Marine Engineering, Xiamen, China

² Harbin Engineering University, College of shipbuilding engineering, Harbin, China

* Corresponding author: sunhanbing@hrbeu.edu.cn (H. Sun)

ABSTRACT

Uniform symmetric bodies can be observed floating asymmetrically under certain circumstances. Previous explanations of this are mostly abstract and lack experimental verification, making their understanding and application difficult. This article presents in detail alternative insights into the floating equilibria of uniform prisms and parabolic cylinders. The intrinsic characteristics of the equilibrium curves are investigated, and several equilibria different from those in the literature are found. The inflection points in the equilibrium curves are analyzed quantitatively due to their significance for floating states. Furthermore, experiments have been conducted for the square prism which validate the derived equilibrium curve, and provide a practical impression of the asymmetric floating phenomenon of symmetric bodies. These results have the potential to be applied in naval and ocean engineering, such as in the design of vessels and floating offshore structures.

Keywords: hydrostatic stability, floating equilibrium, asymmetric floating state, experimental validation

INTRODUCTION

The stability of floating bodies is a classic and fundamental subject in fluid mechanics. The study of the hydrostatic responses of floating bodies is much earlier than the study of the hydrodynamic response due to the interaction between waves and the floating body[1]. Indeed, it can be traced back to the well-known work of Archimedes[2]. Since then, the interest of researchers and engineers in this subject have never ceased[3][4][5][6]. In naval and ocean engineering, the concept of a meta-centre (denoted by M)[7][8][9][10] has been introduced to evaluate the initial stability of a floating body. It is defined as the intersection of two vertical axes passing through the center of buoyancy at two slightly different angles of heel. What is more, a well-known formulation has been derived, formulating

the distance between the buoyancy centre and the meta-centre with the ratio of the moment of inertia of the plane of flotation and the volume of the displaced fluid ($BM = I/\nabla$). A general criterion for the stability of a ship is commonly applied with the use of the meta-center, i.e., the ship remains stable provided the weight and the buoyancy create an upright moment after a limited inclination. Capsizing could happen if the sign of the moment is the opposite. Generally, the meta-centre is assumed consistent at a limited inclination angle ($< 8^\circ$)[11], in the scope of initial stability. Since the ship's hull is usually symmetric, the arm of the upright moment is dependent on the relative position of the meta-centre with respect to the centre of gravity (denoted by G)[12]. The floating state can be regarded as stable, neutral, or unstable when M is located above, on, or below G , respectively. In the preliminary phase of ship design, the stability curve is usually

used to characterize the capability of the hull's maintaining an upright floating state when subjected to limited inclinations. Therefore, the evaluation of the floating equilibrium would be significant for the design of floating structures, especially those involving large variations of weight. To simplify the problem, the present article will start with fundamental homogenous floating bodies.

Physically speaking, could a uniform and symmetric body float asymmetrically in still water? As the general criterion of hydrostatic stability of a floating body is commonly identified under a specified floating state, researchers have attempted to figure out the 'equilibrium' of a random floating state of some fundamental geometries such as a floating ball, circular cylinder, rectangular box, and so on. For example, Auerbach[13] demonstrated that a non-circular cylinder could float indifferently with respect to the cylinder's central axis. Likewise, Ulam[14] raised a question: whether a uniform body that is able to float stably at any orientation must be a sphere. Assuming the body's density ρ approaches zero, the problem is equivalent to whether a body's being able to hold on in any inclination on a horizontal plane is necessarily a sphere. As a partial answer, Montejano[15] proved that if a body with the above-mentioned character was connected, closed, and bounded, then its shell should be a sphere. This implies that the sphere is one possible geometry with the desired property. Consequently, Gilbert[1] analysed the stable floating equilibrium for several geometries such as an ellipsoid, cylinder and cube, employing the law of minimum energy which is further extended into more complex geometries by Mège[2]. More recently, a comprehensive review of the floating equilibria of regular solids has contributed to integrating the main results and predicting the potential for applications in engineering[5]. According to the above-mentioned research, a symmetric body is proven theoretically to be able to float asymmetrically. However, the proofs of equilibria are quite abstract, and an extensive investigation of the equilibrium curve is still needed. Also, the characteristics of an equilibrium are yet to be verified by physical experiment.

In naval and ocean engineering, the ship and offshore structures are commonly designed to float in an upright state[3][4][6]. Meanwhile, the consideration of the entire floating states is practical and crucial under certain circumstances such as improper loading and damage. In the present article, the entire equilibrium curve of stability is, for the uniform square prism and rectangular prism, derived in a more straightforward manner (these are similar to common geometries of a ship hull and of offshore structures like breakwaters and floating piers). Further, the characteristics of the equilibrium curves of a parabolic cylinder with arbitrary profile are extended. With respect to the previous results provided by Gilbert[1], several different characteristics of the equilibrium curve are observed and explained in terms of physics. Furthermore, the floating state of a uniform square prism has been investigated by experiments which validate the theoretical results and provide an experimental impression of the interesting phenomenon that a symmetric floating geometry could float asymmetrically in certain conditions. The present work could be regarded as

a preliminary for an extensive study of the floating stability of various more complex floating structures, and demonstrates the asymmetric floating state could be induced by improper loading and design of a floating body with a symmetric sectional profile.

MATHEMATIC MODELLING OF FLOATING EQUILIBRIUM

As shown in Fig. 1, the floating state of a uniform square prism can be represented by its transversal section under the assumption of its being a uniform body. According to Archimedes' principle, the ratio of the draught T to the depth D equals the ratio of the body's density ρ to the density ρ_w of the water, which is denoted by λ ($\lambda = T/D = \rho/\rho_w$). To identify the waterline, a vector \mathbf{n}_0 is defined normal to the original waterline (blue line) and oriented into the air. Then, the vector can be formulated as $\mathbf{n}(-\sin\theta, \cos\theta)$ where θ denotes the angle of inclination relative to the upright state. Setting the origin $O(0,0)$ fixed on the centroid of the immersed edge, the coordinate of the centre of gravity $G(0, D/2)$ and buoyancy $B_0(0, T/2)$ can be formulated at the upright state. Also, any arbitrary centre of buoyancy $B(B_y, B_z)$ can be formulated as a function of λ and θ . It should be noted that the meta-centre M will move along with B until an equilibrium is reached.

The floating states can be classified into two categories according to the geometry of the submerged volume, namely the quadrilateral prism (state 1) or triangular prism (state 2 which includes the critical state). A critical state can be recognized between the states 1 and 2, corresponding to a triangular prism of replacement volume. The floating angle of the critical state can be formulated as $\theta_c = \tan^{-1}(2\lambda)$. To reach a stable floating equilibrium, both the force balance and stability condition should be satisfied, namely $\overrightarrow{BG} \parallel \mathbf{n}$ and the vertical coordinate $M_z > G_z$. Thus, the possible floating equilibria can be sought through the variation of λ and θ . Since the floating state is symmetric, the observed range can be reduced to $\lambda \in (0, 1/2]$ and $\theta \in [0, \pi/4]$.

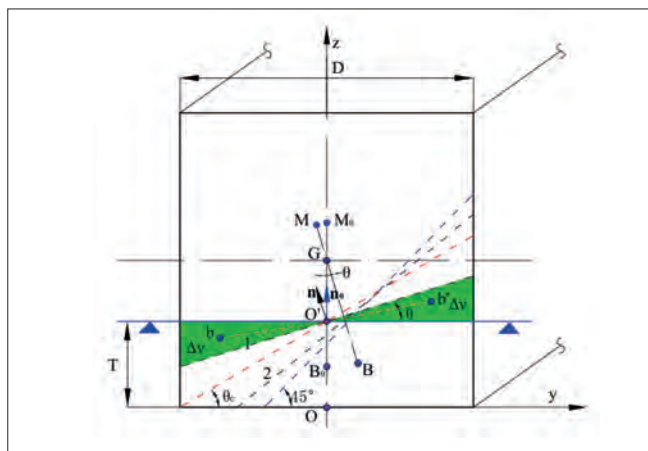


Fig. 1. Illustration of a floating square prism: the green area indicates the equivalent displaced volume of water due to the tilted angle θ ; the dashed lines refer to different cases of floating states (in anti-clockwise order: state 1 \rightarrow critical state $\theta_c \rightarrow$ state 2 $\rightarrow \pi/4$).

At state 1, i.e., $\theta \in [0, \theta_c)$, the following formulation can be obtained according to Archimedes' principle and the law of the translation of the centre of gravity:

$$(\mathbf{B} - \mathbf{B}_0)V = \Delta \mathbf{b} \Delta v \quad (1)$$

where \mathbf{B}_0 and \mathbf{B} refer to the two-dimensional coordinates of the buoyancy centre in the upright and inclined states, respectively. As shown in Fig. 1, \mathbf{b} indicates the centre of equivalently translated volume Δv with respect to the total submerged volume V . Substituting the force balance condition $\overrightarrow{BG} // \mathbf{n}$ into Eq. (1), one obtains

$$\theta = \cos^{-1}\left(\frac{1}{\sqrt{12\lambda(1-\lambda)-1}}\right) \quad (2)$$

which is valid in the domain $\lambda \in [\frac{3-\sqrt{3}}{6}, 1/2]$. Assuming the condition $\theta < \theta_c$ ($\theta_c = \tan^{-1}(2\lambda)$), the domain can be further reduced to $\lambda \in [\frac{3-\sqrt{3}}{6}, 1/4]$. Accordingly, the stable equilibrium $\theta = 0$ can be obtained in the domain $\lambda \in (0, (3-\sqrt{3})/6)$.

At state 2, the immersed section becomes a triangle in the domain $\theta \in [\theta_c, \pi/4]$. It should be noted that the point \mathbf{O}' is not the rotating axis of the flotation plane in this case. Thus, the method of equivalent volume displacement is not available in this case. Employing to the condition $\overrightarrow{BG} // \mathbf{n}$, one obtains

$$\theta = \frac{1}{2}\sin^{-1}\left(\frac{16\lambda}{9-16\lambda}\right) \quad (3)$$

which is valid in the domain $\lambda \in [0, 9/32]$. Assuming $\theta \geq \theta_c = \tan^{-1}(2\lambda)$, the domain can be reduced to $\lambda \in [1/4, 9/32]$. Analogously, the equilibrium $\theta = \pi/4$ can be derived in the domain $\lambda \in [9/32, 1/2]$.

In conclusion, the following formula is derived as a function of the angle of inclination θ and the draught ratio λ :

$$\theta = \begin{cases} 0, & \lambda \in (0, \frac{3-\sqrt{3}}{6}] \\ \cos^{-1}\left(\frac{1}{\sqrt{12\lambda(1-\lambda)-1}}\right), & \lambda \in (\frac{3-\sqrt{3}}{6}, \frac{1}{4}] \\ \frac{1}{2}\sin^{-1}\left(\frac{16\lambda}{9-16\lambda}\right), & \lambda \in (\frac{1}{4}, \frac{9}{32}] \\ \pi/4, & \lambda \in (\frac{9}{32}, \frac{1}{2}] \end{cases} \quad (4)$$

As shown in Fig. 2, the stable equilibrium angle θ versus λ is plotted. Notably, there are three inflection points (A, B and C) on the equilibrium curve in the domain $\lambda \in [0, 1/2]$. Observing the curve, one can see the discontinuity at points A and C, which implies severe change of floating state across these points. Comparing this curve with the curve obtained by Gilbert[1], the present curve coincides with it before the inflection point B, but behaves differently approaching to the peak angle, yielding two extra inflections points (B and C).

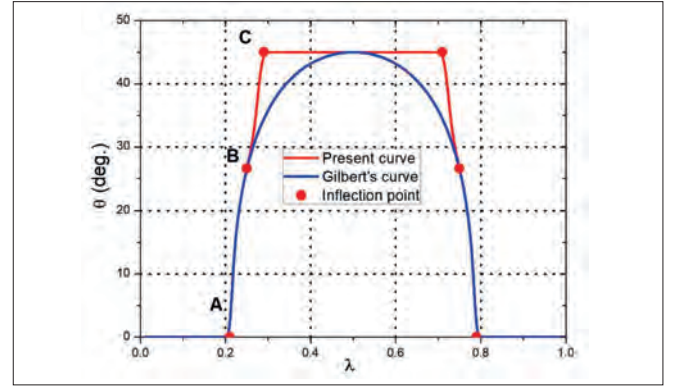


Fig. 2. The comparison of the present equilibrium curve with that of Gilbert [1].

Further, to analyse the implication of the inflection point A, equation (2) can be expressed as

$$\theta = \cos^{-1}(x) \quad (5)$$

where $x = \sqrt{12\lambda(1-\lambda)-1}$. Taking the derivative of λ , equation (5) can be rewritten as

$$\frac{d\theta}{d\lambda} = \frac{6x^2(1-2\lambda)}{\sqrt{1-x^2}} \quad (6)$$

According to equation (5), one can see that x approaches 1 and θ approaches zero when λ approaches $(3 \pm \sqrt{3})/6$. From equation (6), one can see the derivative will approach infinity when x approaches 1, which means it is a singularity and the slope approaches $\pi/2$ at point A.

Similarly, for the inflection point C, equation (3) can be rewritten as

$$\theta = \frac{1}{2}\sin^{-1}(x) \quad (7)$$

where $x = 16\lambda/(9-16\lambda)$. Taking the derivative of λ , equation (7) yields

$$\frac{d\theta}{d\lambda} = \frac{72}{\sqrt{1-x^2}(9-16\lambda)^2} \quad (8)$$

so, analogously, one can find that the derivative will approach infinity as θ approaches $\pi/4$, which implies there is also a singularity whose slope approaches $\pi/2$ at point C. As a result, θ varies severely when λ approaches these singularities.

Meanwhile, the inflection point B is associated to a transitional floating state between states 1 and 2, corresponding to the critical stable equilibrium $\theta = \theta_c$. Combining equation (6) and equation (8), the identical real derivative ($d\theta/d\lambda = 4.8$) can be obtained approaching from both the increasing and decreasing direction. This implies the floating state varies continuously across the inflection point.

PRISM WITH ARBITRARY RECTANGULAR SECTION

The equilibrium curve of a prism with arbitrary rectangular section can be explored extensively. As shown in Fig. 3, the section of the prism has breadth D and width W (we assume $W > D$). Therefore, the prism will tend to float on the larger

face to be at the minimum of potential energy [1]. Likewise, the relation between θ and the upright draught T can be derived as listed in Table 1, where the floating equilibrium is found dependent on the aspect ratio (D/W) and upright draught T . The critical draughts T_1 , T_2 and T_3 are formulated as follows:

$$\begin{aligned} T_1 &= \frac{3D - \sqrt{9D^2 - 6W^2}}{6}; \\ T_2 &= \frac{3D - \sqrt{9D^2 - 8W^2}}{8}; \\ T_3 &= \frac{3D + \sqrt{9D^2 - 8W^2}}{8} \end{aligned} \quad (9)$$

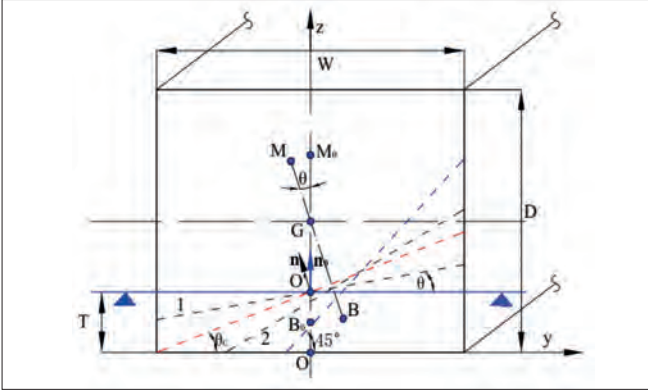


Fig. 3. Illustration of a floating prism with arbitrary rectangular section: the dashed lines refer to varied floating states (in anti-clockwise order, state 1 \rightarrow critical state $\theta_c \rightarrow$ state 2 $\rightarrow \pi/4$)

Tab. 1. The floating equilibria for prism with arbitrary rectangular section

D/W	T	Floating equilibrium
$(0, \sqrt{6}/3)$	$(0, D/2]$	$\theta = 0$
$[\sqrt{6}/3, \sqrt{8}/3]$	$(0, T_1)$	$\theta = 0$
	$[T_1, D/2]$	$\theta = \tan^{-1} \left(\sqrt{\frac{12D(D-T) - 2W^2}{W^2}} \right)$
$[\sqrt{8}/3, 1]$	$(0, T_1)$	$\theta = 0$
	$[T_1, T_2]$	$\theta = \tan^{-1} \left(\sqrt{\frac{12D(D-T) - 2W^2}{W^2}} \right)$
	(T_2, T_3)	$T = \frac{9 \tan \theta (D \tan \theta - W^2)^2}{8W(\tan^2 \theta - 1)^2}$
	$[T_3, D/2]$	$\theta = \tan^{-1} \left(\sqrt{\frac{12D(D-T) - 2W^2}{W^2}} \right)$

Analogously, the floating equilibria can be derived in terms of the sectional aspect ratio, assuming the symmetry of the floating state. Furthermore, the equilibrium curves of a prism with varied aspect ratios (D/W) can be derived where the inflection points (the non-zero inflection points) can be observed distributed along lines as shown in Fig. 4. According to Fig. 4(a), a non-zero floating angle exists when the aspect ratio D/W is approximately larger than 0.82, which implies that asymmetrical floating states tend to occur at relatively large values of D/W . Otherwise, the prism would float symmetrically at any draught. That's why in most circumstances, only symmetric floating states are observed. Interestingly, the equilibrium curve is smooth when the sectional aspect ratio is less than around 0.96. Under this circumstance, the angle of inclination is less than the critical

angle which could yield an inflection point. Note that there are two non-zero inflection points for each curve in the domain $\lambda \in [0, 0.5]$. Specifically, one inflection point approaches to around 25° and the other one approaches 45° with an increase of D/W . As shown in Fig. 4(b), the distribution of inflection points can be regressed into a linear function ($\theta = 73.1\lambda + 8.2$), except for the singular inflection point of $D/W = 1$.

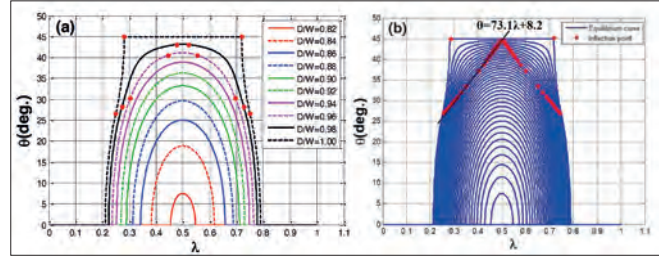


Fig. 4. The distribution of equilibrium curves and corresponding inflection points: (a) equilibrium curves for different sectional aspect ratios; (b) the distribution of inflection points and regressed function.

PARABOLIC CYLINDER

To illustrate the potential applications in naval and ocean engineering, the study of equilibrium is further extended to floating parabolic cylinders. As shown in Fig. 5, the parabolic profile curve can be assumed as the cross-section of a ship. To present the approach in a simplified manner, the cylinder is assumed uniform and then the centre of gravity $G(0, T(3D^2 - 5L^2)/5DL^2)$ can be derived, where T , D and L refer to the draught, breadth and the width of the flotation plane in the upright state, respectively.

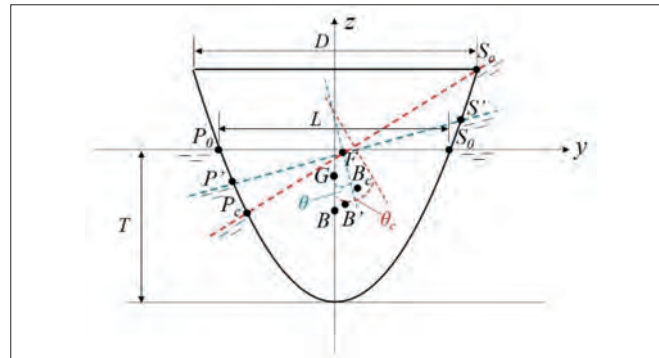


Fig. 5. Schematic section of a floating parabolic cylinder.

To generalize the derivation, the parabolic profile is written in a non-dimensional formula:

$$Z = KY^2 - N \quad (10)$$

where $Z = z/D$ and $Y = y/D$. The parameters K and N can be formulated as follows:

$$\begin{aligned} K &= \frac{4TD}{L^2} \\ N &= \frac{T}{D} \end{aligned} \quad (11)$$

Further, the area of the immersed section can be derived as $A = 2TL/3D^2$. As illustrated in Fig. 5, assuming the cylinder

floats stably at an angle of inclination θ , the buoyancy centre translates from B to B' and the floatation line P_0S_0 becomes $P'S'$. For each specified floating cylinder, the maximum inclination angle θ_c is defined as the topside of the cylinder's contact with the water, yielding the corresponding floatation line P_cS_c . According to the conservation of the displaced volume and equation (10), the abscissas of the endpoints (P' and S') at inclination angle θ can be formulated as follows:

$$Y_{P'} = -\frac{L}{2D} + \frac{L^2}{8TD} \tan\theta \quad (12)$$

$$Y_{S'} = \frac{L}{2D} + \frac{L^2}{8TD} \tan\theta \quad (13)$$

In addition, θ_c can be obtained when $Y = 1/2$:

$$\theta_c = \tan^{-1}\left(\frac{4T(D+L)}{L^2}\right) \quad (14)$$

Therefore, the coordinate of the buoyancy centre can be obtained by calculating the double integral over the immersed section [13], taking into consideration the conservation of the area A of the immersed section. The coordinate of the buoyancy centre B can be formulated as follows:

$$Y_{B'} = Y_F + \frac{D^2}{A} \left[\frac{1}{12} L_\theta^3 \sin\theta \cos^2\theta + \int_{Y_{P'}}^{Y_{S'}} (Y_F - Y) Z dY \right] \quad (15)$$

$$Z_{B'} = Z_F + \frac{D^2}{A} \left[\frac{1}{2} L_\theta \left(\frac{1}{12} L_\theta^2 \sin^2\theta - Z_F^2 \right) \cos\theta + \int_{Y_{P'}}^{Y_{S'}} \left(Z_F Z - \frac{1}{2} Z^2 \right) dY \right] \quad (16)$$

where $L_\theta = (Y_{S'} - Y_{P'})$ is the length of the floatation line at an inclination angle of θ . Point F refers to the floatation centre, which is located at the centre of the line $P'S'$. Therefore, the coordinates of F are

$$Y_F = \frac{L^2}{8TD} \tan\theta \quad (17)$$

$$Z_F = \frac{L^2}{16TD} \tan^2\theta \quad (18)$$

Substituting equations (10), (12), (13), (17) and (18) into equations (15) and (16), the coordinate of B' can be derived as follows:

$$Y_{B'} = \frac{L^2}{8TD} \tan\theta \quad (19)$$

$$Z_{B'} = -\frac{2T}{5D} + \frac{L^2}{16TD} \tan^2\theta \quad (20)$$

Note that the abscissas of B' and F are identical [2]. According to Bouguer's theorem [16], the distance between B' and the metacentre M can be expressed as follows:

$$d_{B'}^M = \frac{I}{V} \quad (21)$$

where I and V refer to the moment of inertia of the plane of floatation and the immersed volume, respectively. Taking into consideration the homogeneity of the cylinder in the longitudinal direction, equation (19) can be simplified to

$$d_{B'}^M = \frac{R}{A} \quad (22)$$

where R denotes the moment of inertia of the floatation line with respect to F , which can be calculated as follows:

$$R = \int_{-\frac{1}{2}L_\theta}^{\frac{1}{2}L_\theta} s^2 ds = \frac{1}{12} L_\theta^3 \quad (23)$$

where L_θ is the floatation line at an inclination angle of θ , which can be written as $(Y_{S'} - Y_{P'})/\cos\theta$. Substituting equations (19), (20) and (23) into equation (22), the coordinates of M can be derived:

$$Y_M = \frac{L^2}{8TD} \tan^3\theta \quad (24)$$

$$Z_M = -\frac{2T}{5D} + \frac{L^2}{16TD} \left(\frac{3}{\cos^2\theta} - 1 \right) \quad (25)$$

To investigate the characteristics of the equilibrium curve practically, we confine the parameter $K \in [2, 3]$. Similarly, we use the relative density λ as the variant; it can be obtained as follows:

$$\lambda = \frac{\rho}{\rho_w} = \frac{L^3}{D(D^2 - L^2)} \quad (26)$$

According to equation (26), we can obtain the relation between the normalized draught and floatation line $T/D = KL^2/4D^2$. The equilibrium can be calculated by the conditions of force balance and stability as described before. Furthermore, the equilibrium curve can be derived along with $L/D \in (0, 1]$. Fig. 6(a) shows the profiles of a series of parabolic cylinders in the range $K \in [2, 3]$. The corresponding stable equilibrium curves are given in Fig. 6(b), where one can recognize the continuity of the equilibrium curves, located between approximately 60 degrees to 70 degrees. Also, the angle of inclination is increasing with an increase in the topological parameter K . Exploring a broader range of K , the equilibrium curve is found to be discontinuous (inflection points exist) for K around 1 (as shown in Fig. 7). Fig. 8 shows more profiles and their corresponding equilibrium curves around $K = 1$, through which the inflection point is found to be in the range $K \in [0.9, 1.7]$. Taking the parabolic cylinder as a vessel, we can conclude that the draught span for stable upright flotation is wider when the block coefficient becomes larger. As shown in Fig. 8(c), the distribution of the inflection points can be further formulated as

$$\theta = -1.71 \ln(\lambda) + 55.684 \quad (27)$$

where $\lambda \in (0, 1]$. The above formulation can be applied to estimate the angle of inclination for a specified draught when a discontinuity exists in the equilibrium curve. Those inflection points should be noted during the operation of the ship to avoid a severe variation of the floating state.

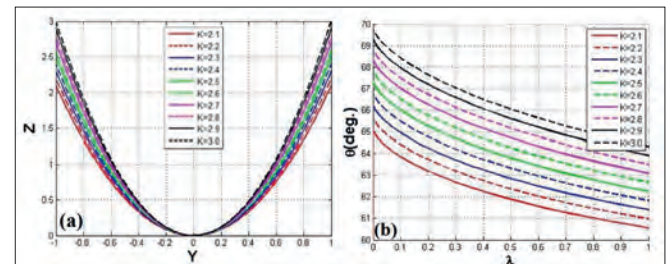


Fig. 6. Profiles of a series of parabolic cylinders (a) and their corresponding equilibrium curves (b) for $K \in [2, 3]$.

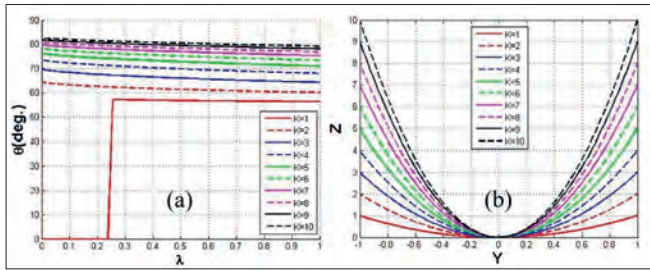


Fig. 7. The distribution of equilibrium curves (a) and corresponding profiles (b) for $K \in [1, 10]$.

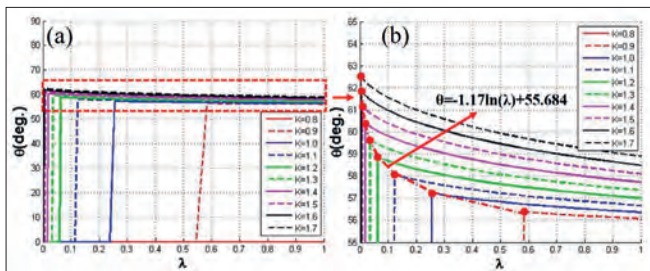


Fig. 8. A series of equilibrium curves (a) for $K \in [0.8, 1.7]$, where the distribution of the inflection points (labeled by rectangles in (a)) is regressed (b).

EXPERIMENTAL VERIFICATION

To verify these theoretical results, an experiment was conducted in the flume of the laboratory LOC (Laboratório de Ondas e Correntes) of the Federal University of Rio de Janeiro. As shown in Fig. 9, a hollow square prism with 5×5 grid was designed to simulate a uniform prism whose weight can be adjusted by filling the grids symmetrically with ballast. In these tests, uniform iron bars with different diameters were applied as ballast: their lengths are identical to that of the prism. Waterproof foam lids were used on both ends. The minimum relative density of the prism (i.e., a hollow prism) was 0.06 and the maximum about 0.87, as listed in Table 2. For each round of testing, the prism was released from an upright state and the inclination angle measured after the reaching of a stable floating state. As shown in Fig. 10, various floating states can be observed, including several asymmetrical ones.

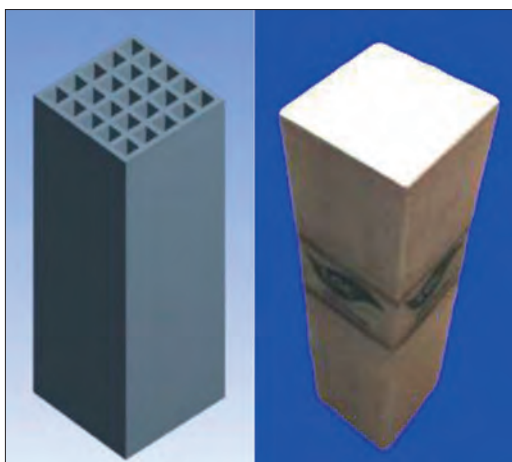


Fig 9. The hollow model with 5×5 grid structure (left) and the practical prism model with lids prepared for testing (right).

Tab. 2. The test matrix and stable floating angle.

Case	Relative density	Stable angle(°)	Case	Relative density	Stable angle(°)
1	0.06	0	10	0.46	45
2	0.20	13	11	0.51	45
3	0.23	24	12	0.56	45
4	0.26	28	13	0.61	45
5	0.29	31	14	0.67	44
6	0.32	44	15	0.72	42
7	0.36	44	16	0.76	27
8	0.39	45	17	0.81	14
9	0.42	45	18	0.87	1

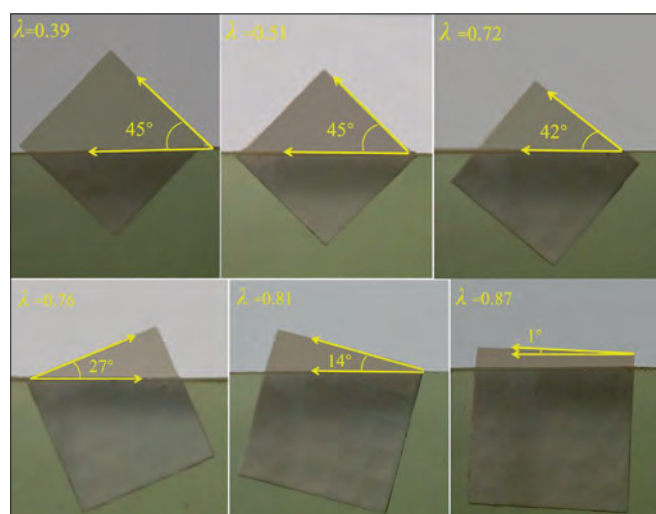


Fig. 10. The typical floating states corresponding to the cases in Table 2.

As shown in Fig. 11, the experimental results have been compared with the analytical results and the results of [1]. Overall, the present analytical results agree better with the experimental results than do those of [1]. It can be noted that the scatter of the experimental results deviates slightly from the analytical results near the inflection points. This is because the floating state becomes quite sensitive to the relative density near those inflection points. The experimental uncertainty should also be responsible for the deviation, due to the machining and assembly error of the square prism. Further, the symmetry of the floating equilibrium curve is also verified by the experimental results, with respect to the centerline at $\rho/\rho_w = 0.5$. It is worth noting that the inflection points revealed in the present work make the equilibrium curve possess a significant 'plateau' and narrow transition range from $\theta = 0^\circ$ to 45° . According to the present floating equilibrium curve, one should note that the magnitude of draught of floating body could affect the stable floating state significantly, which, for many floating structures, must be strictly supervised to avoid operational risks. For example, the relative density of a fully loaded cubic barge is usually larger than 0.8, thus its normal stable floating angle is zero. However, improper loading could make the relative density collapse to 0.2~0.8. Therefore, an initial inclination of the vessel

may occur which could lead to capsizing. In conclusion, the equilibrium curve should be considered by the designer and operator of floating structures whose relative density or weight could be varied frequently, in addition to the use the equilibrium curves to adjust the floating state actively.

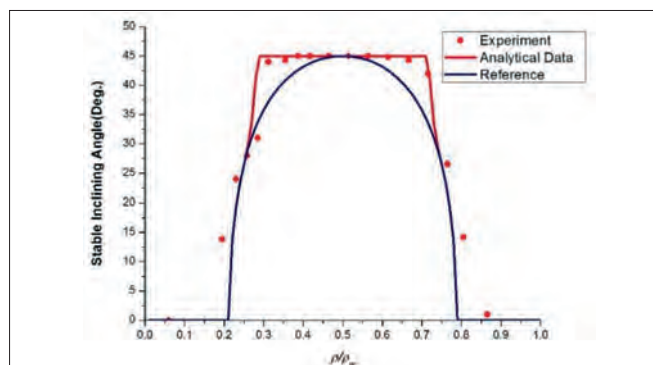


Fig. 11. Comparison of analytical and experimental results

CONCLUSIONS

In the present article, the phenomenon that symmetric geometries can float asymmetrically has been studied analytically and experimentally. The intact floating equilibrium curve for a prism and a parabolic cylinder have been derived in detail, finding several characteristics which are revealed as different from those found in the literature. The characteristics of the inflection points in the equilibrium curve have been analysed, providing an improved interpretation of them in physical terms. Generalizing these results, the analysis of floating equilibria has been extended to prisms with arbitrary rectangular section. Some interesting features are revealed concerning the distribution of the equilibrium curves corresponding to a series of sectional aspect ratios. To illustrate the case of a vessel, the floating equilibrium of a parabolic cylinder was further investigated. The characteristics of its equilibrium curves have been obtained analytically, which could be meaningful to the design of floating structures in naval and ocean engineering.

Moreover, to verify the floating equilibrium curve, experiments were conducted with a uniform square prism with adjustable relative density. According to the experimental results, good agreement is reached relative to the presented analytical results. In terms of the applications of equilibrium curves, the behaviour of the floating equilibrium should be understood and could be taken advantage of to avoid a damaging event of floating structures and enhance the efficiency of operation, especially for those floating vessels with a frequent variation of loading. The present study illustrates an approach to comprehend the floating equilibrium through several fundamental geometries, which can be extended to the investigation of the floating equilibrium of more complex geometries in future work. Besides, the two-dimensional floating state should also be considered in the future, namely considering both transversal and longitudinal inclination simultaneously, which will be more practical for applications.

ACKNOWLEDGMENT

The study is financed in part by the CNPq (Conselho Nacional de Pesquisa-Brazilian National Research Council), the National Natural Science Foundation of China (52201304 and 52271336), which are gratefully acknowledged. The colleagues from LOC have contributed with efforts and ideas, which are gratefully appreciated.

REFERENCES

1. E. N. Gilbert, "How things float," *Journal American Mathematical Monthly*, vol. 3, pp. 201 216, 1991.
2. J. Mégel and J. Kliava, "Metacenter and ship stability," *American Journal, American Association of Physics Teachers*, vol. 78, no. 7, pp. 738 747, 2010.
3. A. Karczewski, "The Influence of The Cuboid Float's Parameters on The stability of A Floating Building," *Polish Maritime Research*, vol. 27, no. 107, pp. 16 21, 2020.
4. J. Li, "Analysis of The Dynamic Response of Offshore Floating Wind Power Platforms in Waves," *Polish Maritime Research*, vol. 27, no. 108, pp. 17 25, 2020.
5. K. J. Spyrou, "The stability of floating regular solids," *Ocean Engineering*, vol. 257, no. 111615, 2022.
6. D. G. AS, *RULERS FOR CLASSIFICATION: Inland Navigation vessels, part 6 Additional class notations*, 2015.
7. H. Auerbach, "Sur un problem de M. Ulam concernant l'équilibre des corps flottants (On a problem of Mr. Ulam concerning the equilibrium of floating bodies)," *Studia Math*, vol. 7, pp. 121 142, 1938.
8. C. L. Bernard, *Stability and equilibrium of floating bodies*, London: Constable and Company Limited, 1914.
9. V. Bertram, *Practical ship hydrodynamics*, 2nd ed., Oxford: Elsevier Butterworth Heinemann, 2012.
10. A. Biran, *Ship hydrostatics and stability*, 1st ed., Oxford: Elsevier Butterworth Heinemann, 2003.
11. S. N. Blagoveshchensky, *Theory of ship motions* (Transl. from the 1st Russian edition), New York: Dover Publications, 1962.
12. H. E. Rossell and L. B. Chapman, *Principles of Naval Architecture, Vol. 1*, New York: Soc. Naval Architecture and Marine Engineering, 1941.
13. E. H. Lockwood, *A book of curves*, Cambridge University Press, 2007.

14. S. M. Ulam, "A collection of mathematical problems," *Science*, vol. 132, pp. 665-666, 1960.
15. L. Montejano, "On a problem of Ulam concerning a characterization of the sphere," *Studies in Applied Mathematics*, vol. 3, pp. 243-248, 1973.
16. P. Bouguer, *Traité du Navire, de sa construction, et de ses mouvemens* (Treatise on Ship's Construction and Movements), Paris: Jombert, 1746.
17. K. D'Angremond and F. C. Van Roode, *Breakwaters and Closure Dams*, London: Spon Press, 2004.
18. P. Erdős, G. Schibler and R. C. Herndon, "Floating equilibrium of symmetrical objects and the breaking of symmetry, Part 1: Prisms," *Am. J. Phys.*, *Am. J. Phys.*, vol. 60, no. 4, pp. 335-345, 1992.
19. H. Ghassemi, I. Ghamari and A. Ashrafi, "Numerical Prediction of Wave Patterns Due to Motion of 3D Bodies by Kelvin-Havelock Sources," *Polish Maritime Research*, vol. 23, no. 92, pp. 46-58, 2016.
20. T. L. Heath, *The works of Archimedes*, Dover Publications, 2005.
21. K. J. Rawson and E. C. Tupper, *Basic Ship Theory*, 5th ed., London: Longman, 2001.
22. D. R. Derrett and C. B. Barras, *Ship stability for masters and mates*, 6th ed., Oxford: Elsevier Butterworth-Heinemann, 2006.

HYDRODYNAMIC LOADS ON A SEMI-SUBMERSIBLE PLATFORM SUPPORTING A WIND TURBINE UNDER A MOORING SYSTEM WITH BUOYS

Thomas Mazarakos ¹

Theodosis Tsaousis²

¹ Department of Naval Architecture, School of Engineering, University of West Attica, Egaleo, Attica, Greece

² School of Naval Architecture and Marine Engineering, National Technical University of Athens, Zografos Campus, Athens, Greece

* Corresponding author: tmazar@uniwa.gr (T. Mazarakos)

ABSTRACT

In this study, the effect of a 10MW DTU wind turbine (WT) on a semi-submersible platform is examined from the point of view of its dynamic behaviour as part of a mooring system with attached buoys. The platform has a rectangular geometry, and consists of four offset and one main cylindrical members. The structure is assumed to receive both wave and wind loading simultaneously. A coupled analysis within the frequency domain is performed using two boundary element method software packages, NEMOH and HAMS. The results are presented in the form of parametric graphs for each of the software packages used and for varying wave directions. The graphs show the hydrodynamic loads exerted on the platform, the wave elevation, the added masses, the hydrodynamic damping coefficients, the mooring line tensions, and the Response Amplitude Operators (RAOs) for the motion of the platform.

Keywords: Hydrodynamic loads; Semi-submersible platform; Wind turbine; Mooring system; Catenary line; Buoys; RAO

INTRODUCTION

Solar, wind and wave energy are unquestionably some of the cleanest forms of energy. Both on land and at sea, they can offer essential resources for the production of electrical power that is sufficient to cover the needs of thousands of homes. It is also clear that the development of alternative forms of energy contributes to the reduction of greenhouse emissions.

In particular, the design of offshore structures for the exploitation of these natural resources, and consequently for the production of renewable energy, is a continuously growing field of research, since most of these technologies are still in their infancy. Despite their limited efficiency compared to onshore renewable systems, several types of structures have been designed with the intention of utilising the vast available potential lying offshore. Floating photovoltaics (FPV) systems have been developed relatively recently in Portugal, Brazil, Japan,

and other countries worldwide, and research on installation locations, cooling mechanisms, efficiency improvements and mooring systems is available in the literature [1-5].

The general principle of operation of a wave energy converter (WEC) is based on the action of waves to produce electricity. There are many types and configurations that have been discussed in the literature [6-9]. Studies of mooring systems for WECs can be found in references [10-13]. More sophisticated hybrid designs have been developed that combine oscillating water column (OWC) devices with floating wind turbines (WTs) [14, 15].

Offshore WTs are used to exploit the potential offered by the wind out at sea. Depending on the water depth in the region of installation, they are either fixed to the bottom of the sea or are allowed to float. The most common types of fixed systems are monopiles and jacket structures [16-19]. However, when the water depth is greater than 50 m, floating structures are needed. Floating WTs may be cost-effective at depths where fixed WTs

are impossible to install, or where the cost is excessively high due to large water depths. One type of structure is a spar-buoy, typically in the form of a cylindrical floater that supports the WT [20-22]. Another type is a semi-submersible platform, which consists of one main, central and some offset cylinders, the exact number of which depends on the geometry of the floater [23, 24]. Fully coupled hydro-aero-elastic analyses of this structure were conducted in [25, 26].

A floating structure is moved from its initial equilibrium position by the forces exerted on it through the combined action of waves and wind. A design that includes a suitable mooring system is therefore urgently needed. A typical fixed structure used in deep water is a Tension Leg Platform (TLP) [27-30]. In this case, the floating structure is permanently moored using tendons, which restrict the platform to very small heave motions due to the large pretension along the z-axis.

Taut-leg mooring lines are also used; in this case, the mooring cables form an angle with the seabed, and the anchoring point needs to withstand both horizontal and vertical forces. Another type of mooring system is based on the use of catenary lines which lie horizontally at the seabed, and may also include clump weights or buoys [31, 32]. A finite difference analysis of a catenary riser was presented in [33]. The buoys may either be positioned at the surface or fully submerged to provide some additional buoyancy, in which case the weight on the mooring lines is decreased and their dynamic behaviour and performance are enhanced. The impact of using submerged buoys on the dynamic tension of the mooring line was numerically and experimentally investigated in [34]. The use of buoys can decrease the tension, provided that their position, size, and number are carefully considered. In order to assess the impact of submerged buoys on the dynamic behaviour of the mooring line, the previous study was extended by using numerical methods in the time and frequency domains [35]. The effects of two hybrid taut mooring lines on the motion of a semi-submersible platform and the tension in these lines have also been studied [36]. These systems combine the use of weights and buoys along the mooring line. In [37], the authors discussed the effects of buoys on the dynamics of a semi-submersible platform, and explored how the system's operational capacity could be increased by adding more buoys to the system in deep and very deep waters. Finally, several configurations of catenary and taut mooring systems for a semi-submersible 5MW WT in shallow waters, involving different materials, mooring components and anchors, were examined in [38]. The material of the mooring lines has also been found to be a key parameter affecting the strength of the system [39, 40].

In this study, we perform a coupled analysis of a catenary line with buoys. The solution to this problem is split into two main parts: firstly, we need to identify how the WT affects the dynamics of the coupled problem, and secondly, we need to solve for the motion of the total floating structure. The effect of the WT is defined by means of inertial, gyroscopic, and gravitational effects, as well as aerodynamic loading. We therefore need to calculate the added mass, damping and stiffness matrices of the WT. To this end, a Hamiltonian dynamic analysis based on blade element momentum theory is employed. This issue is not elaborated in detail within this particular study, and the

reader is referred to the literature instead. The hydrodynamic part of the problem was solved using the open-source codes NEMOH [41] and HAMS [42].

GEOMETRY OF THE SEMI-SUBMERSIBLE PLATFORM AND THE CLUMP BUOYS MOORING SYSTEM

The semi-submersible platform considered here accommodates a 10 MW DTU WT [43]. The water depth at the installation site is 200 m, and the draft of the floating platform is 20 m. A three-dimensional schematic representation of the platform and the mooring system is provided in Figure 1. The floater is rectangular, and is composed of one main, central column and four offset column-cylindrical tubes at each corner of the floater. Thinner, horizontal, and inclined tubular members connect these members to provide the required buoyancy, along with cross braces. Top and side views of the floater are shown in Figures 2 and 3. To reach the top of the main column of the floating platform, the tower of the WT is cantilevered at a height of 10 m above the still water level (SWL). For the purposes of this study, the main parts of the WT that are considered in the analysis are the rotor-nacelle assembly, the tower, and the three blades.

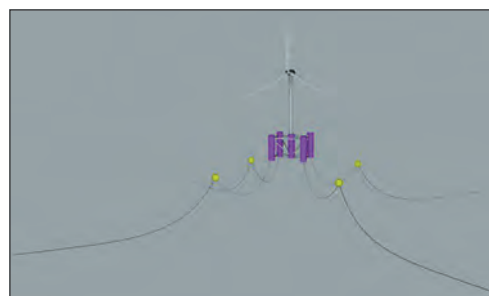


Fig. 1. Rectangular semi-submersible platform supporting the 10MW WT, shown in 3D with the mooring system and buoys

In the static equilibrium position in still water, the platform has a mass of 7,728,000 kg, including all the weights involved and any additional ballast that may be required. The platform's centre of mass (CM), including the ballast, is located along its centreline and 9.91 m below the SWL. The roll and pitch inertias are 7,730,000,000 kgm², while the yaw inertia is 6,700,000,000 kgm².

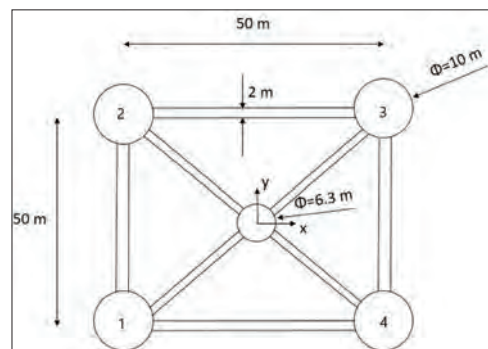


Fig. 2. Top view of the rectangular semi-submersible platform

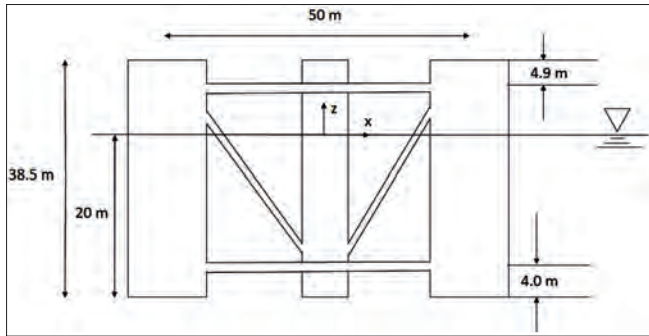


Fig. 3. Right side view of the rectangular semi-submersible platform

Four catenary lines make up the mooring system, each of which has a buoy attached to it. All of mooring lines (and their segments) are made from the same material (R4-RQ4, studless chain, steel). The selected geometrical configuration for the mooring system ensures a zero total sum of the forces in the horizontal and transversal directions. Table 1 lists the mechanical, geometrical and physical characteristics of the mooring system. The points at which the mooring lines are attached to the platform are 14 m below the free surface, and their respective coordinates are given in Table 2.

Tab. 1. Physical, geometrical and mechanical properties of the mooring system with buoys

Number of mooring lines (two elements each, separated by an attached buoy)	4
Angle between two consecutive lines	90°
Water depth	200 m
Depth to fairleads below SWL	14 m
Radius of the mooring system measured from the centre of the platform	635 m
Radius of the mooring lines attachment points measured from the centre of the platform	40.868 m
Total length of the mooring lines	835.5 m
Length of the first segment	484.5 m
Length of the second segment	351.0 m
Diameter of first segment	0.087 m
Diameter of first segment	0.040 m
Mass of the lines per unit length in the air (first segment)	151kg/m
Mass of the lines per unit length in the air (second segment)	30.00kg/m
Weight of the lines per unit length in the water (first segment)	1400 N/m
Weight of the lines per unit length in the water (second segment)	240 N/m
Buoy's Net Buoyancy (NB)	176000 N
Pretension at the top of each mooring line (Tp)	600000 N
Stiffness of mooring lines $K_{xx} = K_{yy}$	140000 N/m

Tab. 2. Coordinates of the mooring lines

Mooring line (#)	Upper attachment point (x, y, z)	Lower attachment point (x, y, z)
1	(-28.56, -28.56, -14)	(-449, -449, -200)
2	(-28.56, 28.56, -14)	(-449, 449, -200)
3	(28.56, 28.56, -14)	(449, 449, -200)
4	(28.56, -28.56, -14)	(449, -449, -200)

By identifying the forces acting on an element of the mooring line (in the 2D xz-plane), we can obtain the following two generic equations for the normal and tangential directions [44; p.258]

$$dT - \rho g A dz = [w \sin \varphi - F(1 + \frac{T}{EA})] ds \quad (1)$$

$$T d\varphi - \rho g A z d\varphi = [w \cos \varphi + D(1 + \frac{T}{EA})] ds \quad (2)$$

where D and F are the mean hydrodynamic forces per unit length in the normal and tangential directions, respectively, w is the weight per unit length of the line in the water, A is the cross-sectional area of the mooring line, E is the elastic modulus, T is the line tension, φ is the angle between the line and the horizontal, and s is an independent parameter along the mooring line. Figure 4 shows a 3D view of the suspended mooring line system, while Figure 5 shows the configuration of one mooring catenary line under various external forces.

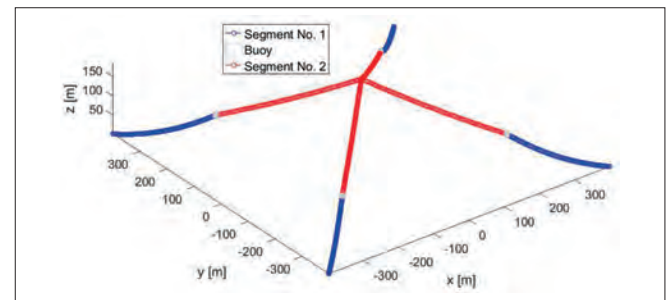


Fig. 4. 3D view of the suspended mooring line system

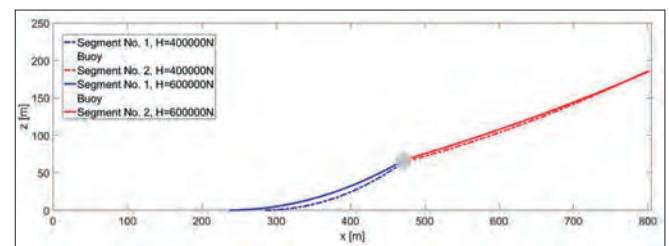


Fig. 5. One-line configuration under different external forces

DISCRETIZATION OF THE FLOATING STRUCTURE AND A FULLY COUPLED ANALYSIS

SOLUTION TO THE HYDRODYNAMIC PROBLEM

As discussed in the introduction, the solution to the coupled problem is found by solving the hydroelastic problem and quantifying the contribution of the WT, by calculating the

added mass, damping and stiffness matrices of the WT (which are superimposed onto those of the floating structure).

The hydrodynamic problem is addressed in the context of the boundary element method (BEM). We treat the problem in 3D, assuming an incompressible, inviscid and irrotational flow so that the linear potential theory can be utilised, and the coordinate system is defined in Figures 2 and 3. For the hydrodynamic calculations of this study, we use BEM solvers called NEMOH and HAMS. NEMOH is an open-source BEM solver developed by the Ecole Centrale de Nantes [41], which solves the linear boundary value problem by using a generalised mode approach and source distribution for the Green function. In the literature, comparisons of results obtained using NEMOH with those from the well-known BEM solver WAMIT have demonstrated satisfactory accuracy. In addition to NEMOH, we also used the open-source BEM solver HAMS, again using the potential flow theory, with a code written in the FORTRAN 90 language [42]. The solver uses boundary integral equations to represent the scattered wave potentials. In both cases, the solvers give several outputs, but the ones considered in this study are the first-order hydrodynamic coefficients, i.e., the added mass, the radiation damping and excitation forces. We also note that the motions of the floater are calculated only with HAMS, as NEMOH v.2 does not allow for calculation of the RAOs of the structure.

In order to solve the problem numerically, the wetted surface of the structure is subdivided into plane facets with a triangular or quadrilateral shape. The panel subdivision of the configuration used here is depicted in Figures 6 and 7. A total of 1500 elements were used to discretise the wetted surface of the body in NEMOH (without the braces), and 7,696 elements were used for discretisation with HAMS (with the braces).

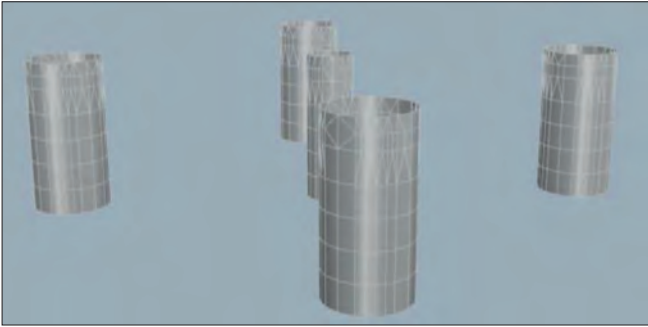


Fig. 6. Panel discretization – NEMOH

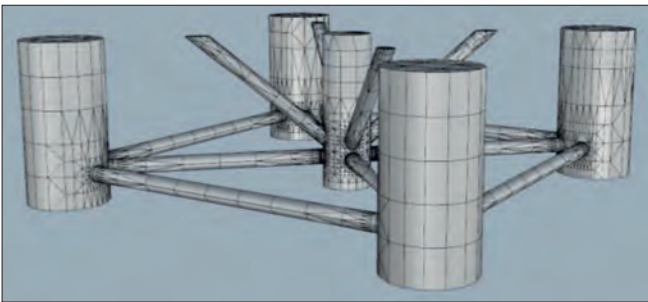


Fig. 7. Panel discretization – HAMS

The impact of the WT on the dynamic behaviour of the floater also needs to be discussed. Due to the presence and operation of the WT (including gravitational and inertial/gyroscopic effects, and aerodynamic loading), the forces owing to the added

masses, damping coefficients, and stiffness coefficients actually superinduce the external loads. Nevertheless, given that the purpose of our study is to focus on the dynamic behaviour of a floating structure subjected to external wind and wave loads, an aerodynamic analysis of the WT is not carried out. The reader is referred to [29] for more details on this issue.

The total mass of the WT is 1,200,000 kg and mass of the tower is 563,000 kg. The mass of the hub is 106,000 kg, and that of the nacelle is 406,000 kg (Figure 1). The total mass of the three blades is 126,000 kg [43].

COUPLED EQUATIONS OF MOTION

After obtaining the solution to the hydrodynamic boundary value problem and defining the multifaceted effects of the WT, we now calculate the responses of the platform. Following Newton's second law, the coupled dynamic equations of motions can be described as follows [29]:

$$\sum_{j=1}^6 \left\{ -\omega^2 [(M_{ij} + A_{ij}) + A_{ij}^{WT} + \frac{i}{\omega} (B_{ij} + B_{ij}^{WT})] + C_{ij, hydro} + C_{ij, mooring} + C_{ij}^{WT} \right\} x_{j0} = F_i, \quad i=1, \dots, 6 \quad (3)$$

where

M_{ij} : mass of the platform

A_{ij} : added mass

B_{ij} : hydrodynamic damping

$C_{ij, hydro}$: hydrostatic stiffness

$C_{ij, mooring}$: stiffness coefficients of the mooring lines

F_i : first-order wave loads, matrices of the floating platform

The equations of motion are solved in the frequency domain.

The matrices of the WT are denoted as follows:

A_{ij}^{WT} : added mass

B_{ij}^{WT} : damping

C_{ij}^{WT} : stiffness.

In this approach, the contribution of the WT is modelled as an external loading due to inertial, gyroscopic, gravitational, and aerodynamic effects, by introducing the last three of these matrices (subscript WT) into the dynamic equation of motion of the floating platform.

The hydrodynamic pressures are integrated over the entire wetted surface of the floater to derive the exciting forces on the right-hand side of Equation (3). These hydrodynamic pressures are caused by (i) the potential arising from the incident wave, and (ii) the diffraction/radiation potential. They are calculated in a straightforward way with the aid of Bernoulli's equation.

NUMERICAL RESULTS: COMPARISON AND DISCUSSION

In this section, we present the most important numerical results. We compare the exciting forces to those originating from the added masses and damping coefficients for the floating structure, both with and without braces. The figures cited here represent the RAOs of the motions of the floating platform. Particular attention is also paid to the free surface elevation around the floating structure,

both in 2D and 3D, as well as to the mooring tensions exerted on the mooring lines at the point where they are attached to the floater (for the coordinates of this point, see Table 2). Finally, the results are discussed in terms of the wave direction, the wave frequency, and the qualitative behaviour of each graph, and their maximum values. The numerical results presented in the following correspond to regular waves of height $H = 2$ m.

EXCITING FORCES AND MOMENTS

The excitation forces and the wave moments are calculated with the aid of NEMOH and HAMS software. More details can be found in [41, 42]. The wave forces are derived by integrating the hydrodynamic pressures acting on the wetted part of the floater. The potential of the incident wave and the diffraction potential are considered in the calculation of the hydrodynamic pressures. By exploiting the linearised Bernoulli equation, the following general form of Equation (4) is derived:

$$F_i = -i\omega\rho \iint_S \varphi n dS \quad (4)$$

where φ is the incident and diffracted potential, n is the normal vector pointing outwards from the wetted surface into the fluid, and S denotes the wetted surface. Similarly, the overturning moments acting on the floating structure are given by Equation (5):

$$M_i = -i\omega\rho \iint_S \varphi (x \times n) dS \quad (5)$$

Figures 8–10 show the first-order wave loads and moments for a range of angular frequencies and wave directions. Due to the double symmetry of the rectangular floater, the forces F_y and the moments M_x are omitted.

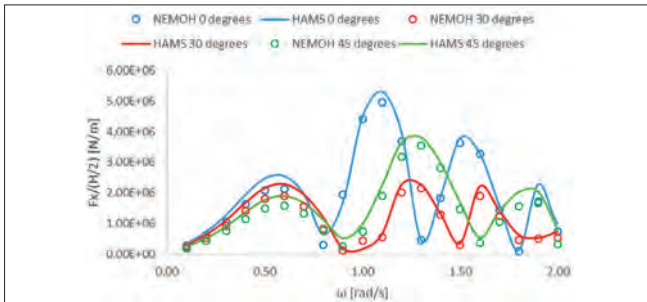


Fig. 8. First-order wave loads in the direction exerted on the floating platform versus ω for wave headings of 0° , 30° and 45°

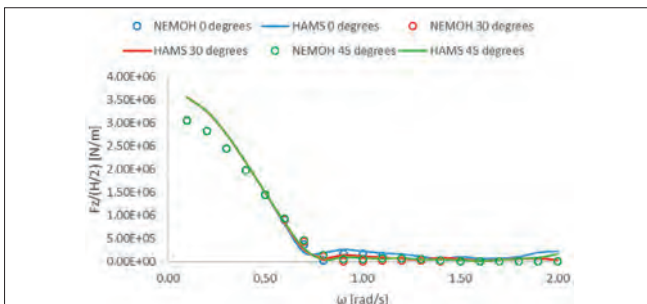


Fig. 9. First-order wave loads in the direction exerted on the floating platform versus ω for wave headings of 0° , 30° and 45°

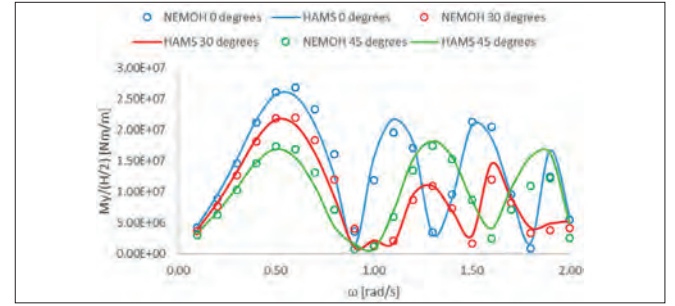


Fig. 10. First-order wave loads M_y on the floating platform versus ω for wave headings of 0° , 30° and 45°

From Figures 8–10, it can be observed that all the curves obtained from NEMOH and HAMS follow the same trend. The horizontal forces presented in Figure 8 form three peaks, with the first one at $\omega = 0.6$ rad/s, while the second (with a higher value) and third clearly depend on the wave heading. The vertical forces start with a maximum value at $\omega = 0.1$ rad/s, and then decrease drastically at $\omega = 0.8$ rad/s. The curves related to the bending moments around the y -axis follow a similar trend to those of the horizontal forces, but for wave headings of 0° and 30° , the maximum value is seen for the first peak, and specifically at $\omega = 0.6$ rad/s. All of these behaviours are attributed to the interactions between the cylinders and the incoming regular waves.

WAVE ELEVATION AROUND THE PLATFORM

In this section, the free surface elevation around the structure is discussed for values of $\omega = 0.6$ rad/s with a wave heading 0° , $\omega = 1.1$ rad/s for a wave heading of 30° , and $\omega = 1.6$ rad/s for a wave heading of 45° , using the open-source code NEMOH. These frequencies are considered due to the fact that the exciting forces reach a peak at these values, as described in the previous section.

In potential flow theory, the free surface elevation is given in terms of the velocity potential (which is actually derived based on the kinematic condition of the free surface at $z = 0$), as shown in Equation (6):

$$\eta = \frac{i\omega}{g} \frac{\partial \varphi}{\partial t} \quad (6)$$

where η denotes the free surface elevation, and φ represents the incident wave and diffraction potentials.

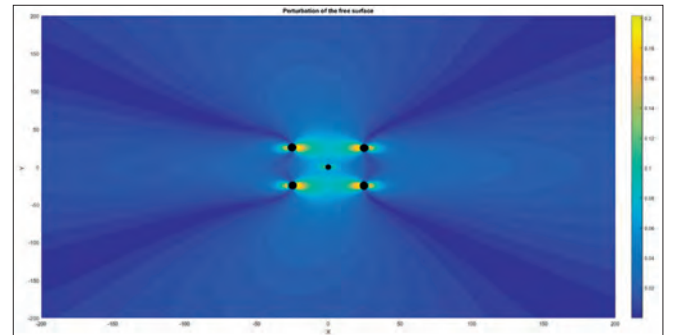


Fig. 11. 2D perturbation of the free surface around the floating structure for $\omega = 0.6$ rad/s and wave heading 0°

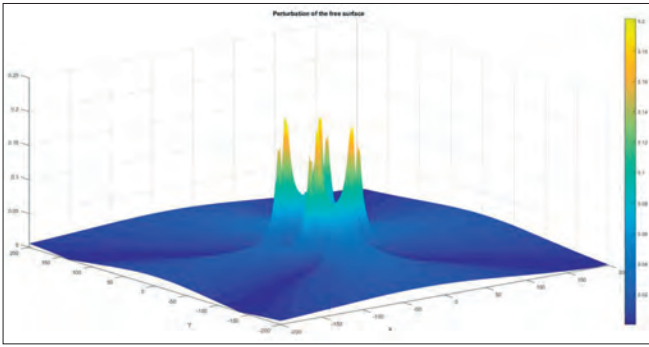


Fig. 12. 3D perturbation of the free surface around the floating structure for $\omega = 0.6$ rad/s and wave heading 0°

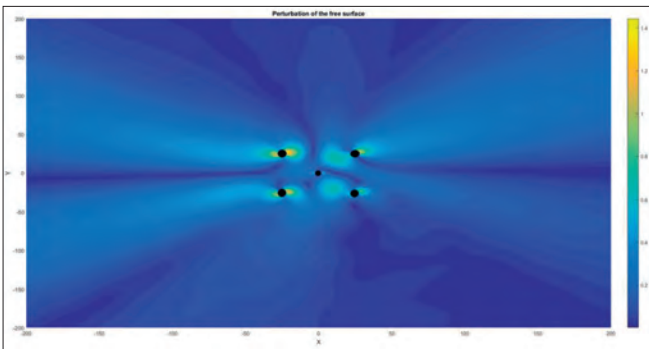


Fig. 13. 2D perturbation of the free surface around the floating structure for $\omega = 1.1$ rad/s and wave heading 3°

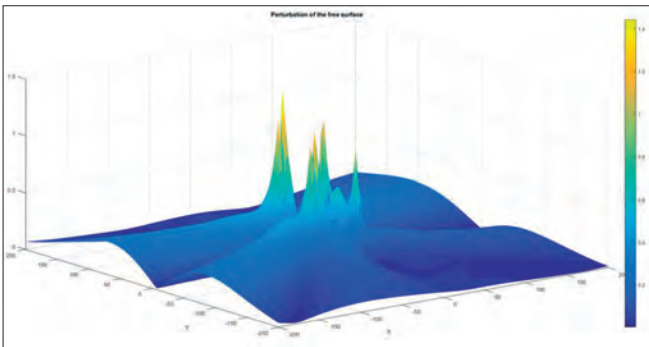


Fig. 14. 3D perturbation of the free surface around the floating structure for $\omega = 1.1$ rad/s and wave heading 30°

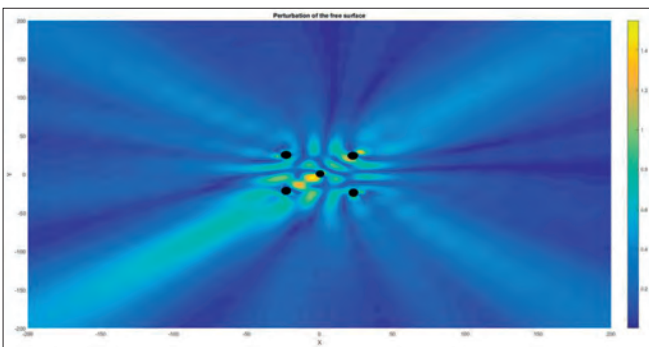


Fig. 15. 2D perturbation of the free surface around the floating structure for $\omega = 1.6$ rad/s and wave heading 45°

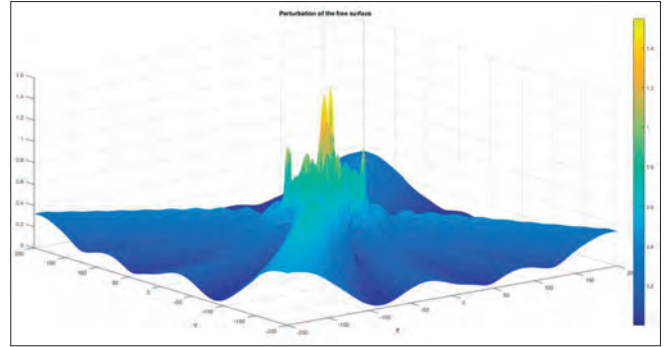


Fig. 16. 3D perturbation of the free surface around the floating structure for $\omega = 1.6$ rad/s and wave heading 45°

At $\omega = 0.6$ rad/s (Figures 11, 12), the maximum value of the free surface elevation is approximately 0.2, around the four offset cylindrical tubes. At $\omega = 1.1$ rad/s (Figures 13, 14), the free surface elevation obtains its maximum value of approximately 1.4, at the back of the second offset cylinder of the floating structure (see Figure 2). Finally, at $\omega = 1.6$ rad/s (Figures 15, 16), the maximum value is around 1.5 at a position between the first cylinder and the main central column of the floater.

ADDED MASSES AND HYDRODYNAMIC DAMPING OF THE FLOATER

The behaviour of the added mass coefficients as a function of the incident wave frequency is shown in Figures 17 and 18, while the behaviour of various damping coefficients is shown in Figures 19 and 20. As discussed above, these hydrodynamic parameters were explicitly derived from the two software packages that were used in this study [41, 42].

The solution to the radiation problem is related to the added mass and damping matrices; as depicted in the following graphs, these coefficients are frequency-dependent.

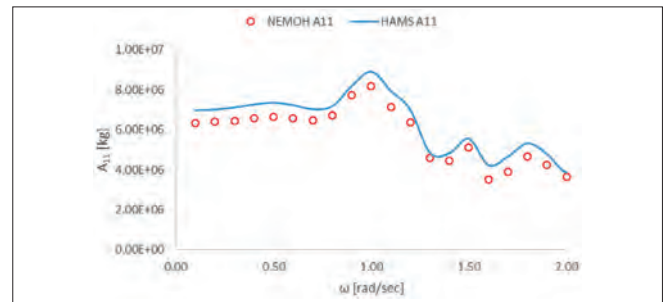


Fig. 17. A_{11} as a function of the wave frequency

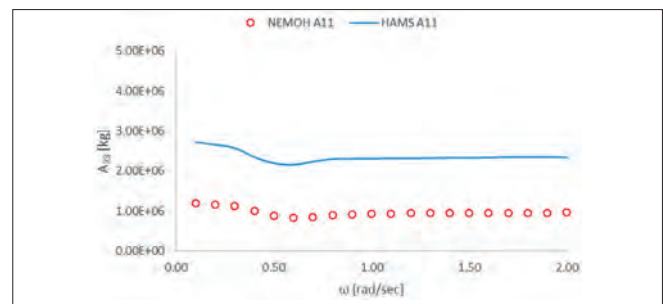


Fig. 18. A_{33} as a function of the wave frequency

From Figure 18, a pronounced difference between the two graphs can be observed. This can be attributed to whether or not the brackets that interconnect the cylindrical columns of the floating structure are included in the discretisation needed for the solution to the hydrodynamic problem. More specifically, although the curves follow the same qualitative trend, when HAMS is used (i.e., the brackets are taken into account), the A_{33} added masses are approximately 1500 t larger than those predicted by NEMOH, where the brackets are excluded from the discretisation. This difference is equal to the additional buoyancy due to the brackets of the floater. This is because when the brackets are included in the discretisation of the structure, the displacement volume of the structure is greater, and hence the additional mass is greater. Consequently, in order to ensure a more precise calculation of the movements of the floating structure, the brackets should be included in the discretisation.

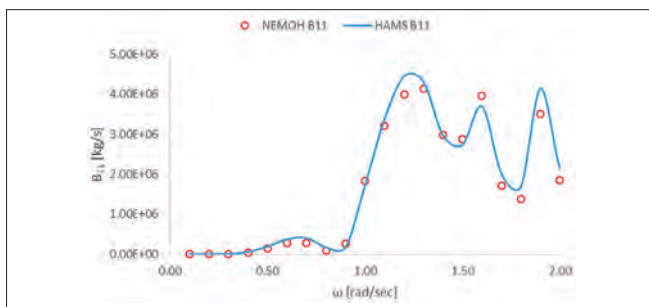


Fig. 19. B_{11} as a function of wave frequency

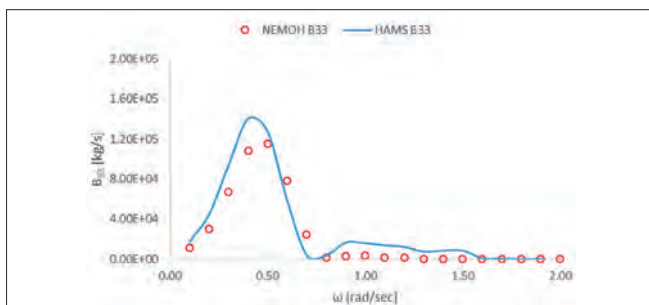


Fig. 20. B_{33} as a function of wave frequency

MOTION OF THE FLOATING PLATFORM

In this subsection, we present some numerical results for the RAOs of the platform. It was assumed for these calculations that the wind speed was 11.4 m/s. Figures 21 and 22 show the RAOs of the surge and heave motions of the floater. These RAOs are nondimensionalised by the term $H/2$, which is the wave amplitude, where H is the wave height ($H = 2$ m). Due to the double symmetry of the platform, the sway motions are not considered here; as expected, they exhibit an analogous configuration with the surge motions, relative to the direction of the incoming wave. As expected from a physical analysis, when the incoming wave is parallel to the x-axis, the surge motion is higher ($\beta = 0^\circ$), and this decreases as the wave's direction becomes vertical to the x-axis (or equivalently parallel to the y-axis) (see Figure 2). We also observe that all the curves start from an initial maximum value at $\omega = 0.1$ rad/s which then

decreases rapidly, with an explicit (although significantly smaller) peak at $\omega = 0.3$ rad/s. For greater values of the wave frequency, the platform is only very slightly affected.

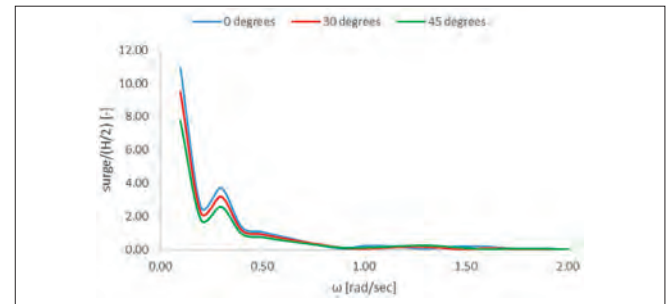


Fig. 21. Surge RAOs for the floating platform with the WT, for three different directions of the incident wave, under the buoy mooring system

Figure 22 shows the RAOs of the heave motion of the floater. The heave motions have a particular feature: the curves for $\omega = 0.1$ to 0.7 rad/s and $\omega = 1.1$ to 2.0 rad/s coincide, for each pair of directions. The heave motion reaches a maximum value of 1.453 at $\omega = 0.8$ rad/s and the corresponding curve then exhibits an abrupt decrease. We can also observe that the vertical motion of the platform is practically zero for all wave directions when $\omega > 1.7$ rad/s.

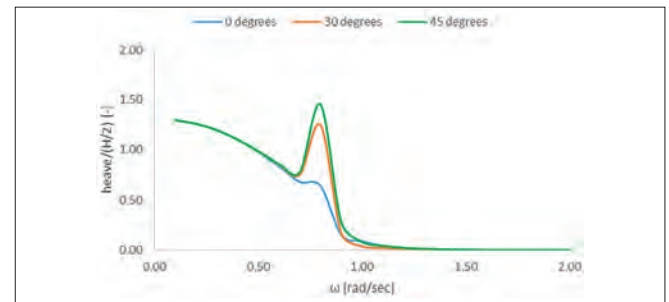


Fig. 22. Heave RAOs for the floating platform with the WT for three different directions of the incident wave, under the buoy mooring system

Figure 23 shows the results for the pitch motion of the platform. Once again, the graph for the roll motion is neglected here, since it is analogous to the pitch motion, as expected. The RAOs of the rotational motions are nondimensionalised by the term $kH/2$, where k is the wavenumber. The maximum rotation around the y-axis is obtained when the x-axis is parallel to the incident wave. Its value is 5.678 for a wave frequency of $\omega = 0.3$ rad/s.

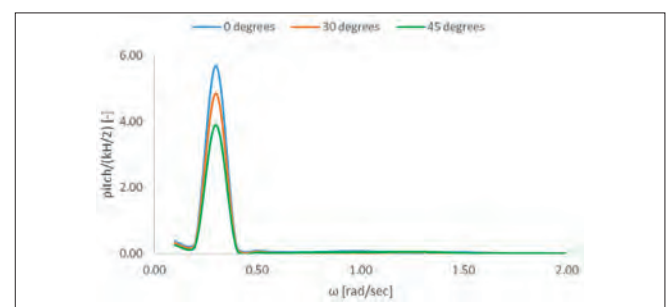


Fig. 23. Pitch RAOs for the floating platform with the WT for seven different directions of the incident wave, under the buoy mooring system

MOORING LINE TENSIONS

Neither NEMOH and HAMS could be used to calculate the tensions exerted on the floating structure by the mooring system. However, by applying the method presented in [30, 45] the tension in each branch of the mooring system was obtained. Figs. 24–27 present the tensions of the mooring system for three different wave headings of 0°, 30° and 45°.

The first observation that can be made is that all the curves follow a similar trend. We can also see that the mooring tensions are only slightly affected by the wave heading, and that the relevant discrepancies are small. The maximum mooring forces are seen at $\omega = 0.1$ rad/s, and decrease drastically with increasing ω . In addition, as can be seen in Figures 24 and 25, there is an initial peak at $\omega = 0.3$ rad/s and a smaller secondary one at $\omega = 0.8$ rad/s. Moreover, the mooring tensions become greater at a wave heading of 45° in all cases. Finally, for $\omega > 1.5$ rad/s, the mooring tensions tend practically to zero.

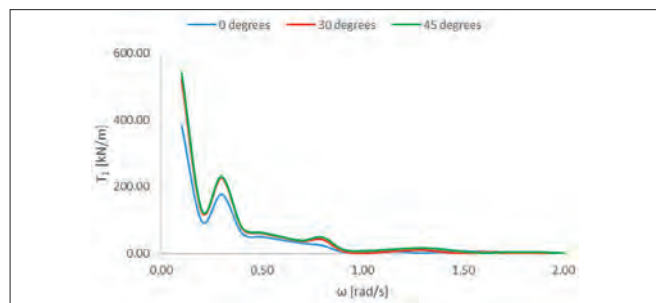


Fig. 24. Total mooring forces on the first mooring line

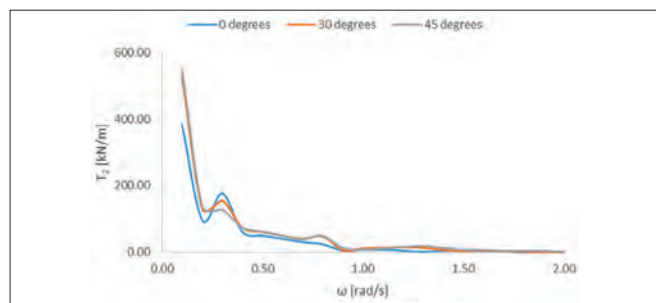


Fig. 25. Total mooring forces on the second mooring line

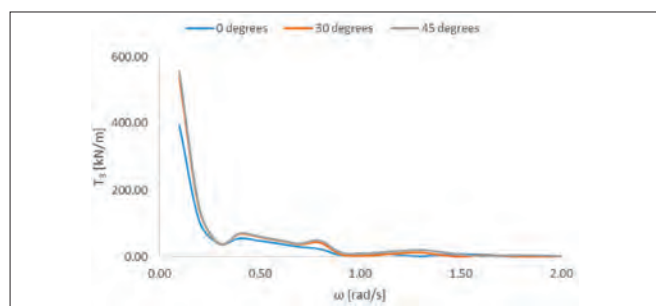


Fig. 26. Total mooring forces on the third mooring line

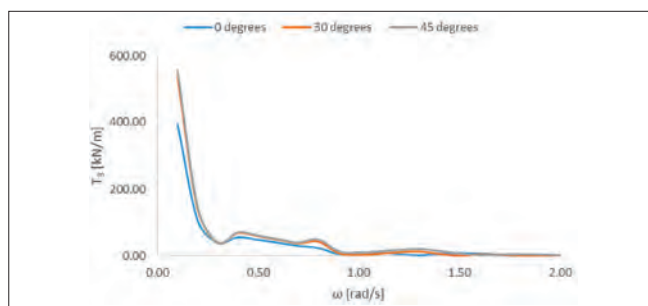


Fig. 27. Total mooring forces on the fourth mooring line

CONCLUSION

The aim of this study was to analyse the dynamic behaviour of a semi-submersible platform supporting a 10MW WT, under a four-branch mooring system with buoys. To this end, a coupled analysis was employed. It was assumed that the wind speed was 11.4 m/s. The hydrodynamic boundary value problem was solved numerically using two BEM software packages called NEMOH and HAMS. The added masses, damping coefficients, and stiffness matrices of the WT were taken into consideration in order to reduce and incorporate the gravitational, inertial, gyroscopic, and aerodynamic effects of the WT on the floating structure. The results were examined primarily in terms of the impact of the wave heading and angular frequency on the maximum values of the physical quantities under consideration. The hydrodynamic behaviour of the floater was examined both with and without braces.

Several numerical results were presented for the RAOs of the floater, and the exciting forces were compared to those originating from the added masses and damping coefficients of the floating structure, with and without braces. The curves of the exciting forces were found to follow a similar pattern, while the wave heading seemed to have an influence on the incoming wave frequency at which the maximum value appeared. For the RAO of the surge motion, it was found that all the curves started from an initial maximum value at $\omega = 0.1$ rad/s and then decreased rapidly, with a pronounced but much smaller peak at $\omega = 0.3$ rad/s. In regard to the heave motion, the curves coincided for specific directions of the incoming wave, and the same effect was also observed for the yaw motion. The maximum value for the RAO of the pitch was reached at $\omega = 0.3$ rad/s. The position of the maximum value of free surface elevation was not constant, and clearly depended on the wave frequency. The mooring tensions were not greatly affected by the wave heading. The relevant curves started from a maximum value and then formed two more peaks with a significantly smaller magnitude. Finally, in all cases, the mooring tensions tended to zero for $\omega > 1$ rad/s.

ACKNOWLEDGEMENTS

This research was partially funded by the Research Committee of the University of West Attica.

REFERENCES


1. L. Liu, Q. Sun, H. Li, H. Yin, X. Ren, and R. Wennersten, "Evaluating the benefits of integrating floating photovoltaic and pumped storage power system," *Energy Conversion and Management*, Vol. 194, pp. 173-185, 2019, doi.org/10.1016/j.enconman.2019.04.071.
2. G. Da Silva and D. Branco, "Is floating photovoltaic better than conventional photovoltaic? Assessing environmental impacts," *Impact Assessment and Project Appraisal*, Vol. 36(5), pp. 390-400, 2018, doi.org/10.1080/14615517.2018.1477498.
3. S. Kim, Y. Lee, S. Seo, H. Joo, and S. Yoon, "Structural design and installation of tracking-type floating PV generation system," *Composites Research*, Vol. 27(2), pp. 59-65, 2014, doi.org/10.7234/composres.2014.27.2.059.
4. B. Chico Hermanu, B. Santoso, S. Suyitno, and F. Wicaksono, "Design of 1 MWp floating solar photovoltaic (FSPV) power plant in Indonesia," *AIP Conference Proceedings*, Surakarta, Indonesia, 9-11 October, 2019, doi.org/10.1063/1.5098188.
5. E. Do Sacramento, P. Carvalho, J. De Araujo, D. Riffel, R. Da Cruz Correa, and J. Neto, "Scenarios for use of floating photovoltaic plants in Brazilian reservoirs," *IET Renewable Power Generation*, Vol. 9(8), pp. 1019-1024, 2015, doi.org/10.1049/iet-rpg.2015.0120.
6. X. Zhao, X. Du, M. Li, and M. Goteman, "Semi-analytical study on the hydrodynamic performance of an interconnected floating breakwater-WEC system in presence of the seawall," *Applied Ocean Research*, Vol. 109, 2021, doi.org/10.1016/j.apor.2021.102555.
7. B. Guo, Q. Elmoosa, C. Windt, and J. Ringwood, "Impact of nonlinear hydrodynamic modelling on geometric optimization of a spherical heaving point absorber," *14th European Wave and Tidal Energy Conference*, Plymouth, UK, 5-9 September, 2021.
8. S. Michele and E. Renzi, "A second-order theory for an array of curved wave energy converters in open sea," *Journal of Fluids and Structures*, Vol. 88, pp. 315-330, 2019, doi.org/10.1016/j.jfluidstructs.2019.05.007.
9. D. Evans and R. Porter, "Efficient calculation of hydrodynamic properties of OWC type devices," *Journal of Offshore Mechanics and Arctic Engineering*, Vol. 119(4), pp. 210-218, 1997, doi.org/10.1115/1.2829098.
10. J. Fitzgerald and L. Bergdahl, "Considering mooring cables for offshore wave energy converters," *7th European Wave and Tidal Energy Conference*, Porto, Portugal, 11-13 September, 2007.
11. J. Fitzgerald and L. Bergdahl, "Including moorings in the assessment of a generic offshore wave energy converter: A frequency domain approach," *Marine Structures*, Vol. 21(1), pp. 23-46, 2008, doi.org/10.1016/j.marstruc.2007.09.004.
12. L. Johanning and G. Smith, "Improved measurement technologies for floating wave energy converter (WEC) mooring arrangements," *Underwater Technology*, Vol. 27(4), pp. 175-184, 2008, doi.org/10.3723/ut.27.175.
13. S. Yang, J. Ringsberg, E. Johnson, Z. Hu, and J. Palm, "A comparison of coupled and de-coupled simulation procedures for the fatigue analysis of wave energy converter mooring lines," *Ocean Engineering*, Vol. 117(1), pp. 332-345, 2016, doi.org/10.1016/j.oceaneng.2016.03.018.
14. T. Mazarakos, D. Konispoliatis, D. Manolas, S. Mavrakos, and S. Voutsinas, "Coupled hydro-aero-elastic analysis of a floating structure for offshore wind and wave energy sources exploitation," *12th International Conference on Stability of Ships and Ocean Vehicles*, Glasgow, Scotland, UK, 14-19 June, 2015.
15. T. Mazarakos, D. Konispoliatis, D. Manolas, S. Voutsinas, and S. Mavrakos, "Modelling of an offshore multi-purpose floating structure supporting a wind turbine including second-order wave loads," *11th European Wave and Tidal Energy Conference*, Nantes, France, 6-11 September, 2015.
16. S. Seng, C. Monroy, and S. Malenica, "Dynamic response of monopile wind turbine in large waves," *38th International Conference on Ocean, Offshore and Arctic Engineering*, Glasgow, Scotland, UK, 9-14 June, 2019.
17. K. Maes, W. Weijtjens, E. De Ridder, and G. Lombaert, "Inverse estimation of breaking wave loads on monopile wind turbines," *Ocean Engineering*, Vol. 163(1), pp. 544-554, 2018, doi.org/10.1016/j.oceaneng.2018.05.049.
18. S. Jalbi and S. Bhattacharya, "Concept design of jacket foundations for offshore wind turbines in 10 steps," *Soil Dynamics and Earthquake Engineering*, Vol. 139, 2020, doi.org/10.1016/j.soildyn.2020.106357.
19. I. Chen, B. Wong, Y. Lin, S. Chau and H. Huang, "Design and analysis of jacket substructures for offshore wind turbines," *Energies*, Vol. 9(4), 2016, doi.org/10.3390/en9040264.
20. M. Karimirad and T. Moan, "Wave and wind induced motion response of catenary moored spar wind turbine," *3rd International Conference on Computational Methods in Marine Engineering*, Trondheim, Norway, 15-17 June, 2009.
21. M. Karimirad and T. Moan, "Wave- and wind-induced dynamic response of a spar-type offshore wind turbine," *Journal of Waterway, Port, Coastal, and Ocean Engineering*, Vol. 138(1), 2012, doi.org/10.1061/(ASCE)WW.1943-5460.0000087.

22. T. Utsunomiya, T. Sato, H. Matsukuma, and K. Yago, "Experimental validation for motion of a spar-type floating offshore wind turbine using 1/22.5 scale model," 28th International Conference on Ocean, Offshore and Arctic Engineering, Honolulu, Hawaii, May 31-June 5, 2009.
23. F. Huijs, R. De Bruijn, and F. Savenije, "Concept design verification of a semi-submersible floating wind turbine using coupled simulations," *Energy Procedia*, Vol. 53, pp. 2-12, 2014, doi.org/10.1016/j.egypro.2014.07.210.
24. M. Hall and A. Goupee, "Validation of a lumped-mass mooring line model with DeepCwind semisubmersible model test data," *Ocean Engineering*, Vol. 104(1), pp. 590-603, 2015, doi.org/10.1016/j.oceaneng.2015.05.035.
25. T. Mazarakos, D. Manolas, and S. Mavrakos, "Design and hydro-aero-elastic modeling of a multi leg mooring concept for floating wind turbine applications," 16th International Conference on Ecological Vehicles and Renewable Energies, Monte-Carlo, Monaco, 5-7 May, 2021.
26. T. Mazarakos, D. Manolas, and S. Mavrakos, "Design and hydro-aero-elastic modeling of a TLP concept for floating wind turbine applications," 31st International Ocean and Polar Engineering Conference, Rhodes, Greece, 16-21 June, 2021.
27. G. Katsaounis, S. Polyzos, and S. Mavrakos, "An experimental study of the hydrodynamic behavior of a TLP platform for a 5MW wind turbine with OWC devices," 7th International Conference on Computational Methods in Marine Engineering, Nantes, France, 15-17 May, 2017.
28. Y. Bae, M. Kim, and Y. Shin, "Rotor-floater-mooring coupled dynamic analysis of mini TLP-type offshore floating wind turbines," 29th International Conference on Ocean, Offshore and Arctic Engineering, Shanghai, China, 6-11 June, 2010.
29. T. Mazarakos, D. Manolas, T. Grapsas, S. Mavrakos, V. Riziotis, and S. Voutsinas, "Conceptual design and advanced hydro-aero-elastic modelling of a TLP concept for floating wind turbine applications," 1st International Conference on Renewable Energies Offshore, Lisbon, Portugal, 24-26 November, 2014.
30. T. Mazarakos, T. Tsaoasis, S. Mavrakos, and I. Chatjigeorgiou, "Analytical investigation of tension loads acting on a TLP floating wind turbine," *Journal of Marine Science and Engineering*, Vol. 10(3), 2022, doi.org/10.3390/jmse10030318.
31. Z. Yuan, A. Incecik, and C. Ji, "Numerical study on a hybrid mooring system with clump weights and buoys," *Ocean Engineering*, Vol. 88(15), pp. 1-11, 2014, doi.org/10.1016/j.oceaneng.2014.06.002.
32. N. Bruschi, G. Ferri, E. Marino, and C. Borri, "Influence of clumps-weighted moorings on a spar buoy offshore wind turbine," *Energies*, Vol. 13(23), 2020, doi.org/10.3390/en13236407.
33. I. Chatjigeorgiou, "A finite differences formulation for the linear and nonlinear dynamics of 2D catenary risers," *Ocean Engineering*, Vol. 35(7), pp. 616-636, 2008, doi.org/10.1016/j.oceaneng.2008.01.006.
34. S. Mavrakos, V. Papazoglou, M. Triantafyllou, and J. Hatjigeorgiou, "Deep water mooring dynamics," *Marine Structures*, Vol. 9(2), pp. 181-209, 1996, doi.org/10.1016/0951-8339(94)00019-0.
35. S. Mavrakos and J. Chatjigeorgiou, "Dynamic behaviour of deep water mooring lines with submerged buoys," *Computers & Structures*, Vol. 64(1-4), pp. 819-835, 1997, doi.org/10.1016/S0045-7949(96)00169-1.
36. C. Ji and Z. Yuan, "Experimental study of a hybrid mooring system," *Journal of Marine Science and Technology*, Vol. 20, pp. 213-215, 2015, doi.org/10.1007/s00773-014-0260-7.
37. D. Qiao, J. Yan, and J. Ou, "Effects of mooring line with buoys system on the global response of a semi-submersible platform," *Brodogradnja*, Vol. 65(41), pp. 79-96, 2014.
38. K. Xu, K. Larsen, Y. Shao, M. Zhang, Z. Gao, and T. Moan, "Design and comparative analysis of alternative mooring systems for floating wind turbines in shallow water with emphasis on ultimate limit state design," *Ocean Engineering*, Vol. 219(1), 2021, doi.org/10.1016/j.oceaneng.2020.108377.
39. J.-T. Wu, J.-H. Chen, C.-Y. Hsin, and F.-C. Chiu, "Dynamics of the FKT system with different mooring lines," *Polish Maritime Research*, Vol. 26(1), pp. 20-29, 2019, doi.org/10.2478/pomr-2019-0003.
40. H. Zhang, J. Zeng, B. Jin, C. Chou, H. Li, and H. Dong, "Experimental study of the nonlinear behaviour of deep-sea mooring polyester fibre ropes," *Polish Maritime Research*, Vol. 30(3), pp. 153-162, 2023, doi.org/10.2478/pomr-2023-0048.
41. A. Babarit and G. Delhommeau, "Theoretical and numerical aspects of the open source BEM solver NEMOH," 11th European Wave and Tidal Energy Conference, Nantes, France, 6-11 September, 2015.
42. L. Yingyi, "HAMS: A frequency-domain preprocessor for wave-structure interactions—Theory, development, and application," *Journal of Marine Science and Engineering*, Vol. 7(3), 2019, doi.org/10.3390/jmse7030081.
43. C. Bak, F. Zahle, R. Bitsche, T. Kim, A. Yde, L. Henriksen, A. Natarajan, and M. Hansen, "Description of the DTU 10 MW reference wind turbine," *Wind Energy Report-I-0092*, 2013.

44. O. Faltinsen, Sea loads on ships and offshore structures. Cambridge University Press, Ocean Technology Series, 1990.
45. T. Mazarakos, D. Konispoliatis, G. Katsaounis, S. Polyzos, D. Manolas, S. Voutsinas, T. Soukissian, and S. Mavrakos, "Numerical and experimental studies of a multi-purpose floating TLP structure for combined wind and wave energy exploitation," *Mediterranean Marine Science*, Vol. 20(4), pp. 745-763, 2019, doi.org/10.12681/mms.19366.

STUDY OF THE HYDRODYNAMIC CHARACTERISTICS OF ANTI-HEAVE DEVICES OF WIND TURBINE PLATFORMS AT DIFFERENT WATER DEPTHS

Hongyuan Xu ¹

Wei Wang ^{1, 2, 3 *}

Yonghe Xie¹

¹ School of Naval Architecture and Maritime, Zhejiang Ocean University, Zhoushan, China

² School of Naval Architecture Ocean and Civil Engineering, Shanghai Jiaotong University, Shanghai

³ Marine Design and Research Institute of China, Shanghai, China

* Corresponding author: wangwei1981@zjou.edu.cn (Wei Wang)

ABSTRACT

This paper focuses on the effect of water depth on the hydrodynamics of floating offshore wind turbines with open-hole anti-heave devices. The three-floating-body wind turbine platform is used as the primary research object in this paper. The effect of water depth on the reduction of the heave motion of a floating platform with anti-heave devices is systematically investigated through a series of experiments and numerical simulations. The results show high agreement between the test results and simulations, with larger values of heave motion in deep water. A wind turbine platform with anti-heave devices can effectively reduce the lifting and sinking motions when the wave period is large.

Keywords: anti-heave device; hydrodynamic analysis; different water depths

INTRODUCTION

Wind energy is a non-polluting, high retention and high potential renewable energy source, which has good prospects for development and application. Wind speed at sea is more stable and stronger than that on land because of its higher energy yield. By the end of 2020, offshore wind power's installed capacity surpassed 30 GW [1]. In areas of shallow water, there is considerable potential for bottom-fixed foundations, such as gravity and monopile types, which are limited to a maximum water depth of 15 and 30 m, respectively [2]. However, most of the offshore wind potential is located at sites with water depths of more than 60 m, where there is a greater advantage over the fixed type [3]. Floating offshore wind turbine (FOWT) platforms are more versatile in deep-sea applications [4]. In addition, semi-FOWTs can be efficiently used in a wide range of water depths [4]. Therefore, it is of great significance to study the platform's dynamic characteristics of semi-FOWTs at different water depths.

Many scholars have investigated the performance of FOWTs. Nematbakhsh et al. [6][7] investigated the dynamic response characteristics of TLP-type floating wind turbine systems and Spar-type floating wind turbine systems by using the CFD method and simplifying the turbines at a constant thrust. Hu et al. [8] investigated the dynamic response of a semi-submersible FOWT system under various excitations. The structural loading, in the case of emergency shutdown, has a stronger dynamic response. Abou-Rayan et al. [9] investigated the dynamic responses of triangular, square and pentagonal TLP configurations under multidirectional regular and random waves. Barrera et al. [10] explored the role of spectral wave characteristics and wave time histories in estimating extreme mooring loads for a floating offshore wind turbine. Zhao et al. [11] investigated the analysis of a kinematic fully-coupled time-domain simulation of a DTU10MW, comparing the motion response of DTU10MW with NREL5MW. The conclusions showed that the wind and waves had a more pronounced excitation effect on the DTU10MW wind turbine. Alkarem

et al. [12] investigated the effect of wave irregularities on the hydrodynamic response of a floating offshore wind turbine for FOWT at different water depths. Bae et al. [13] combined CHARM3D and FAST software to calculate the TPL floating wind turbine under different operating conditions and operating at water depths of 80 m and 200 m, carrying out numerical simulations in time domain analyses. Bayati et al. [14] analysed the effects of water depth on a semi-submersible type FOWT, where the water depth ranged from 30-200 m. It is claimed that water depths influence heave motion more than surge motion, when water depth decreases from 200 m to 30 m. Chen et al. [15] analysed the motion response of a wind turbine support platform, considering water depth effects. It is claimed that the effects of water depth mainly happen at shallower water depths. From a structural safety point of view, water depth effects need to be considered during the design process and the motion analysis of floating wind turbines. Le C et al. [16] proposed a new submerged offshore wind turbine aimed at operating in intermediate water depths between 20 and 200 m. Feasibility studies concerned different environmental conditions, tether length, tether pretension, and tether failure scenarios. Zhang et al. [17] studied the fully coupled analysis of the V-shaped floating wind turbine platform at different water depths; the mooring tension characteristics were analysed under different load conditions, yielding possible mooring schemes for different water depths. Studies have shown that surge, heave, and pitch motions are more stable at medium water depths. Lin [18] conducted a study of the impact of water depth (ranging from 200-300 m) on the performance of a floating offshore wind turbine. The results indicated that, as the water depth increases, the platform's heave motion tends to noticeably increase with mooring configuration.

In the design of FOWTs, water depth is considered as a design factor that must be addressed. In most of the research into reducing platform motion for improved stability, most of the tests are only conducted for a single water depth, ignoring the effect of water depth on platform motion. The 'deepCwind' platform base is taken as the research object in this paper. The hydrodynamic performance of a model with a chamfered perforated anti-heave device is systematically investigated through experiments with different water depth variations. Then, the models tested are compared and validated by full-scale numerical simulations. Finally, the effect of water depth variation on the reduction of heave motion is analysed by numerical simulation.

TOWING TANK EXPERIMENT

FLOATING BODY WITH ANTI-HEAVE DEVICES

Heave plates have the advantage of increasing the damping and additional mass coefficients in floating platforms, which can effectively increase the resistance of the platform and enhance stability. Wang et al. [19] studied the effect of opening holes on the pendulum plate, with chamfering angles of the holes from 0-35°, through a large number of experiments and numerical simulations. Among these, the 35° chamfered holes

of the three-floating-body wind turbine platforms have the best effect on heave reduction. This paper selected a baseline offshore wind turbine designed by NREL 5 MW [20]. The data for the floating wind turbine platform with anti-heave devices are shown in Table 1. The single pontoon model, cross-section of the anti-heave device, and model of the platform with an anti-heave device are shown in Fig. 1.

Tab. 1 Overall parameters of floating offshore wind turbine

Parameters of wind turbine	Values
Rated power [MW]	5
Rotor diameter [m]	126
Cut in/Rated wind speed [m/s]	3/11.4
Cut in/Rated rotor speed [rpm]	6.9/12.1
Parameters of single floating body	Values
Height [m]	32
Diameter [m]	12
Diameter of anti-heave device [m]	24
Height of central column [m]	6
Number of perforations	10
Chamfer angle [deg]	35
Overall parameter	Values
Total mass [kg]	1.37×10^7

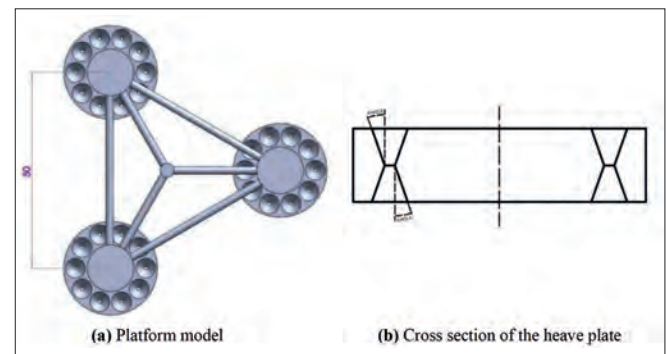


Fig 1. Anti heave device model

DESIGN OF EXPERIMENTS

Selection of scale ratio

According to the purpose of the test and the overall response characteristics of the floating wind turbine, it is necessary to satisfy the geometric similarity, kinematic similarity, and dynamic similarity [22]. At the same time according to the aerodynamic properties of the blade rotation, the TSR (tip speed ratio) was ensured to be similar [23]. In order to achieve similar overall load and wind turbine rotational effects, similar criteria were used in the equations:

$$\frac{L_s}{L_m} = \lambda \quad (1)$$

$$\frac{V_m}{\sqrt{gL_m}} = \frac{V_s}{\sqrt{gL_s}} \quad (2)$$

$$V_s = \lambda^{\frac{1}{2}} V_m \quad (3)$$

$$R_{TS} = \frac{\Omega_s R_s}{U_s} = \frac{\Omega_m R_m}{U_m} \quad (4)$$

$$R_s = \lambda^{-\frac{1}{2}} R_m \quad (5)$$

L is the length of the object feature, λ is the reduction ratio, V is the average velocity of the object with respect to the flow field, Ω is the rotational velocity of the impeller, R is the radius of the blades, and U is the average wind speed.

Based on the master scale, the scaling ratio was chosen as $\lambda = 60$. Table 2 shows the factors used to model the physical quantity conversion relationships:

Tab. 2. Relationship between model and actual physical quantity conversions

Property	Scale	Speed	Mass	Time	Frequency	Force	Rotor Speed	Inertia moment
Scaling factors	λ	$\lambda^{\frac{1}{2}}$	λ^3	$\lambda^{\frac{1}{2}}$	$\lambda^{-\frac{1}{2}}$	λ^3	$\lambda^{-\frac{1}{2}}$	λ^4

Experimental arrangement

Wave conditions were realised by the towing tank at Zhejiang Ocean University, which can control wave frequency and wave height to create stable regular waves.

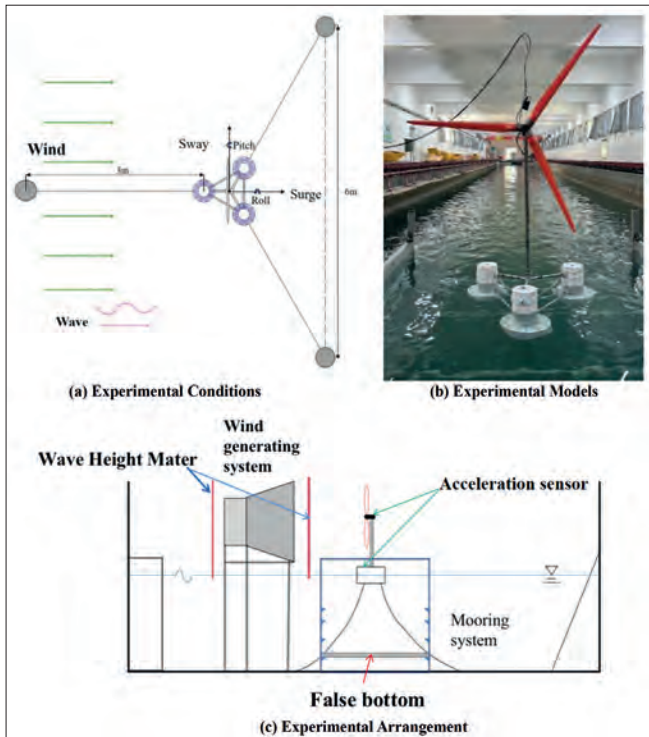


Fig. 2. Floating body model device and experimental arrangement diagram

The experiments included the acceleration of the platform motion, the 3-way accelerometer (Range: $\pm 4g$; Accuracy: 0.1%FS) at the top of the tower, by arranging the accelerometers, and the ULD2000 wave monitoring (Range: 0~0.5 m; Accuracy: 0.1%FS) and wind monitoring (Range: 0~40 m/s; Accuracy: $\pm 0.5g + 2\%$ FS). The pedestal model was obtained by 3D

printing, which ensured smoothness and water tightness. The total mass of the model was 63.5 kg (including bulk) and the draft was 0.34 m. The mooring line (Fig. 2(a)) consisted of a 6.2 mm diameter steel wire rope (13.5 kg per 100 m) with a mass of 0.158 kg/m per unit length as the mooring cable; a 10 kg block was used in the towing tank as the mooring weight to fix the position of the mooring line. The experimental arrangement is shown in Fig. 2(b), consisting of a wind turbine blade and a float. The overall layout of the experiment and the environmental conditions are shown in Fig. 2 (c), which has three main components: the wave generation system, the wind generation system, and the wave dissipation system. The float model had a false bottom with adjustable depth, to control the water depth.

Due to the purpose of the experiment and the limited experimental conditions, this experiment was mainly carried out to study the heave motion response of the floating platform and the effect of the 35° chamfered holes on the heave motion of the anti-heave devices.

CONTENTS OF THE MODEL TEST

Hydrostatic decay tests

The hydrostatic decay test allows for obtaining the intrinsic period of the whole turbine system. For the hydrostatic free decay test, the upper turbine was set to stop and then adjusted so that the azimuth of one of the blades equals 0° (vertically upwards).

Model experiments under combined wind and wave action

According to the NERL-5MW wind turbine rating and the experimental wind and wave conditions, the scale conversion from Table 2 was used to select a constant wind speed of 1.30 m/s for this experiment; the waves were selected from the 15 sets of conditions, in Table 3, for the experimental conditions under combined wind and wave action.

Tab. 3. Experimental working conditions of the model under combined wind and wave action

Condition Number	Wave Frequency [Hz]	Wave Height [m]	Water Deep [m]
1	0.40	0.15	1.2
2	0.50	0.15	1.2
3	0.65	0.15	1.2
4	0.40	0.15	1.5
5	0.50	0.15	1.5
6	0.65	0.15	1.5
7	0.40	0.15	2.0
8	0.50	0.15	2.0
9	0.65	0.15	2.0
10	0.40	0.15	2.5
11	0.50	0.15	2.5
12	0.65	0.15	2.5
13	0.40	0.15	3.0
14	0.50	0.15	3.0
15	0.65	0.15	3.0

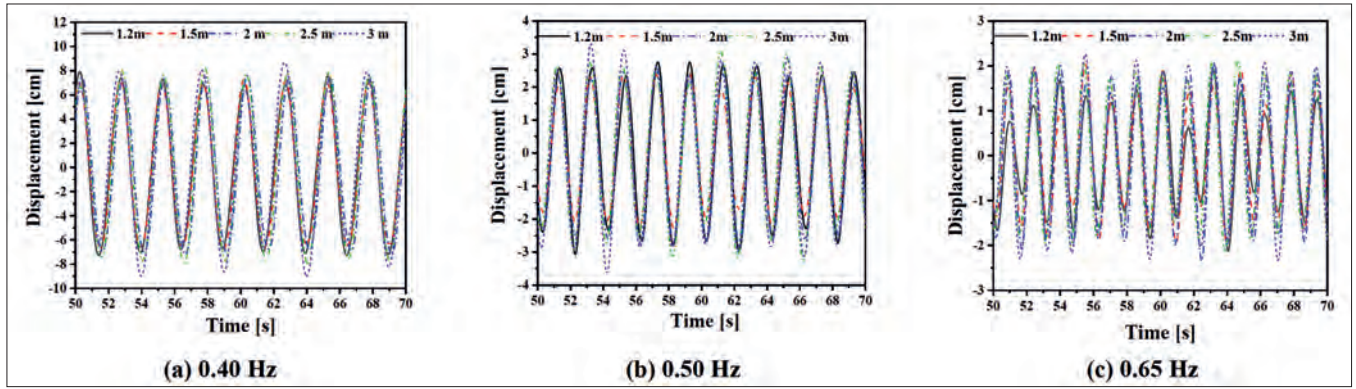


Fig. 3. Heave response of the floating body at different wave frequencies

TOWING TANK EXPERIMENT RESULTS

This experiment was conducted to measure the acceleration of a wind turbine platform with anti-heave devices. However, the actual process can interfere with the acceleration and the interference needs to be processed [24]. Integrating the processed acceleration twice gives the range of motion of the platform. The heave responses at different frequencies for each water depth are represented in Fig. 3.

The amplitude of the heave increases with the increase in water depth; the heave slowly increases when the water depth is 2-3 m.

NUMERICAL SIMULATION AND EXPERIMENTAL COMPARISON OF WIND TURBINE PLATFORMS AT DIFFERENT WATER DEPTHS

In this paper, a complete numerical simulation of a semi-submersible floating platform and NREL 5-MW wind turbine model was analysed using commercial CFD software STAR-CCM+ (17.02). The coupled response of the floating platform with anti-heave devices was specifically analysed under combined wind and wave conditions.

NUMERICAL METHODS

For transient, incompressible, and viscous fluids, the flow is governed by the continuity and Navier-Stokes equations:

$$\nabla \cdot \mathbf{u} = 0 \quad (6)$$

$$\frac{\partial \rho \mathbf{U}}{\partial t} + \nabla \cdot (\rho (\mathbf{U} - \mathbf{U}_g) \mathbf{U}) = -\nabla P_d - \mathbf{g} \cdot \mathbf{x} \nabla \rho +$$

$$\nabla \cdot (\mu_{eff} \nabla \mathbf{U}) + (\nabla \mathbf{U}) \cdot \nabla \mu_{eff} + f_\sigma \quad (7)$$

\mathbf{U} and \mathbf{U}_g represent the velocity of the flow field and grid nodes; P_d is the dynamic pressure of the low field (from subtracting the hydrostatic part from total pressure p); \mathbf{g} is the gravity acceleration vector; ρ is the fluid density; μ_{eff} denotes

the effective dynamic viscosity of fluid, in which μ and ν are the kinematic and eddy viscosity, respectively; and f_σ is a source term due to surface tension, which only takes effect at the free surface and equals zero elsewhere.

In order to capture the interface or free surface between air and water in a FOWT, the volume of fluid (VOF) method was used [25]. In the volumetric fluid method, the surface configuration was realised by the volume fraction, which varied between 0 and 1, depending on the percentage of the water phase in the cell volume. $\alpha = 1$ for the water cell, $\alpha = 0$ for the air cell and $0 < \alpha < 1$ for the air-water interface. The advection equation for a volume fraction is:

$$\frac{\partial \alpha}{\partial t} + \nabla \cdot (\mathbf{U} \alpha) + \nabla \cdot [\mathbf{U}_r \alpha (1 - \alpha)] = 0 \quad (8)$$

A bounded compression technique was adopted to better capture the free surface, introducing an additional third compression term on the left-hand side of the transport equation, where \mathbf{U}_r is a velocity field used to compress the interface.

COMPUTATIONAL DOMAINS AND PHYSICAL MODELS

The fluid domain range was selected to be -200 to 1000 m in the X direction, 200 m in the Y direction, and -160 to 300 m in the Z direction of the platform.

The front of the computational domain was set as the velocity inlet and the velocity was controlled by the velocity of the first-order VOF wave. The back of the computational domain was set as the pressure outlet and the pressure controlled by the hydrostatic pressure of the first-order VOF wave [26]. In addition, concerning the physical conditions of the model tested, a wave-damping zone was set up, considering the wave reflection near the outlet boundary; it minimised the effect of wave reflection on the far downstream outlet boundary [27].

The mooring system was set up in the form of three suspension chain lines, each with an angle of 120°, connected to three cable guide holes located at the bottom of the pontoon and a cable guide anchor located at the bottom of the computational domain [28].

MESH

The convergence of the numerical simulation was verified by comparing three different grid numbers: 1.31×10^7 , 1.08×10^7 , and 7.8×10^6 . Fig. 4 represents the heave motion of the deepCwind turbine platform with different computational domain sizes under the same wave height and wave frequency, under the action of the floating-body heave.

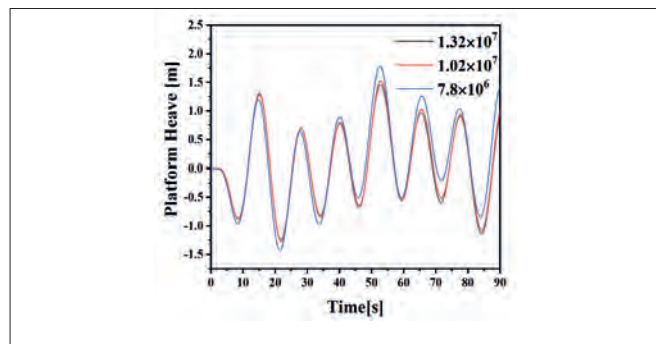


Fig. 4. Verification of the convergence of the calculation results by the number of grids

Comparing the three different calculation mesh quantities, the heave motion value of the three-floating-body wind turbine platform changes less when the calculation domain is small, and the Z-direction displacements of the DeepCwind platform are closer to each other as the calculation domain keeps increasing. Considering the number of grids, computational time consumption, and reliability of the results, 1.08×10^7 grids and 0.1 s time steps were selected for the related numerical analysis. The grid layout is shown in Fig. 5.

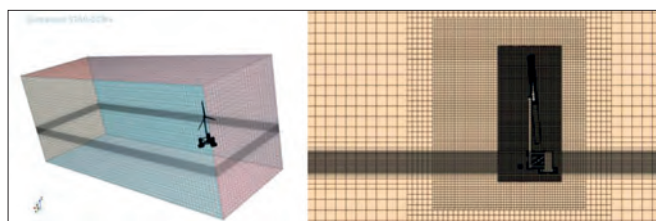


Fig. 5. Computational domain and mesh

RESULTS AND DISCUSSION

The main results discussed in this section include ‘free decay’ and ‘kinematic response’. Numerical analyses were performed on the full-size model and the results scaled, as in Table 2.

COMPARISON OF HYDROSTATIC DECAY EXPERIMENTS

The free decay motion of heave and pitch is illustrated in Fig. 6. On the free decay curve, the time interval between two adjacent peaks or troughs is one oscillation period. The corresponding intrinsic period of the free decay motion can be obtained by randomly selecting multiple neighbouring peaks (troughs) and calculating the average value of multiple oscillation periods.

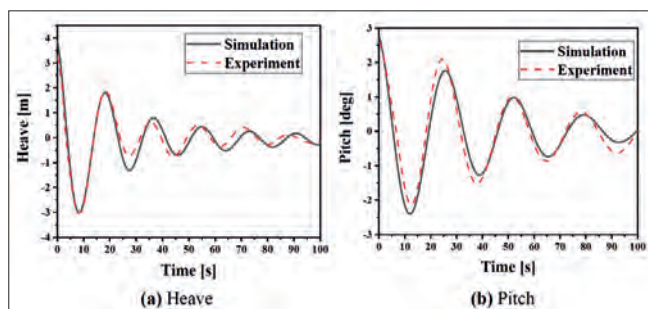


Fig. 6. Free decaying motion

Tab. 4. Natural periodicity of wind turbine platforms with damping devices

Parameters	Model Value [s]	Simulation Values [s]	Difference [%]
Heave period	16.78	17.67	5.0%
Pitch period	26.45	25.61	3.2%

The platform heave and pitch motions between hydrostatic attenuation test results and values were compared. The experimental and numerical simulation values differ between 5.0% and 3.2%. These discrepancies could arise from various sources, including model simplifications, scaling effects, and experimental errors.

COMPARISON OF NUMERICAL SIMULATION AND EXPERIMENTAL RESULTS

Numerical simulations of a real-scale wind turbine platform were carried out by experimental working conditions. The numerical simulation included the analysis of the water depth on the wind turbine platform with anti-heave devices and the original model [20]. The reliability of the numerical simulation was verified through experiments and the analysis of the heave motion in the model with anti-heave devices, as well as the original model.

By simulating the five water depths for the working conditions and comparing them with the experimental results, the time domain curves for different cases are shown in Fig. 7.

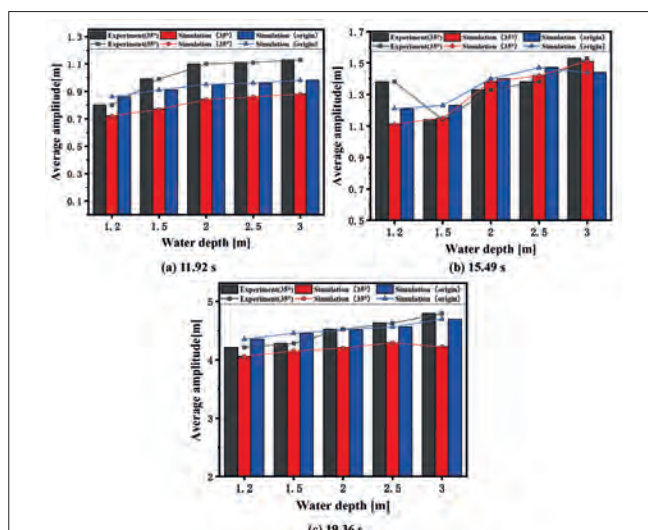


Fig. 7. Numerical and experimental results in the different water depth conditions.

Tab. 5. Summary of simulation and experimental results

Condition number	Frequencies[Hz]	Water depth [m]	Average amplitude [m]		
			Experiment (35°)	Simulation (35°)	Simulation (origin)
1	0.40	1.2	3.71	3.55	3.85
2	0.50	1.2	1.38	1.11	1.21
3	0.65	1.2	0.80	0.72	0.86
4	0.40	1.5	3.78	3.65	3.95
5	0.50	1.5	1.14	1.15	1.23
6	0.65	1.5	0.99	0.77	0.91
7	0.40	2.0	4.02	3.70	4.01
8	0.50	2.0	1.33	1.38	1.40
9	0.65	2.0	1.10	0.84	0.95
10	0.40	2.5	4.13	3.79	4.06
11	0.50	2.5	1.38	1.42	1.47
12	0.65	2.5	1.11	0.86	0.96
14	0.40	3.0	4.29	3.80	4.19
14	0.50	3.0	1.53	1.51	1.44
15	0.65	3.0	1.13	0.88	0.98

The numerical simulation data were converted to a particular scale and compared with the experimental data. As seen in Fig. 7, the numerical simulation and experimental results can maintain the same heave trend in the same cycle and the motion amplitude of the experiment is larger than that of the numerical simulation. It can be seen that, the larger the period, the better the match. At wave period 15.49 s, the difference between the experimental and simulated values for each water depth is minimal. The error may be due to the constraints of the pedestal in the numerical simulation, the difference in the conduit material, and the error of the experimental equipment when capturing the motion. The average amplitudes of the experimental and numerical simulation results are shown in Table 5.

As shown in Table 5, the average amplitude of the heave motion in the numerical simulation and testing kept the same change rule. For the same frequency, the deeper the water depth, the greater the amplitude of the floating body movement when the water depth position was more than 2 m (the actual value was 120 m). When the movement amplitude grows slowly and tends to be stable, at this time, the water depth tends towards the infinite; however, at the same water depth position, the wave period is large, the amplitude of the floating body movement increases, and the numerical simulation results are in better agreement with the experimental results. The anti-heave device with 35° chamfered holes has a similar change in the response of the heave motion to the original model. In most working conditions, the heave motion reduction effect of the 35° chamfered perforation model is obvious.

CONCLUSIONS

In this study, the experimental and numerical methods are used to investigate the kinematic response of a floating wind turbine platform with chamfered holes and anti-heave devices.

The following conclusions were obtained by analysing the heave motion at different water depths and wave periods.

- (1) When the water depth becomes deeper, the amplitude of the heave motion of the three-floating-body wind turbine platform increases. At depths greater than 120 m (deep water) the amplitude of the heave motion increases slowly and stabilises.
- (2) The anti-heave effect of the three-floating-body wind turbine platform is affected by different waves. In most working conditions, the heave motion reduction effect of the wind turbine platform with anti-heave devices is obvious.
- (3) The effect of heave reduction of the wind turbine platform with anti-heave devices is more evident when the water depth increases. The smaller the wave period, the more obvious the effects of the reducing heave.

ACKNOWLEDGEMENTS

This study was financially supported by the Zhejiang Province 'Pointer' and 'Leader Goose' R&D Program of Zhejiang (2022C03023).

REFERENCES

1. Counci, 'https://gwec.net/global-wind-report-2021', GLOBAL WIND REPORT. 2021.
2. G. Nagababu, S.S. Kachhwaha, and V. Savsani, 'Estimation of technical and economic potential of offshore wind along the coast of India', Energy. 2017, doi:10.1016/j.energy.2017.07.032.
3. A. Goupee, B. Koo, R. Kimbal, K. Lambrakos, and H.J. Dagher, 'Experimental Comparison of Three Floating Wind Turbine

- Concepts', International Conference on Ocean, Offshore and Arctic Engineering. 2014.
4. X. Wu, Y. Hu, Y. Li, J. Yang, L. Duan, T. Wang, and S. Liao, 'Foundations of offshore wind turbines: a review', *Renew and Sustain. Energy Review*. 2019, doi:10.1016/j.rser.2019.01.012.
 5. Q. Cao, L. Xiao, Z. Chen, and M. Liu, 'An experimental study on dynamic behavior of a new concept of 10MW semi-submersible wind turbine', *ISOPE International Ocean and Polar Engineering Conference*. ISOPE. 2020.
 6. A. Nematbakhsh, D.J. Olingue, and G. Tryggvason, 'A nonlinear computational model of floating wind turbines', *Journal of Fluids Engineering*. 2013, doi:10.1115/1.4025074.
 7. A. Nematbakhsh, D.J. Olingue, and G. Tryggvason, 'A Nonlinear simulation of a spar buoy floating wind turbine under extreme ocean conditions', *Journal of Renewable and Sustainable Energy*. 2014, doi:10.1063/1.4880217.
 8. Z. Hu, L. Li, J. Wang, Q. Hu, and M.C. Shen, 'Dynamic responses of a semi-type offshore floating wind turbine during normal state and emergency shutdown', *China Ocean Engineering*. 2016, doi:10.1007/s13344-016-0005-y.
 9. A.M. Abou-Raya, N.N. Khali, and M.S. Afify, 'Dynamic behavior of TLP's supporting 5-MW wind turbines under multi-directional waves', *Ocean Systems Engineering*. 2016, doi:10.12989/ose.2016.6.2.203.
 10. C. Barrera, I.J. Losad, R. Guanche, and L. Johanning, 'The influence of wave parameter definition over floating wind platform mooring systems under severe sea states', *Ocean Engineering*. 2019, doi:10.1016/j.oceaneng.2018.11.018.
 11. Z. Zhao, W. Wang, W. Shi, and X. Li, 'Effects of second-order hydrodynamics on an ultra-large semi-submersible floating offshore wind turbine', *Structures*. 2020, doi:10.1016/j.istruc.2020.10.058.
 12. Y.R. Alkarem and B.O. Ozbahceci, 'A complementary analysis of wave irregularity effect on the hydrodynamic responses of offshore wind turbines with the semi-submersible platform', *Applied Ocean Research*. 2021, doi:10.1016/j.apor.2021.102757.
 13. Y.H. Bae, M.H. Kim, and Y.S. Shin, 'Rotor-floater-mooring coupled dynamic analysis of mini TLP-type offshore floating wind turbines', *International Conference on Offshore Mechanics and Arctic Engineering*, OMAE. 2010.
 14. I. Bayati, S. Gueydon, and M. Belloli, 'Study of the effect of water depth on potential flow solution of the OC4 semi-submersible floating offshore wind turbine', *Energy Procedia*. 2015, doi:10.1016/j.egypro.2015.11.419.
 15. X. Chen, H. Yu, W. Wang, and B. Wang, 'Analysis of Motion Response of Wind Turbine Platform Considering Different Heading Angles and Water Depth', *2nd International Conference on Sustainable Energy, Environment and Information Engineering (SEEIE)*. Atlantis Press. 2019.
 16. C. Le, Y. Li, and H. Ding, 'Study on the coupled dynamic responses of a submerged floating wind turbine under different mooring conditions', *Energies*. 2019, doi:10.3390/en12030418.
 17. L. Zhang, C. Michailides, Y. Wang, and W. Shi, 'Moderate water depth effects on the response of a floating wind turbine', *Structures*. 2020, doi:10.1016/j.istruc.2020.09.067.
 18. Z. Lin, X. Liu, and S. Lotfian, 'Impacts of water depth increase on offshore floating wind turbine dynamics', *Ocean Engineering*. 2021, doi:10.1016/j.oceaneng.2021.108697.
 19. W. Wei, Z. Chen, J. Panpan, L. Zhiqiang, and X. Yonghe, 'Numerical simulation and experimental study on perforated heave plate of a DeepCwind floating wind turbine platform', *Ships and Offshore Structures*. 2022, doi:10.1080/17445302.2022.2062157.
 20. W. Wei, F. Sheming, Y. Yunxiang, Z. Cheng, X. Liqun, W. Guibiao and L. Zhiqiang. 'Study on the Influence of Chamfer Perforation on Heave and Pitch of a Single Floating Platform' *Polish Maritime Research*. 2023. doi:10.2478/pomr-2023-0005
 21. A. Robertson, J. Jonkman, M. Masciola, H. Song, A. Goupee, A. Coulling, and C. Luan, 'Definition of the semi-submersible floating system for phase II of OC4', *National Renewable Energy Lab (NREL)*. Golden, CO (United States). 2014, doi:10.2172/1155123.
 22. J. Chen, Z. Liu, Y. Song, Y. Peng, and J. Li, 'Experimental study on dynamic responses of a spar-type floating offshore wind turbine', *Renewable Energy*. 2022, doi:10.1016/j.renene.2022.06.149.
 23. L. Meng, Y. He, Y. Zhao, T. Peng, and J. Yang, 'Experimental study on aerodynamic characteristics of the model wind rotor system and on characterization of a wind generation system', *China Ocean Engineering*. 2019, doi:10.1007/s13344-019-0014-8.
 24. A. Kafeel, S. Aziz, M. Awais, M.A. Khan, K. Afaq, S.A. Idris, and S.M. Mostafa, 'An expert system for rotating machine fault detection using vibration signal analysis', *Sensors*. 2021, doi:10.3390/s21227587.
 25. C.W. Hirt and B.D. Nichols, 'Volume of fluid (VOF) method for the dynamics of free boundaries', *Journal of Computational Physics*. 1981, doi:10.1016/0021-9991(81)90145-5.

26. T.T. Tran and D.H. Kim, 'A CFD study of coupled aerodynamic-hydrodynamic loads on a semi-submersible floating offshore wind turbine', *Wind Energy*. 2017, doi:10.1002/we.2145.
27. Y. Zhang and B. Kim, 'A fully coupled computational fluid dynamics method for analysis of semi-submersible floating offshore wind turbines under wind-wave excitation conditions based on OC5 data', *Applied sciences*. 2018, doi:10.3390/app8112314.
28. T.T. Tran and D.H. Kim, 'The coupled dynamic response computation for a semi-submersible platform of floating offshore wind turbine', *Journal of wind engineering and industrial aerodynamics*. 2015, doi:10.1016/j.jweia.2015.09.016.

ANALYSIS AND EXPERIMENTAL VERIFICATION OF IMPROVING THE EEDI OF A SHIP USING A THRUSTER SUPPLIED BY A HYBRID POWER SYSTEM

Janusz Mindykowski  ¹ *

Łukasz Wierzbicki  ²

Mariusz Górniak  ¹

Andrzej Piłat ¹

¹ Gdynia Maritime University, Faculty of Electrical Engineering, Gdynia, Poland

² Gdańsk Remontowa Shiprepair Yard S.A., Gdańsk, Poland

* Corresponding author: j.mindykowski@we.umg.edu.pl (J. Mindykowski)

ABSTRACT

In this study, the authors present a theoretical analysis and experimentally verified methods to improve the Energy Efficiency Design Index (EEDI) of ships. The improvements were studied via the application of an innovative solution of a thruster supplied by a hybrid power system on board a passenger-car ferry. The authors performed sea trials of a ship's electrical power system supplied by battery packs with diesel generating set power units. The experimental study focused on energy balance and management, which were considered together with related power quality issues. The authors found that the application of an energy storage system to the ferry, such as batteries, with the simultaneous adaption of the operation modes of the electrical power system for current exploitation, significantly improved energy efficiency. Fuel consumption and CO₂ emission were reduced, while adequate parameters of electrical power quality were maintained to meet classification standards.

Keywords: Energy Efficiency Design Index, thruster supplied by hybrid power system, energy balance, power management, electrical power quality parameters, classification institutions

INTRODUCTION

Increased energy/fuel efficiency and reduced greenhouse gas emissions, such as CO₂, NOX and SO₂, have become important challenges for shipbuilders, operators and regulators. These challenges are the most intensively explored issues in the domain of maritime transport. Greenhouse gas emissions are typically limited to CO₂ emissions [1] and are associated with fuel consumption by ships. Ship fuel consumption is dependent on the total energy demand of the ship, including electrical energy. Therefore, optimising and utilising generated electricity is important for limiting fuel consumption and, consequently, CO₂ emissions. CO₂ emissions in global maritime transport are controlled by the International Maritime Organisation (IMO), and other organisations, via the internationally regulated Energy

Efficiency Design Index (EEDI). This index applies to all vessels built after 2013 with a tonnage exceeding 400 GT and the goal is to establish the minimum energy efficiency of ships according to their type and size. The EEDI is expressed as the ratio of CO₂ emissions (in grams) to the transport work of a vessel in ton-miles. Following the IMO concept [1], the CO₂ reduction level for the first phase has been set to 10%, covering the following ship types: tankers, bulk carriers, gas carriers, general cargo ships, container ships, refrigerated cargo carriers and combination carriers. In 2014, the IMO stated [1] that the adopted amendments to the EEDI regulations will extend the scope of this coefficient to LNG carriers, ro-ro cargo ships (vehicle carriers), ro-ro cargo ships, ro-ro passenger ships and cruise passenger ships with non-conventional propulsion. This extension also includes ships equipped with hybrid power systems, such as battery-powered systems.

The next step of the considered rules development proceeded under the auspices of the Marine Environment Protection Committee (MEPC), during its last session on July 3-7, 2023. The MEPC 80 session adopted the 2023 IMO Strategy on the 'Reduction of GHG Emissions from Ships', with enhanced targets, to tackle harmful emissions [2]. The revised IMO GHG Strategy includes an enhanced common ambition to reach net-zero GHG emissions from international shipping close to 2050, a commitment to ensure an uptake of alternative zero and near-zero GHG fuels by 2030, and indicative check-points for 2030 and 2040. Amendments to the International Convention for the Prevention of Pollution from Ships (MARPOL) Annex VI came into force on 1 November 2022. Developed under the framework of the Initial IMO Strategy on the Reduction of GHG Emissions from Ships (agreed in 2018), these technical and operational amendments require ships to improve their energy efficiency in the short term, thereby reducing their greenhouse gas emissions [3]. From 1 January 2023 it is mandatory for all ships to calculate their attained Energy Efficiency Existing Ship Index (EEXI), to measure their energy efficiency and to initiate the collection of data for the reporting of their annual operational carbon intensity indicator (CII) and CII rating [3]. EEXI is calculated using the same formula as EEDI and represents "the amount of CO₂ emissions from a ship when the ship sail transports one ton cargo for one nautical mile". Regardless of a ship's delivery date, ships of 400 GT and above, which are engaged in international voyages, are subject to the EEXI regulations and the EEXI of each ship needs to be calculated. Ships of a specific size are subject to the EEXI regulations and need to comply with the requirements, equivalent to the EEDI requirements of 2023. Under the EEXI regulations, vessels classified as a 'Bulk carrier', 'Tanker', and 'Ro-ro cargo ship (vehicle carrier)' need to comply with the EEXI requirement equivalent to the Phase 2 EEDI requirement, while a 'Containership', 'General cargo ship', 'LNG carrier', and 'Gas carrier' would need to comply with the EEXI requirement equivalent to the Phase 3 EEDI requirement. Therefore, a ship subject to EEDI regulations, which complies with the Phase 2 or Phase 3 requirement, automatically complies with the EEXI regulations. If a ship does not meet the EEXI requirement, the ship needs to implement any countermeasures, such as engine power limitation or the installation of energy saving devices, etc., to improve their EEXI.

In recent years, battery-powered ships have been widely explored in various studies [4–7]. These studies analysed many aspects. For example, [4], [5], and [8], analysed the impact of new conversion technologies, such as power electronics, battery energy storage and DC power systems, on overall energy efficiency, power quality and emission levels and discussed them thoroughly. Some studies [6] used specific methods and tools to provide accurate estimates of the battery state of charge (SoC), which is a critical factor for the safe and reliable operation of battery systems. A few papers have presented the main problems encountered by designers of small, hybrid-powered ferries powered by lithium batteries, including energy balance issues and the development of an energy management policy [7]. In this study, the authors considered and compared their results with existing state-of-the-art research in this field and present an analysis and experimental verification of methods to improve the energy efficiency of ships using a thruster supplied by a hybrid power system. The presented article focuses on the

new challenges in energy balance and energy management policy and considers related power quality issues in modern ferries, when using innovative propulsion systems. This study focuses on a passenger-car ferry, which began operation in 2021.

In this paper, improving the EEDI is presented by using an example of a modern, two-way hybrid electric ferry. The ferry was designed for coastal shipping between Norwegian fjords and designed with the understanding that, during crossings between ports, energy will be primarily sourced from battery banks, which will be charged during stops. However, in unforeseen situations, it is possible to use diesel generating set power units (part of a hybrid propulsion system) in the electric power system of passenger-car ferries. Using the operational strategy adopted by the Norwegian ferry operator, the project focuses on minimising energy consumption. This involves the following solutions: (I) powering the vessel from battery banks combined with diesel generating sets, (II) energy-efficient LED lighting, (III) flexible power supply systems using power electronic frequency converters, (IV) underwater hull coatings to reduce friction, (V) specially designed hull shapes to minimise water resistance, and (VI) lightweight ship hull construction. All of these solutions were implemented in practice by the designers and shipbuilders of the ferry but they are presented in this paper with different importance. The solutions I, II and III, concerning the limitation of electrical energy consumption on board the ship, are considered in this way, and the authors concentrate on examining the impact of implementing the conditions outlined in the introduction, mainly solution I. This examination was experimentally verified on the basis of the sea trials case study and is presented in the related chapters of the article. Solutions II and III were analysed and discussed on the basis of the literature on the subject and the authors' professional experiences, but only in the context of their influence on a worsening of power quality in the considered ship electrical power system. The remaining solutions, i.e. solutions IV, V and VI, concern improving the EEDI by minimising ship hull friction and reducing its resistance to water. Moreover, the latter solution enables the increase in deadweight tonnage of cargo transported by the ship. In consequence, the aforementioned solutions provide the means to increase the ship's transport work and reduce fuel consumption.

This paper is organised as follows. In the second section, we provide a short description of the selected design and operational indexes characterising the energy efficiency of the ship. The following sections present a standard passenger-car ferry as the object of investigation, formulation of the problem, and a short description of the plan and conditions of experiments performed during the sea trials. The fifth section highlights the issues of energy balance, energy management and power quality as the main aspects of the experimental verification of the improvement of the ship's energy due to the hybrid power system. The experimental results are then presented and discussed. The last section concludes the study and includes recommendations.

ENERGY EFFICIENCY MEASURES

The full description of the algorithm for the EEDI is complicated [8]. However, its simplified form can be found in [9].

$$EEDI = \frac{1}{E} (A + B + C - D) \quad (1)$$

A , B , and C represent the CO₂ emissions of the main engine(s), auxiliary engine(s), and shaft generator/motor(s), respectively. D is the reduction in CO₂ owing to innovative technologies and E is the transport work of the ship.

Detailed descriptions of the parts in Eq. (1) are described in [9].

Additionally, another simplified version of the EEDI can be expressed as follows [6]:

$$EEDI = \frac{P_{\text{installed}} \times SFC \times CF}{DWT \times V_{\text{ref}}} \quad (2)$$

where $P_{\text{installed}}$ is the installed power of a ship (in kW), SFC is the specific fuel consumption (in g/kWh), CF is the carbon conversion factor, DWT is the deadweight tonnage of the ship, and V_{ref} is the reference speed.

The initial analysis of Eq. (1) leads to the conclusion that the value of the EEDI will be smaller and more favourable for the intended objectives when A , B , and C are smaller and when D and E are larger.

It is also worth noting that, on the basis of Eq. (2), the EEDI value is directly proportional to the installed ship power and the coefficients characterising the specific fuel consumption and carbon conversion of this ship, as well as varying inversely proportional to the product of deadweight capacity and speed of the vessel.

Technologies and methods for improving the EEDI that implement the above actions are widely described in the literature [10,11]. These methods include hydrodynamic optimisations (hull design optimisations), propulsion optimisations (innovative propulsion system solutions), alternative fuels (LNG - Liquefied Natural Gas, CNG - Compressed Natural Gas), and other approaches (the use of renewable energy sources, operational methods, and innovative solutions for controlling the equipment in shipboard electrical systems).

The lower the design value of the EEDI from Eq. (1), compared to the threshold value established based on the reference line concept [12,13], the more energy-efficient the ship will be according to the IMO criteria, which can be expressed by Eqs. (3), (4) and (5).

$$EEDI_{\text{attained}} \leq EEDI_{\text{required}} \quad (3)$$

Here, $EEDI_{\text{attained}}$ is the calculated index based on the complete algorithm described in [4] and $EEDI_{\text{required}}$ is defined by The International Convention for Prevention of Pollution from Ships (MARPOL), following conventional requirements [7]:

$$EEDI_{\text{required}} = (1 - \frac{X}{100}) \times L_{\text{ref}} \quad (4)$$

where X is the reduction factor for selected types of ships and L_{ref} is the line reference value, described by the following formula [7]:

$$L_{\text{ref}} = a \times b^{(-c)} \quad (5)$$

Here, a , b , and c are the tabulated parameters for individual ship types.

The EEDI threshold value ($EEDI_{\text{required}}$) will be successively limited and extended to new ship types following the extension

program schedule and guidelines adopted by the IMO [1]. Finally, these amendments mean that ship types responsible for approximately 85% of the CO₂ emissions from international shipping are included under the international regulatory regime.

It should be noted that EEDI represents a measure of the design efficiency of a new ship but it does not explain its operational efficiency [9]. Additionally, twin ships with the same EEDI may have different operational efficiencies due to their different operational profiles and sailing conditions [14]. To extend the EEDI design approach, the IMO has also developed the Energy Efficiency Operational Indicator (EEOI), to indicate the fuel consumption of a specific ship, including detailed information, such as cargo mass and the number of passengers carried. Appropriate values of EEOI are given for single and multiple vessels, according to the description and explanation in [15].

OBJECT OF THE INVESTIGATION

The object of this study was a standard double-ended passenger-car ferry (Fig. 1) equipped with an innovative electric propulsion system, operating in a diesel-electric hybrid configuration. It was powered by battery packs working in combination with generators using biodiesel fuel.

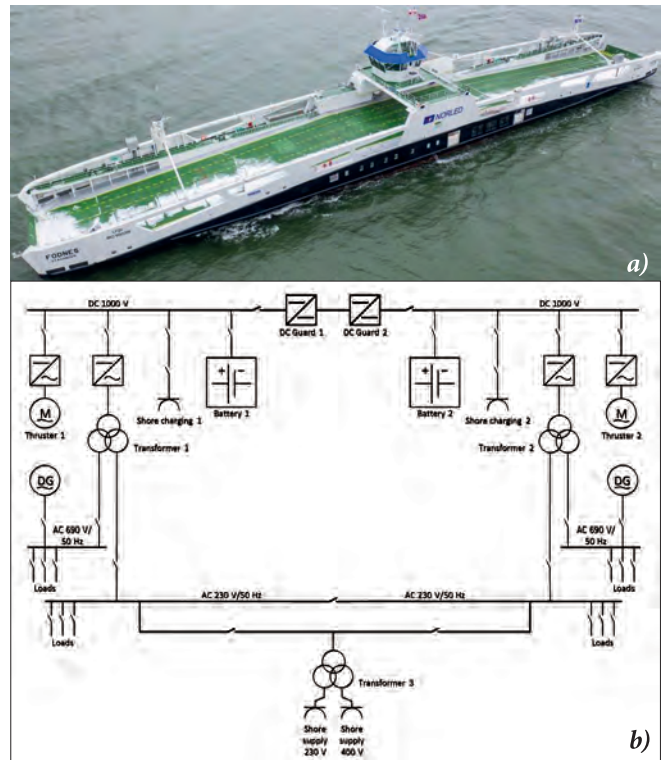


Fig. 1. Standard double-ended passenger-car ferry: (a) ship view based on [16] and (b) diagram of the power system equipped with diesel-electric hybrid electric propulsion

The electrical power system of this ferry is divided into two symmetrical sections: the bow (FWD – Forward part of vessel) and the stern (AFT – After part of vessel). Each section contains a power generation unit supplying an AC distribution board rated at 690 V / 50 Hz, a transformer with ratings of 500/99/500 kVA and 690/230/540 V / 50 Hz connecting the

AC distribution board at 230 V / 50 Hz and the DC at 1000 V, battery banks and a propulsion system with a motor rated at 960 kW, 600 V, and 64 Hz, which is powered by a DC/AC converter. The propulsion unit from SCHOTTEL is supplied from a DC 1000 V distribution board using a VACON NXI power electronic converter, which is an inverter. The inverter consists of IGBT switches and produces a symmetrical, 3-phase PWM-modulated AC voltage to the motor.

The elements on the configuration diagram (Fig. 1b) have designated indexes. '1' refers to the forward part of the electrical power system and '2' refers to the aft part of this system. 'DG' indicates the generating sets and the diesel generator. The ship's electrical power system is equipped with shore charging and shore supply (SS), connections for charging battery packs and supplying the ship from the shore, and DC guard protection modules [17], which enable fast disconnection and full selectivity between forward and aft DC grids.

FORMULATION OF THE PROBLEM

The goal of this study was to examine the impact of implementing the conditions outlined in the Introduction (I), (II), and (III)) for improving the energy balance of the ship while maintaining the appropriate parameters of electrical energy quality, following the standards of Det Norske Veritas (DNV) [16], which surveys the construction process before classification of the vessel. Notably, the DNV rules for DC battery-powered systems are exclusively focused on the DC busbar voltage as the main supply of the system. Other switchboards supplying ship systems, such as AC 690 V / 50 Hz and AC 230 V / 50 Hz in complementary configurations of electric power systems (without energy storage systems), fulfil the function of the main switchboards and should comply with full verification conditions according to the requirements defined in the appropriate rules [18]. However, additional checking of the power quality standards related to currents is justified by the fact that the systems described under conditions (II) and (III) can significantly minimise electrical energy consumption on one side. However, strongly non-linear elements (LED lighting and power electronic inverters) can cause a worsening of the power quality in the considered electrical power system.

The first condition (the use of an electric power system powered by batteries with DG generating sets) is an energy-saving solution without the additional consequences of power quality degradation in the power system.

The second condition (the application of energy-saving LED lighting) has negative effects on the selected electricity quality parameters [19]. Results have shown that LED lamps result in significant savings in electricity consumption but they behave as nonlinear loads, generating higher frequency harmonics, which can worsen power quality in the distribution network [20].

In our case, with a DC main switchboard, the problem concerns the large number of power supplies equipped with rectifiers applied to supply a large number of LED lamps in the AC system.

The third implemented option includes flexible power supply systems of selected devices using power electronic inverters. Some of the load circuits consist of systems with motors driven by power converters, such as propulsion drives, ventilation and air conditioning systems and cooling systems. Powering motors with variable frequency drives allows the adaptation of the motor load to real needs. In such cases, the total energy consumed by all electric motors on the ship can be considerably reduced. The consequence of using multiple-power electronic converters may be an increase in total harmonic distortion (THD) in the current waveforms.

Thus, although the primary concern for the shipbuilder and operator is energy saving, checking whether the power quality parameters comply with the classifying institution standards is justified and required.

RESEARCH PLAN

The study involved the improvement of electricity generation and its use for effective power management supported by solutions that minimise energy consumption. We also determined the power quality parameters for this power system.

To determine the power quality parameters, the authors measured the voltages and currents during sea trials of the ferry using the FWD system as follows: FWD Generating set (DG1), FWD Transformer with 540 V side (Transformer 1), FWD DRIVE SWBD at DC 1000 V (DC 1000 V) and FWD Thruster Unit (Thruster 1). In the DC 1000 V distribution board, there was an installed DC/AC converter, producing up to 600 V / 64 Hz voltage to supply the Thruster 1 motor. Therefore, the measurement system consisted of 15 channels, as specified in Table 1. The voltage measurements were carried out via transducers from LEM (Life Energy Motion) and current measurements were conducted using Rogowski coils from PEM (Power Electronic Measurements). The measurement system consisted of an industrial computer from National Instruments, equipped with a PXIe-8135 controller and three PXIe-6358 data acquisition cards. The measurement results, recorded as instantaneous samples of voltage and current values, were used to determine the parameters in the sea trial. The voltage and current parameters (Table 1) were calculated using home-built software and a dedicated spreadsheet.

Tab. 1. Specifications of the measurement channels and parameters

No.	Channels	Object	Measured parameters	Connection points for measuring probes
1	1,2,3	DG1	U12, U23, U31	AC 690 V / 50 Hz
2	4,5	Transformer 1	U12, U23	Transformer 1
3	6	DC 1000 V	U	DC 1000 V
4	7,8,9	DG1	I1, I2, I3	AC 690 V / 50 Hz
5	10,11,12	Transformer 1	I1, I2, I3	Transformer 1
6	13,14,15	Thruster 1	I1, I2, I3	DC 1000 V / DC/AC Converter 1

ENERGY BALANCE AND ENERGY MANAGEMENT

The energy balance includes the specification of DC and AC energy sources and their parameters and the specifications and characteristics of the most important loads in the analysed system. These specifications are provided in Table 2. The table was prepared with loads active during the sea trials highlighted. The other loads have been presented as a complementary component.

Table 2 shows that the total sum of the energy loads from the thrusters supplied by the 1000 V DC voltage (and other loads supplied from the 690 V AC and 230 V AC voltages) reaches up to 2619.7 kW (including 1920 kW in the thrusters) and exceeds

the sum of the energy sources corresponding to 978 kVA (DGs, generating sets) plus 1130 kWh (batteries). However, many of the loads shown in Table 2 (for positions 1-4, 9-17, and 19-23) only work during limited and different time intervals, and depend on the given mode of ferry operation. Thrusters typically work by using power below their rated values and an appropriately designed simultaneity coefficient for the analysed power system. With regard to the scope of the article focusing on the sea trials case study, only the simplified energy balance for the ferry operation in electric mode and hybrid mode, corresponding to normal, routine voyages between the Norwegian fjords, is analysed more carefully. Under these circumstances the thrusters do not work together at full power in the continuous work regime. Thrusters can either work

Tab. 2. Specifications of the loads and sources of energy for the analysed ferry's electrical power system

No	Name of device	Power [kW]	Switchboard	Estimated load [kW]	Simultaneity load factor / degree of power source use
Loads active during the sea trials					
1	HP-1 Aers Central Heat/Cool System	43.0	AC 690V/50Hz FWD	16.0	0.37
2	Steering, Cooling, SW Circulation, LO Transfer and Fuel Oil Pumps	53.0	AC 690V/50Hz FWD	32.0	0.60
3	HP-2 Aers Central Heat/Cool System	43.9	AC 690V/50Hz AFT	13.5	0.31
4	Provision Cooling Plant 1	1.5	AC 690V/50Hz AFT	1.5	1.00
5	Lighting, navigation and hotel load (superstructure load)	≤60.0	AC 230V/50Hz	48.0	0.80
6	CPI/2/3-Fans	17.1	AC 230V/50Hz	9.0	0.53
7	Thruster FWD	960.0	DC 1000V FWD	528.0	0.55
8	Thruster AFT	960.0	DC 1000V AFT	432.0	0.45
Other Loads					
9	Bilge Pump 1	11.0	AC 690V/50Hz FWD	NA*	NA
10	Fire Bilge Pump 1	43.6	AC 690V/50Hz FWD	NA	NA
11	Fire Pump 1	30.0	AC 690V/50Hz FWD	NA	NA
12	Deluge Pump	160.0	AC 690V/50Hz FWD	NA	NA
13	MOB Davit	10.2	AC 690V/50Hz FWD	NA	NA
14	Watermist Pump 1	22.0	AC 690V/50Hz FWD	NA	NA
15	Deck Foam System	13.2	AC 690V/50Hz FWD	NA	NA
16	HPU Pump 1	30.0	AC 690V/50Hz FWD	NA	NA
17	HPU Pump 2	30.0	AC 690V/50Hz FWD	NA	NA
18	Provision Cooling Plant 2	1.5	AC 690V/50Hz FWD	NA	NA
19	Deck Washing Pump	5.5	AC 690V/50Hz FWD	NA	NA
20	Bilge Pump 2	11.0	AC 690V/50Hz AFT	NA	NA
21	Fire Bilge Pump 2	43.6	AC 690V/50Hz AFT	NA	NA
22	Fire Pump 1	30.0	AC 690V/50Hz AFT	NA	NA
23	Watermist Pump 2	22.0	AC 690V/50Hz AFT	NA	NA
24	Black Water Pump, Hydrophore Pumps, Oily Bilge Pumps, Grey Water Pump, SW Circulation 2, Cooling 2 and Transfer Pumps	18.5	AC 230V/50Hz	NA	NA
*NA - not applicable, loads out of the work during the sea trials					
Sources of power active during the sea trials					
1	DG1	489 kVA / 440 kW	AC 690V/50Hz FWD	388.0	0.88
2	DG2	489 kVA / 440 kW	AC 690V/50Hz AFT	388.0	0.88
3	Battery 1	565 kWh	DC 1000V FWD	260.0 **	0.46 ***
4	Battery 2	565 kWh	DC 1000V AFT	260.0	0.46
** - Power necessary to complete an energy balance during the sea trials					
*** - Degree of power source use estimated for 1h of the sea trials					

individually or in sequence, e.g. at 55% (first thruster) and 45% (second thruster) of the load, i.e. a total thrusters' power of 960 kW. During the sea trials, the remaining load of the system listed in positions 1-6, was about 120 kW. This means that the total sum of the load of the system was 1080 kW, taking into account the simultaneity coefficients for the thrusters and remaining loads shown in Table 2, listed in positions 1-8. At the same time, the related sources of power active during the sea trials corresponded to 776 kW (DGs) and 520 kWh (batteries). Some of the simultaneity load coefficient and degrees of power source values shown in Table 2 have been determined on the basis of the shipyards' ferry documentation and the sea-going practice experience of the authors. It was assumed that the sea trials combinations of loads and power sources corresponded to the routine, regular conditions of shipping planned between two Norwegian fjords. Therefore, the operating conditions assumed the estimated values of the load coefficients and degrees of power sources used, as well as a very specific regime of ferry operation, i.e. a vessel operating a 15 minute crossing of the Norway fjords, 26 times in a normal day, where a single crossing distance is 3 km. It is, therefore, possible to achieve an energy balance in the analysed electrical power system. This balance was achieved in all possible modes of operation of the ferry by implementing energy management recommendations. These recommendations focused on improving energy efficiency, analysing and implementing appropriate operational maintenance of the batteries, and analysing and verifying all required functionalities in all modes of operation of the ferry.

The lifetime and reliability of the batteries are crucial for realising the recommendations. These recommendations were formulated by the batteries' manufacturer and the ship's designers. The lifetime of the installed batteries is closely related to the number of charge and discharge cycles. Batteries must operate within their optimal discharge and charge limits. Table 3 presents the essential parameters (and their values) for energy storage systems (ESSs) for the optimisation of fuel consumption and safety.

Figure 2 provides the planned operational profile of the ship sailing during very bad weather conditions (changing SoC from 70% to 56%). Based on this plan (Fig. 2) and agreements with the shipowner, suitable ESS parameters were selected (Table 3) to ensure the proper operation of the thruster supplied by the hybrid power system. Detailed data concerning battery exploitation are described by the energy and power management system (EPMS), which allows for the monitoring and control of power flow, battery charge levels, charge and discharge limits, and coordination with the SSs and shore chargers (Fig. 1b).

Tab. 3. Recommended parameters of battery-powered systems

ESS parameters	Unit	Value
Battery capacity	[kWh]	565
Setpoint: Low Low Level	[kWh]	190
Setpoint: Low Level	[kWh]	225
Take-me-home (return to nearest port)	[kWh]	35
SoC after sailing	[%]	56
SoC after charging	[%]	70
Setpoint: Low safe level limit	[kWh]	14
	[%]	2.5

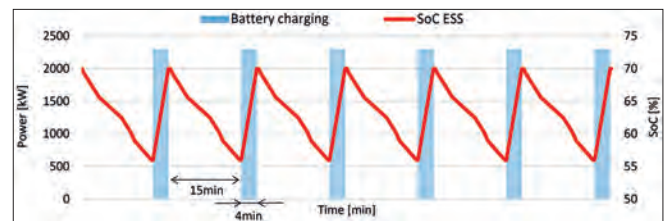


Fig. 2. Planned operational profile of sailing for the studied ferry: red line indicates change of SoC ESS, blue columns represent available high power DC-plug from the built shore infrastructure

In the case of a low-level alarm (indicating a low level of available energy from the batteries), the diesel generator (DG) starts automatically and, in the case of a low low-level alarm (indicating critically low ESS charge), less critical/important devices are automatically shut down. Exceeding the low safe level limit can result in permanent damage to the ESS. In the case of hybrid mode operation (e.g. navigation to the shipyard), the DGs transfer energy to the ESS and, during normal navigation in the electric mode (M1), they work as an emergency power source. Redundancy is based on the previously discussed separation into two ship power systems: AFT and FWD. In the case of a failure in one system, there is the possibility of full control and operation of the other. Redundancy also applies to the integrated automation system (IAS), meaning that the control of devices, such as valves, fans, and pumps, is divided into two separate and independent parts of the system. The ESS has been designed to provide full power to both thrusters, while satisfying the superstructure load requirements (approximately 60 kW). Additionally, during the design phase, considerations were given to the possibility of adverse weather conditions, which could result in higher ESS loads. The connection to the SS at 230/400 V is realised at the AC distribution switchboard at 230 V / 50 Hz. The primary role of the SS is to supply the hotel load and additional systems when the ship is docked in port or at a quay. There is also the possibility of charging the batteries with low power through the SS. The SS system also synchronises and verifies the voltage phase compatibility between the vessel and the port power system.

EXPERIMENTAL VERIFICATION

The examination of the impact of implementing the conditions outlined in the Introduction, as solution I, was experimentally verified on the basis of the sea trials, which mainly addressed electric and hybrid modes of the ferry operation.

Table 4 shows the five possible operational modes of the ferry.

The purpose of the trials was to examine the correct operation of the ship's electrical power system in each of the tested modes and to verify the efficiency of the cooperation between the battery banks and the associated power generation units for optimal power management by the system.

The analysis of the results depends on three operating cases of the electrical power system resulting from positions M1 and M2, as shown in Table 4. The selected cases, T1, T2 and T3, subjected to tests during sea trials, are explained in Table 5.

Tab. 4. Five possible modes of operation of the ferry

Operating modes			
No	Name	Source of power	Description of the system operation
M1* (T1)	Electric mode	ESS	Normal operating mode: AC 690 V / 50 Hz and AC 230 V / 50 Hz distribution boards are powered by a converter from DC 1000 V.
M2* (T2/T3)	Hybrid mode	ESS & DG	Mode used during extended voyages: depending on current power needs, generators provide propulsion requirements and extra energy is transferred to the batteries (charging of battery). With an increased power demand, the batteries release/transfer power to the grid, known as „peakshaving”.
M3	Diesel-electric mode	DG	Emergency operation mode: DG supplies AC 690 V / 50 Hz, AC 230 V / 50 Hz distribution boards, and thrusters through DC 1000 V.
M4	Shore mode	Shore grid	Supply via SS: the possibility of charging ESS with low power; normal battery-charging mode at night.
M5	Charging mode	Shore grid	High-power charging from shore: the ability to charge the battery banks quickly during a few-minute stop in port.
* under consideration in this study			

In the first mode, Thruster 1 and Thruster 2 operate with step load changes in the range of 20-100% and power is delivered from the ESSs, with their initial SoC ranging from 58-59%.

In the next mode, Thruster 1 operates with the load continuously changing from 0 to 100%, while DG 1 and 2 provide power to the grid and the ESS battery banks charge from the initial state of 49 and 51% up to 55 and 56% (for each battery set). In the last considered mode, T3, there are step changes in the loads of Thruster 1 and 2, in the range 20-100%. In this mode, both DG 1 and 2 operate in parallel and the ESS battery banks cooperate with the grid.

After exceeding the discharge level threshold, the DGs are switched on according to the set priority and their allowed number.

Tab. 5. Modes of operation of the electrical power system verified during the sea trials

Mode of work	Thruster 1	Thruster 2	DG1	DG2	Battery 1	Battery 2
T1	Step load change 20...100%	Step load change 20...100%	–	–	Load	Load
T2	Continuous load change 0...100%	–	Load	Load	Hybrid	Hybrid
T3	Step load change 20...100%	Step load change 20...100%	Load	Load	Hybrid	Hybrid

An essential part of the energy management process is analysing the power management of the thrusters, considering the battery charge/discharge process. An example of this analysis, conducted for operating mode T3 (described in Table 5), is illustrated in Fig. 3.

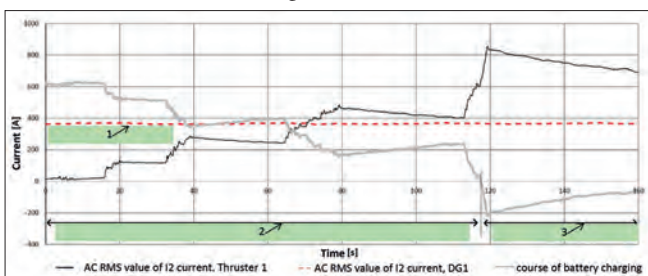


Fig. 3. Time and current traces of DG 1 and Thruster 1 for the T3 operating mode in the context of the energy charging/discharging from the battery packs; 1 - effective point of work of DG1, a constant load of the generator unit DG1, 2 - energy delivered to the battery, charging of the battery, 3 - energy taken from the battery, an increase in the level of available power

The plots in Fig. 3 show the currents when the battery is being charged and discharged, while maintaining a constant current from generator unit DG1, corresponding to the effective operating point of DG1. The battery provides electrical energy when increased power is required and it charges (takes power from the grid) when the system can operate with less available power. The effective DG1 current (dashed red line) is set using the ESS manufacturer's software. It is a result of how the battery charging/discharging processes are controlled, as defined in the ship's control system (SoC, charging current limit and discharging current limit) and in accordance with the previously discussed operational profile of the vessel for various conditions. During battery charging from the DG (hybrid mode M2), the load capacity of the thrusters is limited until the batteries are charged to a level that enables safe operation of the system. Fixed-pitch propellers allow economic ship operation with a shipping speed of 10 knots. During the sea trials (T3 mode), the effective point of work of DG1 was established for a load less than its nominal value, which was approximately 88% of the nominal value.

POWER QUALITY ISSUES

Another objective of the study was to determine and analyse selected parameters of electrical power quality related to voltage and current, in both the DC and AC parts of the system and the frequency values in the AC part. This was to assess the shape of the voltage and current waveforms and to verify whether these parameters were within the limits set by the DNV classification guidelines. Maintaining these parameters at appropriate levels is crucial for ensuring the safety and reliability of maritime systems [21].

The configuration diagram of this power system (Fig. 1b) shows that the 1000 V DC bus bars are the main supply for this ship. Therefore, appropriate DNV limits and measurement results from the tests were compared. The results of this comparison are presented in Table 6.

Tab. 6. Comparison of the DNV voltage limits and test results for electric DC battery-powered systems

Indexes of power quality	DNV voltage limits	Ship tested	
		Measurement results	Mode of tests
δU_{dev} Voltage deviation in equipment connected to battery during charging	+30 to -25%	-11.90% -10.90%	T2 T3
δU_{dev} Voltage deviation in equipment connected to the battery not being charged	+20 to -25%	-13.70%	T1
δU_{var} Voltage cyclic variation	max 5%	4.07% 4.12% 4.07%	T1 T2 T3
δU_{rip} Voltage ripple	max 10%	<<10.00%*	T1, T2 and T3
*did not observe considerable voltage ripples			

The measurement results in Table 6 are illustrated in Figs. 4 and 5.

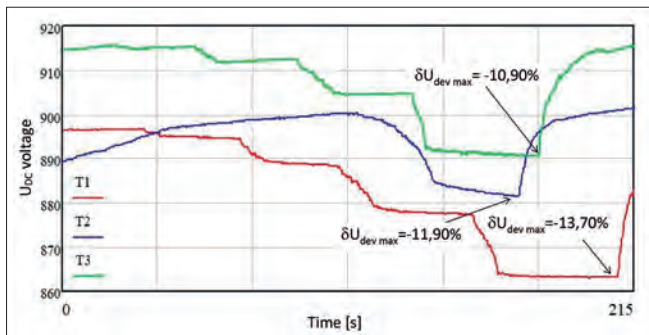


Fig. 4. Changes in the UDC voltage on main bus bar FWD 1000 V for different modes of operation of the hybrid thruster power supply system: T1 - red line, T2 - blue line, T3 - green line

Examples of voltage cyclic variations (δU_{var}) are shown in Fig. 5.

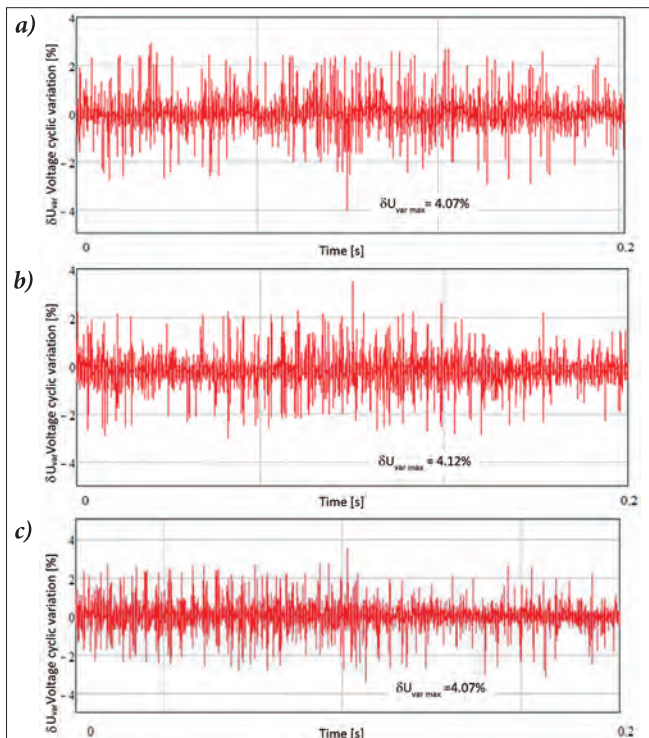


Fig. 5. Voltage cyclic variation (δU_{var}) based on the measurements in the FWD DRIVE SWDB 1000 V (channel 6) for the different modes of operation: a) T1, b) T2 and c) T3

Examples of the cyclic voltage variations (δU_{var}) in DC voltage, within the range of 0.2 s, are illustrated in Fig. 5. We also determined the highest observed values of the δU_{var} (%) parameter obtained during full-time recording for the T1, T2 and T3 modes of operation. Calculations of the δU_{var} values were carried out based on the relative instantaneous difference in UDC voltage values from the average.

The maximum δU_{var} was 4.12% (for T2 mode) and values of this index complied with the DNV standards for all of the regimes (T1, T2 and T3).

The experiments on voltage limits, as well as the analysis of the supply voltage parameters characterising the related DC network presented in Table 6 and Figs. 4 and 5, confirmed that all the requirements set by the DNV classification limits were met by a significant margin. The results were used to receive the appropriate DNV certificate for this passenger-car ferry.

In addition to the research on the 1000 V DC network, regarding voltage limits following DNV standards, experiments were carried out for AC voltage limits at 690 V / 50 Hz. The results of these experiments are presented in Table 7.

Tab. 7. Comparison of the DNV voltage limits and test results for electric AC-powered systems

Analysed parameters	DNV limits	Measurement results	Test modes
δU_{dev} , Voltage deviation - Steady state			
Deviation of nominal AC system voltage for main power distribution	$\pm 2.5\%$	<0.19%	T2 and T3
Deviation of nominal AC system voltage for emergency power distribution	$\pm 3.5\%$	–	T2 and T3
δU_{dev} , Voltage deviation - Transient state			
Deviation of nominal AC voltage	from -15 to +20%	<0.35%	T2 and T3
δf_{dev} , Frequency deviation			
Deviation of nominal frequency of AC voltage:			
- under steady state load	$\pm 5\%$	<0.24%	T3
- under transient load	$\pm 10\%$	<0.6%	T2
Voltage harmonic distortion			
THD _u	8%	<4.5%	T2 and T3

All of the results in Table 7 complied with the DNV classification requirements.

The research scope not only included the acceptable voltage DC and AC deviations from their reference values, but also the acceptable levels of higher voltages and current harmonics in the ship's electrical power system (690 V AC, inverter supplying the thruster).

Research on the variability of current distortion factors has been performed using measured factors: Subgroup total harmonic distortion (THDS), Subgroup total waveform distortion (TWDS) and Subgroup total interharmonic distortion (TIHDS) [22,23]. These are more demanding criteria than the traditional THD factor, as included in [18]. These factors, based on [23], were determined for frequency spectra up to the 100th harmonic.

Figure 6 shows waveforms of the changes in TWDS and THDS distortions of the I1 current of Thruster 1, as a function of time during various system operation modes.

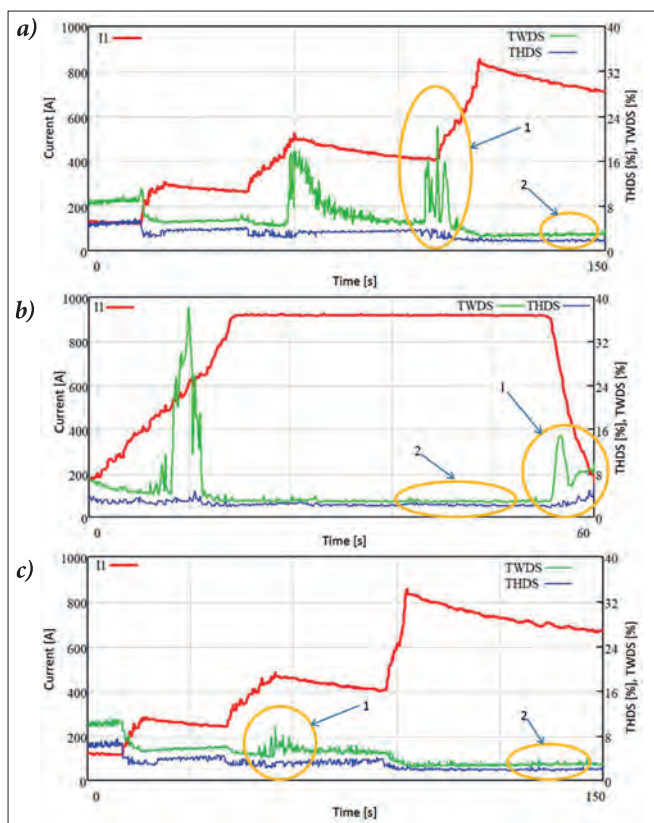


Fig. 6. Selected courses of changes in TWDS and THDS current distortion coefficients for the I1 current of Thruster 1 and its root mean square (RMS) values for different modes of operation; 1 - Transient state values, 2 - Steady state values: T1 - energy delivered from the battery (a), T2 - continuous load change of Thruster 1 (b), T3 - step load change of the Thruster 1 (c)

Figure 6 shows the courses carried out for the T1, T2 and T3 modes and additionally scaled (T1) to the full power of the DC/AC converter, which was dependent on the switching on power procedure during sea trials realisation. The applied inverter was constructed as a switchable device with two symmetrical power levels [24].

The TWDS values are higher than the THDS values at the same moments of time because of their definitions, except for the higher harmonics and other components distorting the signals, such as inter-harmonics. Higher TWDS values were mainly observed in the transient states of the thruster rpm control, which is connected with related step load changes. By contrast, in the steady state, they tend towards values similar to the THDS coefficient (Fig. 6a, 6b, and 6c). The analysed TWDS values should be considered at the ship-design stage, in reference to the selection of the related power-supplying cable cross sections. The operation in T1 mode permits a larger thruster load than in T2 and T3 modes. In T2 and T3, the battery charging process limits the available power of the cooperating generators, which are started and switched on to charge the battery. The course differences in RMS values of the current (shown in Fig. 6) result from the different characteristics of the set load (battery mode, continuous or step load) and the manual value-setting procedure. Additionally, ship operation under the T1 mode (energy delivered from the battery) resulted in a local reduction in the ship's environmental impact, as manifested by noiselessness, a lack of vibrations and CO₂ emission-free navigation.

This effect also concerns the T3 mode but to a lesser degree, because the sources of power are environmentally friendly ESS and DG, as complementary options. The thruster is controlled with step load changes, which is an advantageous option from an environmental point of view. The discussed effect does not apply to the T2 mode, where sources of power are mainly DGs, and the thruster is controlled with continuous load changes, which have more harmful influences on the local environment.

The THDS, TWDS and TIHDS coefficient results characterising the current supply of the thruster (Thruster 1) motor are presented in Table 8. These data are steady-state values for the maximal thruster load.

Tab. 8. Comparison of the current limit requirements from the classifying institutions and test results for the DC battery power systems on the AC side of the inverter installed on the Thruster 1 line

Indexes of power quality from [21]	DNV current harmonic limits	I1 current measurement results for the ship [%]	Mode of test
THDS	Not applicable	1.90	T1
TWDS		2.96	
TIHDS		1.86	
THDS	Not applicable	2.07	T2
TWDS		2.89	
TIHDS		1.70	
THDS	Not applicable	1.96	T3
TWDS		2.99	
TIHDS		1.86	

The measured I2 and I3 current results for Thruster 1 are approximately the same as the values for the I1 current.

Due to the lack of appropriate DNV standards regarding the limitation of emission of harmonic current in thruster power supply systems, the power quality criteria for THDS and TWDS for the I1 thruster current were examined with reference to the PN/IEC 61000-3-4 standard. This standard addresses the "limitation of emission of harmonic current in low-voltage power supply systems for equipment with rated currents greater than 16 A" [25].

Although this standard could be helpful, due to its scope, a rough analysis showed that, unfortunately, this standard only covers devices with a rated current limited to 75 A. Next, for equipment exceeding 75 A, as the input current per phase, it has been stated: "... the supply authority may accept the connection of the equipment on the basis of the agreed active power of the consumer's installation. The local requirements of the power supply authority apply in this case". Taking into account the fact that the analysed passenger-car ferry, classified under DNV rules, successfully began operation on February 2021 [16], this means that all technical conditions for regular shipping, including power quality conditions, were fulfilled and accepted by the ferry operator.

CONCLUSIONS AND RECOMMENDATIONS

- According to the theoretical analysis, and based on the experimental results for improving a ship's energy efficiency using existing energy efficiency measures (primarily the

EEDI), the limitation of CO₂ emissions in this case study was realised, based on increases in the 'D' and 'E' components in Eq. (1) with the application of innovative technologies. These innovative technologies concern solutions for minimising energy consumption, which are expressed by the solutions outlined in the Introduction I, II and III and related to the reduction of the demand for the ship's electrical energy (component D in Eq. (1)). These also include the solutions IV, V and VI, leading to minimising ship hull friction and reducing its resistance to water, related to the increase of the value of the product DWT × V_{ref}, which is the transport work of the ship (component E in Eq. (1)).

- In the analysed system, energy consumption was minimised by implementing solutions, such as an appropriately controlled power supply of battery packs, in combination with generator sets. This was partly achieved by selecting a fixed efficient generator operation mode (Fig. 3), using energy-efficient lighting and power supply systems of selected devices, such as propulsion drives, ventilation and air conditioning systems controlled by power electronic converters.
- The implementation of the solutions given above and adaptation of the operating modes of the ship's power system to current operational needs (based on the strategy from the shipbuilder and Norwegian ferry operator), provided a considerable improvement in the vessel's energy balance, while reducing fuel consumption and CO₂ emissions.
- This operation, which assumes that the passenger-car ferry is dedicated to inland shipping and crossing between Norwegian fiords, is achieved using energy from a battery system that is charged during port stays, requiring an appropriate schedule of ship operation. This schedule (Table 4 and Table 5) has been successfully tested during sea trials, especially regarding the electric and hybrid mode functionalities. The study confirmed the functionality and effectiveness of powering the ferry's thrusters using the hybrid battery system, combined with generator units, for effective power management in the system and minimising energy consumption.
- The improved energy balance, in this case, was possible due to appropriately supplied thrusters, many other specific load controls and operations (Table 2) and an appropriately designed simultaneity factor for the loads and degree of power source use. Special attention was paid to the energy balance analysis during the sea trials, which corresponded to the routine operation of the ferry.
- The energy balance was determined in all possible modes of operation for the ferry (Table 4) in combination with energy management recommendations, which are based on the verification of all required functionalities in all operation modes. The authors also used the energy management guidelines within the range of appropriate operational maintenance of batteries (Table 3), in combination with the ESS characteristics and the operational shipping profile (Fig. 2).
- One very important component for the successful realisation of energy management, besides the appropriate choice of the operation mode of the analysed system (Table 4), is the experimental verification of the related design assumptions. The test results are consistent with the ship's design assumptions

and confirmed the ability to achieve fuel savings and reduce CO₂ emissions. Moreover, it has been shown that the influence of the ferry operation on the local environment mainly depends on the characteristics of the load changes and the mode of the ferry operation. The most advantageous option is connected with the step load changes and the operation mode supplied by batteries, T1. Under these conditions a local reduction in the ship's environmental impact, as manifested by noiselessness, a lack of vibrations and CO₂ emission-free navigation, will occur.

- The experimental verification of the improvements in ship energy due to the application of a hybrid thruster power supply system considered the variables mentioned above, including the energy balance and management combined with power quality issues. Although the primary concern for a shipbuilder and operator is energy saving, checking whether the power quality parameters are complying with the classification standards is also important and should be required. The checked power quality parameters for 1000 V DC network cover are: $\delta U_{dev} \in [-10.90\%, -13.70\%]$, $\delta U_{var} \in [4.07\%, 4.12\%]$, $\delta U_{rip} < 10\%$, and for 690 V AC network: $\delta U_{dev} < 0.19\%$ (steady state), $\delta U_{dev} < 0.35\%$ (transient state), $\delta f_{dev} < 0.24\%$ (steady state), $\delta f_{dev} < 0.6\%$ (transient state), and THDu < 4.5%. All of the analysed parameters characterising power quality in the 1000 V DC and 690 V AC networks fully comply with the mandatory requirements of the classification standards.
- Additionally, some power quality parameters, related to the thruster current on the AC side of the inverter, were tested in this case study and the following results were obtained: THDS $\in [1.90\%, 2.07\%]$, TWDS $\in [2.89\%, 2.99\%]$ and TIHDS $\in [1.70\%, 1.86\%]$. Taking into account the fact that the presented data are steady-state values for the maximal thruster load, these values are acceptable from a practical operating point of view. However, this analysis was outside the IEC standards.
- In summary, the detailed conclusions and findings regarding the experimental verification for improving the ship's energy with the application of a hybrid thruster power supply system are:
 - Hybrid power supply systems for thrusters enable efficient load compensation, resulting in fuel savings and a reduction in CO₂ emissions.
 - Hybrid systems, along with the operational profile, increase the vessel's operational safety because the energy from battery packs can provide a stable power source and immediate backup power in the case of DG failures. This design approach for ship power systems is necessary and recommended for use in the future.
 - In this analysed system, the DG worked successfully at an optimal, fixed point of work with a constant load of its generator, which also reduced emissions.
 - The installed battery system allows their charging using shore power and replacing with DGs during stays at the port. Consequently, this provides a local reduction in the ship's environmental impact when operating in battery mode.

- The advantages described above were achieved due to the innovative application of the thruster supplied by the hybrid power system without altering the power quality requirements of the analysed system.

ACKNOWLEDGEMENTS

The authors are grateful to the authorities, designers and shipbuilders from Remontowa Shipbuilding S.A. and Remontowa Electrical Solutions for providing us with company procedures to perform the sea trials and for the related databases and raw measurements for this case study.

LIST OF ABBREVIATIONS

AC	– Alternating Current
AFT	– After part of vessel
CII	– Carbon Intensity Indicator
CNG	– Compressed Natural Gas
DC	– Direct Current
DG	– Diesel Generator unit
DNV	– Det Norske Veritas
DWT	– Deadweight Tonnage of the Ship
EEDI	– Energy Efficiency Design Index
EEOI	– Energy Efficiency Existing Ship Index
EEOI	– Energy Efficiency Operational Indicator
EPMS	– Energy and Power Management Ship
ESS	– Energy Storage System
FWD	– Forward part of vessel
GHG	– Greenhouse Gas Emission (from Ship)
GT	– Gross Tonnage of the Ship
IEC	– International Electrotechnical Commission
IGBT	– Insulated-Gate Bipolar Transistor
IMO	– International Maritime Organization
LED	– Light Emitting Diode
LEM	– Life Energy Motion
LNG	– Liquefied Natural Gas
M	– Motor
MARPOL	– The International Convention for Prevention of Pollution from Ships
MEPC	– Marine Environmental Protection Committee
PEM	– Power Electronic Measurements
PWM	– Pulse Width Modulation
RMS	– Root-Mean-Square (value)
RPM	– Revolutions per minute
SFC	– Specific Fuel Consumption
SoC	– State of Charge
SS	– Shore Supply
SWBD	– Switchboard
THD	– Total Harmonic Distortion
THDS	– Subgroup Total Harmonic Distortion
TIHDS	– Subgroup Total Interharmonic Distortion
TWDS	– Subgroup Total Waveform Distortion

REFERENCES

1. IMO documents on “Improving the energy efficiency of ships”, Available online: <https://www.imo.org/en/OurWork/Environment/Pages/Improving%20the%20energy%20efficiency%20of%20ships.aspx> (accessed on 29.06.2023).
2. <https://www.imo.org/en/MediaCentre/MeetingSummaries/Pages/MEPC-80.aspx> (accessed on 11.12.2023).
3. IMO Annex 1, Resolution MEPC.328(76), “Amendments to the annex of the protocol of 1997 to amend the international convention for the prevention of pollution from ships, 1973 - As modified by the protocol of 1978 relating thereto”. 2021. Revised MARPOL Annex VI. Date of entry into force: 1 November 2022.
4. O. Alnes, S. Eriksen, and B. Vartdal, “Battery-Powered Ships: A Class Society Perspective”, IEEE Electrification Magazine. 5(3), pp. 10-21, 2017. doi:10.1109/MELE.2017.2718823.
5. E. Skjong, R. Volden, E. Rødskar, M. Molinas, T.A. Johansen, and J. Cunningham, “Past, Present, and Future Challenges of the Marine Vessel’s Electrical Power System”, IEEE Transactions on Transportation Electrification. Vol. 2, No 4, pp. 522-537, 2016. doi:10.1109/TTE.2016.2552720.
6. P. Geng, X. Xu, and T. Tarasiuk, “State of Charge Estimation Method for Lithium-Ion Batteries in All-Electric Ships Based on LSTM Neural Network”, Polish Maritime Research. 3 (107), Vol. 27, pp. 100-108, 2020. doi:10.2478/pomr-2020-0051.
7. M. Kunicka and W. Litwin, “Energy efficient small inland passenger shuttle ferry with hybrid propulsion - concept design, calculations and model tests”, Polish Maritime Research. Vol. 26, No 2, pp. 85-92, 2019. doi:10.2478/pomr-2019-0028.
8. IMO Resolution MEPC 308(73), Annex 5, “Guidelines on the method of calculation of the attained energy efficiency design index (EEDI) for new ships”, London, 2018.
9. D. Kumar and F. Zare. “Comprehensive review of Maritime Microgrids”, IEEE Access. Volume 7, pp. 67249-67277, 2019. doi:10.1109/ACCESS.2019.2917082.
10. W. Zeńczak, “The selected ways of improving the factors of energy efficiency of ships”, Journal of Gdynia Maritime University. No 108, pp.181-196, 2018. doi:10.26408/108.15.
11. T. Szelangiewicz, T. Abramowski, K. Żelazny, and K. Sugalski, “Reduction of Resistance Fuel Consumption and GHG Emission of Small Fishing Vessel by Adding a Bulbous Bow”, Energies. 14, 1877, 2021. doi:10.3390/en14071837.
12. IMO Resolution MEPC 62(24) Add.1, Annex 19 – Resolution MEPC 203(62), 2011.

13. IMO Annex 11, Resolution MEPC 337 (76), 2021 Guidelines on the reference lines for use with operational Carbon Intensity Indicators, related to the revised MARPOL Annex VI, November 2022.
14. "Energy Efficiency of Ships: What Are We Talking About?" Accessed on: 29.06.2023, Available: https://www.transportenvironment.org/wp-content/uploads/2021/05/2012_12_Ship_efficiency_briefing.pdf.
15. "Guidelines for Voluntary Use of the Ship Energy Efficiency Operational Indicator (EEOI)", document MEPC.1/arc.684, Aug.2009.
16. "Information materials about considered passenger-car ferry". Available online: <https://www.gospodarkamorska.pl/stocznia-remontowa-shipbuilding-przekazala-norwegom-prom-elektryczny-fodnes-57277#lg=1&slide=0> (accessed on 22.06.2023).
17. Information materials about VACON® NXP DCGuard. Available online: https://files.danfoss.com/download/Drives/DKDDPFP906A402_VACON%20NXP%20DCGuard_LR.pdf (accessed on 13.12.2023).
18. DNV, Rules for the Classification of Ships, Part 4 Systems and Components, Chapter 8, Electrical installations, July 2022 edition.
19. A. Wantuch and M. Olesiak, "Effect of LED Lighting on Selected Quality Parameters of Electricity", *Sensors*. 23(3), 1582, 2023. doi:10.3390/s23031582.
20. IEC 61000-3-2:2019-04-Electromagnetic Compatibility (EMC). Part 3-2: Limits. Limits for Harmonic Current Emissions (Equipment Input $\leq 16A$ per Phase).
21. P. Gnaciński, T. Tarasiuk, J. Mindykowski, M. Pepliński, M. Górniak, D. Hallmann, and A. Piłat, "Power Quality and Energy – Efficient Operation of Marine Induction Motors", *IEEE Access*. Vol.8, pp.152193-152203, 2020. doi:10.1109/ACCESS.2020.3017133.
22. J. Mindykowski and T. Tarasiuk, "Problems of power quality in the wake of ship technology development", *Ocean Engineering*. Vol.107, pp.108-117, 2015. doi:10.1016/j.oceaneng.2015.07.036.
23. J. Mindykowski, T. Tarasiuk, and P. Gnaciński, "Review of legal aspects of electrical power quality in ship systems in the wake of the novelisation and implementation of IACS rules and requirements", *Energies*. 14(11), 3151, 2021. pp. 1-21, doi:10.3390/en14113151.
24. Technical documentation concerning VACON-NXI-Inverters, FI9-FI14, <https://files.danfoss.com/download/Drives/VACON-NXI-Inverters-FI9-FI14-Operating-Guide-DPD00909F-EN.pdf> (accessed on 13.12.2023).
25. IEC 61000-3-4 standard, "Limitation of emission of harmonic current in low-voltage power supply systems for equipment with rated current greater than 16A.", First edition 1998-10, Geneva, Switzerland.

UNIVERSAL SEA/FEM BASED METHOD FOR ESTIMATION OF VIBROACOUSTIC COUPLING LOSS FACTORS IN REALISTIC SHIP STRUCTURES

Michał Dręzek* 

¹⁾ Fem4cad Sp. z o.o, Gdynia,

²⁾ Gdańsk University of Technology, Industrial Doctoral School, Gdańsk, Gdańsk, Poland,

Marek Augustyniak

Gdansk University of Technology, Institute of Nanotechnology and Materials Engineering, Poland

* Corresponding author: michaldrezek@gmail.com (Michał Dręzek)

ABSTRACT

Despite the fact that there is an existing body of literature addressing the computation of Coupling Loss Factors (CLFs) via the Finite Element Method (FEM), no publications have sufficiently taken into account real structural joints in their approach. Previous research has focused on academic cases of trivial connections, rarely involving more than two steel plates. To enable Statistical Energy Analysis (SEA) on a real ship, a methodology for determining CLFs for non-trivial systems is proposed, considering realistic boundary conditions and irregularities that can occur in marine structures. Based on the method, a library of CLFs is created by selecting the tested connections to enable modelling of about 90% of the acoustic paths on an existing jack-up vessel. Boundary conditions were set by introducing spring elements with a stiffness calibrated to the type of connection and taking the adjacent structure into account. In previous works, CLFs were determined for basic connections of rectangular plates. The lack of scantling variations, ignoring discontinuities and only defining parallel edges in the considered models, lead to the overestimation of energy transmission in real structures. To consider the influence of the above, random deviations from the initial stiffness of the springs at individual edges and point restraints at random points are introduced in this paper.

Keywords: Statistical Energy Analysis, Power Injection Method, Finite Element Method, Coupling Loss Factor

INTRODUCTION

Passenger ships, commercial ships and specialised vessels are treated as ordinary workplaces, with respect to vibroacoustic conditions, although they have their own unique character, being places of both professional and leisure activities [1]. For their health, it is important to reduce the levels of daily noise and vibration to which they are exposed. To do this, one has to be able to predict the transmission of vibroacoustic energy at the design stage. Energy-based modelling approaches are often used to describe the higher frequency vibrational behaviour of complex systems in some average, statistical or approximate way. The most important of these methods is statistical energy analysis (SEA). At low

frequencies, the finite element method (FEM) is used. This article focuses on determining coupling loss factors (CLF) for real-world structural connections in the medium and high frequencies (octaves 63-2000 Hz). CLFs are key parameters for SEA; they describe the energy transmission between connected subsystems.

BASICS OF SEA

SEA involves the prediction of the vibration response of a complex structure by dividing it into subsystems and determining the average energy. The transmission of vibration energy between subsystems is characterised by damping loss factors (DLF) and coupling loss factors (CLF). The DLF

corresponds to the damping in the subsystem itself and the CLF corresponds to the energy dissipation at the subsystem connections. The CLFs and the DLFs form a matrix of coefficients in the energy balance equation, which is used to calculate the energy of subsystems when the input powers are known. The CLFs can be obtained using an analytical wave approach for several types of junctions of semi-infinite plates. An alternative is the power injection method (PIM), which is an approach in which the CLF values can be obtained by measuring subsystem energy and power input [2].

The fundamental relationship, on which the SEA and PIM is based, is the balance between the input power and the output power of the subsystem (a part of the whole system e.g. a single wall). For the i -th subsystem, this equation has the following form:

$$P_{i,in} = P_{i,out} \quad (1)$$

$$P_{i,in} = P_{i,dissipated} + \sum_{j \neq i}^N P_{ij} \quad (2)$$

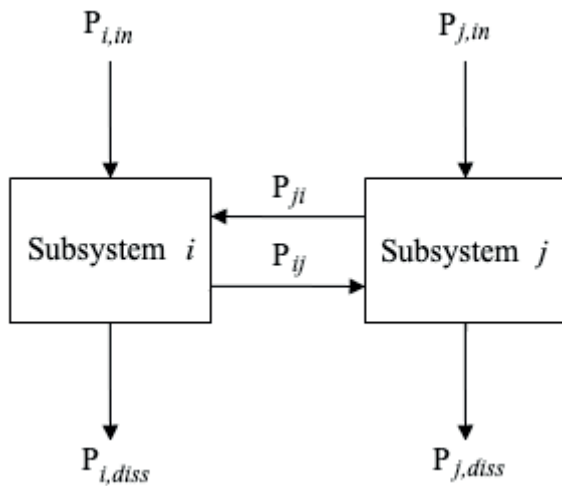


Fig. 1. Scheme of energy exchange in the SEA system

where $\sum_{j \neq i}^N P_{ij}$ is the power transferred by the i th subsystem to the subsystems coupled with it. It is assumed that there is no indirect coupling of subsystem s (only subsystems in the immediate vicinity can transfer energy to each other). The power dissipated by the subsystem depends on the damping loss factor and is calculated as follows:

$$P_{i,diss} = \omega \cdot \eta_i \cdot E_{i,tot} \quad (3)$$

where:

ω – the angular frequency corresponding to the centre frequency f of the band

η_i – damping loss factor (DLF)

$E_{i,tot}$ – total energy of the subsystem

The power transferred from subsystem i to subsystem j depends on the difference in vibration energy between them and can be represented by the following relationship:

$$P_{ij} = \omega \cdot \eta_{ij} \cdot E_{i,tot} - \omega \cdot \eta_{ij} \cdot E_{j,tot} \quad (4)$$

η_{ij} and η_{ji} are coupling loss factors (CLF) which are essential coefficients in SEA.

By knowing the above dependencies, it is possible to compose SEA equations, which can be presented in matrix form:

$$\omega \begin{bmatrix} \eta_i + \sum_{i \neq 1}^N \eta_{1i} & \cdots & -\eta_{1N} \\ \vdots & \ddots & \vdots \\ -\eta_{N1} & \cdots & \eta_N + \sum_{i \neq N}^{N-1} \eta_{Ni} \end{bmatrix} \times \begin{bmatrix} \langle E_1 \rangle \\ \vdots \\ \langle E_N \rangle \end{bmatrix} = \begin{bmatrix} P_{i,1} \\ \vdots \\ P_{i,N} \end{bmatrix} \quad (5)$$

The power injection method (sometimes called the experimental SEA or ESEA) involves exciting successive subsystems one by one with known power, measuring the total energies of the subsystems, and filling in the energy and power matrix. After inverting the energy matrix, a matrix of coefficients is obtained, according to the equation:

$$\omega \begin{bmatrix} \eta_i + \sum_{i \neq 1}^N \eta_{1i} & \cdots & -\eta_{1N} \\ \vdots & \ddots & \vdots \\ -\eta_{N1} & \cdots & \eta_N + \sum_{i \neq N}^{N-1} \eta_{Ni} \end{bmatrix} = \begin{bmatrix} P_1 & \cdots & 0 \\ \vdots & \ddots & \vdots \\ 0 & \cdots & P_N \end{bmatrix} \times \begin{bmatrix} \langle E_{11} \rangle & \cdots & \langle E_{N1} \rangle \\ \vdots & \ddots & \vdots \\ \langle E_{1N} \rangle & \cdots & \langle E_{NN} \rangle \end{bmatrix}^{-1} \quad (6)$$

In practice, both the total energy and input power values are difficult to obtain and are potential sources of inaccuracy. Moreover, creating a classic laboratory measuring system is costly and time-consuming. Therefore, methods using FEM are developed in parallel to experimental research.

STATE OF THE ART

The basics of both SEA and PIM are well described in the literature and yet some of their practical aspects remain challenging.

Le Bot and Cotoni [3] created validity diagrams of the SEA and described its assumptions in detail. The possibility of using PIM was indicated by Lyon as early as 1975 [4]. Laboratory experiments using this method have been described many times [5-7]. Due to the difficulty of controlling the input power and obtaining the energy of the subsystems, as well as the cost of both the measurement system and the test object, all of these tests were carried out for trivial systems. Numerical methods, in the form of a finite element method, became the next step in the development of PIM.

Pankaj et al. [8] described a method to carry out PIM using FEM. The expected results were obtained for an L-type connection for discrete frequencies. For SEA to be useful in industry, the coefficients must be averaged over the frequency domain. Only the simplest system was tested, i.e. two identical perpendicular plates. In a precisely uniform rectangular plate, the waves generated within the source plate propagate

consistently along fixed paths, exhibiting no dispersion to alternate positions as they travel towards the receiving plate. This characteristic behaviour arises due to the absence of internal discontinuities and parallel sides. Such situations rarely occur in real structures. Even in ships built of repetitive structures, there are scantling variations, discontinuities and non-parallel edges. As a result, an irregular system has a smaller overall energy transmission than a regular system.

An interesting approach to estimating CLFs was presented by Thite and Mace [9], who proposed to randomise the properties of the system being analysed and average the resulting estimates but without repeating the full FEA. This allows for very computationally cheap results but is difficult to use in shipbuilding practice. The authors relied on the assumption that “response statistics are somewhat independent of detailed physical variables if the variability is ‘large enough’”. Unfortunately, in the case of ship’s structures, the variability of physical properties is often not large enough, considering the criteria they adopt.

Poblet-Puig [10] developed a strategy to solve the problem of negative CLF values, which are sometimes obtained from Eq. (8). In the case of the structures considered in this article (due to their size), negative CLFs are rare and the proposed averaging technique allows them to be ignored.

There are also numerous publications on vibroacoustic transmission that use techniques other than PIM. Shorter and Langley [11] proposed a general method for predicting the ensemble average steady-state response of vibroacoustic systems. The authors not only decided not to recure to PIM, but bypassed the basic assumptions of SEA as well, concerning the strength of the coupling between the subsystems, the nature of the excitation, or the resonant nature of the response. Their approach also yielded ‘indirect’ CLFs (CLFs between statistical subsystems that are not physically adjacent).

Attempts to include stiffened plates in the framework of Statistical Energy Analysis have led to the creation of a new branch of SEA development, in which subsystems are treated as periodic structures. Yin and Hopkins [12] described the combination of Bloch theory and wave theory, while Pany [13] presented the combination of FEM with Floquet’s theory. The asymmetrical stiffeners found in shipbuilding were not taken into account in any of these cases. The methods mentioned, ingenious as they are in some theoretical respects, remain insufficient for grasping the complexity of typical ship structures, featuring asymmetries, stiffeners and discontinuities.

Using these methods can be helpful but they are insufficient for ship construction, specifically.

The original contributions of the present research are:

- A library of SEA parameters is created for the structural joints of a jack-up vessel; by using this library, one can create many SEA models of vibroacoustic paths on various ships.
- The well-described PIM method is modified to easily reject negative CLFs with a minimal impact on the final result. The coefficients are averaged, both in the frequency domain and for various boundary conditions.

- A method of setting boundary conditions is proposed to take into account the influence of the adjacent structure and internal discontinuities.

NUMERICAL EXPERIMENTS

THE SELECTION OF STRUCTURAL CONNECTIONS

The structural connections shown in this article are parts of an existing jack-up vessel. They were selected based on the possibility of carrying out an SEA analysis for this unit. Using these specific cases, real vibroacoustic transmission paths can be modelled for many ships. Structural elements were ‘cut out’ from a global FEM model created for strength analyses. The global model is shown in Fig. 2. The mesh of finite elements was refined to meet the condition $\lambda > 7l$ for the selected submodels, where λ is the wavelength and l is the element length. This condition was introduced to make sure that the flexural wave was mapped correctly.

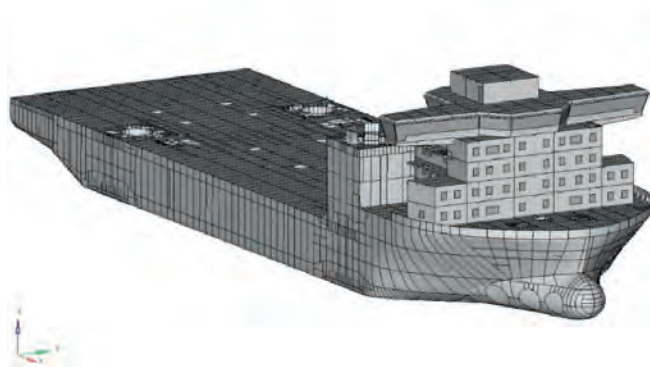


Fig. 2. Global FEM model of jack-up vessel

The numbering convention shown in Fig. 3 was adopted during the calculation and presentation of results. The figure shows an X-type junction; in the case of a T-type junction, the system only consists of subsystems 1, 2 and 3.

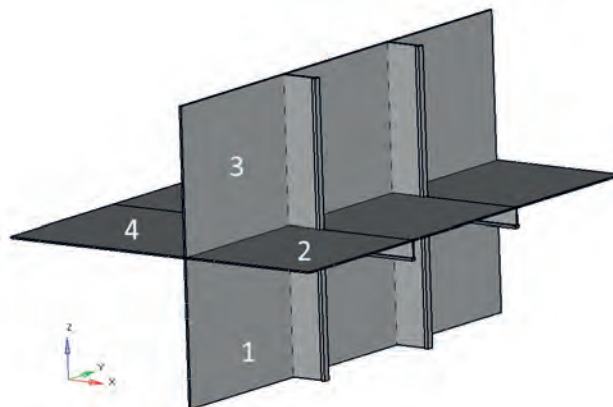


Fig. 3. The numbering convention of subsystems

A typical stiffener spacing of 685 mm was defined in each subsystem. All of the tested systems were made of mild steel and the following material properties were assumed globally: density $\rho = 7850 \text{ kg/m}^3$, Poisson's ratio $\nu = 0.3$, Young's modulus $E = 205 \text{ GPa}$, and internal damping $\eta = 0.04$. It was assumed that the value of internal damping is constant and independent from frequency. The assumed value is in the range of values where the DLF had practically no effect on the CLFs of the tested systems. Individual systems are characterised by the following values: connection length (L_y), length of the first (L_z), second (L_x), third (L_z') and fourth (L_x') subsystem, as well as the thickness of the plating of individual subsystems and types of stiffeners. A description of each tested system is provided in Appendix A.

THE FINITE ELEMENTS

A vibroacoustic computation using FEM was carried out with Ansys software. SHELL181 elements were used to model plates and BEAM188 elements were used to model stiffeners. SHELL181 is a four-node element with six degrees of freedom at each node. A BEAM188 element is suitable for analysing slender to moderately stubby/thick beam structures, based on Timoshenko beam theory, which includes shear-deformation effects. Combin14 elements were used as springs on the edges of the submodels.

INPUT POWER AND SUBSYSTEM ENERGY

The outputs obtained from the numerical simulations are the energy and the input power. Energy associated with the out-of-plane vibrations were computed as:

$$E_i = \frac{M \langle |v_n|^2 \rangle}{2} \quad (7)$$

where M is the mass of the subsystem, v_n is the vector of normal velocity, and $\langle \rangle$ represents the spatial average. The power injected by a single point force is obtained as:

$$P_{in} = \frac{1}{2} \text{Re}\{Fv\} \quad (8)$$

where F is the vector of the point force and v is the vector of the velocity at the application spot in the force direction.

LOADS AND BOUNDARY CONDITIONS

Forces were applied to 100 random nodes, at random phases (but at a constant amplitude), to implement a 'rain on the roof' type of load. A new set of random loads was generated for each harmonic solution.

Six springs were attached to each edge node and each of them acted on only one degree of freedom. This made it

possible to control individual degrees of freedom. The spring stiffness was calibrated as follows:

- The examined intersection was 'cut out' from the global FEM model, along with the adjacent part of the structure, so that the submodel ended with a primary stiffening member.
- A concentrated force was applied to the joint and the result of the static analysis was obtained in the form of displacements.
- The attached structure was removed from the submodel, springs were created and their stiffnesses were iteratively selected to obtain the same displacements.

For each run of harmonic analysis, 1, 2 or 3 nodes were randomly selected and some of their degrees of freedom were fixed (i.e. locked from translation or translation and rotation). In the rest of this article, such restraints will be called single point constraints (SPC).

THE COMPUTATIONAL WORKFLOW

The entire procedure was programmed in Ansys Parametric Design Language (APDL) and the procedure was as follows:

- Each octave (or third) was represented by seven discrete frequencies.
- N harmonic analyses were performed for each frequency, where N is the number of subsystems.
- For each harmonic analysis, the 'rain on the roof' load on the subsequent subsystem was applied and specific boundary conditions were generated. After each harmonic analysis, the matrices from Eq. (6) were filled in.
- After calculating the CLFs for each frequency, averaging was performed for the entire band. Negative CLFs were not taken into account.
- After calculating the CLFs for all octaves, the boundary condition settings were changed and the next iteration took place. The final result was an average of seven iterations.

VALIDATION METHOD

The method was validated in two ways: by comparing the CLFs with measurements performed by Treszkai et al. [7] and by comparing energy level differences with measurements made by Yin and Hopkins [12]. In the first case, two steel plates without stiffeners (junction #1) were tested while, in the second case, two periodically ribbed Perspex plates (junction #2) were tested. The scheme of the stiffened plates is shown in Fig. 4. The material properties used in both cases are given in Table 1 and the geometrical details are presented in Table 2.

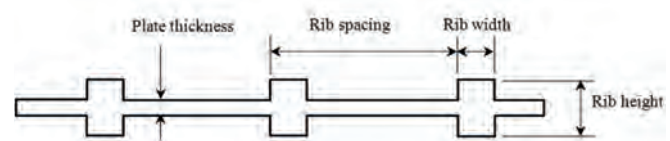


Fig. 4. Periodic ribbed plates scheme. These types of stiffeners were only used for the purposes of comparison with work [12].

Tab. 1. Material properties of the L-junction plates

Junction	Plate	Material	Young's modulus [Pa]	Density [kg/m ³]	Poisson's ratio [-]	Internal loss factor [-]
#1	1	Steel	2.05E+11	7850	0.3	0.04
	2	Steel	2.05E+11	7850	0.3	0.04
#2	1	Perspex	4.63E+09	1220	0.3	0.06
	2	Perspex	4.63E+09	1220	0.3	0.06

Tab. 2. Geometrical description of plates

Junction	Plate	Rib orientation to junction line	Plate dimensions [mm]	Rib spacing [mm]	Rib width [mm]	Rib height [mm]
#1	1	N/A	2	N/A	N/A	N/A
	2	N/A	2	N/A	N/A	N/A
#2	1	Perpendicular	10	200	10	60
	2	Parallel	10	100	10	60

RESULTS AND DISCUSSION

VALIDATION

Fig. 5 shows the minimum and maximum values of the CLFs (measured experimentally), FEM/SEA results with a 95% confidence interval and analytically calculated values, based on wave theory for junction #1. The 95% confidence intervals were calculated using the Student's 't' distribution.

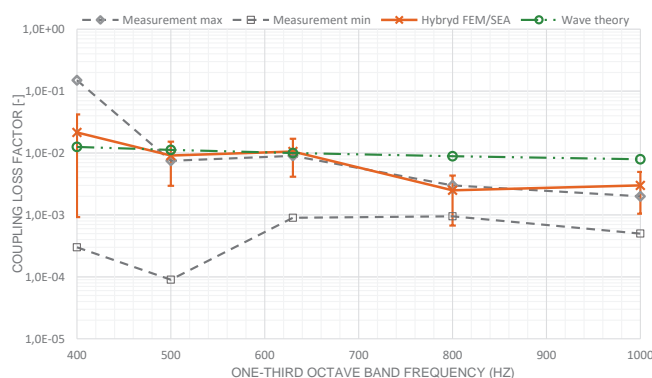


Fig. 5. Junction #1, comparison between hybrid FEM/SEA results, measurements and wave theory prediction.

The graph in Fig. 5 shows a good consistency between hybrid FEM/SEA measurements. As expected, the FEM/SEA values are closer to the maximum measurement results. This could be caused by the fact that the FEM model does not take into account weld imperfections.

The energy level difference (in dB) obtained for junction #2, by hybrid FEM/SEA and the measurements in one-third octave bands, are compared in Fig. 6. Both results are plotted with 95% confidence intervals.

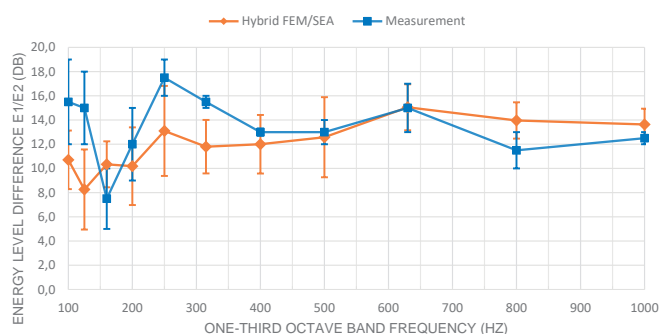


Fig. 6. Junction #2, comparison between hybrid FEM/SEA results and the measurements.

In general, the results can be considered to be acceptably consistent. As expected, larger differences in average values occur in lower frequencies but, in thirds above 300 Hz, the results do not differ by more than 2 dB. Discrepancies for some bands may result from several factors. Firstly, the sampling during the measurements was 1 Hz, while the FEM/SEA result is averaged over seven frequencies for one-third octave. The method of excitation was also different; the rain on the roof used in FEM simulations is unattainable in the conditions of a real experiment, and so point excitations were used. During the experiment, the boundary conditions did not change. Meanwhile, during the FEM simulation, the stiffness of the model edge restraint changed randomly and random SPCs appeared. This indicates that the ensemble average represents deterministic systems well.

THE INFLUENCE OF THE BOUNDARY CONDITIONS

SEA is used to predict vibration and noise levels at the design stage. One should bear in mind that a shipyard-constructed structure may exhibit variations, compared to the documentation. Sometimes, very small changes can cause a large impact on the subsystems' vibration response, as shown in Figs. 7-8. Fig. 7 shows how the response of the system changes after introducing one more restraint point in a random place on each subsystem. At the statistical energy analysis stage, the stiffness of the connected structure may change and pillars/cutouts may appear. The best solution is to average the random spring stiffness and random SPCs. If any of these unknowns are eliminated, this part of the randomness can be removed from the procedure. In the cases described in this paper, the stiffness of the springs at the edges of the models was randomly selected in the range 70-130% of the mean value.

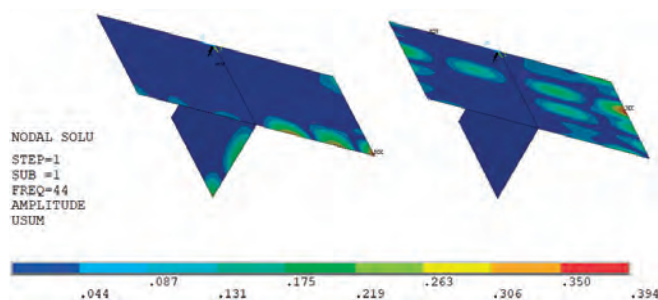


Fig. 7. Displacement graph [mm], result of a steady state harmonic analysis in an exemplary frequency of 44 Hz, at which the influence of irregularity is clearly visible. On the left, there is one single point constraint in a random place for each subsystem. On the right, there are two single point constraints in a random place for each subsystem.

The scatter of CLF values, for one system with seven random boundary conditions, is shown in Fig. 8.

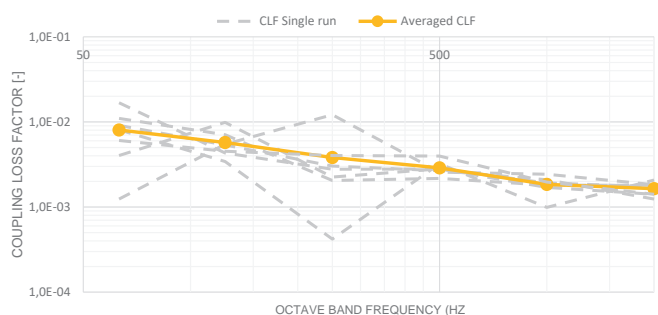


Fig. 8. The coupling loss factors for seven boundary conditions and the averaged value

Fig. 8 shows that a small change in the system can change the CLF value by two orders of magnitude. The dispersion of the results significantly decreases above the 250 Hz octave.

CONCLUSIONS

This paper presents a hybrid FEM/SEA method for estimating the CLF for complex structural joints found on ships. The results obtained with this method were compared to experimental results from two different papers. Acceptably good agreement with the measurement results was achieved. The presented method differs from previous solutions in the following ways:

- The coefficients are averaged in the frequency domain and for various boundary conditions. This allows us to easily reject negative CLFs with minimal impact on the final result.
- By using springs at the edges of the model, the influence of the adjacent structure can be taken into account. Random deviations in spring stiffness allow the result to be obtained more for the ensemble average than for the deterministic case.
- Potential structural discontinuities or additional wave-scattering elements (such as pillars) are introduced into

the system as point restraints in random places in the subsystem.

- If the uncertainty associated with any of the above types of boundary conditions disappears, it can be removed from the analysis, making it more deterministic.

Using a hybrid FEM/SEA method, a library of CLFs was created for the structural joints of a jack-up vessel (Appendix A). With the help of this library, one can create many SEA models of vibroacoustic paths on various ships. The presented method is universal and the library can be freely expanded.

ACKNOWLEDGMENTS

This work was performed as a part of the Industrial Doctorate Programme financed by the Polish Ministry of Science and Higher Education. The authors wish to acknowledge the Fem4cad staff in regard to their support for this research.

REFERENCES

1. DNV, "Class documents - Rules for classification, class programmes, class guidelines, offshore standards and statutory interpretations", 2023. <https://www.dnv.com/rules-standards/index.html>
2. L. Cremer, M. Heckl, and E.E Ungar, "Structure-Borne Sound", Springer-Verlag, New York. 1973.
3. A. Le Bot and V. Cotoni, "Validity diagrams of statistical energy analysis", Journal of sound and vibration, vol. 329, pp. 221-235, 2010, doi:10.1016/j.jsv.2009.09.008.
4. R.H. Lyon "Statistical Energy Analysis of Dynamical Systems: Theory and Applications", M.I.T. Press. 1975.
5. D.A. Bies and S. Hamid, "In situ determination of loss and coupling factors by the Power Injection Method", Journal of the Acoustical Society of America, vol.66, 1980, doi: 10.1121/1.2017651.
6. [6] R., Panuszka, J. Wiciak, and M. Iwaniec, "Experimental assessment of coupling loss factors of thin rectangular plates", Archives of acoustics, vol. 30, pp. 533-551, 2005.
7. M.F. Treszkai, A. Peiffer, and D. Feszty, "Power Injection Method-based evaluation of the effect of binding technique on the Coupling Loss Factors and Damping Loss Factors in Statistical Energy Analysis simulations", Manufacturing Technology, vol. 21, pp. 544-558, 2021, doi: 10.21062/mft.2021.065.
8. A.C. Pankaj, S. Sastry, and S.M. Murigendrappa, "A comparison of different methods for determination of

- coupling factor and velocity response of coupled plates”, *Journal of Vibroengineering*, vol. 15, pp. 1885-1897, 2013.
9. A.N Thite and B.R. Mace, “Robust estimation of coupling loss factors from finite element analysis”, *Journal of sound and vibration*, vol. 303, pp. 814-831, 2007, doi.org/10.1016/j.jsv.2007.02.004
 10. J. Poblet-Puig, “Estimation of the coupling loss factors of structural junctions with in-plane waves by means of the inverse statistical energy analysis problem”, *Journal of Sound and Vibration*, vol. 493, pp. 115850, 2021, doi.org/10.1016/j.jsv.2020.115850.
 11. P.J. Shorter and R.S. Langley, “Vibro-acoustic analysis of complex systems”, *Journal of Sound and Vibration*, vol. 288, pp. 669-699, 2005, doi.org/10.1016/j.jsv.2005.07.010.
 12. J. Yin and C. Hopkins, “Treating periodic ribbed plates with symmetric ribs as individual subsystems in Statistical Energy Analysis: Models for bending wave transmission across L-junctions in the low- and mid-frequency ranges”, *Journal of Sound and Vibration*, vol. 344, pp.221-241, 2015, http://dx.doi.org/10.1016/j.jsv.2015.01.031.
 13. C. Pany, “An Insight on the Estimation of Wave Propagation Constants in an Orthogonal Grid of a Simple Line-Supported Periodic Plate Using a Finite Element Mathematical Model”, *Frontiers in Mechanical Engineering*, vol. 8, p. 926559, 2022, doi.org/10.3389/fmech.2022.926559.

APPENDIX A

Tab. 3 Description of subsystems included in the submodels

ID	Length [mm]					Thickness [mm]				Stiffener type			
	Lx	Ly	Lz	Lx'	Lz'	P1	P2	P3	P4	P1	P2	P3	P4
1	2740	1500	-	-	-	10	10	-	-	FB10x100	HP120x6	-	-
2	2740	1500	-	-	-	20	10	-	-	FB10x100	HP200x9	-	-
3	1500	3500	1950	-	1950	8	10	8	-	HP120x7	FB10x100	HP120x7	-
4	1500	3500	1950	-	1950	20	10	20	-	HP200x9	FB10x100	HP200x9	-
5	1500	2640	1950	-	1950	20	12	20	-	HP200x9	FB10x100	HP200x9	-
6	1500	2640	1950	-	1950	8	12	8	-	HP120x7	FB10x100	HP120x7	-
7	1500	3500	1950	-	1950	9	10	9	-	HP120x6	FB10x100	HP120x6	-
8	1950	2055	3700	-	3100	7	7	7	-	HP120x7	HP100x8	HP120x7	-
9	1950	2055	1500	1950	2400	8	6	8	6	HP160x7	HP80x6	HP160x7	HP80x6
10	1500	3425	1950	2040	1950	8	10	8	8	HP120x7	FB10x100	HP120x7	HP160x7
11	1500	3425	1950	2040	1950	18	18	12	24	HP120x7	FB10x100	HP120x7	HP120x7
12	1500	3425	1950	2040	1950	8	10	8	8	HP120x6	FB10x100	HP120x7	HP160x7
13	1500	3425	1950	2040	1950	8	12	8	8	HP120x6	FB10x100	HP120x7	HP160x7

Table 4 CLF values for selected junctions


ID	Octave	Coupling loss factor [-]											
		1_2	2_1	1_3	2_3	3_2	3_1	1_4	2_4	3_4	4_1	4_2	4_3
1	63	1.2E-01	1.7E-01	-	-	-	-	-	-	-	-	-	-
	125	1.6E-02	1.2E-02	-	-	-	-	-	-	-	-	-	-
	250	1.4E-02	1.2E-02	-	-	-	-	-	-	-	-	-	-
	500	8.1E-03	7.1E-03	-	-	-	-	-	-	-	-	-	-
	1000	7.4E-03	5.8E-03	-	-	-	-	-	-	-	-	-	-
	2000	5.2E-03	4.0E-03	-	-	-	-	-	-	-	-	-	-
2	63	9.5E-03	1.2E-02	-	-	-	-	-	-	-	-	-	-
	125	4.7E-03	6.1E-03	-	-	-	-	-	-	-	-	-	-
	250	3.5E-03	5.7E-03	-	-	-	-	-	-	-	-	-	-
	500	3.6E-03	5.7E-03	-	-	-	-	-	-	-	-	-	-
	1000	3.4E-03	4.7E-03	-	-	-	-	-	-	-	-	-	-
	2000	2.2E-03	3.1E-03	-	-	-	-	-	-	-	-	-	-
3	63	4.1E-03	5.4E-03	2.0E-02	8.0E-03	6.7E-03	1.9E-02	-	-	-	-	-	-
	125	2.5E-03	4.4E-03	3.3E-02	7.7E-03	5.3E-03	3.3E-02	-	-	-	-	-	-
	250	3.2E-03	6.5E-03	6.4E-03	6.5E-03	3.4E-03	6.3E-03	-	-	-	-	-	-
	500	2.8E-03	4.4E-03	4.2E-03	4.4E-03	2.5E-03	4.3E-03	-	-	-	-	-	-
	1000	2.3E-03	4.0E-03	2.2E-03	4.0E-03	2.4E-03	2.2E-03	-	-	-	-	-	-
	2000	1.7E-03	2.8E-03	1.1E-03	2.7E-03	1.8E-03	1.1E-03	-	-	-	-	-	-
4	63	2.6E-03	1.3E-03	7.2E-02	2.4E-03	2.9E-03	5.7E-02	-	-	-	-	-	-
	125	1.3E-03	6.8E-04	6.3E-02	8.0E-04	3.3E-03	6.3E-02	-	-	-	-	-	-
	250	2.1E-03	9.9E-04	3.4E-02	7.4E-04	1.6E-03	3.8E-02	-	-	-	-	-	-
	500	1.7E-03	1.0E-03	1.0E-02	8.5E-04	1.4E-03	1.1E-02	-	-	-	-	-	-
	1000	2.0E-03	1.1E-03	8.5E-03	9.4E-04	1.8E-03	9.2E-03	-	-	-	-	-	-
	2000	1.5E-03	8.4E-04	4.6E-03	7.8E-04	1.5E-03	4.5E-03	-	-	-	-	-	-
5	63	4.8E-02	3.4E-02	4.9E-01	7.2E-03	1.5E-02	3.5E-01	-	-	-	-	-	-
	125	8.1E-03	3.1E-03	7.9E-02	5.9E-03	1.4E-02	1.1E-01	-	-	-	-	-	-
	250	5.7E-03	2.3E-03	3.1E-02	1.9E-03	1.8E-03	2.9E-02	-	-	-	-	-	-
	500	2.0E-03	1.7E-03	1.1E-02	1.6E-03	1.7E-03	1.1E-02	-	-	-	-	-	-
	1000	2.5E-03	1.9E-03	7.0E-03	2.0E-03	2.7E-03	8.2E-03	-	-	-	-	-	-
	2000	2.0E-03	1.3E-03	4.3E-03	1.2E-03	1.8E-03	4.2E-03	-	-	-	-	-	-
6	63	8.5E-03	1.0E-02	1.3E-02	1.7E-02	7.0E-03	1.4E-02	-	-	-	-	-	-
	125	5.9E-03	7.4E-03	7.5E-03	7.9E-03	4.7E-03	1.0E-02	-	-	-	-	-	-
	250	2.4E-03	7.0E-03	4.2E-03	6.4E-03	2.6E-03	3.4E-03	-	-	-	-	-	-
	500	2.6E-03	6.2E-03	3.0E-03	6.5E-03	2.9E-03	3.1E-03	-	-	-	-	-	-
	1000	2.0E-03	4.0E-03	1.6E-03	3.9E-03	2.0E-03	1.7E-03	-	-	-	-	-	-
	2000	1.6E-03	3.0E-03	7.6E-04	3.0E-03	1.7E-03	7.5E-04	-	-	-	-	-	-
7	63	4.6E-03	9.9E-03	2.0E-02	3.3E-03	4.1E-03	1.6E-02	-	-	-	-	-	-
	125	3.6E-03	5.5E-03	1.3E-02	6.4E-03	4.5E-03	1.4E-02	-	-	-	-	-	-
	250	4.3E-03	4.5E-03	6.7E-03	4.3E-03	2.8E-03	7.5E-03	-	-	-	-	-	-
	500	2.7E-03	4.5E-03	5.3E-03	4.5E-03	2.9E-03	5.6E-03	-	-	-	-	-	-
	1000	2.8E-03	4.0E-03	2.7E-03	3.9E-03	2.5E-03	2.5E-03	-	-	-	-	-	-
	2000	1.9E-03	2.7E-03	1.4E-03	2.6E-03	2.0E-03	1.5E-03	-	-	-	-	-	-

ID	Octave	Coupling loss factor [-]											
		1_2	2_1	1_3	2_3	3_2	3_1	1_4	2_4	3_4	4_1	4_2	4_3
8	63	2.6E-03	5.4E-03	7.0E-03	7.7E-03	4.9E-03	1.0E-02	-	-	-	-	-	-
	125	2.3E-03	4.6E-03	3.6E-03	5.1E-03	2.7E-03	4.4E-03	-	-	-	-	-	-
	250	1.9E-03	4.3E-03	2.3E-03	3.2E-03	2.3E-03	4.1E-03	-	-	-	-	-	-
	500	2.1E-03	3.2E-03	1.7E-03	2.9E-03	2.2E-03	2.0E-03	-	-	-	-	-	-
	1000	1.2E-03	2.2E-03	1.0E-03	2.5E-03	1.7E-03	1.2E-03	-	-	-	-	-	-
	2000	7.4E-04	1.3E-03	6.0E-04	1.4E-03	9.2E-04	6.8E-04	-	-	-	-	-	-
9	63	5.0E-03	3.8E-03	3.5E-02	1.3E-03	2.5E-03	2.5E-02	6.7E-03	4.7E-03	1.1E-03	8.6E-04	4.0E-03	2.5E-03
	125	2.0E-03	1.5E-03	1.2E-02	1.3E-03	2.0E-03	6.0E-03	3.2E-03	2.1E-03	1.4E-03	1.6E-03	1.2E-03	1.6E-03
	250	1.9E-03	1.3E-03	7.0E-03	1.3E-03	1.1E-03	4.6E-03	2.2E-03	1.5E-03	1.1E-03	1.1E-03	1.4E-03	1.7E-03
	500	2.4E-03	1.4E-03	4.6E-03	1.3E-03	1.2E-03	2.5E-03	2.5E-03	1.2E-03	1.0E-03	9.2E-04	1.3E-03	1.3E-03
	1000	1.7E-03	9.9E-04	3.3E-03	1.1E-03	1.1E-03	2.2E-03	1.7E-03	9.6E-04	5.6E-04	4.9E-04	1.2E-03	1.0E-03
	2000	1.1E-03	6.1E-04	1.9E-03	6.2E-04	6.2E-04	1.0E-03	1.1E-03	5.6E-04	3.1E-04	2.9E-04	6.6E-04	5.9E-04
10	63	2.5E-03	3.4E-03	9.5E-03	3.9E-03	2.5E-03	8.9E-03	3.5E-03	4.5E-03	6.3E-03	4.2E-03	3.3E-03	4.4E-03
	125	1.5E-03	3.6E-03	8.2E-03	2.9E-03	1.8E-03	8.7E-03	1.9E-03	2.6E-03	4.7E-03	2.8E-03	4.0E-03	4.2E-03
	250	1.9E-03	3.1E-03	2.5E-03	3.3E-03	2.4E-03	2.8E-03	1.3E-03	1.7E-03	6.6E-03	3.4E-03	1.6E-03	2.2E-03
	500	1.5E-03	2.3E-03	1.8E-03	2.4E-03	1.5E-03	2.1E-03	1.0E-03	1.2E-03	3.0E-03	2.4E-03	2.0E-03	2.3E-03
	1000	1.7E-03	2.6E-03	1.3E-03	2.5E-03	1.4E-03	1.1E-03	8.6E-04	1.0E-03	2.0E-03	1.5E-03	1.3E-03	1.7E-03
	2000	1.0E-03	1.8E-03	6.0E-04	1.6E-03	1.0E-03	6.5E-04	5.9E-04	6.6E-04	1.4E-03	9.5E-04	6.9E-04	7.7E-04
11	63	3.1E-03	4.0E-03	2.0E-02	1.5E-03	7.0E-04	1.9E-02	4.8E-02	4.4E-02	8.8E-03	4.7E-03	1.6E-02	7.4E-03
	125	1.7E-03	8.5E-03	9.1E-03	3.0E-03	9.0E-04	6.2E-03	6.1E-02	5.9E-02	4.0E-03	7.6E-03	3.5E-02	4.1E-02
	250	2.4E-03	3.6E-03	2.4E-03	1.6E-03	1.0E-03	2.2E-03	4.0E-03	5.4E-03	3.5E-03	6.0E-03	1.9E-03	4.6E-03
	500	1.5E-03	2.4E-03	8.8E-04	1.0E-03	6.3E-04	5.9E-04	2.4E-03	3.8E-03	3.5E-03	3.4E-03	1.0E-03	2.3E-03
	1000	1.3E-03	1.6E-03	6.4E-04	1.0E-03	4.6E-04	3.4E-04	3.0E-03	3.3E-03	3.0E-03	2.4E-03	9.7E-04	2.0E-03
	2000	1.5E-03	2.1E-03	1.1E-03	1.0E-03	3.9E-04	5.8E-04	2.7E-03	3.3E-03	2.1E-03	1.9E-03	8.2E-04	1.5E-03
12	63	4.0E-03	8.4E-03	8.7E-03	2.0E-02	1.4E-02	5.8E-03	2.7E-03	1.4E-03	7.3E-03	3.2E-03	4.3E-03	8.0E-03
	125	3.2E-03	4.4E-03	4.5E-03	4.3E-03	1.9E-03	4.8E-03	1.3E-03	1.6E-03	5.2E-03	3.3E-03	2.7E-03	2.8E-03
	250	3.0E-03	5.2E-03	1.0E-03	3.9E-03	1.9E-03	7.4E-04	1.9E-03	2.2E-03	4.9E-03	2.2E-03	1.4E-03	2.0E-03
	500	1.8E-03	2.9E-03	8.5E-04	4.4E-03	2.1E-03	7.7E-04	1.4E-03	1.4E-03	2.5E-03	1.3E-03	1.5E-03	1.8E-03
	1000	2.0E-03	3.4E-03	1.1E-03	2.5E-03	1.1E-03	7.9E-04	7.6E-04	7.8E-04	2.2E-03	1.4E-03	1.1E-03	1.4E-03
	2000	1.7E-03	2.8E-03	7.0E-04	2.0E-03	9.9E-04	5.8E-04	5.7E-04	5.5E-04	1.7E-03	8.5E-04	4.7E-04	5.2E-04
13	63	4.0E-03	8.4E-03	8.7E-03	2.0E-02	1.4E-02	5.8E-03	2.7E-03	1.4E-03	7.3E-03	3.2E-03	4.3E-03	8.0E-03
	125	3.2E-03	4.4E-03	4.5E-03	4.3E-03	1.9E-03	4.8E-03	1.3E-03	1.6E-03	5.2E-03	3.3E-03	2.7E-03	2.8E-03
	250	3.0E-03	5.2E-03	1.0E-03	3.9E-03	1.9E-03	7.4E-04	1.9E-03	2.2E-03	4.9E-03	2.2E-03	1.4E-03	2.0E-03
	500	1.8E-03	2.9E-03	8.5E-04	4.4E-03	2.1E-03	7.7E-04	1.4E-03	1.4E-03	2.5E-03	1.3E-03	1.5E-03	1.8E-03
	1000	2.0E-03	3.4E-03	1.1E-03	2.5E-03	1.1E-03	7.9E-04	7.6E-04	7.8E-04	2.2E-03	1.4E-03	1.1E-03	1.4E-03
	2000	1.7E-03	2.8E-03	7.0E-04	2.0E-03	9.9E-04	5.8E-04	5.7E-04	5.5E-04	1.7E-03	8.5E-04	4.7E-04	5.2E-04

RE-IDENTIFYING NAVAL VESSELS USING NOVEL CONVOLUTIONAL DYNAMICAL ALIGNMENT NETWORKS ALGORITHM

Sudipta Roy

Gangarampur College, Dakshin Dinajpur, India

Dipak Kumar Jana 

Department of Computer Science and Engineering (Cyber Security), Haldia Institute of Technology, Haldia, India

Nguyen Long*

Faculty of Navigation, Vietnam Maritime University, Hai Phong, Viet Nam

* Corresponding author: nguyenxuanlong@vimaru.edu.vn (Nguyen Long)

ABSTRACT

Technological innovation for re-identifying maritime vessels plays a crucial role in both smart shipping technologies and the pictorial observation tasks necessary for marine reconnaissance. Vessels are vulnerable to varying gradations of engaging in the marine environment, which is complicated and dynamic compared to the conditions on land. Fewer picture samples along with considerable similarity are characteristics of warships as a class of ship, making it more challenging to recover the identities of warships at sea. Consequently, a convolutional dynamic alignment network (CoDA-Net) re-identification framework is proposed in this research. To help the network understand the warships within the desired domain and increase its ability to identify warships, a variety of ships are employed as origin information. Simulating and testing the winning of war vessels at sea helps to increase the network's ability to recognize complexity so that users can better handle the effects of challenging maritime environments. The impact of various types of ships as transfer items is also highlighted. The research results demonstrate that the enhanced algorithm increases the overall first hit rate (Rank1) by approximately 5.9%; it also increases the mean average accuracy (mAP) by approximately 10.7% and the correlation coefficient by 0.997%.

Keywords: Warship re-identification; Transfer learning; Domain adaptability; CoDA-Net; Convolutional Sea environment

INTRODUCTION

The precise recognition of targets on the sea surface is a crucial requirement to safeguard maritimesecurity, preserve marine ecosystems, and efficiently harness marine resources [1]. To make possible a linear breakdown of the output into distinct input contributions, convolutional dynamic alignment networks (CoDA-Nets) describe the classification prediction through a sequence of input-dependent linear adjustments. The generated contribution maps align with discriminative input patterns given the alignment of the dynamic alignment units (DAUs). These model-inherent breakdowns have excellent visual quality and perform better in terms of quantitative measures than the current attribution

techniques. Additionally, CoDA-Nets are effective classifiers that provide outcomes comparable to those of the ResNet and VGG algorithms. This article introduces CoDA-Nets, a novel category of neural network models that excel at classification, with a notable inherent capacity for interpretability. These models are constructed based on DAUs [2], which dramatically transform the input using weighted vectors that spontaneously coordinate alongside task-relevant features.

The accurate identification of ocean surface points is a crucial factor for ensuring naval security, safeguarding the maritime environment, and efficiently utilising marine resources. The current marine environment involves increasing challenges in marine traffic, coupled with growing concerns related to piracy, terrorist activities, the illicit drug

trade, and other unlawful practices. Therefore, enhancing the precise identification of ocean surface destinations has become imperative. The precise identification of sea surface targets has the potential to enhance maritime navigation capabilities, foster international cooperation, preserve marine ecosystems, and contribute to economic development while ensuring maritime safety [3].

The distinctive characteristics of the maritime environment and the inflexibility of ships contribute to notable variations in ship appearance due to changes in viewpoint and scale, posing a challenge to intelligence, surveillance, and reconnaissance (ISR). Additionally, the scarcity of publicly available datasets specific to ISR exacerbates the recognition difficulty. While substantial efforts have focused on coarse or fine-grained classification, there is a limited amount of research dedicated to ISR [4]. The COLREG [5] at Sea stipulates that all passenger vessels, as well as cargo vessels that displace over 300 tons, must be fitted with an automated navigation system (AIS).

This paper aims to investigate the extent to which the performance of methods for vessel detection can be enhanced by utilising a pre-trained deep learning model specifically trained on marine data [6]. However, because of the greater interpretation of the marine environment and farther-away vessel goals, the capacity of the vessel fluctuates significantly under various positions, making radar recognition more challenging [7]. The identification of the maritime environment surrounding ships may now be greatly aided by visible light cameras because of the quick advancement of computer vision equipment.

The primary objective in maritime transportation surveillance and autonomous ship navigation is to establish an effective visual perception system that has both high efficiency and accuracy in detecting marine objects. Consequently, there is a necessity to compile advanced deep-learning algorithms and top-notch datasets specific to maritime scenarios [8]. Additionally, visible cameras can give deeper target data, including the target shape, measurements, and other features, in comparison to AIS and radar mechanisms, which can only deliver rudimentary data, such as the target position and speediness. Visual cameras can aid in more precise target identification and classification, enhancing the recognition precision [9].

Moreover, recent studies on ship re-identification utilise ships that are either anchored in ports or floating effortlessly as identifiable entities [10], [11], [12]. In contrast to solid shooting conditions on land, the ocean's surface, where the vessel is situated, moves a great deal; therefore, the point of focus is frequently tilted. The speed and sea state will determine the degree of tilting for a typical moving vessel. Due to the weight, both the draft and the form of the portion of the sea surface that is visible will be altered.

The identification of ships is crucial for effective maritime surveillance, port administration, and secure navigation. Nevertheless, the advancement of ship detection methods significantly lags behind other detection techniques like face detection, pedestrian detection, traffic sign/light detection, text

detection, etc. [13]. First, VesselReid and VesselReid-539 [9] are two datasets used to re-identify known ships, but they are not open source. Based on the publicly available resource collection approach, we produced and annotated a dataset of ships that included six more kinds of non-military containers in addition to war vessels. We replicated the vessels' routes that were visible on the surface of the water by spinning them at a small inclination. The targeted area instructional set, as well as the test collection, were selected to have an elevated resemblance to images of battleships in various situations, whereas the other forms of private citizen containers were utilised as the foundation field training set.

A novel dataset for boat re-identification is introduced; it consists of annotated images captured during the previous summer within the marine protected area of Porto Cesareo. The baseline results are established by applying a discriminative learning convolutional neural network (CNN) for boat re-identification [14].

This paper makes the following contributions:

VesselReid [10] and VesselReid-539 [12] are two datasets used to re-identify known ships, but they are not open source. Based on the publicly available resource collection approach, we produced and annotated a dataset of ships that included six more kinds of non-military vessels in addition to warships. By rotating them at a small angle, we mimicked the vessel routes that appeared on the water's surface. The supplementary types of noncombatant boats are employed as the foundation field training set, while the goal field training set and assessment set are selected to have a high likeness to battleship photos in various circumstances.

Next, we provide a transfer learning-based CoDA-Net re-identification technique. By transfer-ring the relevant aspects of the photos, this technique can train the system with a small number of training pictures of war vessels while employing different classes of boats. As a result, the network can recognise battleships more accurately and does not need to label the photos from the training set's local information again.

Ultimately, the research analysis segment examines the impact of vessels as transference data re-garding the accuracy of net re-identification while taking into consideration a variety of categories, and sampling sizes, as well as the decision to use the marine sway modelling technique.

ASSOCIATED WORKS

RE-IDENTIFICATION OF INDIVIDUALS AND AUTOMOBILES

The issue of recovering the identity of a person, which primarily focuses on the enhancement of the network topology to boost the metric learning impact, is the most researched application of identity recovery methods. A regional dynamics aligning technique was presented

by [15] to address the issue of misaligned human pose models, avoiding the need for extra supervision and including global characteristics for training. By assessing the worldwide mean assembling layer and utilizing a consideration method to enhance the attention of altitudinal relationships in elemental graphs, enhanced the network structure. To address the biased estimation issue, [17] enhanced the extrapolation impact for the measurement framework and suggested a semi-supervised continuous projection metric modelling approach.

In addition to human re-identification, the area of vehicle re-identification has also received much study, and tweaks to the algorithm's network structure continue to be its primary means of performance enhancement. The influence of the vehicle direction was limited, while the identification accuracy and speed were increased, thanks to the addition of ring concentration slabs to the feature pyramid edifice by [18]. The loss function was calculated by [19] using the group loss, which improved the network's learning of the association between the global and local properties of the vehicle and the detailed recognition of related samples.

STATE-OF-THE-ART VESSEL/BOAT RE-IDENTIFICATION

The current state-of-the-art vessel/boat re-identification method involves the utilisation of CoDA-Net, a cutting-edge method in computer vision. This advanced approach leverages the strengths of co-occurrence and distribution alignment to achieve the robust and accurate re-identification of vessels or boats. CoDA-Net has demonstrated significant advancements in handling the complexities of maritime scenarios, providing enhanced capabilities in recognising and tracking vessels across various conditions. Its effectiveness lies in its ability to align co-occurrence patterns and distributions, resulting in improved accuracy and reliability in the re-identification process for vessels and boats.

The current state-of-the-art methods in vessel/boat re-identification involve advanced techniques and technologies aimed at accurately identifying and tracking maritime vessels. This field has witnessed significant advancements in recent years, driven by the growing need for robust maritime surveillance and security. The following are some key aspects of the state of the art in vessel/boat re-identification:

Deep Learning Techniques: State-of-the-art methods often leverage deep learning architectures, such as CNNs and siamese networks, for feature extraction and similarity measurement. These models can effectively learn discriminative features from maritime imagery.

Appearance and Motion Features: Vessel re-identification systems consider both appearance features (colors, shapes, and textures) and motion features (trajectory, speed, and direction) to enhance identification accuracy. This comprehensive approach improves the robustness of re-identification systems across different environmental conditions.

Object Detection and Tracking: Advanced object detection and tracking algorithms play a crucial role in accurately locating and following vessels in dynamic maritime

environments. These techniques help maintain consistent tracks and improve the reliability of re-identification.

Data Fusion and Multi-Modal Analysis: State-of-the-art methods often integrate data from multiple sources, such as radar, AIS data, and optical imagery. This fusion of information allows for a more comprehensive understanding of the maritime scenario, enhancing the accuracy of re-identification.

Benchmark Datasets: The availability of benchmark datasets specifically designed for vessel re-identification has contributed to the advancement of the field. These datasets facilitate the training and evaluation of algorithms, promoting the development of more accurate and generalised models.

Real-Time Re-identification Systems: The current state of the art includes the development of real-time re-identification systems capable of processing streaming maritime data. These systems are crucial for timely response in applications such as maritime security and surveillance.

Adaptive and Robust Algorithms: State-of-the-art re-identification algorithms are designed to be adaptive to changing environmental conditions, illumination variations, and occlusions. Robustness is a key consideration, ensuring a reliable performance in diverse maritime scenarios.

Privacy and Ethical Considerations: As with any surveillance technology, ethical and privacy concerns are integral to the state of the art in vessel re-identification. Modern systems incorporate features to address these issues, such as anonymization techniques and compliance with privacy regulations.

Continuous research and development in vessel re-identification aim to further enhance the accuracy, efficiency, and applicability of these systems in real-world maritime scenarios.

METHODOLOGY

There are significant differences in target shapes between pedestrians and warships, as well as when the same battleship is viewed from various angles. The frontal perspective (panel a) and the side view (panel b) of Fig. 1 both demonstrate how the target's entire aspect ratio is inconsistent. As a result, the size standardisation procedure must be done first. By adding gray bars as fillers, the goal proportion is made constant and scaled to the same sharpness as the neural network's input parameter. To determine the local loss, the input data from various pictures are then simultaneously split, evenly divided into numerous rectangular parts of the same shape, and aligned. The input information is also used to compute the cross-entropy loss of global characteristics. Using the label information from each batch of photos, the identification loss is determined. Next, transfer learning is used to quantify the transfer loss using civilian vessels. The network weights are modified after combining the outcomes associated with these four loss functions. A nine-layer CoDA-Net uses a matrix $W_{0 \rightarrow 9}(\sigma_0)$ to calculate the outcome σ_9 for an input variable

a_0 as a linear transformation to ensure that the outcome may be linearly deconstructed into input components, which are depicted in Fig. 2. Several levels of Dynamic Alignment Units (DAUs) are used to compute $W_{0 \rightarrow 9}$ in stages, producing matrices

W_l that are aligned with the corresponding inputs a_{l-1} . The resulting matrix $W_{0 \rightarrow 9}$ consequently aligns favourably with task-relevant patterns.

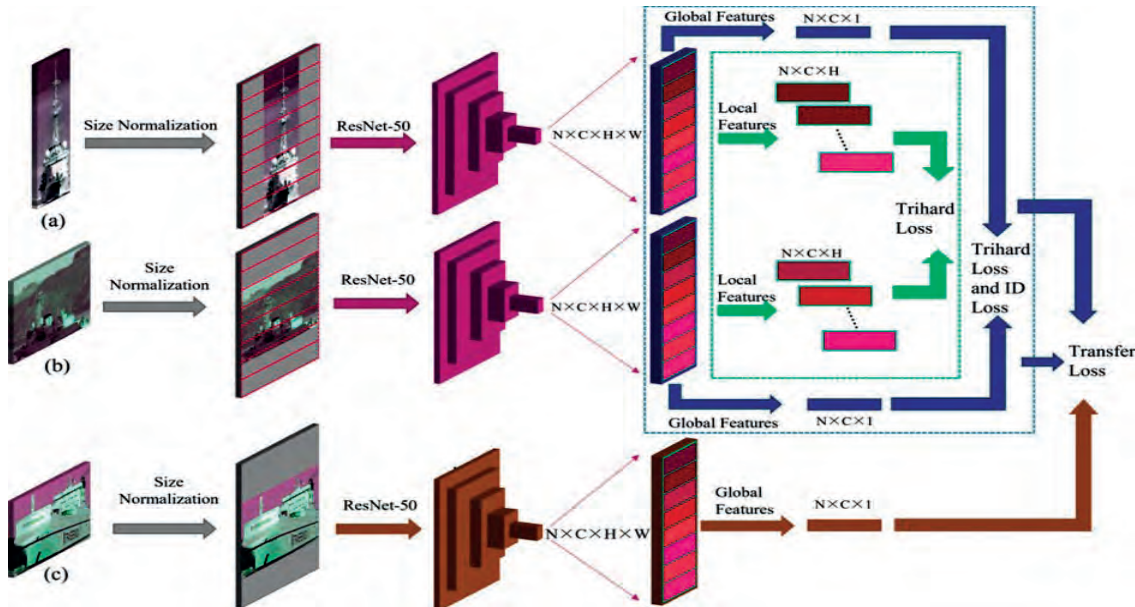


Fig. 1: The structure of Tran-AlignedReID.

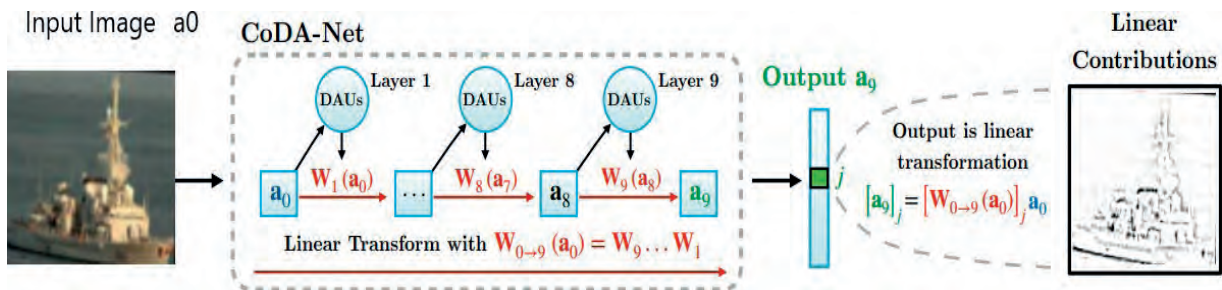


Fig. 2: Graphical representation of a nine-layer CoDA-Net.

LOCAL FEATURE INVESTIGATION

Each differently shaped warship target map is going to be employed as the consistent input information for a convolutional dynamic neural network, along with identifying features obtained using a ResNet50 backbone network framework that has been compressed for dynamic characteristic positioning. The scheming procedure is shown in Fig. 3.

GLOBAL FEATURE ANALYSIS

In addition, local characteristics need to be extracted for feature extraction, but global characteristics cannot be disregarded. The network was utilised to extract the characteristics of the given input information at various depths and the computation of the global characteristic distances and recognition loss across samples is presented in Fig. 4.

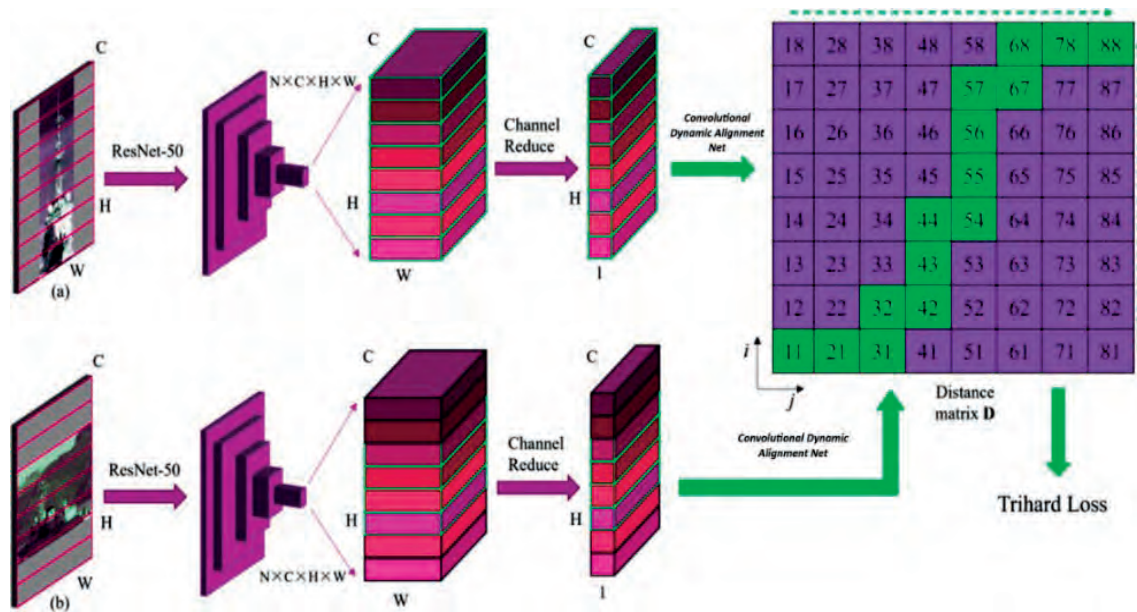


Fig. 3: The local characteristics are dynamically aligned using the loss computation methodology.

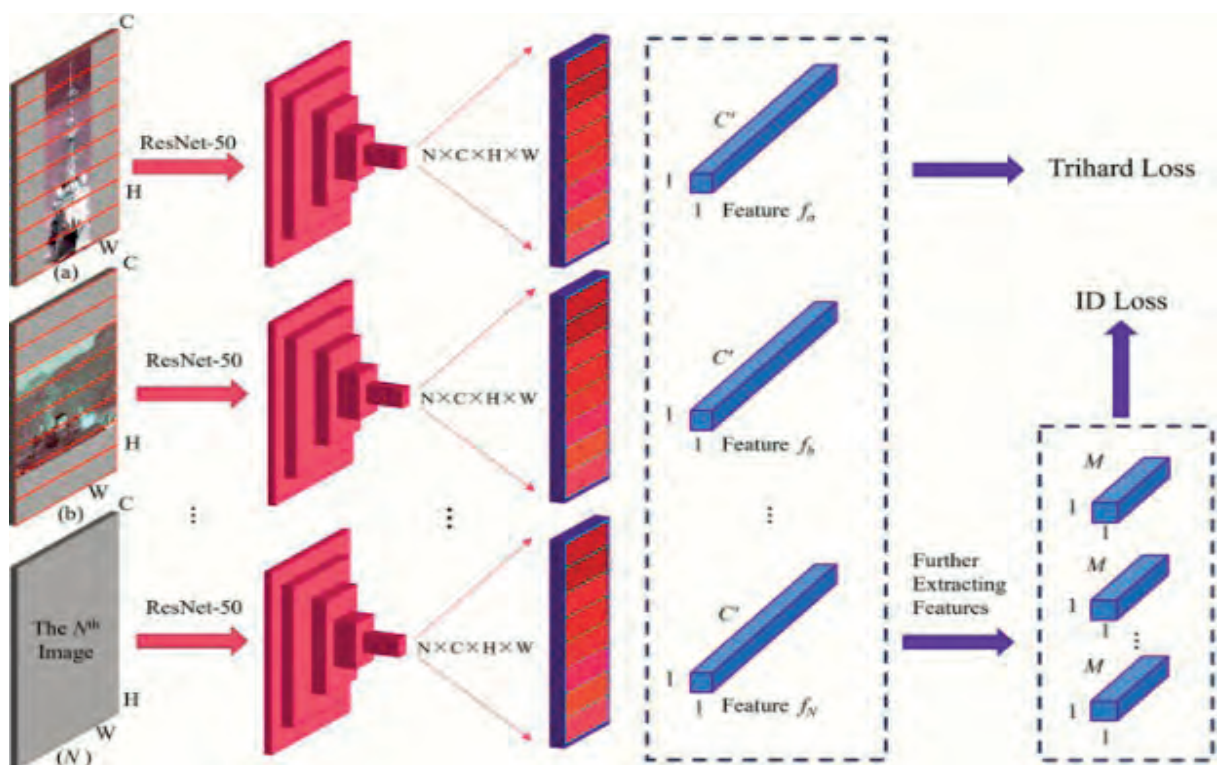


Fig. 4: The method used to calculate the feature distance, as well as the overall loss.

DYNAMIC ALIGNMENT UNITS

DAUs are specified as follows (1):

$$DAU(x) = g(ABx + b)^T x = w(x)^T x \quad (1)$$

In this equation, $x \in \mathbb{R}^d$ denotes an involvement direction. $A \in \mathbb{R}^{d \times r}$ and $B \in \mathbb{R}^{r \times d}$ are fix something on, modification conditions, $b \in \mathbb{R}^d$ is the bias vector, and $g(u) = \alpha(||u||)$ u is a non-linear purpose that balances the quality of its environment. In contrast with a single matrix $M \in \mathbb{R}^{d \times d}$, using AB permits us to regulate the supreme rank r of the alteration and to decrease the numeral of limits; we will hereafter denote by r as the rank of a DAU. U represents units, which can be perceived on the right side of Eq. (1), the DAU linearly converts the contribution $x(P1)$.

Assuming the quadratic procedure ($x^T B^T A^T x$) and the rescaling function $\alpha(||u||)$, the yield of theDAU is a non-linear function of its input.

CoDA-Net

Comparable to an individual linear classification algorithm, a single layer of DAUs has a limited modeling capability. DAUs may, however, be utilised as the fundamental component of deepconvolutional neural networks, which results in effective classifiers. Most significantly, we demonstrate in the following subsection that a Convolutional Dynamic Alignment Network (CoDA-Net) of this type mutually maintains the dynamic linearity (P1) and the alignment maximization (P2) features of the DAUs. Similarly, to dynamic localized filtering stages, every single filter associated with a CoDA level is modeled by a DAU [20]. The proposed CoDA-Net is shown in Figure 5.

It is important to emphasise that the outcome at this phase is a dynamic linear transformation of the input to the layer, mirroring the intricacy seen in rectilinear layers constrained by specific weight limits. The details of this process are outlined in the supplementary section. Toward the conclusion of this segment, we underscore a significant distinction between maximising the output and optimising for classification using the binary cross-entropy (BCE) loss. We delve into the ramifications of temperature scaling in the case study and illustrate the ideal loss function employed in our investigation.

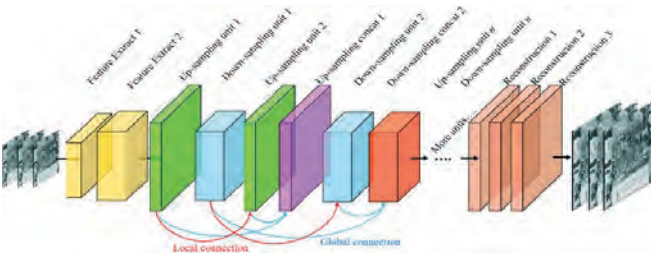


Fig. 5: Proposed CoDA-Net model.

DYNAMIC LINEARITY (P1):

We observe that linearity is preserved and that adaptive linear projection also occurs from the sequential application of many layers of DAUs based on Eq. (2):

$$DAU(x) = ||w(x)|| ||x|| \cos(\angle(x, w(x))) \leq ||x|| \quad (2)$$

As previously indicated, every column in the array W_i corresponds to the weighted vector of just one DAU. Let W_i be the linearly transformed matrix generated by a given layer of DAUs and consider the given input vector information of that layer. As a result, the outcome of this particular layer is represented by the Eq. (3):

$$a_i = W_i(a_{i-1})a_{i-1} \quad (3)$$

Thus, the sequential linear changes in a network of DAUs may be compacted. For instance, the vector a_{l_2} may be written as Eq. (4) a linear modification of a_{l_1} given any combination of activating vectors a_{l_1} and a_{l_2} using $l_1 > l_2$:

$$a_{l_2} = W_{l_1 \rightarrow l_2}(a_{l_1})a_{l_1} \quad (4)$$

$$W_{l_1 \rightarrow l_2}(a_{l_1}) = \prod_{k=l_1+1}^{l_2} W_k(a_{k-1}) \quad (5)$$

For instance, the linear progression from the starting point to the resultant space is modelled by the matrix $W_0 L(a_0 = x) = W(x)$; see Fig. 6. Since a similar linearity is maintained for any two layers, it is possible to dissect the j^{th} entry for every activated vector a_1 in the network's structure into incoming contributions by using Equation (6):

$$S_j^l(x_i) = [W_{0 \rightarrow l} x_i]_j^T \odot x_i \quad (6)$$

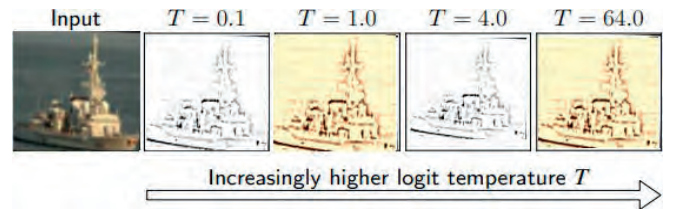


Fig. 6: The correlation maximisation in the DAUs can be emphasized by reducing the upper bound (see Eq. (2)). We display contribution maps using an approach trained under various temperature conditions.

ALIGNMENT MAXIMISATION (P2):

Because each DAU functioning can only, independently of its variables, replicate the standard of its input Eq. (2), the outcome of a CoDA-Net has constraints and is self-governing of the system parameters. Therefore, the linear chain of these processes must also have a superior bound that must be independent of the parameter values. Consequently, all DAUs in the network must provide weights $w(a)$ that are well-aligned with their respective class characteristics to attain maximum average outputs (for example, the class logit over the subset of pictures of that class). In simpler terms, the weights will correspond to input discriminatory characteristics.

CoDA Net COMPARED TO TRANSFER LEARNING

Convolutional Dynamic Alignment Networks (CoDA-Net) and transfer learning are related concepts but address different aspects of machine learning and neural network training. Let's explore the key differences between CoDA-Net and transfer learning:

Objective:

CoDA-Net: CoDA-Net specifically focuses on domain adaptation, which is a subfield of transfer learning. Its primary objective is to align feature distributions between different domains to improve the performance of a model on a target domain that may have a different distribution from the source domain.

Transfer Learning: Transfer learning is a broader concept that includes various strategies for transferring knowledge gained from one task (or domain) to another. It encompasses approaches such as fine-tuning pre-trained models, using pre-trained feature extractors, and leveraging knowledge across related tasks.

Alignment Mechanism:

CoDA-Net: CoDA-Net employs conditional adversarial training to dynamically align feature distributions between the source and target domains. It explicitly addresses the challenge of distribution shift during domain adaptation.

Transfer Learning: Transfer learning encompasses a variety of methods, and the alignment of feature distributions may not be the primary focus. It includes techniques like fine-tuning, where a pre-trained model is adjusted to a new task, and feature extraction, where certain layers of a pre-trained model are used for a related task.

Use Cases:

CoDA-Net: CoDA-Net is specifically designed for scenarios where there is a significant distribution shift between the source and target domains. It is well-suited for domain adaptation tasks, particularly in computer vision applications.

Transfer Learning: Transfer learning is a more general concept applicable to a wide range of machine learning tasks. It is used in various domains, including image classification, natural language processing, and speech recognition.

Architecture:

CoDA-Net: CoDA-Net introduces a specific neural network architecture that incorporates conditional adversarial training for dynamic domain alignment.

Transfer Learning: Transfer learning can be implemented using different architectures, and it doesn't prescribe a specific neural network structure. It is more of a paradigm or strategy than a unique architecture.

In summary, CoDA-Net is a specialized approach within the broader field of transfer learning. It explicitly addresses the challenge of domain adaptation by dynamically aligning feature distributions. Transfer learning, on the other hand, encompasses a range of techniques beyond domain adaptation and can be applied to various tasks using different strategies.

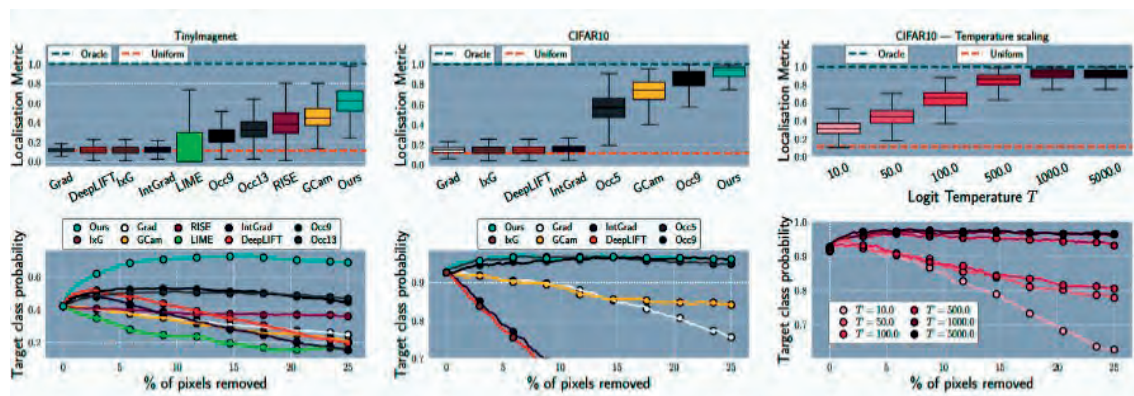


Fig. 7: Upper row: Outcomes for the localization metric. Lower row: Metric for pixel removal. Specifically, we graph the average target class probability following the removal of $x\%$ of the least significant pixels. The outcomes of a CoDA-Net trained on TinyImagenet are illustrated in the left column, while the outcomes of those trained on CIFAR-10 are pre-sented in the center column. Additionally, the impact of the temperature parameter on the interpretability of CoDA-Nets is demonstrated in the right column: as anticipated, a higher temperature results in increased interpretability.

We show the temperature parameter on the interpretability of CoDA-Nets result in Figure 7.

Scalability of temperature along with and loss function:

We have assumed up until this point that applying a maximisation or minimisation loss to each CoDA-Net outcome is similar to minimising the BCE loss for a specific sample. While in theory, this is true, BCE imposes a further, insignificant impact called saturation. In particular, well-aligned weight vectors are not necessary to obtain a minimal BCE loss using a CoDA-Net. Once the classification accuracy is high and the network outputs are significant, the gradient and, as a result, the alignment pressure, will vanish. Because every single DAU within the networks is superior-bounded, as stated in the paragraph above, the effect of a CoDA-Net is superior-bounded regardless of the network configurations, making it possible to easily decrease this impact. The BCE loss function is defined mathematically in Eq. (7):

$$BCE_{y,\hat{y}} = -\frac{1}{N} \sum_{i=1}^N [y_i \cdot \log(\hat{y}_i) + (1 - y_i) \log(1 - \hat{y}_i)] \quad (7)$$

We may explicitly lower this maximum limit by modulating the network response with a temperature variable T such that $\hat{y}(x) = T^{-1}W_{0 \rightarrow L}(x)x$ and thus boost the orientation compression in the DAUs by preventing the early saturation caused by BCE. Particularly, the greater the induced DAU output maximisation should be, the lower the upper bound should be, as the network has to accumulate more signal to acquire high class logits (and a negligible gradient), which requires high-class logits.

Hence, the total loss given a vector of input x_i as well as the target variable y_i is calculated as Equation (8):

$$\lambda(|W_{0 \rightarrow L}(x_i)|) + \mathcal{L}(x_i, y_i) = BCE(\sigma(T^{-1}W_{0 \rightarrow L}(x_i)x_i + b_0), y_i) \quad (8)$$

Here, λ denotes the degree of regularisation, σ activates each vector element using the sigmoid function, b_0 denotes a fixed bias term, and $\langle |W_{0 \rightarrow L}(x_i)| \rangle$ denotes the mean of the absolute values of all the entries in the matrix $W_{0 \rightarrow L}(x_i)$.

IMPLEMENTATION DETAILS

Shared matrix B:

In our tests, we chose to distribute the matrix $B \in \mathbb{R}^{r \times d}$ to all DAUs in a certain layer. Having the DAUs improves the parameter efficiency. They share a similar r -dimensional subspace while maintaining the fixed maximum rank for each DAU at the selected r value.

Input encoding:

In associated works, we demonstrated how the dynamic weights' norm-weighted cosine correlation to the layer resources' norm is optimised, along with how a DAU's outcome can only be as high as the norm of its input. This benefits pixel with high RGB values since they have a higher norm and may provide higher outputs during the maximisation process. To reduce this bias, we encrypt each incoming pixel as $[r, g, b, 1 - r, 1 - g, 1 - b]$, with $r, g, b \in [0, 1]$, by adding the negative pictures as all three supplementary colour pathways.

EXPERIMENTAL RESULTS AND ANALYSIS

DATASET

The proposed maritime ship picture dataset VesselID-539 from the Marine Traffic homepage is the source of the photos for this paper's dataset. The photographs were captured all over the world at various points in time and places, onboard ships and on land, and a given boat exhibits a wide range of

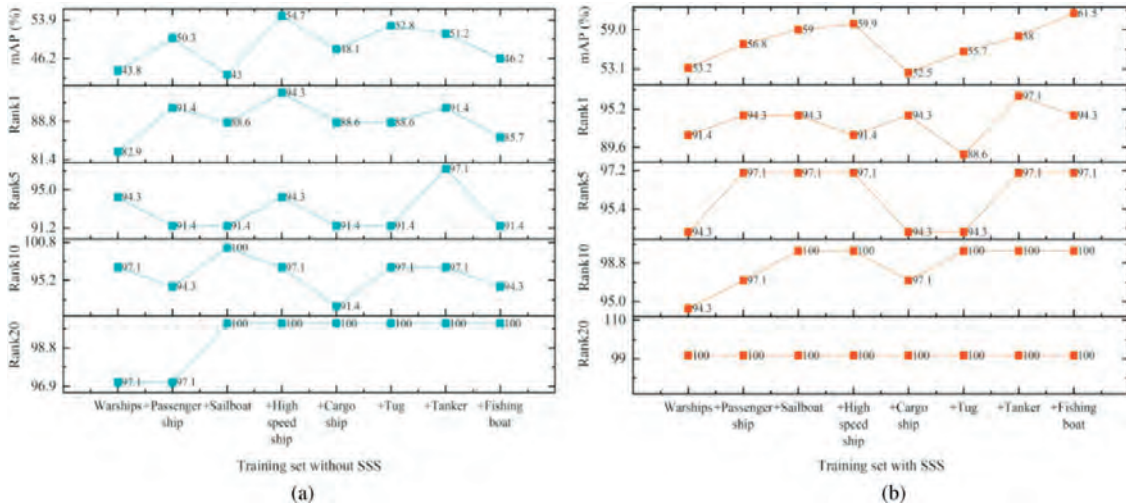


Fig. 8: Outcomes of re-identifying the vessels utilising CoDA Networks. (a) The training instruction set without SSS, and (b) Alongside the training set using SSS.

stances as a result of the many periods and positions in which the pictures were shot.

Warships are the sorts of ships with the highest criteria for portability and camouflage, giving them a more uniform colour, a comparatively quick speed, and flexible behaviour, which requires greater manoeuvring capabilities than civilian vessels. As a result, the training and test sets for this paper's investigations contain battleship images, with different kinds of boats serving as the transferred collection of data.

Regarding the vessel pictures gathered for this study, there are a total of 163 vessels and 4780 photos. Table 1 lists the precise categories and quantities. Additionally, the photographs of battle-ship categorization are split into training and test sets with a 1 : 1 ratio, with 20% of the experiment set's pictures coming from the query database.

Tab. 1: Comparison between the findings of the current study and existing literature.

Method	SSS	mAP (%)	Rank1 (%)	Rank5 (%)	Rank10 (%)	Weight size (MB)
Trans-Reid [21]	No	62.5	88.6	100	100	386.62
PSD-Net [22]		17.2	5.7	20	20	575.21
AN-Net [23]		53.2	82.9	97.1	97.1	318.62
Tran-AlignedReID		56.6	97.1	100	100	91.1
PSD-Net [21]		12.2	17.1	51.4	68	575.21
Trans-Reid [22]	Yes	38.3	68.6	85.7	94.3	386.62
AN-Net [24]		55.4	91.4	100	100	318.62
CoDA-Net (Proposed work)		65.9	97.5	97.5	97.5	91.8

SEA SWAY (SSS) SIMULATION

Sea sway simulation (SSS) involves replicating the motion or oscillation of the sea surface due to various environmental factors. This simulation is crucial for various applications, including maritime engineering, ship design, virtual maritime training, and video game development. The following is a general description of how one might simulate sea sway:

Physical Factors:

Wind Forces: Consider incorporating algorithms that simulate wind forces on the sea surface, as wind is a primary factor influencing sea sway.

Currents and Tides: Include the effects of ocean currents and tides, which contribute to the overall motion of the sea.

Wave Generation: Use wave generation algorithms to create realistic wave patterns. Different types of waves, such as regular waves, irregular waves, and swell, should be considered based on the specific application.

Mathematical Models: Apply mathematical models that describe the motion of the sea. These may include sinusoidal

functions for regular waves or more complex wave models for irregular sea conditions.

Physics-Based Simulation: Implement physics-based simulations that take into account the dynamics of water particles. Consider using fluid dynamics principles to model the interactions between waves and the sea surface.

Real-Time Interaction: For applications like maritime training or ship simulation, ensure that the sea sway simulation can interact in real-time with external factors such as ship movements or user inputs.

Graphic Rendering: Use graphic rendering techniques to visualize the simulated sea sway. This involves creating realistic animations or visual representations of the sea surface motion.

Adjustable Parameters: Provide adjustable parameters for users to customize the simulation based on specific environmental conditions, including wave height, frequency, and direction.

Integration with External Data: Integrate the simulation with real-time environmental data sources, such as weather conditions and oceanographic data, to enhance the accuracy of the simulation.

Validation and Calibration: Validate and calibrate the simulation by comparing its output to observed or measured sea sway data. This step ensures that the simulation accurately represents real-world conditions.

Application-Specific Features: Tailor the simulation to the specific requirements of the application. For example, in ship design, the focus may be on how vessels respond to different sea states.

Simulating sea sway is a complex task that involves the integration of physics, mathematics, and computer graphics to create realistic and accurate representations of the dynamic sea surface. The level of detail and sophistication in the simulation will depend on the intended application and the available computational resources.

COMPARATIVE ANALYSIS OF THE CoDA NeT APPROACH WITH THE SSS METHODOLOGY

When both strategies are used at once, the recognition proficiency is reduced. As a result, the SSS can complete the data augmentation by itself. The statistics indicate that the GridMask approach as well as the overall hide-and-seek approach have a minimal impact on the feature improvement of battleship photos.

Because of the limitations of the testing apparatus, the height and the width of our input pictures are fixed to 256X512, and the precision comparative outcomes are displayed in Table 1. The suggested approach is examined with various best methodologies.

VISUAL COMPARISON

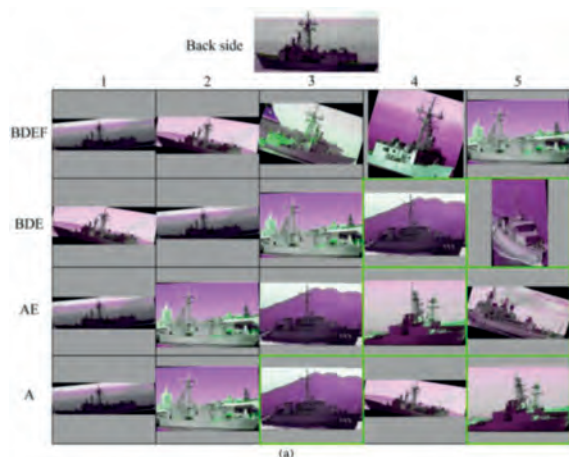


Fig. 9: Results of investigating set validation using various training techniques: Back.

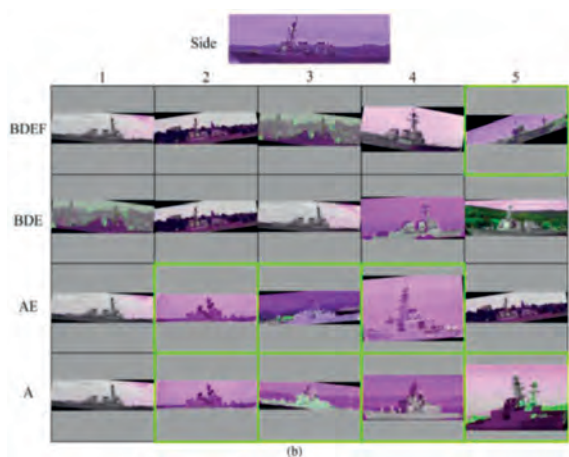


Fig. 10: Results of investigating set validation using various training techniques: Side.

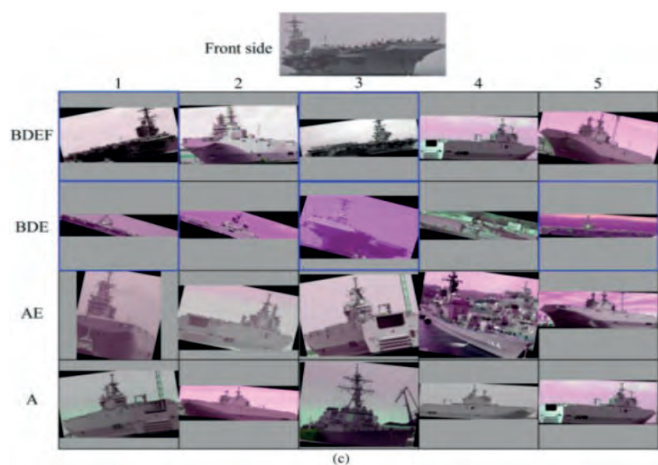


Fig. 11: Results of investigating set validation using various training techniques: Front side.

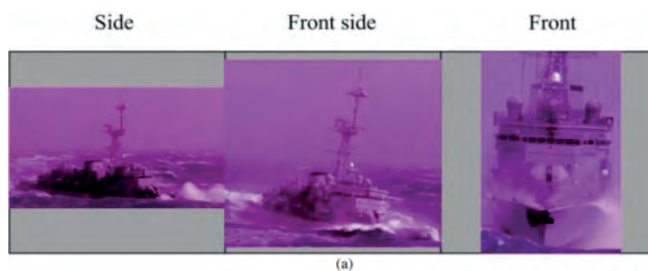


Fig. 12: Effects of query set validation for real-life video investigations using various training approaches: Side.

The side that contains the fewest samples is chosen for labelling in Figs. 9, 10, and 11, which display the results of evaluating the query set for three distinct perspectives of the battleship. Without Greenboxes indicate samples that were mistakenly recognised, while green boxes indicate samples that were successfully identified. In Figs. 9 and 10, the test findings are more encouraging. The impact of the networks created using the four distinct training techniques varies, but the first graph of these search results is accurate. The network that has been trained using the transfer approach functions haphazardly but the initial graph of the finding is precise, whereas the network that was not trained using the transfer method is unable to search for precise outcomes. This is in contrast to the average test outcomes shown in Figure 11.

A navigational video showing the marine destroyer was filmed to test the proposed approach's efficacy. In Figure 12, the identification effect under various angles is depicted. The side with the fewest samples is chosen for labelling, while the olive box and green box represent the mistakenly recognized specimens and the purple box represents the successfully identified samples.

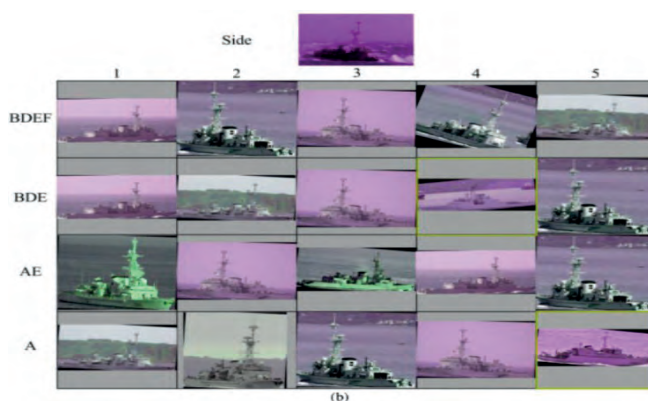


Fig. 13: Effects of query set validation for real-life video investigations using various training approaches: (b) Side.

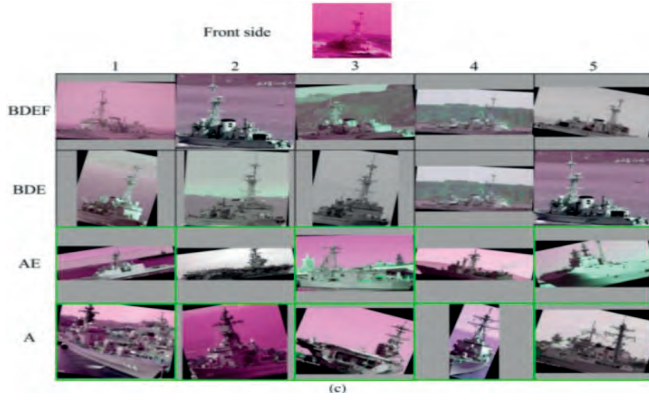


Fig. 14: Effects of query set validation for real-life video investigations using various training approaches. (c) Front side.

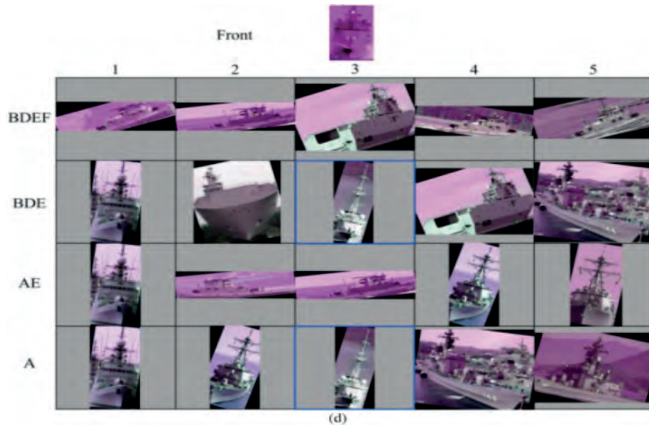


Fig. 15: Effects of query set validation for real-life video investigations using various training approaches. (d) Front.

STATISTICAL ANALYSIS

After the modelling process is complete, the root mean square error $RMSE$ and the correlation coefficient (R^2) are used to consider the expected and predicted benefits of a flexible modulus [25]. The equation that follows Eq. 9 may be used to calculate the $RMSE$:

$$RMSE = \sqrt{\frac{1}{m} \sum_{i=1}^m (y_{pred_i} - y_{obs_i})^2} \quad (9)$$

The value of the determinant coefficient, or (R^2), can be calculated using Eq. 10, which is calculated as follows:

$$R^2 = 1 - \frac{\sum_{i=1}^m (y_{pred_i} - y_{obs_i})^2}{\sum_{i=1}^m y_{obs_i}^2} \quad (10)$$

Tab. 2: Data analysis using CoDA-Net.

Techniques	$RMSE$	MAE	$MAPE$	R^2
CoDA-Net	0.05817	0.0698	0.880	0.9973
Res-Net 50	0.06341	0.07231	0.901	0.9067

The mean of the squared errors may be measured by the mean absolute percentage error ($MAPE$). The more moderate upsides of the $MAPE$ ensure that the anticipated models will be presented in a more advanced manner. The subsequent Eq. 11 can be used to calculate the $MAPE$ [26]:

$$MAPE = \frac{1}{m} \sum_{i=1}^m \frac{|(y_{pred_i} - y_{obs_i})|}{y_{pred_i}} \times 100\% \quad (11)$$

The MAE , which is defined by Eq. 12, is used to further investigate the display and effectiveness of the predicted frameworks:

$$MAE = \frac{1}{m} \sum_{i=1}^m |y_{pred_i} - y_{obs_i}| \quad (12)$$

where m represents the total number of information designs present in the informative collection, y_{pred_i} represents the value that is expected for each information point i , and y_{obs_i} represents the value is calculated for each information point i . The comparative analysis has been carried out, presenting the anticipated output from the CoDA-Net, while the actual results are provided in Table 2.

CONCLUSION

Regarding the re-identification of warships, a convolutional dynamic alignment re-identification network model combining transfer learning techniques is put forth in this research. On the dataset, Sea sway simulations were run on the dataset replicate the sway seen by onboard cameras during rough seas. To test the applicability of the transfer method, several experiments were conducted using transfer data from various types of civilian boats. On the training set and the transferred dataset, the impacts of the sea sway simulation approach are contrasted. The battleship re-identification problem's suitability for SSS and image enhancement techniques is also covered. To demonstrate the method's superiority, many of the best re-identification techniques are compared in this re- search.

The CoDA-Nets, a novel family of neural networks, were introduced in this study, and it was demonstrated that they are efficient classifiers with good comprehension. We first introduced the DAUs, which have a structural propensity for alignment maximisation, and characterise their out-put as a dynamic linear transformation of their input. We model filters in a convolutional network using DAUs to produce Convolutional Dynamic Alignment Networks (CoDA-Nets). It

is feasible to linearly partition the outcome into expenditures from different measurements of input thanks to the network's DAUs' subsequent linear translations of the network's DAUs. We evaluate the quality of these contribution maps' quality by comparing them to different imputation techniques, as shown in Eq. (6).

The research results indicate that, in the absence of a marine control simulation, the modified procedure increases the typical mAP accuracy by 10.7% and the Rank1 accuracy by 11.2%. In the instance of marine control recreation, the enhanced method increased the Rank1 accuracy by .9% and the mAP accuracy by an average of 10.7%. As a result, the transfer dynamic alignment algorithm performs battleship re-identification duties more effectively, particularly when warship wobble is involved.

DECLARATION OF COMPETING INTEREST

The researchers affirm that they have not encountered any interpersonal or financial disputes that would seem to have an impact on the research presented in this study.

REFERENCES

1. G. Zeng, R. Wang, W. Yu, A. Lin, H. Li, and Y. Shang, "A transfer learning-based approach to maritime warships re-identification," *Engineering Applications of Artificial Intelligence*, vol. 125, p. 106 696, 2023, ISSN: 0952-1976. DOI: <https://doi.org/10.1016/j.engappai.2023.106696>. [Online]. Available: <https://www.sciencedirect.com/science/article/pii/S0952197623008801>.
2. M. Böhle, M. Fritz, and B. Schiele, "Convolutional dynamic alignment networks for interpretable classifications," pp. 10 024–10 033, 2021. DOI: 10.1109/CVPR46437.2021.00990.
3. D. Prasad, D. Rajan, L. Rachmawati, E. Rajabaly, and C. Quek, "Video processing from electro-optical sensors for object detection and tracking in a maritime environment: A survey," *IEEE Transactions on Intelligent Transportation Systems*, vol. PP, Nov. 2016. DOI: 10.1109/TITS.2016.2634580.
4. J. Cheng, R. Wang, A. Lin, D. Jiang, and Y. Wang, "A feature enhanced RetinaNet – based for instance-level ship recognition," *Engineering Applications of Artificial Intelligence*, vol. 126, p. 107 133, Nov. 2023. DOI: 10.1016/j.engappai.2023.107133.
5. Q. Yu, A. Teixeira, K. Liu, and C. Guedes Soares, "Framework and application of multi-criteria ship collision risk assessment," *Ocean Engineering*, vol. 250, p. 111 006, 2022, ISSN: 0029-8018. DOI: <https://doi.org/10.1016/j.oceaneng.2022.111006>. [Online]. Available: <https://www.sciencedirect.com/science/article/pii/S0029801822004309>.
6. F. Farahnakian, L. Zelioli, and J. Heikkonen, "Transfer learning for maritime vessel detection using deep neural networks," pp. 1–6, 2021. DOI: 10.1109/ITSC48978.2021.9565077.
7. D. K. Prasad, C. K. Prasath, D. Rajan, L. Rachmawati, E. Rajabaly, and C. Quek, "Challenges in video based object detection in maritime scenario using computer vision," *arXiv preprint arXiv:1608.01079*, 2016.
8. R. Zhang, S. Li, G. Ji, X. Zhao, J. Li, and M. Pan, "Survey on deep learning-based marine object detection," *Journal of Advanced Transportation*, vol. 2021, pp. 1–18, Nov. 2021. DOI: 10.1155/2021/5808206.
9. D. Qiao, G. Liu, T. Lv, W. Li, and J. Zhang, "Marine vision-based situational awareness using discriminative deep learning: A survey," *Journal of Marine Science and Engineering*, vol. 9, no. 4, p. 397, 2021.
10. J. Rodrigues, P. Cardoso, J. Monteiro, et al., *Computational Science – ICCS 2019 19th International Conference, Faro, Portugal, June 12–14, 2019, Proceedings, Part III: 19th International Conference, Faro, Portugal, June 12–14, 2019, Proceedings, Part III*. Jan. 2019, ISBN: 978-3-030-22743-2. DOI: 10.1007/978-3-030-22744-9.
11. D. Qiao, G. Liu, F. Dong, S.-X. Jiang, and L. Dai, "Marine vessel re-identification: A large-scale dataset and global-and-local fusion-based discriminative feature learning," *IEEE Access*, vol. 8, pp. 27 744–27 756, 2020.
12. D. Qiao, G. Liu, J. Zhang, Q. Zhang, G. Wu, and F. Dong, "M3c: Multimodel-and-multicue-based tracking by detection of surrounding vessels in maritime environment for USV," *Electronics*, vol. 8, no. 7, p. 723, 2019.
13. M. Er, Y. Zhang, J. Chen, and W. Gao, "Ship detection with deep learning: A survey," *Artificial Intelligence Review*, vol. 56, pp. 1–41, Mar. 2023. DOI: 10.1007/s10462-023-10455-x.
14. P. Spagnolo, F. Filieri, C. Distanto, P. L. Mazzeo, and P. D'Ambrosio, "A new annotated dataset for boat detection and re-identification," pp. 1–7, Sep. 2019. DOI: 10.1109/AVSS.2019.8909831.
15. H. Luo, W. Jiang, X. Zhang, X. Fan, J. Qian, and C. Zhang, "AlignedReID ++: Dynamically matching local information for person re-identification," *Pattern Recognition*, vol. 94, pp. 53–61, 2019, ISSN: 0031-3203. DOI: <https://doi.org/10.1016/j.patcog.2019.05.028>. [Online]. Available: <https://www.sciencedirect.com/science/article/pii/S0031320319302031>.
16. H. Wang, H. Du, Y. Zhao, and J. Yan, "A comprehensive overview of person re-identification approaches,"

IEEE Access, vol. PP, pp. 1–1, Mar. 2020. DOI: 10.1109/ACCESS.2020.2978344.

2022, ISSN: 2772-7823. DOI: <https://doi.org/10.1016/j.clce.2022.100010>.

17. B. Sun, Y. Ren, and X. Lu, “Semisupervised consistent projection metric learning for person reidentification,” *IEEE Transactions on Cybernetics*, vol. PP, pp. 1–10, Apr. 2020. DOI: 10.1109/TCYB.2020.2979262.
18. N. Martinel, M. Dunnhofer, R. Pucci, G. Foresti, and C. Micheloni, “Lord of the rings: Hanoi pooling and self-knowledge distillation for fast and accurate vehicle re-identification,” *IEEE Transactions on Industrial Informatics*, vol. PP, pp. 1–1, Mar. 2021. DOI: 10.1109/TII.2021.3068927.
19. X. Liu, S. Zhang, X. Wang, R. Hong, and Q. Tian, “Group-group loss-based global-regional feature learning for vehicle re-identification,” *IEEE Transactions on Image Processing*, vol. 29, pp. 2638–2652, 2019.
20. B. Brabandere, X. Jia, T. Tuytelaars, and L. Van Gool, “Dynamic filter networks,” *Neural Information Processing Systems (NIPS)*, Jan. 2016.
21. S. He, H. Luo, P. Wang, F. Wang, H. Li, and W. Jiang, “TransReID: Transformer-based object re-identification,” 2021 IEEE/CVF International Conference on Computer Vision (ICCV), pp. 14 993–15 002, 2021. <https://api.semanticscholar.org/CorpusID:231846818>.
22. T. Wang, H. Liu, W. Li, M. Ban, T. Guo, and Y. Li, “Feature completion transformer for occluded person re-identification,” Mar. 2023. DOI: 10.48550/arXiv.2303.01656.
23. Y. Wu, W. Yang, and M. Wang, “Unsupervised person re-identification with attention-guided fine-grained features and symmetric contrast learning,” *Sensors*, vol. 22, no. 18, 2022, ISSN: 1424-8220. [Online]. Available: <https://www.mdpi.com/1424-8220/22/18/6978>.
24. X. Jia, B. De Brabandere, T. Tuytelaars, and L. V. Gool, “Dynamic filter networks,” in
25. *Advances in Neural Information Processing Systems*, D. Lee, M. Sugiyama, U. Luxburg,
26. Guyon, and R. Garnett, Eds., vol. 29, Curran Associates, Inc., 2016. [Online]. Available: https://proceedings.neurips.cc/paper_files/paper/2016/file/8bf1211fd4b7b94528899de0a43b9fb3-Paper.pdf.
27. D. K. Jana, S. Roy, P. Dey, and B. Bej, “Utilization of a linguistic response surface methodology to the business strategy of polypropylene in an Indian petrochemical plant,” *Cleaner Chemical Engineering*, vol. 2, p. 100 010,
28. S. Roy, D.-P. Vuong, and D. K. Jana, “Priority-aware scheduling method based on linguistic interval type 2 fuzzy logic systems for dense industrial iot networks employing soft computing,” *Results in Control and Optimization*, vol. 14, p. 100 391, 2024, ISSN: 2666- 7207. DOI:<https://doi.org/10.1016/j.rico.2024.100391>.

AUTOMATIC CLASSIFICATION OF UNEXPLODED ORDNANCE (UXO) BASED ON DEEP LEARNING NEURAL NETWORKS (DLNNS)

Norbert Sigiel*

Poland

Marcin Chodnicki 

Air Force Institute of Technology, Aircraft Composite Structures Division, Poland,

Paweł Socik 

Polish Naval Academy, Faculty of Mechanical and Electrical Engineering, Poland

Rafał Kot 

Polish Naval Academy, Faculty of Mechanical and Electrical Engineering, Poland

* Corresponding author: norbert.sigiel@gmail.com (Norbert Sigiel)

ABSTRACT

This article discusses the use of a deep learning neural network (DLNN) as a tool to improve maritime safety by classifying the potential threat to shipping posed by unexploded ordnance (UXO) objects. Unexploded ordnance poses a huge threat to maritime users, which is why navies and non-governmental organisations (NGOs) around the world are using dedicated advanced technologies to counter this threat. The measures taken by navies include mine countermeasure units (MCMVs) and mine-hunting technology, which relies on the use of sonar imagery to detect and classify dangerous objects. The modern mine-hunting technique is generally divided into three stages: detection and classification, identification, and neutralisation/disposal. The detection and classification stage is usually carried out using sonar mounted on the hull of a ship or on an underwater vehicle. There is now a strong trend to intensify the use of more advanced technologies, such as synthetic aperture sonar (SAS) for high-resolution data collection. Once the sonar data has been collected, military personnel examine the images of the seabed to detect targets and classify them as mine-like objects (MILCO) or non mine-like objects (NON-MILCO). Computer-aided detection (CAD), computer-aided classification (CAC) and automatic target recognition (ATR) algorithms have been introduced to reduce the burden on the technical operator and reduce post-mission analysis time. This article describes a target classification solution using a DLNN-based approach that can significantly reduce the time required for post-mission data analysis during underwater reconnaissance operations.

Keywords: Deep Learning Neural Network (DLNN); mine detection and classification; sonar imagery; Mine Countermeasure (MCM); Automatic Target Recognition (ATR)

INTRODUCTION

In today's era of increasing data and the proliferation of visual information, the field of computer vision has become a key technology for understanding and interpreting images and videos. Deep learning neural networks play an important role in this field. Deep learning neural networks (DLNNs) enable the automatic identification and recognition of targets or objects in an image or video stream. Automatic target recognition (ATR) modules have a wide range of applications in various fields, including but not limited to:

Industrial Automation [1] (object recognition and tracking for quality control, inventory management, and robotic systems), Video Surveillance [2] (surveillance systems automatically identifying and tracking objects of interest, such as individuals, vehicles, or specific behaviours, thus improving security and safety), Medicine [3],[4] (medical imaging systems), and Military and Defence [5] (military surveillance, reconnaissance and intelligence).

This article addresses the task of using DLNN as a tool to improve maritime security by detecting the potential threat to shipping posed by UXO objects. Thousands of mines were

deployed in the Baltic Sea during the First and Second World Wars. Many of these still lie on the seabed and pose a real threat to shipping and the marine environment. The Baltic Marine Environment Protection Commission (HELCOM) reports that approximately 40,000 tonnes of munitions and chemical weapons were dumped into the water during the Second World War alone [6],[7]. Given this fact and the new threats arising from the war in Ukraine [8], where the Black Sea has been invaded by hundreds of mines dropped by both sides, there is a great need to intensify work on monitoring the water space and improving the tactics and techniques of this process.

The designation of objects as Unexploded Ordnance has a significant role in maritime security management in particular. Awareness of the presence of a threat located on the seabed and the risk it poses allows, for instance, the rerouting of waterways for the safe transit of cargo and crisis response shipping, which is particularly important during armed conflicts. The correct classification of objects as UXO and the associated probability of classification allows for a reduction in the time taken to conduct mine countermeasure operations by determining which contacts to identify first using divers and remotely operated vehicles (ROVs), as well as those that, by their nature, should not pose a threat.

The research question addressed in this article is how effective a pre-trained DLNN-based ATR module can be for detecting and correctly classifying UXO in sonar images, and what level of assurance it provides to operators involved in mine countermeasure (MCM) operations, as well as the benefits of using graphics processing units (GPUs) instead of central processing units (CPUs) in the data analysis process. In order to correctly answer these questions, the best structure and parameters of the DLNN must be guaranteed after the learning process. The most promising pre-trained DLNNs are then used and the average values of training accuracy, verification accuracy and the average training time of a single network are presented. Fig. 1 presents the idea of the transfer learning process used in the conducted research.

The following three classes of UXO objects are adopted in this study: Manta Shape Mine, Cylindrical Mine, and Spherical Mine. The NON-MILCO class is assigned to various objects not belonging to the first three classes. The images used to train the network were generated during live operations conducted by the Polish Navy in the Baltic and North Seas from 2015 to 2023. It should be emphasised that

invaluable contributions to the process of building the UXO database used in the project were made by the crews of Polish Mine Countermeasure Vessels that participated in MCM operations.

The initial sections of the article describe the method of trajectory planning and analysing data from unmanned underwater vehicle (UUV) missions carried out to collect reliable and useful data for DLNN training. The subsequent sections compare the performance of different pre-trained neural networks in terms of the training accuracy, verification accuracy and average training time of each network. These sections also compare the performance of a single GPU and a single CPU, based on the computational performance of the DLNN. The final section summarises the results of the research and highlights the role of ATR modules in ensuring maritime safety by detecting and classifying underwater mines and other explosive hazards.

UUV-BASED SONAR DATA COLLECTION METHOD FOR DEEP LEARNING NEURAL NETWORKS

The process of generating data, i.e. images of objects, is described in [10] as part of the sonar checking procedure. The above procedure starts with the deployment of a reference object on the seabed. The reference object or target's shape, size and material should correspond with the actual mine threat. Once the object is deployed on the seabed, the operator should plan and evaluate the mission according to the trajectory shown in Fig. 2.

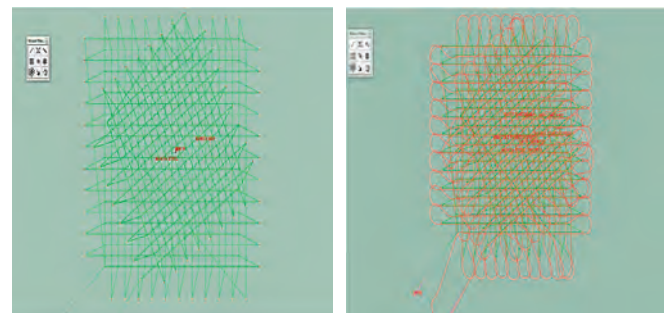


Fig. 2. The mission plan and evaluation focused on the data collection process - Courtesy of 13 MCM Squadron

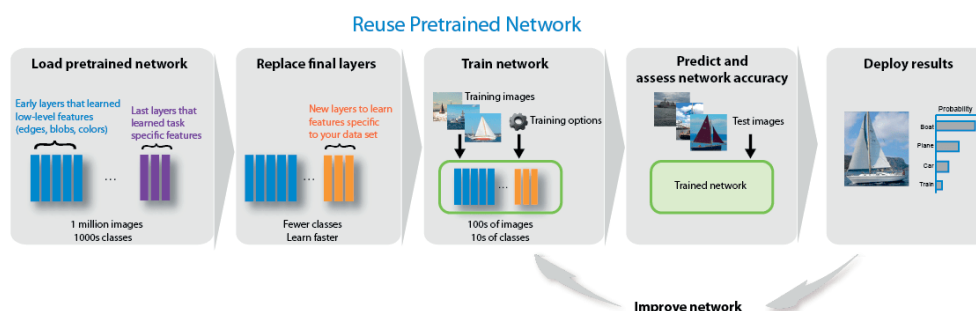


Fig. 1. Pre-trained DLNN transfer learning [9]

The mission plan should include the ability to record the reference target across the entire spectrum of sonar coverage, both in close proximity to the sonar transducer and at maximum range. Cross-path patterns with a 45-degree offset are recommended, in order to obtain multiple path orientations and present the target from different perspectives. This is particularly important when creating a target database in an area with a varied and undulating seabed (Fig. 3).

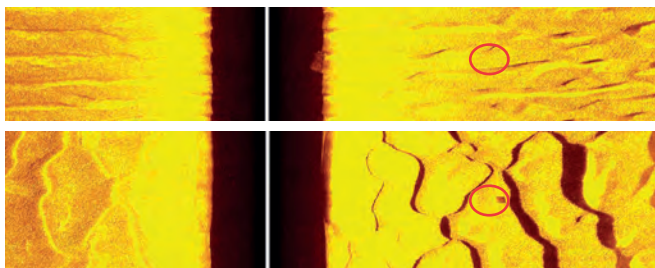


Fig. 3. Seabed projection on sonar image registered by EDETECH sonar for angles 0° and 90° - Courtesy of 13 MCM Squadron

Detections should only be specified for one type of object, e.g. a special type of mine. For one object, it is possible to obtain a limited number of detections due to the planned track spacing. Fig. 2 shows that it is possible to obtain eight detections for each target within the specified range beam. Due to the drift of inertial navigation system (INS) accuracy over time, it is possible to obtain more than eight detections within a certain range and this situation must be taken into account [10].

Once the vehicle has been recovered and the mission data has been downloaded, a detailed analysis focusing on object detection and classification should be carried out. The registration of detected objects, together with the background, in images of similar resolutions and dimensions is important for the construction of the ATR module (Fig. 4).

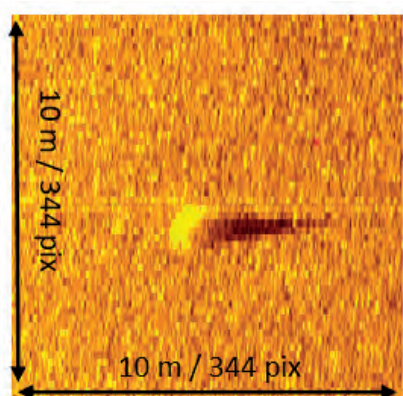


Fig. 4. Manta shape object on sonar image covering an area of 10 x 10 m - Courtesy of 13 MCM Squadron

For future operations, it is important to maintain a standard for numbering and describing images. Each object/image should then be assigned to a class, based on which DLNN will assign them to UXO or NON-MILCO objects.

Fig. 5 shows the objects assigned to four classes: Cylinder, Manta, NON-MILCO and Spherical.

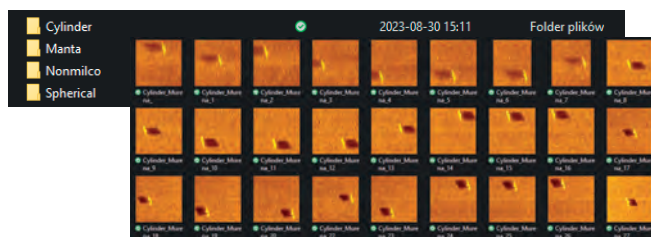


Fig. 5. Images assigned to four classes: Cylinder, Manta, NON-MILCO and Spherical

SONAR DATA COLLECTED FOR DEEP LEARNING OF NEURAL NETWORKS

Due to the nature of the research environment and the risks associated with the verification of UXO objects found in the marine environment, there is a very narrow and elite group of individuals and institutions with data that can be used to train neural networks and build algorithms to automatically identify objects in the underwater domain. This group is largely populated by navies operating in waters with a history of mine warfare. Given that a selected pre-trained DLNN has to be learned from data from a single sensor (sonar) operating on a single operating frequency, that also defines the range of the sonar technology, building an automatic detection and classification module is a time-consuming process. A range of dangerous objects [11] recorded during live mine countermeasure operations were used in the research (Fig. 6).

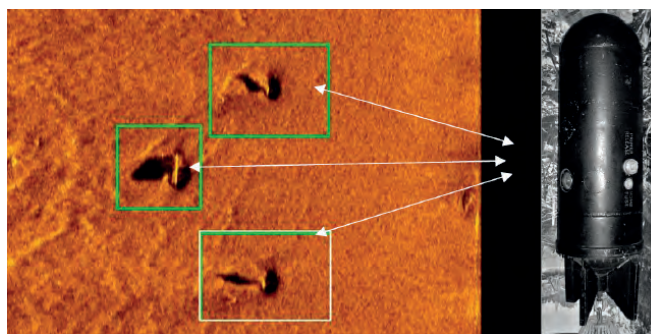


Fig. 6. German mines from World War II on sonar image [12] - Courtesy of 13 MCM Squadron

Due to limited data on the actual mine threat and the required accuracy of DLNN training, the study also used reference objects (i.e. Manta, Murena, Mk16 training mines) to simulate the actual threat (Fig.7).

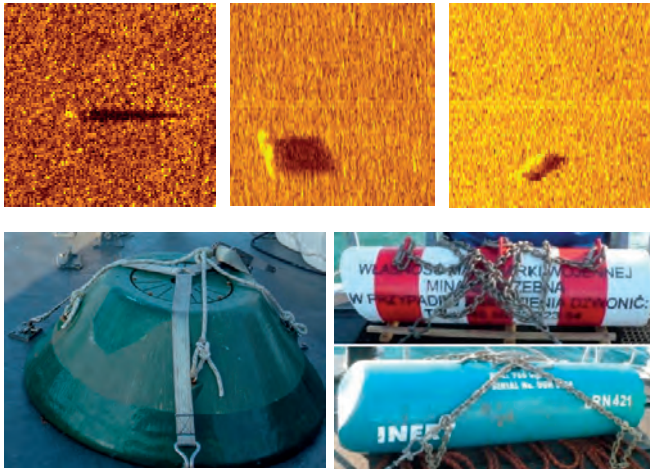


Fig. 7. Training mines detected on sonar images in sequence: Manta [13], Murena, Mk16 - Courtesy of 13 MCM Squadron

As part of the research, the following images were generated using the Gavia UUV system, equipped with EDGETECH side scan sonar: 431 cylindrical objects, 537 Manta shape objects, 105 Spherical objects (mainly M-08 and M-12 mines) and 638 NON-MILCO objects. These 1,711 images represent the number of independent sonar images, by which it should be understood that, for one object located on the seabed, it is possible to generate several to several dozen sonar images according to the methodology proposed in the article. In the study, each image was generated during an independent vehicle run. It should be emphasised that the collection of several images of dangerous or training objects takes several hours to several days of research, depending on the characteristics of the UUV used. Therefore, the idea and research discussed in this article will continue, in order to obtain satisfactory results for automatic object detection and classification.

USING PRE-TRAINED DLNNS FOR UXO CLASSIFICATION

Pre-trained DLNNS are neural network models that have been trained on large datasets for specific tasks, such as image classification. These models have learned to recognise patterns, features and representations in the data, making them very valuable for a wide range of applications beyond their initial training task. In the context of UXO classification, pre-trained DLNNS can use their learned knowledge to distinguish UXO from non-hazardous objects. DLNN processing requires resizing each image to the dimensions of the first layer. The size of the input image for each neural network analysed is shown in the last column of Table 1 [14].

Tab. 1. DLNN Parameters [14]

Neural Network	Depth	Size (MB)	Parameters (Millions)	Image Input Size
squeezenet	18	5.2	1.24	227-by-227
googlenet	22	27	7.0	224-by-224

Neural Network	Depth	Size (MB)	Parameters (Millions)	Image Input Size
inceptionv3	48	89	23.9	299-by-299
densenet201	201	77	20.0	224-by-224
mobilenetv2	53	13	3.5	224-by-224
resnet18	18	44	11.7	224-by-224
resnet50	50	96	25.6	224-by-224
resnet101	101	167	44.6	224-by-224
xception	71	85	22.9	299-by-299
places365-Googlenet	22	27	7.0	224-by-224
shufflenet	50	5.4	1.4	224-by-224
nasnetmobile	*	20	5.3	224-by-224
alexnet	8	227	61.0	227-by-227
vgg16	16	515	138.0	224-by-224
vgg19	19	535	144.0	224-by-224
darknet19	19	78	20.8	256-by-256
darknet53	53	155	41.6	256-by-256
efficientnetb0	82	20	5.3	224-by-224

*nasnetmobile do not consist of a linear sequence of modules.

The research problem in this paper is to evaluate the performance of pre-trained DLNNS in classifying 1711 images (1073 UXO images and an additional 638 images representing non-military objects) and 3422 images obtained using image data augmentation. Data augmentation plays an important role in enhancing the performance of pre-trained deep neural networks (DLNNS). This importance comes from the challenges of acquiring sonar data of UXO objects, which are often sparse for security reasons, and the rarity of such events. By applying data augmentation techniques on the limited available sonar data, we can effectively multiply the size of our dataset while maintaining its representativeness. This augmentation introduces changes in object orientation, scales and contextual conditions, which are essential for DLNN training to accurately recognise both UXO and non-military objects. In addition, the augmentation of sonar data serves to improve the generality of the model in different underwater environments and acoustic conditions. Simulating real-world scenarios through extensions such as rotations, translations, and reflections equips the DLNN with the adaptability needed to make informed classifications in unpredictable circumstances. Essentially, data augmentation enables the DLNN to achieve better classification results for UXO and non-military objects, even in the face of inherent difficulties in obtaining sufficient and representative sonar data for training.

Based on previous studies [15], the Adam method was chosen for testing due to its highest average accuracy and shortest training time. The criteria for evaluating the performance of DLNN were: (1) training and verification accuracy, (2) mini-batch loss and (3) the CPU/GPU computation time needed to classify objects with the highest accuracy. The comparison of pre-training time is important because it indicates the potential to use data collected during

the mission to train neural networks in real time. This means that algorithms are able to adapt and learn during the mission, using the current information. This allows them to respond quickly to changing conditions and needs, which is crucial in rapidly evolving environments.

The task of the DLNN was to classify underwater images into one of four object categories: (1) Cylinder, (2) Manta, (3) Spherical, and (4) NON-MILCO. This classification is related to the utilitarian aspect of the research, namely the ability to detect and classify the main types of mines and other UXO objects found in the Baltic Sea. It is estimated that mine warfare, intense during both World War I and World War II, introduced some 160,000 mines into the Baltic Sea, of which only 20% have been removed or destroyed in MCM operations [16].

All images contain one object to be classified, such as one type of mine or rock. They were taken in different waters (Baltic Sea and North Sea) under different conditions (e.g. salinity, temperature, and depth) but using a single EDGETECH 600 kHz sonar frequency. It seems that it will be difficult to obtain an optimal solution for the deep neural network, taking into account the fact that operators may also have problems with the classification of the above images. A total of 70% of the images were randomly selected for training and the remaining 30% were used for verification.

A comparison of 18 pre-trained DLNNs was carried out. The type of DLNNs tested and their results, as the average of 30 trials of training accuracy, verification accuracy and time needed to train a single network using the CPU and GPU, are included in Tables 2 and 3.

Tab. 2. DLNNs evaluation on CPU (i7)

Neural Network	Average Training Accuracy [%]	Average Verification Accuracy [%]	Average Training Time [h:min]	Remarks
squeezenet [17]	78.91	85.54	0:46	
googlenet [18]	94.34	94.33	1:19	
inceptionv3 [19]	99.22	96.48	5:15	
densenet201 [20]	100.00	93.94	13:45	Warning: Graphics timeout occurred.
mobilenetv2 [21]	100.00	95.90	2:27	Warning: Graphics timeout occurred.
resnet18 [22]	100.00	96.87	1:19	
resnet50 [22]	98.44	93.16	3:36	Warning: Graphics timeout occurred.
resnet101 [22]	100.00	96.48	9:52	

Neural Network	Average Training Accuracy [%]	Average Verification Accuracy [%]	Average Training Time [h:min]	Remarks
xception [23]	100.00	93.36	17:30	Warning: Graphics timeout occurred.
places365-Googlenet [24]	96.67	93.164	2:16	
shufflenet [25]	100.00	96.44	1:05	
nasnetmobile [26]	100.00	97.27	3:45	
alexnet [27]	68.75	61.13	0:24	
vgg16 [28]	52.54	48.63	9:16	
vgg19 [28]	56.25	57.22	11:42	
darknet19 [29]	77.34	72.07	2:53	
darknet53 [29]	90.00	84.77	13:09	Warning: Graphics timeout occurred.
efficientnetb0 [30]	97.66	96.67	4:53	

Tab. 3. DLNNs evaluation on single GPU (RTXA3000)

Neural Network	Average Training Accuracy [%]	Average Verification Accuracy [%]	Average Training Time [h:min]	Remarks
squeezenet	82.03	76.56	0:03	
googlenet	96.88	91.99	0:07	
inceptionv3	99.22	95.70	0:52	
densenet201	100.00	95.70	2:43	
mobilenetv2	99.22	96.48	0:21	
resnet18	99.22	96.23	0:03	
resnet50	99.22	95.89	0:38	
resnet101	100.00	93.94	1:10	Warning: Graphics timeout occurred.
xception	100.00	95.89	2:34	
places365-Googlenet	85.16	79.10	0:05	
shufflenet	100.00	96.68	0:05	
nasnetmobile	100.00	96.48	0:54	Warning: Graphics timeout occurred.
alexnet	60.94	60.35	0:01	
vgg16	56.67	48.24	1:02	
vgg19	73.33	78.71	1:38	
darknet19	80.00	81.05	0:18	
darknet53	96.67	93.94	2:40	
efficientnetb0	96.67	95.31	2:00	Warning: Graphics timeout occurred.

DISCUSSION

The study aimed to evaluate the performance of pre-trained DLNN models in classifying images representing UXO objects and additional objects that do not pose an underwater threat to fisheries and marine users. Based on the test results given in Tables 2 and 3, and considering that the DLNN models were trained on a single PC (CPU i7) and a single GPU (RTXA3000), it can be concluded that a computing platform with multiple GPUs is suggested for optimal performance. The tests showed that a single GPU performed numerical tests almost 15 times faster than the CPU.

The results of this work can be used to verify and evaluate the performance of each network for the main task of UXO classification. The research clearly shows that, due to the limited access to sonar data associated with UXO objects, data augmentation techniques are essential for improving the performance of DLNN models. They give the models the ability to generalise across different underwater and acoustic conditions, which is crucial for accurate classification.

The obtained network verification accuracy (higher than 90%) proved the effectiveness of using DLNNs pre-trained on sonar images for UXO classification. This can be further confirmed by analysing examples of the images that were misclassified.

True Class	Cylinder	Manta	Nonmilco	Spherical
	Cylinder	Manta	Nonmilco	Spherical
	128	2	186	5
	11	20		

Fig. 8. True vs predicted classifications – Shufflenet Confusion Matrix

Man-made objects in sonar images tend to have sharp edges and may be easier to grasp. Therefore, it is not surprising that the greatest errors in classification were made when distinguishing between reference objects, in the form of stones and rocks on the seabed, and Spherical mine types (Fig. 8). Most people also make mistakes when looking at these images. Looking at the processed images on the first convolutional layer, it is clear that the feature selected by the network is similar to what a human would select.

When comparing the networks, it should also be noted that, for some of them, satisfactory results were obtained in a much shorter time, i.e. after 15 epochs out of a total of 30 (Fig. 9).

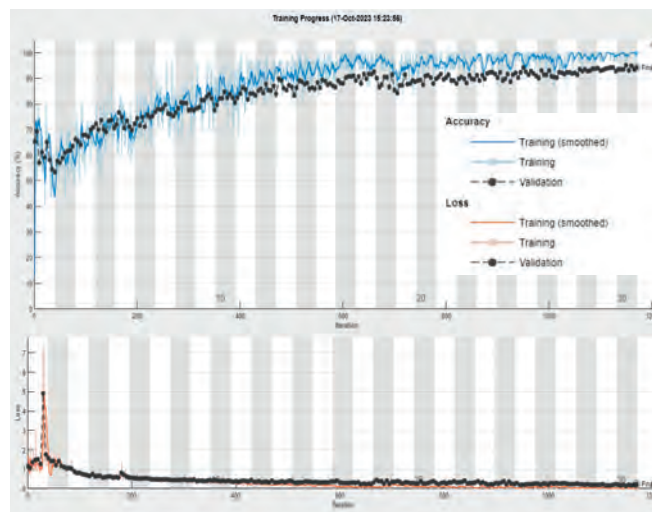


Fig. 9. ResNet101 Training Progress

The results of the research have practical applications in ensuring safety at sea through effective detection and classification of underwater objects, such as mines from World War I and World War II. Given the existing threats on the seabed, effective tools to automatically identify such objects are becoming increasingly important.

CONCLUSION AND FURTHER RESEARCH

The aim of this study was to present the results of a project focused on the use of a pre-trained DLNN for UXO object classification. This project developed a methodology for obtaining the data required to train DLNNs in the specific environment of the Baltic Sea. The authors believe that the results should help other researchers trying to use pre-trained DLNNs and suggest a way to collect data using UUV systems for this process.

These results provide an understanding that the choice of an appropriate DLNN model and data augmentation technique is crucial for the effectiveness of underwater object classification, especially for the classification of UXO objects in sonar images. Models such as 'shufflenet' (accuracy of 96.44%) or 'resnet18' (accuracy of 96.87%) have achieved high accuracy and short average training times, making them promising solutions for the implementation of automatic target recognition (ATR) systems. On the other hand, some models, such as 'vgg16' and 'vgg19', cannot be used effectively in related work, due to their low accuracy and up to ten times longer training times.

Our research provides a starting point for further research. This future research, planned by the authors, will be related to the use of deep networks to detect UXO objects, classify them correctly, identify them with additional sensors and then automatically build a risk map for ships moving in the area, according to the mapping tool shown in Fig. 10.

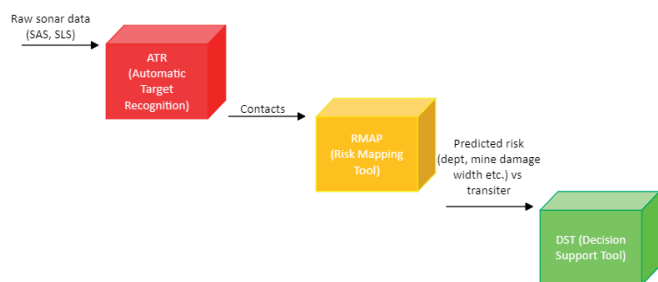


Fig. 10. Risk Mapping Tool for units entering dangerous waters

Considering the difficulty of accessing sonar data for UXO objects, further improvements in models and augmentation techniques will help achieve even better classification results. With the further development of computer vision and machine learning, the future of ATR modules has great potential. The incorporation of deep learning architectures, such as convolutional and recurrent neural networks, can further improve the accuracy and reliability of object recognition. In addition, the fusion of data from multiple sensors, such as combining visual and sonar data, can improve performance in challenging environments.

REFERENCES


1. D. Cireşan, U. Meier, J. Masci, and J. Schmidhuber, „Multi-column deep neural network for traffic sign classification. Neural Networks”, in *The International Joint Conference on Neural Network, IDSIA-USI-SUPSI| Galleria*, 2012, doi:10.1016/j.neunet.2012.02.023.
2. Y. Zhao, M. Qi, X. Li, Y. Meng, Y. Yu, and Y. Dong, „P-LPN: Towards real time pedestrian location perception in complex driving scenes”, *IEEE Access*, t. 8, s. 54730–54740, 2020, doi:10.1109/ACCESS.2020.2981821.
3. E. Byvatov, U. Fechner, J. Sadowski, and G. Schneider, „Comparison of support vector machine and artificial neural network systems for drug/nondrug classification”, *J. Chem. Inf. Comput. Sci.*, t. 43, nr 6, s. 1882–1889, 2003, doi:10.1021/ci0341161.
4. S. Lu, Z. Lu, and Y. Zhang, „Pathological brain detection based on AlexNet and transfer learning”, *J. Comput. Sci.*, t. 30, s. 41–47, 2019, doi:10.1016/j.jocs.2018.11.008.
5. Ø. Midtgaard; R.E. Hansen; P.E. Hagen; and N. Størkersen. “Imaging sensors for autonomous underwater vehicles in military operations”. *Proc.SET-169 Military Sensors Symposium*. Friedrichshafen, Germany, May 2011.
6. HELCOM CHEMU, “Report to the 16th Meeting of Helsinki Commission 8-11 March 1994 from the Ad Hoc Working Group on Dumped Chemical Munition”, *Danish Environ. Protec. Agency*, 1994.
7. J. Fabisiak and A. Olejnik, „Amunicja chemiczna zatopiona w morzu bałtyckim - poszukiwania i ocena ryzyka-projekt badawczy CHEMSEA (Chemical munitions dumped in the Baltic Sea - search and risk assessment- CHEMSEA research project)”, *Pol. Hyperb. Res.*, s. 25–52, 2012.
8. “Sea mines Ukraine waters Russia war Black Sea,” *The Guardian*, 2022. [Online]. Available: www.theguardian.com/world/2022/jul/11/sea-mines-ukraine-waters-russia-war-black-sea. [Accessed: June 21, 2023].
9. “Pretrained Convolutional Neural Networks,” MathWorks, 2023. [Online]. Available: <https://uk.mathworks.com/help/deeplearning/ug/pretrained-convolutional-neural-networks.html>. [Accessed: June 21, 2023].
10. M. Chodnicki; P. Krogulec; M. Żokowski; and N. Sigiel. „Procedures concerning preparations of autonomous underwater systems to operation focused on detection, classification and identification of mine like objects and ammunition”, *J. KONBiN*, t. 48, nr 1, s. 149–168, 2018, DOI: 10.2478/jok-2018-0051.
11. Dowództwo Marynarki Wojennej, „Album Min Morskich” (Naval Command, „Sea Mines Album). Gdynia, Polska: MAR. WOJ., Sep 1947.
12. “Image Colorization Using Generative Adversarial Networks,” Pinterest, 2023. [Online]. Available: <https://www.pinterest.co.uk/pin/145944844154595254/>. [Accessed: Sep. 14, 2023].
13. “SNMCMG1 Photos,” Facebook, 2023. [Online]. Available: <https://www.facebook.com/snmcmg1/photos/a.464547430274739/2304079142988216/>. [Accessed: Oct. 9, 2023].
14. “Pretrained Convolutional Neural Networks,” MathWorks, 2023. [Online]. Available: https://www.mathworks.com/help/deeplearning/ug/pretrained-convolutional-neural-networks.html?searchHighlight=pretrained%20neural%20networks&s_tid=srchtitle_support_results_1_pretrained%2520neural%2520networks. [Accessed: Sep. 14, 2023].
15. P. Szymak, P. Piskur, and K. Naus, „The effectiveness of using a pretrained deep learning neural networks for object classification in underwater video”, *Remote Sens.*, t. 12, nr 18, s. 3020, 2020, DOI:10.3390/rs12183020.
16. “NATO forces clear mines from the Baltic in Open Spirit operation,” NATO, 2021. [Online]. Available: <https://mc.nato.int/media-centre/news/2021/>

nato-forces-clear-mines-from-the-baltic-in-open-spirit-operation. [Accessed: Sep. 14, 2023].

17. F. N. Iandola, S. Han, M. W. Moskewicz, K. Ashraf, W. J. Dally, and K. Keutzer, „SqueezeNet: AlexNet-level accuracy with 50x fewer parameters and < 0.5 MB model size”, *ArXiv Prepr. ArXiv160207360*, 2016.
18. Z. Cui, C. Tang, Z. Cao, and N. Liu, „D-ATR for SAR images based on deep neural networks”, *Remote Sens.*, t. 11, nr 8, s. 906, 2019, doi:10.3390/rs11080906.
19. C. Szegedy, V. Vanhoucke, S. Ioffe, J. Shlens, and Z. Wojna, „Rethinking the inception architecture for computer vision”, in *Proceedings of the IEEE conference on computer vision and pattern recognition*, 2016, s. 2818–2826, doi:10.1109/CVPR.2016.308.
20. G. Huang, Z. Liu, L. Van Der Maaten, and K. Q. Weinberger, „Densely connected convolutional networks”, in *Proceedings of the IEEE conference on computer vision and pattern recognition*, 2017, s. 4700–4708.
21. M. Sandler, A. Howard, M. Zhu, A. Zhmoginov, and L.-C. Chen, „Mobilenetv2: Inverted residuals and linear bottlenecks”, in *Proceedings of the IEEE conference on computer vision and pattern recognition*, 2018, s. 4510–4520, doi:10.1109/CVPR.2018.00474.
22. K. He, X. Zhang, S. Ren, and J. Sun, „Deep residual learning for image recognition”, in *Proceedings of the IEEE conference on computer vision and pattern recognition*, 2016, s. 770–778, doi:10.1109/CVPR.2016.90.
23. F. Chollet, „Xception: Deep learning with depthwise separable convolutions”, in *Proceedings of the IEEE conference on computer vision and pattern recognition*, 2017, s. 1251–1258, doi:10.1109/CVPR.2017.195.
24. K. Nazeri, E. Ng, and M. Ebrahimi, „Image colorization using generative adversarial networks”, in *Articulated Motion and Deformable Objects: 10th International Conference, AMDO 2018, Palma de Mallorca, Spain, July 12-13, 2018, Proceedings 10*, Springer, 2018, s. 85–94, doi: 10.1007/978-3-319-94544-6_9.
25. X. Zhang, X. Zhou, M. Lin, and J. Sun, „Shufflenet: An extremely efficient convolutional neural network for mobile devices”, in *Proceedings of the IEEE conference on computer vision and pattern recognition*, 2018, s. 6848–6856, doi:10.1109/CVPR.2018.00716.
26. B. Zoph, V. Vasudevan, J. Shlens, and Q. V. Le, „Learning transferable architectures for scalable image recognition”, in *Proceedings of the IEEE conference on computer vision and pattern recognition*, 2018, s. 8697–8710, doi:10.1109/CVPR.2018.00907.
27. O. Russakovsky; J. Deng; H. Su; J. Krause; S. Satheesh; S. Ma; Z. Huang; A. Karpathy; A. Khosla; M. Bernstein et al. „Imagenet large scale visual recognition challenge”. *Int. J. Comput. Vis.*, t. 115, s. 211–252, 2015, doi:10.1007/s11263-015-0816-y.
28. K. Simonyan and A. Zisserman, „Very deep convolutional networks for large-scale image recognition”, *ArXiv Prepr. ArXiv14091556*, 2014.
29. W. Wu, L. Guo, H. Gao, Z. You, Y. Liu, and Z. Chen, „YOLO-SLAM: A semantic SLAM system towards dynamic environment with geometric constraint”, *Neural Comput. Appl.*, s. 1–16, 2022, doi:10.1007/s00521-021-06764-3.
30. Ü. Atila, M. Uçar, K. Akyol, and E. Uçar, „Plant leaf disease classification using EfficientNet deep learning model”, *Ecol. Inform.*, t. 61, s. 101182, 2021, doi:10.1016/j.ecoinf.2020.101182.

INVESTIGATING FUEL INJECTION STRATEGIES TO ENHANCE SHIP ENERGY EFFICIENCY IN WAVE CONDITIONS

Hossein Ghaemi  ^{1*}

Hamid Zeraatgar  ²

Mojtaba Barjasteh  ²

¹ Gdansk University of Technology, Institute of Naval Architecture, Poland

² Amirkabir University of Technology, Faculty of Maritime Technology, Iran

* Corresponding author: wugang@shmtu.edu.cn (H. Ghaemi)

ABSTRACT

The prediction of fuel consumption and resulting transportation costs is a crucial stage in ship design, particularly for conditions involving motion in waves. This study investigates the real-time fuel consumption of a container ship when sailing in waves. The overall ship performance is evaluated using a novel non-linear coupled hull-engine-propeller interaction model. A series of towing tank experiments for hull resistance in waves and propeller performance are conducted. The ship engine is mathematically modelled by a quasi-steady-state model equipped with a linear Proportional-Integrator (PI) governor. Various scenarios of shipping transportation are studied, and the resulting instantaneous fuel consumptions and their correlation to other dynamic particulars are demonstrated. Additionally, daily fuel consumption and fuel cost per voyage distance are presented. It is also shown that the controller can effectively adjust the fuel rate, resulting in minimum fuel consumption. The study concludes that there is no correlation between fuel consumption and the frequency of fuel rates. The present framework and mathematical model can also be employed for ship design and existing ships to predict the total required energy per voyage.

Keywords: Fuel consumption, Energy efficiency, Hull-Engine-Propeller interaction, Ship engine dynamics, Added resistance, Sea wave

INTRODUCTION

More than 80 per cent of all goods transferred are carried over the seas [1]. This results in the consumption of millions of tonnes of fuel every year, costing several million dollars. Higher levels of fuel consumption lead to more gas emissions. Additionally, the expense of shipping is generally governed by the fuel cost for large ships [2]. Therefore, accurate estimates of ship fuel consumption are required. Researchers widely investigate the prediction and reduction of ship fuel consumption. Generally, various methods can be categorized into three distinctive models consisting of white-box models (WBM), black-box models (BBM), and grey-box models

(GBMs) [3]. In WBMs, or deterministic models, all parameters or determinants are known in advance. The most important parameters are hull resistance, characteristics of the propulsion system, weather conditions, and engine performance [4]. In contrast, BBMs, or machine learning models, are based on the onboard measurement of data during voyages. The system trains on data and becomes more precise with increased data input [5]. The primary apparatus of these models (WBMs and BBMs) is an artificial neural network [6]. The GBMs use some known parameters and start training with data recorded onboard, but are usually established on a statistical approach [7].

The fuel consumption of any vessel is dependent on all its operational parameters, such as ship speed, hull resistance,

draft, trim, loading condition, weather, and sea condition [8]. Once an accurate estimation of fuel consumption is acquired, different methods to reduce this consumption can be investigated. Shipping companies concentrate on two separate methods of reducing fuel consumption, either the design of new ships or retrofitting and operational techniques for existing ships. [9]. The former method, which requires more investment, investigates hulls with lower drag, lighter materials, hybrid engines with improved performance, etc. This method certainly has a stronger contribution to the reduction of fuel consumption compared to operational techniques for existing ships. However, this comes at a higher expense [10]. The latter method is available for all ships which are already built and come at a lower price. This method of reducing fuel consumption does not introduce any major modifications in the main ship systems and mostly emphasizes the optimal use of fuel onboard and voluntary and involuntary speed loss. These techniques include but are not limited to, slow steaming [11], weather routing [12], optimized speed [13], trim optimization [14], and voyage optimization [4]. Using these techniques usually increases the shipping time but reduces fuel consumption. The ship owner should always make a balance between shipping time and consumed fuel in total shipping expenditures. Moreover, there are other criteria, for example, general strength, that should be combined with energy efficiency to select the final solution [15].

Engine dynamics also have a significant impact on fuel consumption. Larsen et al. [16] investigated different configurations of two-stroke, diesel-based machinery systems for large ships. They used uncoupled analytical models of the ship's subsystems, such as engine dynamics, propulsion system, and hull resistance. Yin et al. [17] designed an accurate real-time fuel consumption monitoring system based on the engine speed, its power, and the ship speed. A correlation between generated power and consumed fuel was established. A similar interesting study was also carried out by Sandvik et al. [18], with the results of their simulation found to be in reasonable agreement with onboard full-scale measurement of a cargo ship. Different determinants involving engine dynamics, fuel consumption, speed, position, and wind speed are measured on this ship. Degiuli et al. [19] showed that fuel consumption is increased for a container ship as a function of different speeds and wave frequencies. Engine or propeller dynamics were not included in this study. Tilling and Ringsberg [20] employed a 4-DOF (surge, drift, yaw and heel) model for the prediction of fuel consumption, which considers added resistance. The proposed model incorporates important determinants, but not as a coupled system. It is worth mentioning that the fuel pre-injection and injection processes and systems also have a significant influence on fuel consumption, particularly in unsteady states [21-23].

Most of the mentioned studies cannot simulate the ship dynamics and sea conditions as an integrated system. Thus, the suggested models cannot be easily studied if one of the determinants is changed or generalized for use in other ships. Therefore, their applications are restricted and are also difficult

to develop further. To remove this weakness, the present research focuses on establishing a white-box, or deterministic, model, for the prediction of fuel consumption in displacement ships, with a further goal of reducing this fuel consumption to meet the UN's sustainability goals (items 7, 12, and 13) [1]. The ship dynamics and sea conditions are simulated through a non-linear coupled hull-engine-propeller interaction model and all influencing parameters are investigated simultaneously. Ship motion in waves is of more importance due to higher resistance and therefore higher fuel consumption, rather than motion in calm waters.

FORMULATION

The main determinants in this study are hull geometry, engine dynamics, propeller performance, and sea conditions. Although it is complicated to capture this coupled problem in an exact manner, it can be presented with some assumptions [24] using the following 1-DOF (surge) system of equations:

$$\begin{cases} T_n(t) - R_C(u(t)) - R_A(u(t)) = (\Delta + x_{ii})\dot{u}(t) \\ Q_E(t) - Q_P(t) = (I_P + I_{Pa} + I_E + I_S)\dot{\omega}(t) \end{cases} \quad (1)$$

where R_C , R_A , T_n , Δ , and x_{ii} are the total ship resistance in calm water, as a function of surge speed, $u(t)$; mean added resistance; net generated thrust; ship mass; and the ship added mass, respectively. The second equation is the engine-propeller interaction stated as the law of angular motion where $Q_E(t)$, $Q_P(t)$, I_P , I_{Pa} , I_E , I_S , and ω are the delivered engine torque; required propeller torque; propeller moment of inertia; propeller added moment of inertia; engine moment of inertia; shaft moment of inertia; and shaft angular speed, respectively. The proposed system of equations introduces five sets of determinants:

1. Ship resistance (both in calm water and sea waves);
2. Propeller characteristics (thrust and torque);
3. Engine dynamics (torque, angular velocity, and controller);
4. Vessel specifications (moments of inertia, mass, and added mass);
5. Ship dynamics (surge speed).

All of these determinants are time-dependent variables, excluding vessel specifications. Thus, the solution of this system of equations results in instantaneous ship response.

SHIP RESISTANCE

When ships sail in waves, the total resistance increases by up to 15–30% compared with calm water sailing [25]. The added resistance considerably influences the ship's motion and its attainable speed, resulting in an increased power requirement and higher fuel consumption. The proposed governing system of equations are capable of estimating additional fuel consumption due to added resistance. The ship resistance in calm waters can be computed using different formulas, such as those recommended by International Towing Tank Conference (ITTC). However,

the calculation of the added resistance is not straightforward because of its dependency on several influencing parameters, such as ship speed, hydrostatic trim, wave frequency, heading angle, wave period, draft, radii of gyration, etc.

To obtain an accurate estimation of added resistance, a series of model test experiments are conducted in a towing tank for a Series 60 with $C_B = 0.6$. The added resistance of the model is computed with a known value of calm water resistance using the following equation:

$$R_{Am}(t) = R_{Tm}(t) - R_{Cm}(t) \quad (2)$$

and usually presented as time-averaged added resistance, \hat{R}_{Am} , or mean added resistance:

$$\hat{R}_{Am} = \frac{1}{\Delta T} \int_{t_1}^{t_2} R_{Am} dt \quad (3)$$

Here, the subscripts A , m , T , and C stand for the added resistance; model; the total resistance; and calm water resistance, respectively. The full-scale ship added resistance is related to the measured value for model by applying Froude's law of similitude:

$$R_{As}(t) = \lambda^3 \times R_{Am}(t) \quad (4)$$

Hence, R_{As} and λ are the ship added resistance and model length scale, respectively. Table 1 indicates the setup of the model tests.

Tab. 1. Configuration of the model test experiments

Model specification			
Hull offset	C_B	LOA	λ
Series 60	0.6	4.57 m	1:40
Wave dynamics			
Heading	Height	Period	Length
180 deg	8 cm	1.6 sec	4.0 m

The dominant parameter in added resistance studies is the characteristic wavelength, which is defined as the ratio of the wavelength to the ship length. In practice, this is about 0.8–1.1 for long waves [26]. This non-dimensional length is set to $\lambda/L = 4/4.57 = 0.88$ for the present experiments. Resistance, heave and pitch motions, and wave profile are recorded in each run. The measured data is scaled using the law of similarity for a real full-scale ship with the main particulars presented in Table 2.

Tab. 2. Main particulars of the full-scale ship

LOA	Beam	Draft	C_B	Speed	∇
182.9 [m]	24.4 [m]	9.8 [m]	0.6	23.8 [Kn]	26245.4 [m ³]

Fig. 1 depicts the calm water resistance and time history of the added resistance for the fullscale ship, scaled from the measured data with a length scale of 1:40.

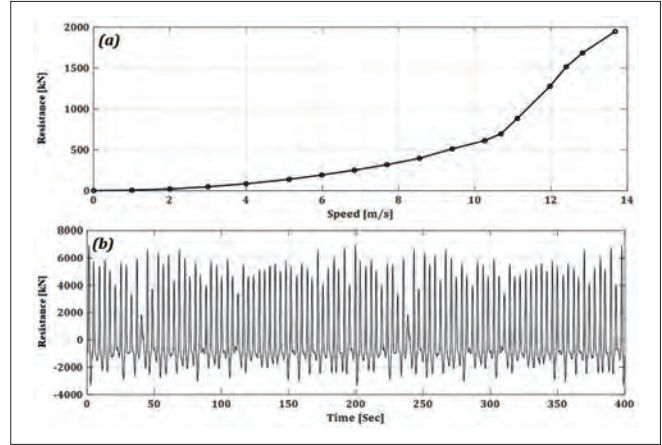


Fig. 1. Full-scale ship resistance, (a) variation of calm water resistance at different surge speeds, (b) time history of the added resistance

PROPELLER CHARACTERISTICS

Additional important determinants are the propeller dynamics, including shaft angular velocity; propeller thrust; and propeller torque. A series of experiments has been conducted for the measurement of the open water performance of the selected propeller. The selected propeller is a fully submerged 5-blade B-Wageningen with a diameter of 25 cm. The experimental setup and measured characteristics are shown in Fig. 2.

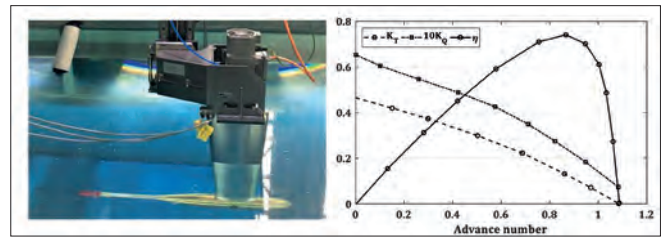


Fig. 2. Propeller open water performance, experimental setup and measured data

The thrust coefficient, K_T , torque coefficient, K_Q , and open water performance, η_0 , are measured for different advance numbers, J_P . Table 3 introduces the geometrical specification of the full scaled propeller based on the selected length scale of 1:40.

Tab. 3. Specification of full-scale propeller

Geometry	Type	Diamete	Blades	Area ration	Pitch ration
B-Wageningen	FPP	7.6 m	5	0.58	1.00

To compute the generated thrust of the full-scale propeller, the required torque, and corresponding efficiency, one can use the following set of equations:

$$T_n = (1 - t) K_T \rho \omega_p^2 D_P^4 \quad (5)$$

$$Q_P = K_Q \rho \omega_p^2 D_P^5 \quad (6)$$

calculated at different advance numbers, J_P ,

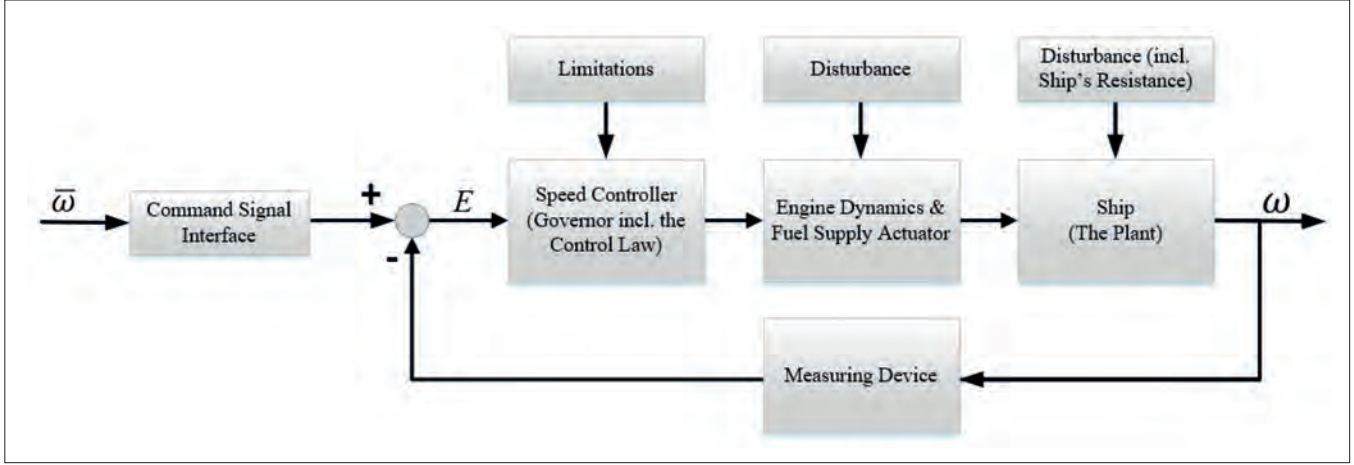


Fig. 3. Controller block diagram

$$J_P = \frac{u(1-w)}{\omega_P D_P} \quad (7)$$

$$\frac{Q_E(S)}{X_f(S)} = \frac{K_E}{1+T_E S} e^{-\tau S} \quad (11)$$

Here, t and w are thrust deduction and wake fraction factors, respectively.

ENGINE DYNAMICS

The key set of determinants in this research are the diesel engine dynamics. The dynamics of marine diesel engines has been studied using different models with various levels of detail, such as zero-dimensional, steady-state delayed response, mean value first principle (MVFP), and discrete-events models (DEM) [27, 28]. A complete understanding of the diesel engine performance needs adequate knowledge of the in-cylinders thermodynamic processes. However, once the diesel engine is investigated as a subsystem of a larger system, i.e. in a ship, an in-cylinder model is neither practical nor necessary due to unsatisfactory real-time capability and inappropriate adaptability with the unsteady operating conditions [29]. Quasi-steady delayed engine dynamics are employed in this study, which is governed by the following differential equation [30]:

$$T_E \dot{Q}_E(t - \tau) + Q_E(t - \tau) = K_E X_f(t) \quad (8)$$

where T_E , τ , K_E , and X_f are engine time constant; response delay; gain factor; and fuel flow rate in kg/s, respectively. The time constant reflects the inertial behaviour of the engine for generating torque after receiving the necessary fuel for combustion and is approximated as 90% of the time between two successive ignitions in one cylinder.

$$T_E = 0.9 \cdot \frac{2\pi}{\omega_E} \quad (9)$$

The time delay is determined as half of the time needed for two successive ignitions:

$$\tau = \frac{1}{2} \cdot \frac{2\pi}{Z_E \omega_E} \quad (10)$$

where ω_E and Z_E are angular shaft velocity and the number of engine's cylinders, respectively. The transfer function of the engine dynamics is directly used in the speed control system.

The recommended model requires that the time constant of the engine is higher than the time constant of the exciting force fluctuation, e.g. added resistance. Therefore, the engine can be effectively simulated using this quasi-steady model and can be directly included in a general system of equations as follows:

$$\begin{cases} T_n(t) - R_C(u(t)) - R_A(u(t)) = (\Delta + x_{ii})\dot{u}(t) \\ Q_E(t) - Q_P(t) = (I_P + I_{Pa} + I_E + I_S)\dot{\omega}(t) \\ T_E \dot{Q}_E(t - \tau) + Q_E(t - \tau) = K_E X_f(t) \end{cases} \quad (12)$$

Regarding the selected full-scale ship and the corresponding propeller, a MAN-B&W 8S65ME-C8.5 low-speed diesel engine is chosen as the prime mover with a Service Maximum Continuous Rating (SMCR) of 19,433 kW at 92.8 RPM. The steady state specification of the selected engine is publicly accessible [24].

Controller implementation

Engines exhibit an immediate response as feedback of any changes in the rate of injected fuel, even for rapid and small changes. Thus, the primary component which controls diesel engines is the fuel rate. The fuel rate in diesels engines is controlled using different techniques, but primarily with speed governors. The selected engine in the present study is also assumed to be equipped with a governor. Different control strategies are available for controlling the diesel engine. Captains usually prefer to maintain a constant shaft speed while sailing. Thus, the controller is designed based on this strategy, with a schematic of the control system block diagram shown Fig. 3.

The controller receives a set-point signal which is defined as the shaft speed corresponding to the steady state operating condition of the engine, $\bar{\omega}$. This set-point forces the engine to continuously operate at its Maximum Continuous Rating (MCR) condition regardless of the sea conditions. The controlled signal, ω , is the instantaneous shaft speed and is designed as the feedback signal. Thus, the error signal, E , is defined as

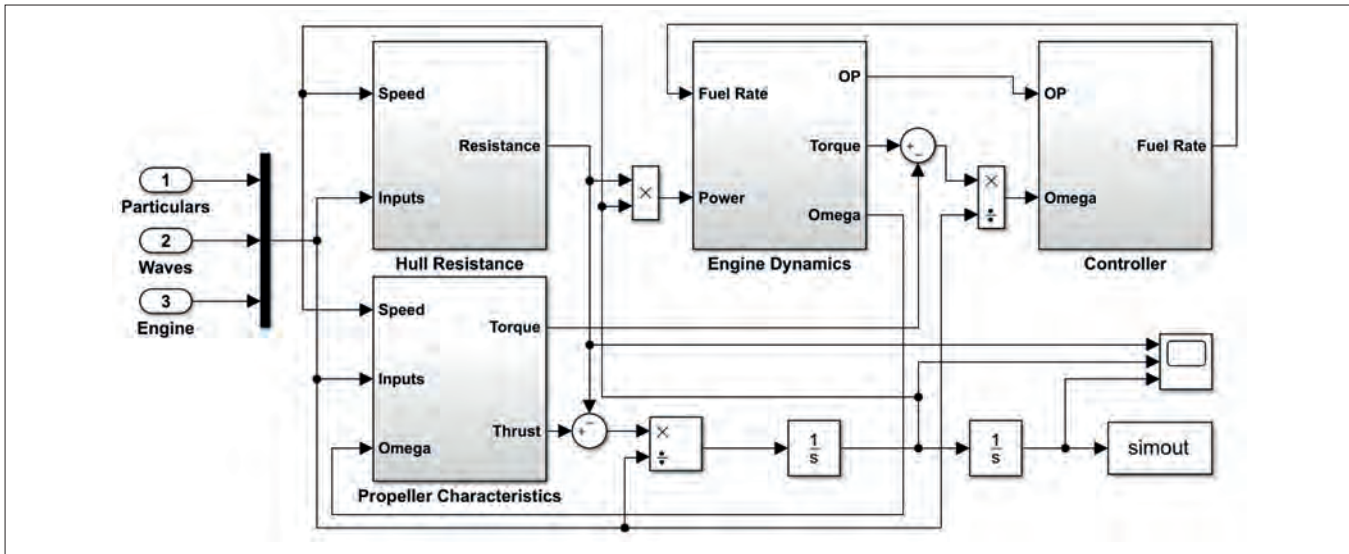


Fig. 4. Block diagram of the whole ship system established in Simulink

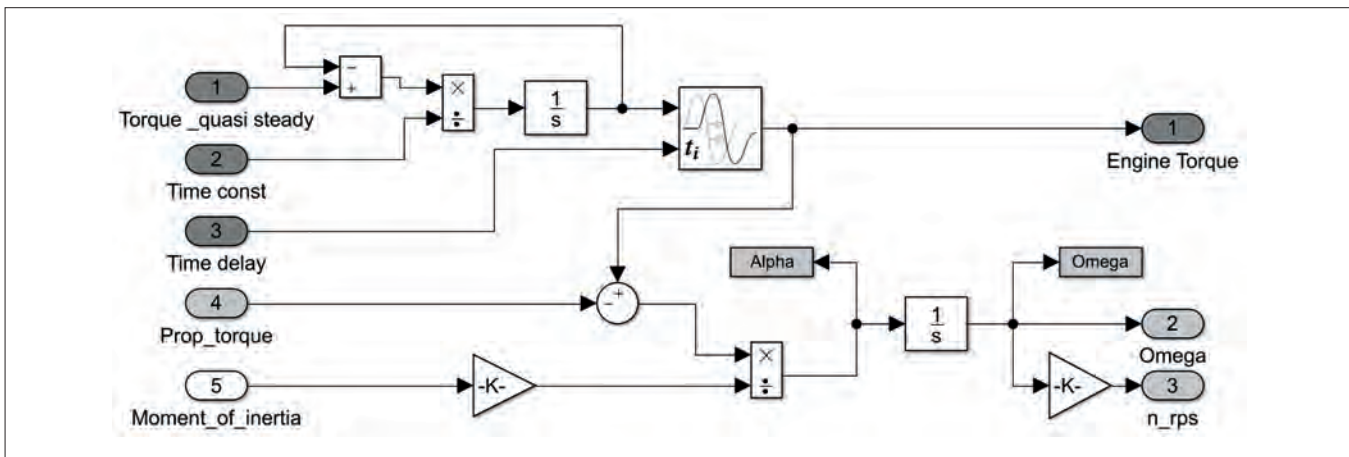


Fig. 5. The internal subsystem of computing unsteady engine dynamics

$$E = \bar{\omega} - \omega \quad (13)$$

The obtained error signal is then amplified and filtered for noise reduction. The processed error signal is fed into the speed governor. The present governor is modelled as a proportional-integral type (PI-action) controller based on the concept of the common diesel engine governors [31]. A proportional-integral-derivative (PID) block with zero derivation gain is employed for the simulation of the governor's performance. The proportional and integrator gains are tuned using a varied Ziegler-Nichols method [32] to account for different sailing scenarios. The output of the governor block is the instantaneous fuel rate of the engine. According to this produced fuel rate signal, the engine performance is adapted for reducing the error signal at each time step. To simulate the ship performance as an integrated system in general, other subsystems apart from the engine and its controller should also be modelled. These subsystems involve the hull resistance, propeller characteristics, and the interconnecting signals. The architecture of the subsystems and the coupling techniques are determined using the governing system of equations and related subsystem formulas as depicted in control block diagram of Fig. 4.

The ship resistance and propeller characteristics are evaluated using given data at the current time step. These characteristics stand as the initial conditions for estimation of the engine dynamics. The results are specified as the input signals of the controller. The controller computes the required fuel rate based on the value of input and error signals. Once the fuel rate is computed by the controller, this rate is fed back to the engine. This loop continues at each time step to reach a converged result. Computation of the engine torque is performed at two other subsystems defined as "Engine Dynamics" shown in Fig. 4. At the first step, the steady torque of the engine, e.g. quasi-steady torque, is interpolated from the engine steady-state performance. This quasi-steady torque is then called by another internal subsystem to evaluate its unsteady value based on Eq. (10) as depicted in Fig. 5.

RESULTS AND DISCUSSIONS

To investigate the performance of the governor, two simulations were conducted. The first involved activating the governor so the fuel rate is determined by the controller and

in the second the governor was deactivated with manually forced fuel rates.

GOVERNOR ACTIVATED

The simulations are systematically carried out for separate scenarios, as summarized in Table 4. Fig. 6 indicates the results of the simulations for Scenarios #1 and #3.

Tab. 4. Different scenarios of fuel consumption at the present study

Scenarios	Sea conditions	Engine operating point (OP)	Objective
#1	Calm	100%	Max. speed
#2	Calm	10%~100%	Ship performance
#3	Calm-Waves	100%	Sailing in waves
#4	Calm-Waves-Calm	100%	Controller response
#5	Calm-Waves-Calm	80% in waves	Speed reduction
#6	Calm-Waves-Calm	Varies	Sustain speed
#7	Calm	Varies	Max. acceleration
#8	Waves	Varies	Governor performance

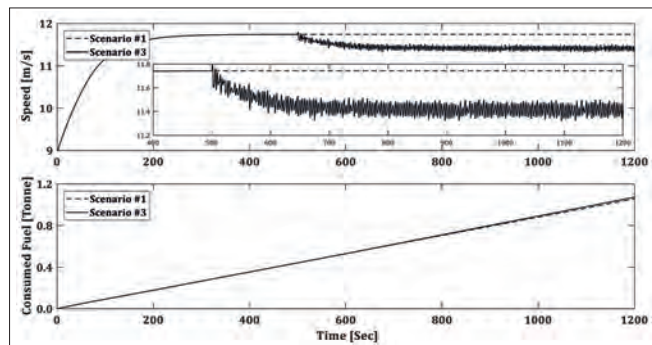


Fig. 6. The overall ship response for scenarios #1 and #3

In the first scenario indicated by the dashed line in Fig. 6, the ship starts with an initial speed of 8.9 m/s and attains a steady state speed of 11.7 m/s. More than 95% of this speed increase occurs in the first 200 seconds. This is clear evidence of the controller performance. The ship consumes about 1.1 tonnes of fuel at the rate of 0.88 kg/s, i.e., 76 MT/day. The ship meets the waves at a speed of 11.74 m/s in the third scenario after 500 seconds of sailing in the calm waters and the speed reduces to 11.4 m/s 300 seconds later. This speed reduction is called involuntary speed reduction. Fuel consumption is essentially identical in both scenarios because of the identical OPs. Fig. 7 shows the results obtained from Scenario #2 when investigating ship performance under different operating conditions.

The ship speed decreases from 11.7 m/s to 6.1 m/s when the operation point reduces from 100% to 10%. Furthermore, the engine power and shaft speed reduce from 19 MW to 1.9 MW and 92.8 RPM to 43.1 RPM, respectively. Fig. 8 illustrates the performance of the engine at different operating conditions.

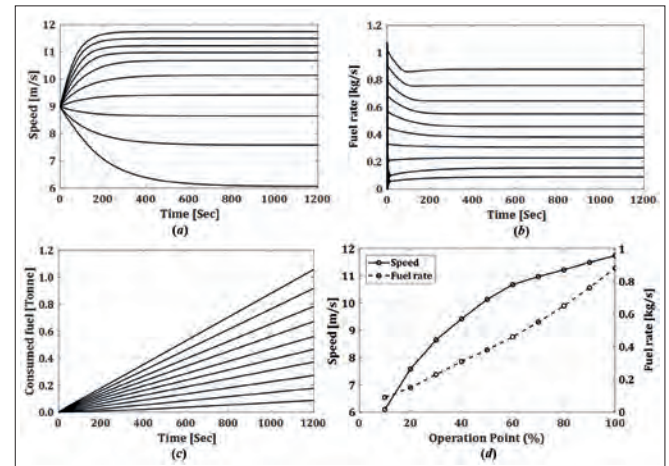


Fig. 7. Overall ship performance for different engine operating points. a) time history of ship speed, b) instantaneous fuel rate, c) overall consumed fuel, and d) variation of ship speed and fuel rate versus different operating points. The operating points reduce from 100% to 10% downward in figures a, b, and c

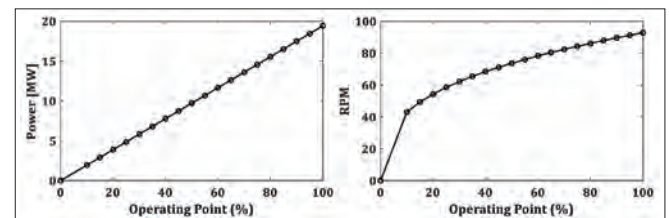


Fig. 8. Engine performance at its different operating points

Fig. 9. shows the response of the controller for different sea conditions in the fourth scenario. The results show that the speed of the ship before and after the waves is the same, indicating the successful trace of different sea conditions by the controller.

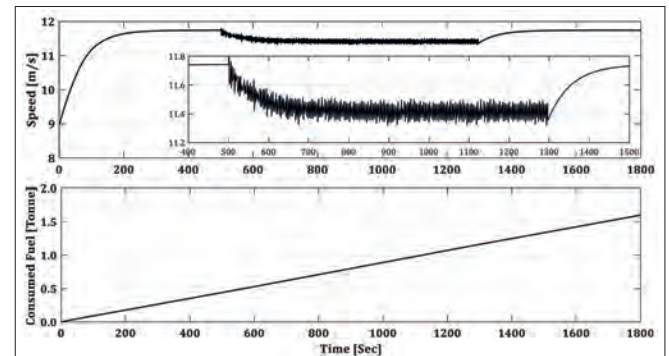


Fig. 9. Controller response for different conditions studied in Scenario #4

The stimulated structural load on the ship hull during sailing in waves is a function of the ship speed. Therefore, captains commonly decide to decrease the ship speed in waves, usually between 0.5 to 4 knots slower than the service speed, in a process known as voluntary speed reduction. This prevents excess loads on the hull. Scenario #5 studies a 20% reduction in engine operating point once the ship encounters waves which cause a 0.5 m/s speed reduction, as shown in Fig. 10. To compare the performance of the controller between Scenarios #3 and #5, the fuel rates are also reported. The patterns of both rates are similar but with different magnitudes.

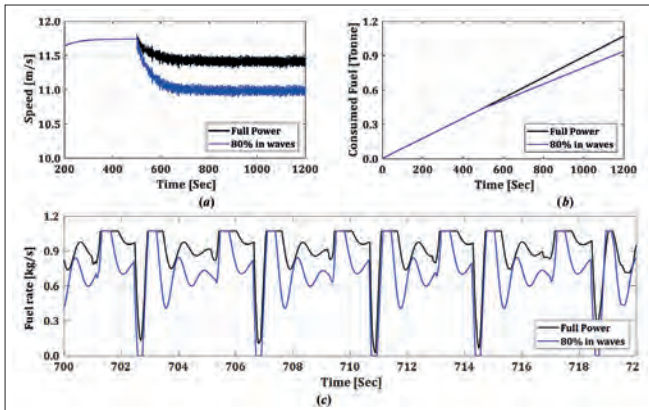


Fig. 10. Simulation results of Scenario #5 defined as voluntary speed reduction in waves compared with the results of Scenario #3. a) Ship speed, b) consumed fuel, and c) fuel rates reported for a typical interval of 20 seconds

In Scenario #6 the ship is initially moving in calm waters and then in waves. The controller's mission is to increase the operating point so that the ship's speed is constant across travelling in waves and in calm waters, as presented in Fig. 11. This shows that the ship speed can be sustained by increasing the engine power by just 4%.

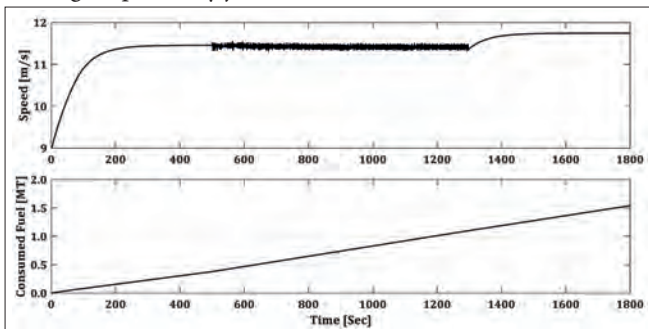


Fig. 11. Sustaining the ship speed in waves introduced in Scenario #6

Fig. 12 shows the simulation results for Scenario #7. Two separate accelerating and decelerating manoeuvres with the same extremums are defined. The results show that the ship speed increased from 6.1 to 11.74 m/s in 300 seconds with an acceleration of about 0.02 m/s². However, the ship deceleration takes three times longer with a deceleration of about 0.006 m/s². This scenario is a classic study of a controller response to a step function.

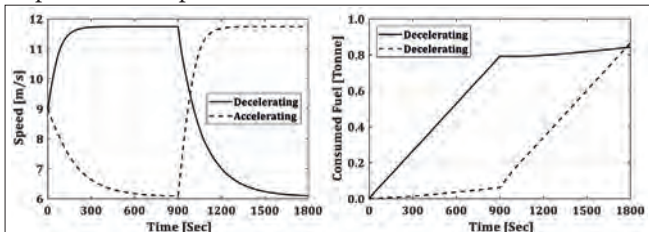


Fig. 12. Evaluation of the ship performance in successive accelerating motions

The voyage distance for different scenarios can be used for the estimation of fuel consumption as a function of travelled distance, which is defined by the parameter Γ and is depicted in Fig. 13. Once the fuel price per unit volume and the voyage distance are known, the crucial fuel cost of shipping can be readily estimated.

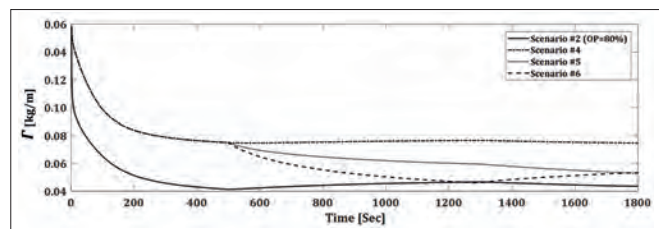


Fig. 13. Instantaneous values of Γ for different shipping scenarios

GOVERNOR DEACTIVATED

The governor is deactivated in the second series of the results. The fuel rates are set to predefined profiles to find any possible reduction in fuel consumption while moving in waves. These rates include constant, sinusoidal, and square rates. Fig. 14 displays the first attempt. Here, the fuel rate is defined as a constant function, with the time averaged rate of 0.902 kg/s used, as obtained from Scenario #4. The solver uses this rate as an initial value and changes it to find the same ship speed in waves. Fig. 15 depicts the results of this simulation via the reported fuel rates. The solver finds the constant value of 0.905 kg/s to attain the same speed, namely 0.4% more than timeaveraged value.

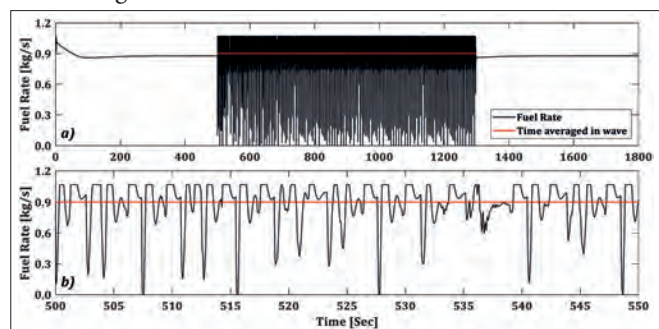


Fig. 14. a) Instantaneous fuel-rate for scenario #4 and its time averaged in waves, b) the magnified view

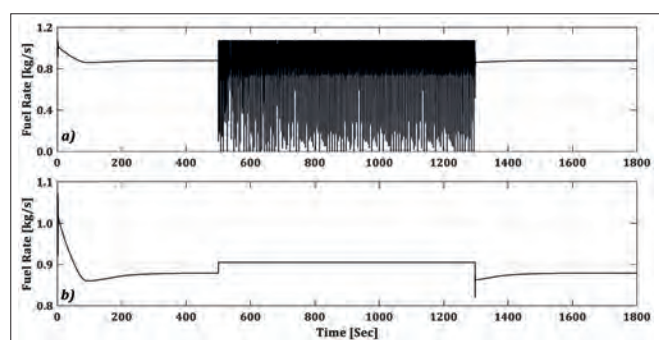


Fig. 15. Comparison of fuel rates, a) controlled by governor, b) forced constant rate

The results show that the governor can be completely turned off during motion in waves. However, it is crucial to note that this does not imply that the controller can be removed from the system. Without a proper controller, the fuel consumption is dramatically increased under different ship operating conditions. A synchronized presentation of the fuel rate and the total resistance is illustrated in Fig. 16. Once the controller finds any local oscillation in the resistance, it immediately changes

the fuel rate to keep the propeller shaft speed constant. The controller responds to the resistance excitation with a very short time delay, as defined by Eq. (12).

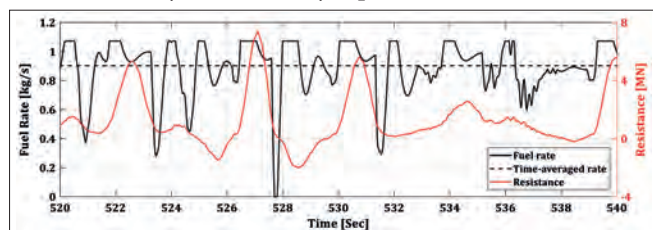


Fig. 16. Synchronized representation of time histories of the fuel rate computed by the controller and the total resistance

Other rates with sinusoidal and square behaviour are also generated with the same peaks and the same time-averaged rate according to those shown in Fig. 14. However, different frequencies are used to find any possible correlation between the fuel consumption and the frequencies, as presented in Fig. 17. The computed fuel consumption is normalized using the steady state fuel consumption that is evaluated at the end of motion in waves in scenario #4, defined as η . It is shown that there is no correlation between these parameters.

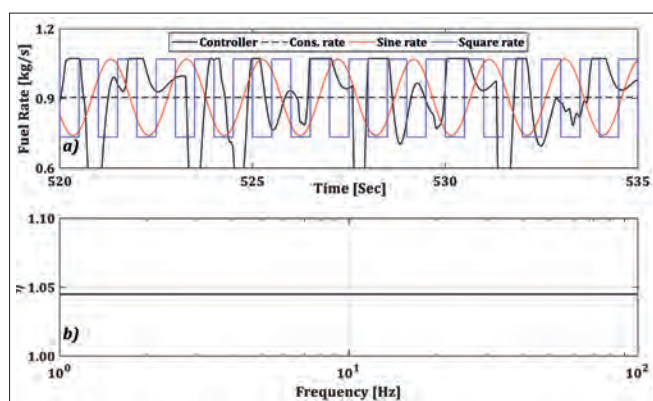


Fig. 17. Different forced fuel rates, a) Typical fuel rate profiles, b) normalized fuel consumption for forced periodic fuel rates with different frequencies

CONCLUSION

The overall ship performance, particularly real-time fuel consumption, is investigated using a new hull-engine-propeller interaction model under different sea conditions. Various voyage scenarios are studied to identify any correlation between fuel consumption and ship dynamics. The results show that the employed controller successfully responds to different challenging scenarios with reasonable performance. Additionally, the benefit of a constant forced fuel rate is illustrated in comparison with the high oscillating response of the governor during motion in waves. Voluntary and involuntary ship speed reductions in waves are introduced, and it is concluded that the proposed model can accurately simulate such speed reductions. Moreover, the capability of the recommended model and simulation framework to predict the instantaneous and total cost of consumed fuel per voyage is also noted. This work offers a practical tool which can be

utilized in all stages of ship design and can be implemented to help manage the energy efficiency of existing ships.

REFERENCES


1. United Nations, "UN Handbook of Statistics." Geneva, 2021.
2. Y. Du et al., "Two-phase optimal solutions for ship speed and trim optimization over a voyage using voyage report data," *Transportation Research Part B*, vol. 122, pp. 88-114, 2019, doi: 10.1016/j.trb.2019.02.004.
3. Coraddu et al., "Vessels fuel consumption forecast and trim optimisation: A data analytics perspective," *Ocean Engineering*, vol. 130, pp. 351-370, 2017, doi: 10.1016/j.oceaneng.2016.11.058.
4. R. Lu, O. Turan, E. Boulougouris, C. Banks, and A. Incecik, "A semi-empirical ship operational performance prediction model for voyage optimization towards energy efficient shipping," *Ocean Engineering*, vol. 110, pp. 18-28, 2015, doi: 10.1016/j.oceaneng.2015.07.042.
5. L. Þ. Leifsson, H. Sævarsdóttir, S. Þ. Sigurðsson, and A. Vésteinsson, "Grey-box modeling of an ocean vessel for operational optimization," *Simulation Modelling Practice and Theory*, vol. 16, no. 8, pp. 923-932, 2008, doi: 10.1016/j.simpat.2008.03.006.
6. P. Karagiannidis and N. Themelis, "Data-driven modelling of ship propulsion and the effect of data pre-processing on the prediction of ship fuel consumption and speed loss," *Ocean Engineering*, vol. 222, 2021, doi: 10.1016/j.oceaneng.2021.108616..
7. L. Yang et al., "A genetic algorithm-based grey-box model for ship fuel consumption prediction towards sustainable shipping," *Annals of Operations Research*, pp. 1-27, 2019, doi: 10.1007/s10479-019-03183-5.
8. H. Lee et al., "A decision support system for vessel speed decision in maritime logistics using weather archive big data," *Computers & Operations Research*, vol. 98, pp. 330-342, 2018, doi: 10.1016/j.cor.2017.06.005.
9. Y. Denev, "Retrofitting the Bow of a General Cargo Vessel and Evaluating Energy Efficiency Operational Index," *Polish Maritime Research*, vol. 30, no. 4, pp. 17-23, Dec. 2023, doi: 10.2478/pomr-2023-0054.
10. F. Tillig et al., "A generic energy systems model for efficient ship design and operation," *Proceedings of the Institution of Mechanical Engineers, Part M: Journal of Engineering for the Maritime Environment*, vol. 231, pp. 649-666, 2017, doi: 10.1177/1475090216680672.


11. P. Gusti et al., "Reduction in ship fuel consumption and emission by sailing at slow speeds," *Journal of Engineering Science and Technology*, vol. 14, no. 6, pp. 3267–3281, 2019.
12. R. Vettor and C. G. Soares, "Development of a ship weather routing system," *Ocean Engineering*, vol. 123, pp. 1–14, 2016, doi: 10.1016/j.oceaneng.2016.06.035.
13. S. Wang and X. Wang, "A polynomial-time algorithm for sailing speed optimization with containership resource sharing," *Transportation Research Part B: Methodological*, vol. 93, pp. 394–405, 2016, doi: 10.1016/j.trb.2016.08.003.
14. L. P. Perera, B. Mo, and L. A. Kristjánsson, "Identification of optimal trim configurations to improve energy efficiency in ships," in *10th IFAC Conference on Manoeuvring and Control of Marine Craft*, 2015, pp. 267–272.
15. O. Kanifolskyi, "General Strength, Energy Efficiency (EEDI), and Energy Wave Criterion (EWC) of Deadrise Hulls for Transitional Mode," *Polish Maritime Research*, vol. 29, no. 3, pp. 4–10, Sep. 2022, doi: 10.2478/pomr-2022-0021.
16. U. Larsen et al., "Development of a model for the prediction of the fuel consumption and nitrogen oxides emission trade-off for large ships," *Energy*, vol. 80, pp. 545–555, 2015, doi: 10.1016/j.energy.2014.12.009.
17. Q. Yin et al., "Design of a real-time ship fuel consumption monitoring system with self-checking function," in *4th International Conference on Transportation Information and Safety*, Banff, Canada, 2017, pp. 735–738.
18. E. Sandvik et al., "Estimation of fuel consumption using discrete-event simulation - a validation study," in *Marine Design XIII*, P. Kujala, Ed., Helsinki: CRC Press, 2018.
19. N. Degiuli et al., "Increase of Ship Fuel Consumption Due to the Added Resistance in Waves," *Sustainable Development of Energy, Water and Environment Systems*, vol. 5, no. 1, pp. 1–14, 2017, doi: 10.13044/j.sdewes.d5.0129.
20. F. Tilling and J. W. Ringsberg, "A 4 DOF simulation model developed for fuel consumption prediction of ships at sea," *Ships and Offshore Structures*, 2018.
21. C. G. Rodriguez, M. I. Lamas, J. D. Rodriguez, and A. Abbas, "Analysis of the Pre-Injection System of a Marine Diesel Engine Through Multiple-Criteria Decision-Making and Artificial Neural Networks," *Polish Maritime Research*, vol. 28, no. 4, pp. 88–96, Jan. 2022, doi: 10.2478/pomr-2021-0051.
22. R. Varbanets et al., "Concept of Vibroacoustic Diagnostics of the Fuel Injection and Electronic Cylinder Lubrication Systems of Marine Diesel Engines," *Polish Maritime Research*, vol. 29, no. 4, pp. 88–96, Dec. 2022, doi: 10.2478/pomr-2022-0046.
23. Q. Shi, Y. Hu, and G. Yan, "Hierarchical Multiscale Fluctuation Dispersion Entropy for Fuel Injection System Fault Diagnosis," *Polish Maritime Research*, vol. 30, no. 1, pp. 98–111, Mar. 2023, doi: 10.2478/pomr-2023-0010.
24. M. H. Ghaemi and H. Zeraatgar, "Analysis of hull, propeller and engine interactions in regular waves by a combination of experiment and simulation," *Journal of Marine Science and Technology*, vol. 26, pp. 257–272, 2021, doi: 10.1007/s00773-020-00734-5.
25. F. P. Arribas, "Some methods to obtain the added resistance of a ship advancing in waves," *Journal of Ocean Engineering*, vol. 34, pp. 946–955, 2007, doi: 10.1016/j.oceaneng.2006.06.002.
26. O. M. Faltinsen et al., "Prediction of Resistance and Propulsion of a Ship in a Seaway," in *Proceedings of the 13th Symposium on Naval Hydrodynamics*, Tokyo, Japan, 1980, pp. 505–529.
27. J. B. Heywood, "Internal combustion engine fundamentals." USA: Mc-Graw Hill, 1988.
28. M. H. Ghaemi, "Performance and emission modelling and simulation of marine diesel engines using publicly available engine data," *Polish Maritime Research*, vol. 28, no. 4, pp. 63–87, 2021, doi: 10.2478/pomr-2021-0050.
29. J. B. Woodward and R. G. Latorre, "Modeling of diesel engine transient behavior in marine propulsion analysis," *Society of Naval Architects and Marine Engineers-Transactions*, 1984, vol. 92.
30. M. H. Ghaemi, "Changing the ship propulsion system performances induced by variation in reaction degree of turbocharger turbine," *Journal of Polish CIMAC*, vol. 6, pp. 55–70, 2011.
31. N. Xiros, "Robust Control of Diesel Ship Propulsion." London: Springer, 2002.
32. G. Ellis, "Control System Design Guide." Elsevier, 2012.

EFFECTS ON OF BLENDED BIODIESEL AND HEAVY OIL ON ENGINE COMBUSTION AND BLACK CARBON EMISSIONS OF A LOW-SPEED TWO-STROKE ENGINE

Cunfeng Wei ¹

Guohe Jiang¹

Gang Wu ¹ *

Yu Zhou ¹

Yuanyuan Liu¹

¹ Merchant Marine College, Shanghai Maritime University, China

* Corresponding author: wugang@shmtu.edu.cn (Gang Wu)

ABSTRACT

The effects of heavy fuel oil and biodiesel blends on engine combustion and emissions were studied in a marine two-stroke diesel engine. The engine was operated under propeller conditions using five different fuels with biodiesel blends of 10% (B10), 30% (B30), 50% (B50), and sulphur contents of 0.467% low sulphur fuel oil (LSFO) and 2.9% high sulphur fuel oil (HSFO). Tests have shown that using a biodiesel blend increases the engine fuel consumption due to its lower calorific value. Heavy fuel oil has a high Polycyclic aromatic hydrocarbons (PAH) content, which leads to higher exhaust temperatures due to severe afterburning in the engine. A comparison of engine soot emissions under different fuel conditions was carried out, and it was found that the oxygen content in biodiesel promoted the oxidation of soot particles during the combustion process, which reduced the soot emissions of biodiesel. Compared to HSFO, B10, B30, B50 and LSFO, the soot emission concentrations were reduced by 50.2%, 56.4%, 61% and 37.4%, respectively. In our experiments, the soot particles in the engine exhaust were sampled with a thermal float probe. Using Raman spectroscopy analysis, it was found that as the biodiesel ratio increased, the degree of carbonisation of the soot particles in the exhaust became less than that in the oxygenation process, resulting in a decrease in the degree of graphitisation.

Keywords: Low-speed engine; biodiesel; black carbon; Raman spectroscopy; degree of graphitisation

INTRODUCTION

Global warming is causing continuous melting of the Arctic glaciers, and although the opening of new Arctic shipping routes offers great convenience to international shipping, it poses a great threat to the Arctic environment at the same time. Black carbon (BC) emissions from international shipping vessels are the main source of BC in the Arctic, and these emissions have greatly accelerated the melting rate of Arctic glaciers [1]. Maritime shipping is a key component of the global economy, representing 80–90% of international trade [2]. In view of the current impact of BC from international ship emissions on the

deteriorating ecosystem of the Arctic, there is an urgent need for new alternative marine fuels to reduce BC emissions from ships. With its high oxygen content, biodiesel can reduce the emissions of BC in the exhaust gas during engine operation, and can reduce carbon emission over the whole life cycle; it has therefore attracted attention from researchers as an ideal alternative fuel in the field of shipping.

Teams from many countries have studied the effect of biodiesel on engine performance. Huang et al. [3] investigated the effects of intake pressure and EGR ratio on the performance and emission characteristics of a diesel engine running on biodiesel-diesel blends (B20, B30 and B40) and pure diesel (B0). Khanjani [4]

et al. prepared different formulations of WFO biodiesel (made from waste fish oil) by ultrasound radiation, and used this WFO biodiesel to make emulsion fuel. Compared with the use of diesel, the engine torque decreased, the braking power decreased, and the brake fuel consumption increased. Nabi [5] et al. prepared three kinds of biodiesel mixtures and compared them with traditional diesel fuel; it was found that although the performance of the engine changed little, the combustion efficiency was improved. Zeńczak et al. [6] converted solid biomass into marine fuel by mechanical densification or pyrolysis, and described the results from the points of view of fire safety, environmental protection, rising liquid fuel prices and dwindling crude oil resources. The potential for fire hazards on board ships arising from the storage and transport of pellet fuels and the decomposition of pellet fuels due to high temperatures were also assessed. An et al. [7] carried out experiments on biodiesel with different blending ratios and ultra-low sulphur diesel under different loads, and found that biodiesel had a significant effect on the brake-specific fuel consumption and braking thermal efficiency of generators under partial load. Wang and Yao [8] and Changxiong et al. [9] investigated the effect of in-cylinder temperature and pressure of an engine at different mixing ratios for dimethyl ether (DME) and the oxygenated fuel polyoxymethylene dimethyl ether (PODE). Ghaemi et al. [10] presented a quick and relatively simple method of building a simulation model for a specific marine diesel engine based only on steady-state data, which are widely available in the publicly available data. These authors also described how to tune the model parameters for the simulation model and how to validate the results.

Biodiesel has good effects in terms of reducing BC emissions from engines. Its use can significantly improve combustion efficiency, as it releases the oxygen atoms in its chemical structure to supplement oxygen in fuel-poor areas [11]. Abboud et al. [12] found that when using oxygenated fuel, the reduction of soot emission was closely related to the oxygen content, while soot formation was related to the ester function groups in the fuel. The alkyl chain length of the fuel was shown to affect the soot characteristics, where longer alkyl chains showed lower soot reactivity. Lemaire et al. [13] found that the soot volume fraction of rapeseed methyl ester (RME) in a turbulent flame was about 16% of that of pure diesel oil. Du et al. [14] studied the pore structure and oxidation activity of biodiesel soot; these authors reported that the carbon-oxygen ratio of biodiesel soot was lower than that of diesel soot, and the porosity of biodiesel soot was higher. Zandie et al. [15] developed a mechanism Compact combined diesel-biodiesel-gasoline kinetic mechanism (CDBG) for diesel-biodiesel-gasoline mixtures, using a mixed Reynolds averaged navier strokes-Large eddy simulation (RANS-LES) model Detached eddy simulation (DES) model to simulate turbulence, in order to study the formation and emission of soot. The results showed that an increase in environmental oxygen concentration could improve the consumption of soot precursors and reduce both PAHs and soot formation. Sundararajan Rajkumar [16] proposed a multi-region phenomenological model to analyse the combustion and emission of biodiesel. The prediction results of the model were in good agreement with the measured data, and the maximum prediction error for soot emission was 18%.

Various methods are currently in use to analyse the composition of soot, such as Fourier transform infrared spectroscopy (FT-IR), transmission electron microscopy (TEM) and thermogravimetric analysis (TGA) [17]. Raman spectroscopy was first applied to the field of aerosol analysis by Raman in 1977, and was later widely used in the field of marine atmosphere analysis. Researchers used Raman techniques to study the morphology and size of soot from gas combustion in relation to fuel and added water [18]. The intensity of graphitisation of a material can be judged according to the height of the two characteristic peaks in the Raman spectrum, as there is a positive correlation between the degree of graphitisation and the microcrystal size of soot particles; that is, the higher the degree of graphitisation, the larger the microcrystal size [19].

Although scholars have extensively researched the combustion and BC emissions from biodiesel and heavy oil in an engine, few comparative studies have focused on combustion analysis of heavy oil and blended biodiesel in the same engine. There is also little research on the degree of graphitisation of BC produced from the combustion of different fuels in marine engines. In this study, the fuel consumption and exhaust temperature of a marine engine are monitored, and the effects of different fuels on the combustion performance of the engine are studied. The filter smoke count method (FSN) recommended by International maritime organization (IMO) is used to measure the BC emission concentration of different fuels, and the effects of different fuels on the BC concentration in engine exhaust are analysed. The degree of graphitisation of black carbon in exhaust gas is characterised by Raman spectroscopy, and the effects of different fuels on the formation of BC particles in marine engine are explained.

TEST CONDITIONS AND TEST METHODS

EXPERIMENTAL STEPS

Tests were carried out on a marine two-stroke low-speed engine, as this type of diesel engine has been widely used for international operation of ships, Therefore the conclusions of this test can be a good response to the results of biodiesel use in ships on international voyages. In this study, the engine was operated in a propeller characteristic mode which also means that the engine speed varies with the engine load. The engine parameters are shown in Table 1.

Tab. 1. Engine parameters

Engine type	MAN 6S35MEB
Engine stroke	2 stroke
Engine speed	142 rpm
Cylinder bore	350 mm
Stroke	1500 mm
Torque	240 kN
Engine power	3570 kW
Charge type	Exhaust gas turbine charge

Blended heavy fuel oil with a high sulphur content has been the main fuel for international ships for a long time, as fuel oil makes up a large proportion of the operating costs. Hence, in order to better study the effects of biodiesel blending on engine performance and BC emission compared with heavy fuel oil, the fuels used in this experiment were marine heavy fuel oil with 2.9% high sulphur content fuel oil (HSFO), marine heavy fuel oil with 0.467% low sulphur content fuel oil (LSFO), and diesel oil blended with 10%, 30%, and 50% biodiesel by volume, denoted as B10, B30, and B50, respectively. The biodiesel used in this trial was refined from waste grease from the restaurant industry. Due to the high viscosity of heavy fuel oil at room temperature, it must be heated to 80°C in the fuel cabinet before use, and the heater in the line must be switched on to ensure good fuel flow. The physicochemical properties of the five fuels used in the test are shown in Table 2.

In this test, a Kistler cylinder pressure sensor (6613C) mounted on the engine cylinder head was employed

to measure the cylinder pressure, and a thermocouple temperature sensor installed in the engine exhaust pipe was used to measure the engine exhaust temperature. Fuel consumption was calculated using an inlet and return oil mass flow meter, which was installed in the engine oil supply unit. Of the current BC testing techniques, the Filtered Smoke Number (FSN) method is the one considered more applicable to marine engine testing. The BC concentration of the engine at 25%, 50%, 75%, and 100% loads with different fuels was measured using AVL415 in these tests. A copper tube and a vacuum pump were used to sample the BC particles in the engine exhaust during the test. According to EPA regulations, the sampling temperature needs to be maintained at $55 \pm 3^\circ\text{C}$ to avoid particulate loss due to coalescence of BC particles and cold-wall adherence during the sampling process. A 47 mm quartz fibre optic filter (filtration accuracy $0.3 \mu\text{m}$) was used for a sampling time of 60 min at a flow rate of about 90 l/min. To prevent the influence of moisture in the air on

Tab. 2. Fuel composition analysis

Fuel type	LSFO	HSFO	B10	B30	B50
Density (20°C) kg/m ³	950.2	974.1	842.8	845.0	849.9
Viscosity (40°C) mm ² /s	122.3	331.2	3.267	3.283	3.437
Flash point °C	73.0	85.0	77.0	79.0	82.0°C
cetane index	/	/	53.0	53.2	53.5
Polycyclic aromatic hydrocarbon (PAH) % (m/m)	11.2	11.9%	1.0%	0.9%	0.7%
Fatty acid methyl ester content % (m/m)	/	/	15.3	29.5	45.3
Net calorific value MJ/kg	41.080	40.068	41.697	41.037	40.236
Sulphur content % (m/m)	0.467	2.91	/	/	/

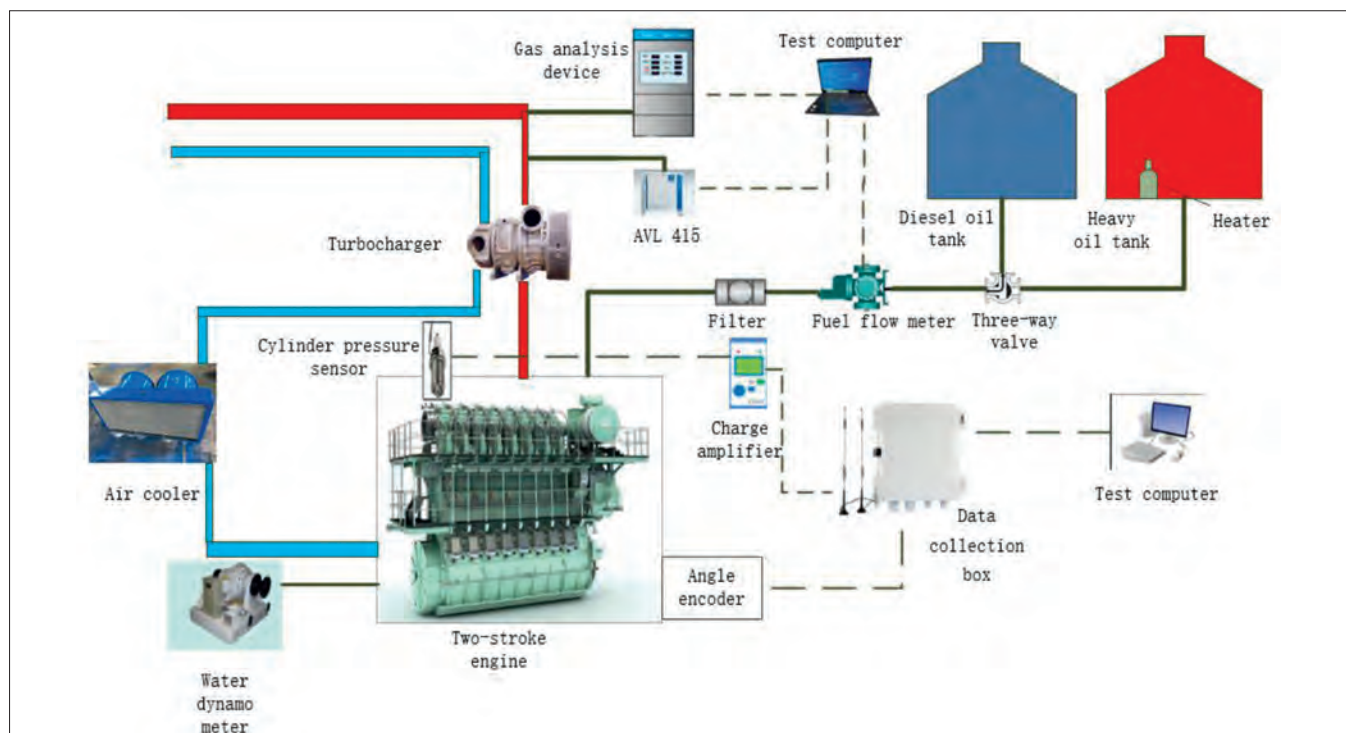


Fig. 1. Layout of the test equipment

the samples, the samples were stored in a desiccator after sampling. The BC particles produced by the combustion of different fuels were monitored using a Raman spectrometer. The experimental setup is illustrated in Fig. 1.

UNCERTAINTY ANALYSIS

Uncertainty affects the reliability and confidence of the test results. The uncertainty of the measurements made by the equipment used in the test is shown in Table 3.

Tab. 3. Uncertainty in measurement equipment

Parameter	Range	Uncertainty(%)
Speed (r/min)	0–150	±1
Flow rate of fuel (kg/h)	0–1800	±0.1
Exhaust temperature (°C)	0–500	±0.5
Black carbon (FSN)	0–10	±2
Cylinder pressure (bar)	0–250	±0.2

CALCULATION OF BC AND ENVIRENTAL CONDITIONS

The formula used to calculate the BC concentration was [20]:

$$\rho = \frac{1}{0.405} * 5.95 * FSN * e^{0.38FSN} \quad (1)$$

where ρ is the concentration of BC (mg/m³) and FSN is the smoke value.

When conducting marine engine bench tests, the laboratory environment needs to be judged by the parameter f_a . The equation used to calculate the laboratory environment was [21]:

$$f_a = \left(\frac{99}{P_s}\right)^{0.7} * \left(\frac{T_a}{298}\right)^{1.5} \quad (2)$$

where T_a (°C) is the absolute temperature of the intake air and P_a (kPa) is the dry air pressure.

The marine engine exhaust emission limits and measurement methods specify that the calculated value of f_a for the laboratory environment should be between 0.93 and 1.07 in order to be considered as meeting the requirements of the marine engine test [21].

RESULTS AND DISCUSSION

EFFECTS OF BIODIESEL ON ENGINE PERFORMANCE

Biodiesel is an alternative fuel that is typically converted from vegetable oils or animal fats. It has different physicochemical properties from traditional petroleum diesel, and therefore has an impact on engine performance and in-cylinder combustion when burned in the same engine. This section analyses the effects of five different fuels on engine performance and in-cylinder combustion during the combustion process in the engine.

Effects of biodiesel on engine cylinder pressure

Fig. 2 shows the cylinder pressure at engine running in 75% rated engine load. It can be seen that an increase in the biodiesel blending ratio causes the pressure in the engine cylinder to increase, and that the pressure of blended biodiesel is higher than that of heavy oil. Specifically, the maximum pressure in the engine cylinder is 1.2% higher when running on B50 compared to B10. The main reason for this is the increase in the oxygen atom content of the fuel as the biodiesel blend ratio increases, which accelerates the combustion rate in the cylinder. The piston moves up to the top stop and then starts to move down, and the faster combustion rate also leads to a higher pressure in the cylinder. Due to the high viscosity of heavy oil, poor atomisation leads to relatively slow combustion, which causes the rate of increase in the in-cylinder pressure to decrease, as can be seen from Fig. 3. In addition, this causes the pressure in the cylinder to decrease.

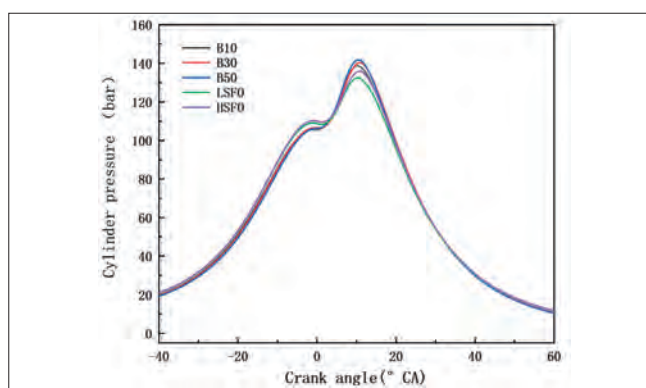


Fig. 2. Cylinder pressure at 75% engine load

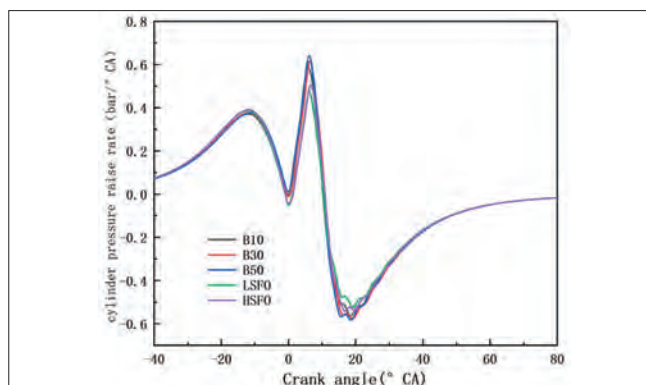


Fig. 3. Rate of rise in cylinder pressure at 75% engine load

Effects of biodiesel on engine thermal efficiency

Thermal efficiency is a metric of the efficiency of the engine in terms of converting the chemical energy of the fuel into useful work. The energy loss during engine operation not only depends on the engine speed but also varies with the combustion characteristics of the fuel. From the variation in thermal efficiency with load for three different biodiesel blends in Fig. 4, it can be seen that increasing the biodiesel content reduces the calorific value of the blended fuel, and more fuel must be injected to meet the set load of the engine under the same engine operating conditions. Under the same injector conditions, an increase in the amount of injected fuel can lead to problems such as poor atomisation, which reduces the

thermal efficiency of the engine. Although HSFO and LSFO have higher viscosities than biodiesel and are heated during use, their higher PAH content results in more incomplete combustion and therefore lower thermal efficiencies.

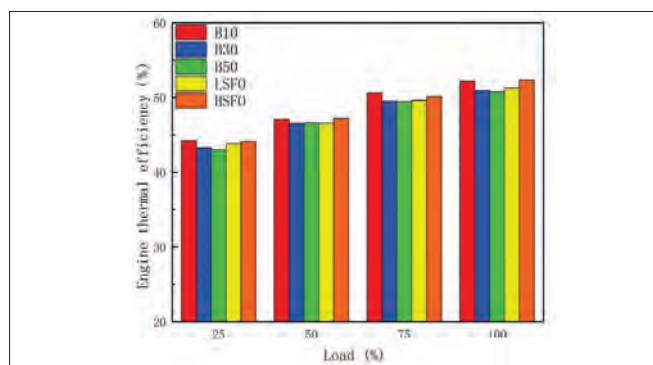


Fig. 4. Engine thermal efficiency of different fuels under different loads

Effects of biodiesel on fuel consumption

The fuel consumption rate is an important indicator of fuel economy. Fig. 5 shows the fuel consumption rate of the engine using B10, B30, B50, LSFO and HSFO, for varying loads. It can be seen that the fuel consumption rate increases with the percentage of biodiesel blend. From a comparison of the average fuel consumption of the engine for each fuel at the four loads, it can be found that the fuel consumption rates for B10, B30 and LSFO compared to HSFO decrease compared to HSFO by 0.6%, 0.4% and 1.2%, respectively, and the fuel consumption rate of B50 increases by 1.7%. This is mainly the result of one increase the other decreases between the calorific value of the fuel and the injection and combustion of the fuel in the cylinder. The calorific value of the fuel is an important factor affecting the fuel consumption of the engine, and under normal circumstances, higher calorific values tend to be associated with lower fuel consumption rates. The atomisation and combustion of the fuel in the engine cylinder are also important factors affecting the fuel consumption, as a good combustion process will also reduce the engine fuel consumption. Of the fuels considered here, B10 has the highest calorific value, and although B50 has more oxygen atoms to promote combustion, the calorific value of the fuel dominates. Compared to HSFO and LSFO, B10 has a lower content of polymer PAHs, which ultimately results in a lower fuel consumption.

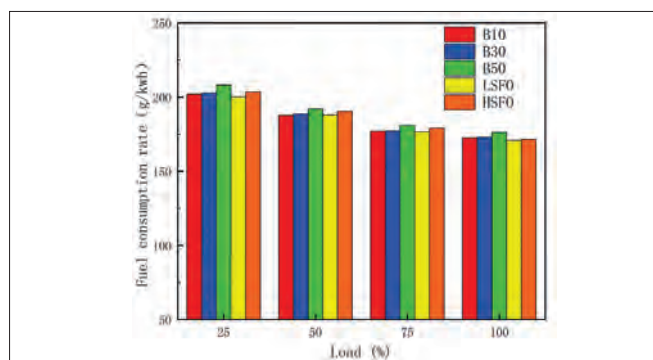


Fig. 5. Engine fuel consumption rates for different fuels at different loads

Effects of biodiesel on engine exhaust temperature

The engine exhaust temperature is a further important indicator of the combustion process in the engine cylinder. Some researchers have suggested that biodiesel gives a better combustion process in the engine due to its higher oxygen content, which leads to higher exhaust gas temperatures; however, the opposite conclusion was reached in this study. From a comparison of the engine exhaust temperatures at different biodiesel blends in Fig. 6, it can be seen that the engine exhaust temperature slightly decreases with an increase in the biodiesel blend. This may be due to the lower calorific value of biodiesel, which gives it a lower temperature for the combustion process in the cylinder, resulting in a lower engine exhaust temperature. A comparison of the engine exhaust temperatures of heavy fuel oil and biodiesel in this experiment shows that the engine exhaust temperature is slightly higher than that of biodiesel blended with heavy fuel oil. This may be due to the fact that heavy oil contains more polymeric PAHs, which are difficult to burn, meaning that the combustion time of heavy oil is longer than that of biodiesel blend, resulting in higher engine exhaust temperatures. In this test, due to the high viscosity of the heavy oil at room temperature, the temperature was heated up to about 92°C during injection, whereas the blended biodiesel was not heated up, which may also have contributed to the relatively high exhaust temperature of the heavy oil.

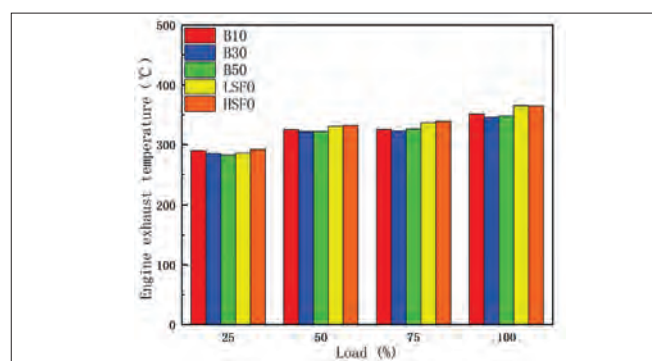


Fig. 6. Engine emission temperatures of different fuels under different loads

IMPACT OF BIODIESEL ON BC EMISSIONS

The quality and composition of the fuel directly affect the degree of completeness of the combustion process. Low-quality or contaminated fuels may contain impurities or incomplete combustion products, which can increase the production of BC. To enable a better assessment of the BC emissions from blended biodiesel and heavy fuel oil, this section presents a comparative analysis of BC emissions and degree of graphitisation for different fuels.

Impact of biodiesel on the concentration of BC in engine exhaust

From Fig. 7, it can be seen that the concentration of BC in the engine exhaust decreases as the engine load increases, and reaches a minimum at 100% load; this is mainly due to the fact that with an increase in the engine load, the increase in the engine exhaust temperature promotes the oxidation process of BC

particles, which reduces the concentration of BC in the engine exhaust. An analysis of the BC emissions of the engine when burning different fuels showed that the emission concentration was reduced by 50.2%, 56.4%, 61% and 37.4% compared to HSFO for B10, B30, B50 and LSFO, respectively. The BC concentration in the engine exhaust decreased as the biodiesel blending ratio increased. This was mainly because the oxygen content in the fuel increased with the biodiesel blending ratio, thus promoting the oxidation of BC during the combustion process and reducing the BC concentration in the exhaust emission. The main reason for the lower BC concentration in LSFO compared to HSFO may be that the heavy oil used in this test was a blend of residual oil and marine diesel fuel, and the HSFO had a higher residual oil content, which was more likely to lead to incomplete combustion and the formation of more BC particles during operation of the engine.

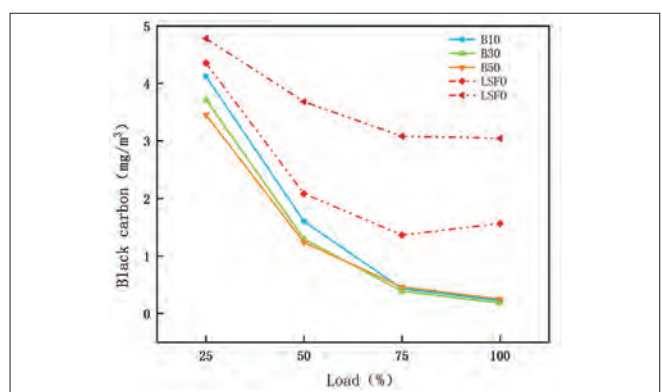


Fig. 7. Black carbon concentrations for different fuels under varying loads

Impact of biodiesel on the graphitisation of black carbon

Fig. 8 shows the Raman spectra for the BC particulate matter produced by engine combustion. The characteristics of the samples at wavelengths of 500–4500 cm^{-1} were scanned in the experiment. Two characteristic peaks near 1345 cm^{-1} and 1594 cm^{-1} can be clearly seen from the Raman spectra of the particles. The peak at 1345 cm^{-1} is generally considered to be generated by the transformation of the local structural hexagonal symmetry of the crystals to a lower symmetry or to a loss of symmetry, and is known as the disordered peak or D-peak. The one located near 1595 cm^{-1} is known as the G-peak, and is generated by the phonon vibrational mode (the in-plane telescopic vibration of the sp^2 hybridisation of carbon atoms). It can be used to characterise the structure of the ordered carbon layers in the particles.

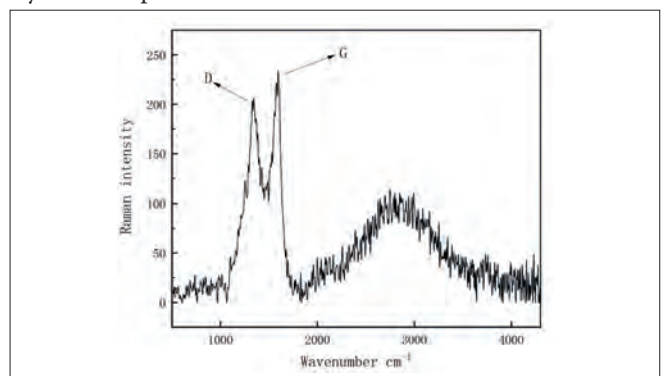


Fig. 8. Raman spectrum for black carbon

In order to enable an analysis of the effects of different fuels on the degree of graphitisation of BC particles in the engine, The collected BC generated from different fuels were subjected to Raman detection, and the Raman spectrograms were smoothed for ease of analysis., and all the spectral lines were normalised with reference to their respective G-peak peaks as a standard. The degree of graphitisation of the particles was characterised by the value of the G peak value divided by the value of the D peak IG/ID, with larger values indicating a lower and smaller ratios a higher degree of graphitisation.

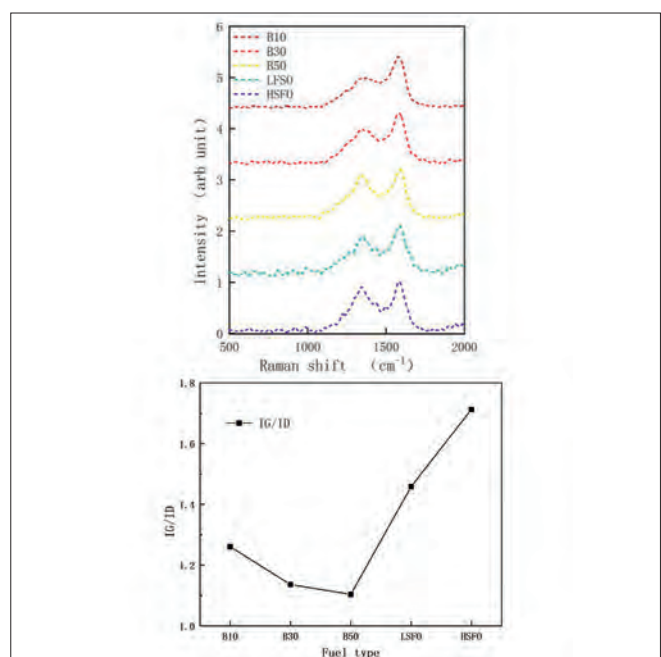


Fig. 9. Degree of graphitisation of black carbon (IG/ID)

From Fig. 9, it can be observed that the degree of graphitisation of BC particles in the engine exhaust decreases as the biodiesel blending ratio increases, and the degree of graphitisation of the BC particles produced by the engine during the combustion of heavy oil is greater than for blended biodiesel. An increase in the biodiesel blending ratio decreases the IG/ID ratio, which is mainly due to the higher oxygen content of biodiesel promoting the oxidation of BC particles in the combustion process. The greater the number of oxygen atoms in biodiesel participating in the combustion, the more obvious the oxidation process compared to the carbonisation process of the fuel, and the lower the degree of graphitisation of the resulting particles. An increase in the maximum flame temperature also leads to an increase in the degree of graphitisation, which is positively correlated with the trend in the engine discharge temperature when burning different fuels, as shown in Fig. 6.

CONCLUSIONS

In terms of engine performance, an increase in the oxygen atom content of the biodiesel blends leads to faster in-cylinder combustion, resulting in a 1.2% increase in maximum in-cylinder pressure with B50 compared to B10. The thermal efficiency of

the fuel and the fuel consumption of the engine are determined by both the calorific value and the combustion characteristics of the fuel. Of the fuels used in this study, B10 has the highest calorific value and combustion characteristics, and hence the highest thermal efficiency and lowest fuel consumption.

Incomplete combustion of heavy fuel oil due to the presence of polymeric compounds such as PAHs and the higher fuel inlet temperatures leads to an increase in exhaust temperature. Marine heavy oils usually have more asphaltenes and lower levels of combustible aromatic and naphthenic hydrocarbons, meaning that the engine has a higher concentration of BC emissions when burning heavy oils compared to blended biodiesel. The higher oxygen content of biodiesel causes the BC concentration in the engine exhaust to decrease with an increase in the biodiesel blending ratio.

The degree of graphitisation of BC also differs slightly when the engine burns different fuels. An increase in the biodiesel blending ratio promotes the oxidation process of BC particles and reduces the degree of graphitisation of BC particles. The higher content of polymeric cycloalkanes and aromatic hydrocarbons and the higher discharge temperature during combustion of heavy fuel oil results in higher BC graphitisation during combustion.

REFERENCES

1. S. Messner, Future Arctic Shipping, Black Carbon Emissions, and Climate Change, Maritime Transport and Regional Sustainability, pp.195–208, Jan. 2020, doi: <https://doi.org/10.1016/B978-0-12-819134-7.00012-5>.
2. R. Zhao et al., “A numerical and experimental study of marine hydrogen–natural gas–diesel tri-fuel engines,” Polish Maritime Research, vol. 4, pp.80-90,2020, doi: <https://doi.org/10.2478/pomr-2020-0068>.
3. Z. Huang, J. Huang, J. Luo, D. Hu, and Z. Yin, “Performance enhancement and emission reduction of a diesel engine fueled with different biodiesel-diesel blending fuel based on the multi-parameter optimization theory,” Fuel, vol. 314,pp. 122753, Apr. 2022, doi: <https://doi.org/10.1016/j.fuel.2021.122753>.
4. A. Khanjani and M. A. Sobati, “Performance and emission of a diesel engine using different water/waste fish oil (WFO) biodiesel/diesel emulsion fuels: Optimization of fuel formulation via response surface methodology (RSM),” Fuel, vol. 288, pp. 119662, Mar. 2021, doi: <https://doi.org/10.1016/j.fuel.2020.119662>.
5. M. N. Nabi and M. G. Rasul, “Influence of second generation biodiesel on engine performance, emissions, energy and exergy parameters,” Energy Conversion and Management, vol. 169, pp. 326–333, Aug. 2018, doi: <https://doi.org/10.1016/j.enconman.2018.05.066>.
6. W. Zeńczak and A. K. Gromadzińska, “Preliminary analysis of the use of solid biofuels in a ship’s power system,” Polish Maritime Research, vol. 27, no. 4, pp. 67–79, Dec. 2020, doi: <https://doi.org/10.2478/pomr-2020-0067>.
7. H. An, W. M. Yang, S. K. Chou, and K. J. Chua, “Combustion and emissions characteristics of diesel engine fueled by biodiesel at partial load conditions,” Applied Energy, vol. 99, pp. 363–371, Nov. 2012, doi: <https://doi.org/10.1016/j.apenergy.2012.05.049>.
8. S. Wang and L. Yao, “Effect of engine speeds and dimethyl ether on methyl decanoate HCCI combustion and emission characteristics based on low-speed two-stroke diesel engine,” Polish Maritime Research, vol. 27, no. 2, pp. 85–95, Jun. 2020, doi: <https://doi.org/10.2478/pomr-2020-0030>.
9. L. Changxiong, Y. Hu, Z. Yang, and H. Guo, “Experimental study of fuel combustion and emission characteristics of marine diesel engines using advanced fuels,” Polish Maritime Research, vol. 30, no. 3, pp. 48–58, Sep. 2023, doi: <https://doi.org/10.2478/pomr-2023-0038>.
10. M. H. Ghaemi, “Performance and emission modelling and simulation of marine diesel engines using publicly available engine data,” Polish Maritime Research, vol. 28, no. 4, pp. 63–87, Dec. 2021, doi: <https://doi.org/10.2478/pomr-2021-0050>.
11. T. Li et al., “Investigation on the applicability for reaction rates adjustment of the optimized biodiesel skeletal mechanism,” Energy, vol. 150, pp. 1031–1038, May 2018, doi: <https://doi.org/10.1016/j.energy.2018.03.026>.
12. J. Abboud et al., “Impacts of ester’s carbon chain length and concentration on sooting propensities and soot oxidative reactivity: Application to diesel and biodiesel surrogates,” Fuel, vol. 222, pp. 586–598, Jun. 2018, doi: <https://doi.org/10.1016/j.fuel.2018.02.103>.
13. R. Lemaire, S. Béjaoui, and E. Therssen, “Study of soot formation during the combustion of diesel, rapeseed methyl ester and their surrogates in turbulent spray flames,” Fuel, vol. 107, pp. 147–161, May 2013, doi: <https://doi.org/10.1016/j.fuel.2012.12.072>.
14. J. Du, L. Su, D. Zhang, C. Jia, and Y. Yang, “Experimental investigation into the pore structure and oxidation activity of biodiesel soot,” Fuel, vol. 310, pp. 122316–122316, Feb. 2022, doi: <https://doi.org/10.1016/j.fuel.2021.122316>.
15. M. Zandie, H. K. Ng, S. Gan, M. F. Muhamad Said, and X. Cheng, “A comprehensive CFD study of the spray combustion, soot formation and emissions of ternary mixtures of diesel, biodiesel and gasoline under compression ignition engine-relevant conditions,” Energy, vol. 260, p. 125191, Dec. 2022, doi: <https://doi.org/10.1016/j.energy.2022.125191>.

16. S. Rajkumar and J. Thangaraja, "Effect of biodiesel, biodiesel binary blends, hydrogenated biodiesel and injection parameters on NO_x and soot emissions in a turbocharged diesel engine," *Fuel*, vol. 240, pp. 101–118, Mar. 2019, doi: <https://doi.org/10.1016/j.fuel.2018.11.141>.
17. B. Zhao, X. Liang, K. Wang, T. Li, X. Lv, and S. Zhang, "Impact of sulfur functional groups on physicochemical properties and oxidation reactivity of diesel soot particles," *Fuel*, vol. 327, p. 125041, Nov. 2022, doi: <https://doi.org/10.1016/j.fuel.2022.125041>.
18. U. Trivanovic et al., "Morphology and size of soot from gas flares as a function of fuel and water addition," *Fuel*, vol. 279, p. 118478, Nov. 2020, doi: <https://doi.org/10.1016/j.fuel.2020.118478>.
19. F. G. Emmerich, "Evolution with heat treatment of crystallinity in carbons," *Carbon*, vol. 33, no. 12, pp. 1709–1715, Jan. 1995, doi: [https://doi.org/10.1016/0008-6223\(95\)00127-8](https://doi.org/10.1016/0008-6223(95)00127-8).
20. X. M. Zheng and C. F. Wei, "Measurement of black carbon emission factor of marine diesel engines," *Journal of Shanghai Maritime University*, vol. 42, pp. 53–57, 2021, doi: <https://doi.org/10.13340/j.jsmu.2021.02.009>.
21. Limits and measurement methods for exhaust pollutants from marine engines, GB 15097-2016, <https://www.chinesestandard.net>.

FAULT DIAGNOSIS OF IMBALANCE AND MISALIGNMENT IN ROTOR-BEARING SYSTEMS USING DEEP LEARNING

Fayou Liu 

Huazhong University of Science and Technology, School of Naval Architecture and Ocean Engineering, China

Weijia Li*

Huazhong University of Science and Technology, School of Naval Architecture and Ocean Engineering, China

Yaozhong Wu

School of Automobile and Traffic Engineering, Wuhan University of Science and Technology, China

Yuhang He

Huazhong University of Science and Technology, School of Naval Architecture and Ocean Engineering, China

Tianyun Li

Huazhong University of Science and Technology, School of Naval Architecture and Ocean Engineering, China

* Corresponding author: liweijia@hust.edu.cn (Weijia Li)

ABSTRACT

Rotor-bearing systems are important components of rotating machinery and transmission systems, and imbalance and misalignment are inevitable in such systems. At present, the main challenges faced by state-of-the-art fault diagnosis methods involve the extraction of fault features under strong background noise and the classification of different fault modes. In this paper, a fault diagnosis method based on an improved deep residual shrinkage network (IDRSN) is proposed with the aim of achieving end-to-end fault diagnosis of a rotor-bearing system. First, a method called wavelet threshold denoising and variational mode decomposition (WTD-VMD) is proposed, which can process original noisy signals into intrinsic mode functions (IMFs) with a salient feature. These one-dimensional IMFs are then transformed into two-dimensional images using a Gramian angular field (GAF) to give datasets for the deep residual shrinkage network (DRSN), which can achieve high levels of accuracy under strong background noise. Finally, a comprehensive test platform for a rotor-bearing system is built to verify the effectiveness of the proposed method in the field. The true test accuracy of the model at a 95% confidence interval is found to range from 84.09% to 86.51%. The proposed model exhibits good robustness when dealing with noisy samples and gives the best classification results for fault diagnosis under misalignment, with a test accuracy of 100%. It also achieves a higher testing accuracy compared to fault diagnosis methods based on convolutional neural networks and deep residual networks without improvement. In summary, IDRSN has significant value for deep learning engineering applications involving the fault diagnosis of rotor-bearing systems.

Keywords: Rotor-bearing system, Vibration signal, Feature extraction, Deep learning, Deep residual shrinkage network, Test platform

INTRODUCTION

Rotor-bearing systems are important components of rotating machinery and transmission system, and are widely used in industrial production and transportation in harsh environments such as ocean vessels and offshore platforms [1]. The lifetime of a rotor-bearing system is influenced by factors such as deformation, load, lubrication, temperature, humidity, and corrosion [2]. Thus, rotor-bearing systems are

prone to wear, leading to long-term exception. According to an authoritative book [3], imbalance and misalignment are two common faults in rotor-bearing systems, and about 70% of rotating machinery faults are caused by or related to these effects. Furthermore, imbalance and misalignment are the faults most likely to cause significant engineering consequences. In an actual rotor-bearing system, the periodic signals of the system are mixed with impact signals caused by faults throughout the entire frequency band. The impact signals caused by different types of faults, such as imbalance

and misalignment, are relatively weak considering the complexity of the transmission path, which makes it more difficult to identify the features of different faults [4]. Hence, the extraction of fault features under strong background noise and the classification of different fault modes have become the main challenges faced by current fault diagnosis methods for rotor-bearing systems.

Fault diagnosis based on signal processing techniques that require specialised knowledge is still a popular area of research. Bechou et al. [5] used a continuous wavelet transform algorithm to achieve fault signal diagnosis for a die-attach assembly. Moreno-Sánchez et al. [6] studied the imbalance and misalignment effects of the acceleration vibration parameters used in early bearing fault diagnosis, and were able to predict the probability of bearing faults with an accuracy greater than 90%. In addition, many scholars [7],[8],[9],[10] have experimented in their professional fields with diagnosing imbalance, misalignment, looseness, rubbing or cracking in rotor systems. At the same time, increasing numbers of researchers have combined fault diagnosis with artificial intelligence in recent years. It was mentioned in [11] that vibration analysis based on signal processing techniques required a significant level of human expertise, and often involved analysis of specific faults for specific objects. In this case, a model based on deep learning was proposed to monitor the imbalance of a rotor. The model gave significantly better results than the classical vibration analysis method, and the accuracy reached 93.61%.

The use of a convolutional neural network (ConvNet) for deep learning [12] has the advantage of local receptive fields, weight-sharing and down-sampling, and these networks have rapidly been introduced into engineering domains. In the classical ConvNet [13], the gradients of the cross-entropy error are backpropagated layer by layer, which can cause problems associated with degradation and over-fitting with an increase in the number of layers of a deep learning model. Although ConvNet has been shown to be effective in the domain of image recognition and classification, there are still certain limitations on its application [14]. A deep residual network (ResNet) [15] is an attractive variant of ConvNet in which identity shortcuts are used to ease the difficulty of parameter optimisation. This is the key aspect that makes ResNet superior to the classical ConvNet. The parameters can be updated more favourably, as the gradients flow effectively to the earlier layers approaching the input layer. In view of this, ResNets have been widely applied to the problem of fault diagnosis in recent years [16]. Tang et al. [17] published a review in 2020 that focused on summarising and discussing the fault diagnosis methods for rotating machinery based on deep learning that had been developed over the previous five years, with the main research objects being bearings, gears or gearboxes, and pumps. After reviewing past studies, it was found that the classical deep learning method could meet the fault diagnosis or condition monitoring requirements of most general rotor-bearing systems. Zhao et al. [18] proposed a novel model called a deep residual shrinkage network (DRSN) in 2020, which was found to have higher

accuracy for noisy signals than the alternatives due to its soft threshold and attention mechanism. This paper shows the better classification performance based on DRSN in machine faults.

Fault diagnosis methods for other special rotor-bearing systems are still emerging. Bach-Andersen et al. [19] proposed a novel data-driven deep-learning system for a large-scale wind turbine drivetrain, and demonstrated its superior performance. Kumar et al. [20] developed a novel fault detection framework for multiple and simultaneous fault detection in SCIM that was found to outperform the existing state-of-the-art techniques and had an accuracy of 99.40%. Huangfu et al. [21] put forward an artificial intelligence approach for detecting engine combustion faults related to spark plugs using existing sensors. Although there was some unstable performance outside of the given operating conditions, it successfully detected faults with high accuracy. Lim et al. [22] proposed an indirect vortex-induced vibration (VIV) detection algorithm based on deep learning, which took the vibration signals from the propeller of a crude oil tanker in sea trials as the training and test sets. Glaeser et al. [23] investigated the feasibility of using deep learning techniques for fault detection in industrial cold forging. Their results suggested that potential faults in cold forging could be detected by the proposed deep learning method. The research objects in the studies described above included turbines, motors, engines, propellers and cold forging in various fields, and the effectiveness of the deep learning method was verified.

The impact signals from imbalance and misalignment are easily submerged by strong background noise, and the target modes cannot be accurately extracted by traditional feature extraction methods. Traditional fault diagnosis models also require a certain level of professional knowledge, and also have poor robustness to low-frequency noisy signals [24]. In this paper, a fault diagnosis method for a rotor-bearing system based on IDRSN is proposed. The core of this method involves transforming the one-dimensional feature of a vibration signal into a two-dimensional image, on the premise of accurately extracting the features of a one-dimensional time series with strong background noise. DRSN, which gives a better learning effect on two-dimensional noisy data, is organically integrated into this scheme, and conditions involving normal operation, imbalance and misalignment are classified to achieve fault diagnosis for a rotor-bearing system. The actual working conditions are simulated on a test platform with imbalance and misalignment, and real signals are collected under the corresponding working conditions. An application experiment and a comparison experiment are conducted based on the datasets described above, and it is found through comparative experimental research that the proposed method significantly improves the diagnostic accuracy compared to classical deep learning methods. The method presented here can be applied to achieve diagnose imbalance and misalignment faults in a rotor-bearing system.

PROPOSED SCHEME

WAVELET THRESHOLD DENOISING

Wavelet threshold denoising (WTD) is an adaptive multi-scale denoising method that uses a threshold function, and was developed on the basis of the wavelet transform. WTD can adaptively remove the noise from a real signal while retaining the original signal, and has been proven to give the best estimate of the original signal [25]. The key feature of WTD is that it uses a threshold function to process real signals in the wavelet domain, and the original signals in the time domain are then calculated based on wavelet reconstruction. The specific steps in this algorithm are as follows:

- 1) The real signal $x(t)$ is transformed into a set of wavelet coefficients $w_{j,k}$ via wavelet transformation.
- 2) The wavelet coefficients $w_{j,k}$ are transformed into wavelet estimated coefficients $\hat{w}_{j,k}$ by applying a threshold function so that $|\hat{w}_{j,k}|$ is as small as possible.
- 3) The wavelet estimation coefficients $\hat{w}_{j,k}$ are transformed to an estimated signal $\hat{x}(t)$, which represents the denoised signal based on wavelet reconstruction.

In this case, we apply a semi-soft threshold function, which takes into account the advantages of the traditional soft threshold function and the hard threshold function, and is written as:

$$w_{j,k} = \begin{cases} \text{sgn}(w_{j,k}) \left| w_{j,k} \right| - \lambda + \frac{2\lambda}{1 + e^{2w_{j,k}/\lambda}}, & |w_{j,k}| \geq \lambda \\ 0, & |w_{j,k}| < \lambda \end{cases} \quad (1)$$

where the threshold λ satisfies the equation $\lambda = \sigma\sqrt{2\ln(N)}$, and N is the number of samples of the signals.

VARIATIONAL MODE DECOMPOSITION

Variational mode decomposition (VMD) is a completely non-recursive variational decomposition model for non-stationary and nonlinear signals that can adaptively decompose real signals into a corresponding intrinsic mode function (IMF) with limited bandwidth [26]. The constrained variational problem in VMD is as follows:

$$\min_{\{u_k\}, \{\omega_k\}} \left\{ \sum_k \left\| \partial_t \left[\left(\delta(t) + \frac{j}{\pi t} \right) * u_k(t) \right] e^{-j\omega_k t} \right\|_2^2 \right\} \quad (2)$$

s.t. $\forall x: \sum_k u_k(x) = f(x)$

where $\{u_k\} := \{u_1, \dots, u_K\}$, $\{\omega_k\} := \{\omega_1, \dots, \omega_K\}$ are shorthand notations for the set of all modes and their centre frequencies, respectively. An augmented Lagrangian is then added to make the problem unconstrained, and a quadratic penalty term is

imposed to enforce strict data fidelity. Finally, we solve the variational problem by the alternating direction multiplier method (ADMM) and Parseval/Plancherel Fourier isometry.

The final equations to be solved are:

$$\hat{u}_k^{n+1}(\omega) = \frac{\hat{f}(\omega) - \sum_{i \neq k} \hat{u}_i(\omega) + \frac{\hat{\lambda}(\omega)}{2}}{1 + 2\alpha_k |\omega - \omega_k|^2} \quad (3)$$

$$\forall \omega \in \Omega_k : \Omega_k = \{\omega | \langle \omega, \omega_k \rangle \geq 0\}$$

$$\omega_k^{n+1} = \frac{\int_{\Omega_k} \omega |\hat{u}_k(\omega)|^2 d\omega}{\int_{\Omega_k} |\hat{u}_k(\omega)|^2 d\omega} \quad (4)$$

GRAMIAN ANGULAR FIELD

The Gramian angular field (GAF) is a method of transforming a one-dimensional time series recoded into polar coordinates into a two-dimensional image by considering the trigonometric sum or difference [27]. This method has the advantage of preserving temporal dependency and containing temporal correlations. In particular, a GAF contains a Gramian summation angular field (GASF) and Gramian difference angular field (GADF), which differ only in terms of the defining equations.

Given a time series $X = \{x_1, x_2, \dots, x_n\}$ of n observations, we can rescale X to the closed interval $[0, 1]$ using Eq. [5] to get the time series $\tilde{X} = \{\tilde{x}_1, \tilde{x}_2, \dots, \tilde{x}_n\}$.

$$\tilde{x} = \frac{x_i - \min(X)}{\max(X) - \min(X)} \quad (5)$$

We then recode the time series \tilde{X} into polar coordinates using Eq. [6]:

$$\begin{cases} \phi = \arccos(\tilde{x}_i), 0 \leq \tilde{x}_i \leq 1, \tilde{x}_i \in \tilde{X} \\ r = \frac{t_i}{N}, t_i \in N \end{cases} \quad (6)$$

where t_i is the time stamp, and N is a constant factor applied to regularise the span of the polar coordinate system. GASF and GADF are defined as follows:

$$\begin{aligned} GASF &= \left[\cos(\phi_i + \phi_j) \right] \\ &= \tilde{X}' \cdot \tilde{X} - \sqrt{I - \tilde{X}'^2} \cdot \sqrt{I - \tilde{X}^2} \end{aligned} \quad (7)$$

$$GADF = \left[\sin(\phi_i - \phi_j) \right] \\ = \sqrt{I - \tilde{X}^2}' \cdot \tilde{X} - \tilde{X}' \cdot \sqrt{I - \tilde{X}^2} \quad (8)$$

where I is the unit row vector.

DEEP RESIDUAL SHRINKAGE NETWORK

In a deep residual shrinkage network (DRSN), soft thresholding is applied to effectively eliminate noise-related features, and a specially designed subnetwork called an attention mechanism is used to adaptively determine the thresholds for each piece of the vibration signal. The process of soft thresholding is illustrated in Fig. 1(a). The derivative of the output is either one or zero, meaning that this approach is effective in preventing gradient vanishing and exploding problems, as shown in Fig. 1(b). The derivative can be expressed as follows:

$$\frac{\partial y}{\partial x} = \begin{cases} 1 & x > \tau \\ 0 & -\tau \leq x \leq \tau \\ 1 & x < -\tau \end{cases} \quad (9)$$

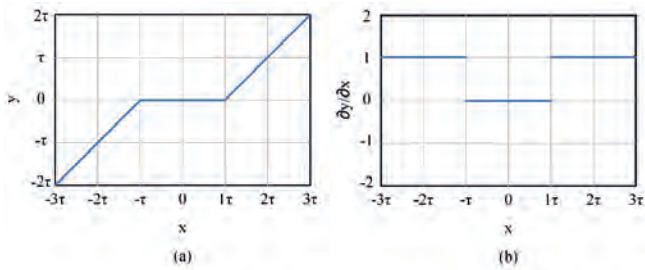


Fig.1. Illustration of (a) soft thresholding and (b) its derivative

Both the proposed DRSN and the ResNet have some basic components that are the same as those of the classical ConvNet, which are called building units (BUs). As shown in Fig. 2(a), the BU in the architecture of the classical Plain Net is composed of convolutional layers and an activation function based on rectifier linear units (ReLUs). The output of the BU can be expressed as follows:

$$H(x) = \text{ReLU}(x) \quad (10)$$

A residual building unit (RBU), as shown in Fig. 2(b), consists of an identity shortcut in addition to convolutional layers and ReLUs. The output of the RBU can be expressed as follows:

$$H(x) = x + \text{ReLU}(x) \quad (11)$$

Fig. 2(c) shows a type of BU called a residual shrinkage building unit (RSBU), which differs from the RBU in Fig. 2(b) as it uses a special module for estimating the threshold. The output of the RSBU can be expressed as follows:

$$H(x) = x + \begin{cases} x' - x'' & x' > x'' \\ 0 & -x'' \leq x' \leq x'' \\ x' + x'' & x' < -x'' \end{cases} \quad (12)$$

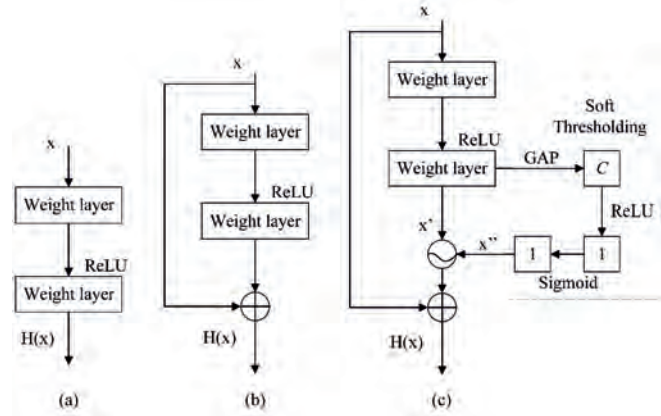


Fig.2. BUs for three kinds of deep learning models: (a) BU in the architecture of the classical Plain Net; (b) BU in the architecture of the ResNet; and (c) BU in the architecture of the developed DRSN

SPEARMAN'S CORRELATION COEFFICIENT

Spearman's correlation coefficient is a statistical method of evaluating the correlation between two variables, and is defined as follows:

$$\rho = \frac{\sum_{i=1}^N (x_i - \bar{x})(y_i - \bar{y})}{\sqrt{\sum_{i=1}^N (x_i - \bar{x})^2 \sum_{i=1}^N (y_i - \bar{y})^2}} \quad (13)$$

The restrictions on the variables in the Spearman's correlation coefficient are less strict than in the Pearson correlation coefficient, and the population distribution and sample size between variables do not require explicit constraints. Hence, Spearman's correlation coefficient can also be defined as the Pearson correlation coefficient between ordinal variables.

STEPS OF THE PROPOSED ALGORITHM

A flow chart of the proposed rotor-bearing system fault diagnosis method based on IDRSN is shown in Fig. 3. The process is as follows:

- (1) Normal, imbalanced and misaligned working conditions are simulated on a test platform.

- (2) The original vibration signals from the bearing housing under these three working conditions are collected, and 1,100 data samples with a length of less than 2,000 are selected for each working condition.
- (3) Wavelet transforms are applied to the evenly divided data to obtain a set of wavelet coefficients. A wavelet estimated coefficient is then calculated using the equation for a semi-soft threshold function. Finally, the time-domain denoised signal is inverse transformed by wavelet reconstruction.
- (4) The corresponding denoised signal is subjected to VMD to obtain several IMFs, and the optimal IMF under specific working conditions is selected based on Spearman's correlation coefficient.
- (5) The optimal IMF is normalised to the closed interval $[0,1]$, and the normalised time series is then recoded into polar space. The recoded series is then transformed by GAF to obtain a two-dimensional image with a size that is scaled to 100×100 .
- (6) The 3,300 images obtained in this way are labelled and randomly shuffled to form a dataset, which is then divided into 2,700, 300 and 300 samples as a training set, validation set and test set.
- (7) The training and validation sets are passed to the DRSN, and the fault diagnosis model is built after training and optimisation.
- (8) The test set is used to evaluate the fault diagnosis model to obtain fault diagnosis results, and the effectiveness of the model is measured based on the test accuracy and confusion matrix.

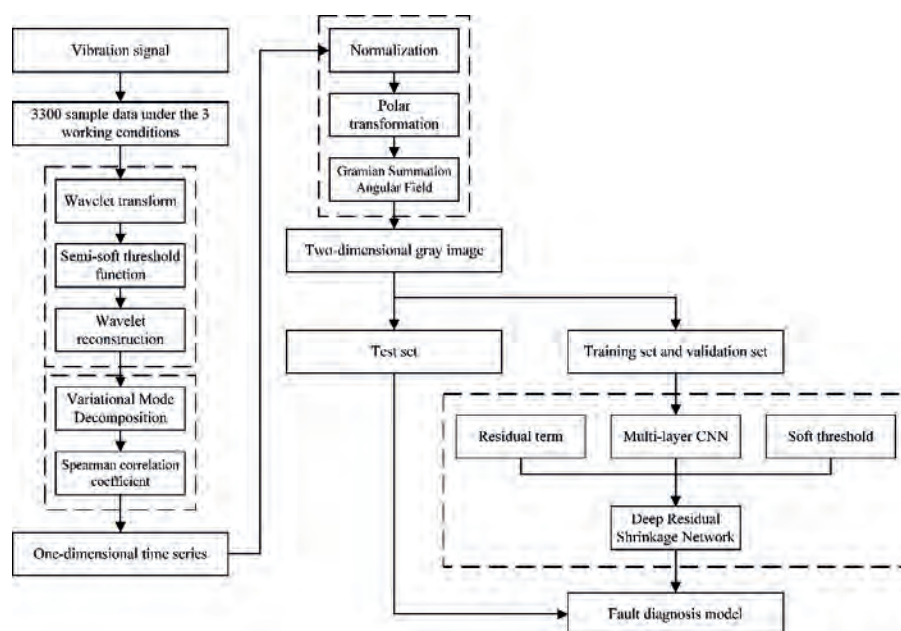


Fig.3. Flow chart of the proposed rotor-bearing system fault diagnosis method based on IDRSN

APPLICATION EXPERIMENT

The proposed deep learning method was implemented using TensorFlow 2.0. Experiments were conducted on a computer with an E3-1226 CPU and a NVIDIA Quadro K2200 GPU.

EXPERIMENTAL SETUP

A comprehensive test platform of a rotor-bearing system was built as shown in Fig. 4(a). In terms of mechanical parts, the test platform contained one cast iron base, one stepping motor, one high-elastic coupling, three shafts, four bearings and four bearing housings. The stepping motor was equipped with a reducer with a reduction ratio of 10:1, all shafts were connected by flanges, and all bearing housings were fixed in a straight line on the cast iron base. In regard to measurement equipment, the test platform included a sensor, sensor signal conditioner and dynamic data acquisition. The sensor was an IEPE (Integrated Electronics Piezo-Electric) accelerometer, model CT1500L, as shown in Fig. 4(b). The sensor signal conditioner was an eight-channel signal conditioner, model PCB 483C05, as shown in Fig. 4(c). The dynamic data acquisition model was a TMR-200 with a sampling frequency of up to 100 kHz, which could collect analogue signals such as strain, voltage, and temperature, as shown in Fig. 4(d). The entire measurement apparatus was used for high-resolution acquisition of vibration signals in real time. In particular, the electrical signal output by the CT1500L was amplified, filtered, and linearised by the 483C05 to generate

a stable analogue signal, which was then converted into a digital signal through the TMR-200 to achieve real-time and high-precision dynamic data acquisition. The technical parameters of the stepper motor and the sensor are shown in Tables 1 and 2.

The experiment was conducted to simulate the three working conditions of normal, imbalanced and misaligned operation, and to collect real vibration signals from the rotor-bearing system under these working conditions. The sensor was located on the intermediate bearing housing to measure the vertical vibration signal in real time. As the normal operating conditions, we used the comprehensive test platform of the rotor-bearing system based on the design and assembly requirements, and artificially changed some installation parameters to cause imbalance or

misalignment. To create imbalance, we screwed three bolts into the threaded holes around a special flange, which had six threaded holes in total. The weight of all bob-weight bolts was 0.35 kg, representing about 0.3% of the shaft weight. For misalignment, we changed the intermediate bearing vertical

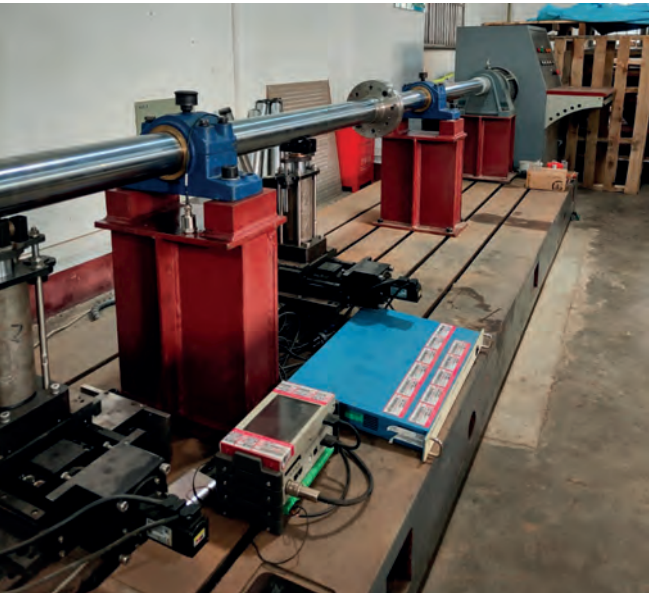
displacement by about 2 mm, which represented about 2.5% of the shaft diameter. The stepper motor speed was set to 500 rpm, the output speed of the reducer was 50 rpm, and the operating frequency of the shafts was 0.87 Hz.

Tab. 1. Technical parameters of the stepper motor

Parameter	Value
Power	5.5 kW
Voltage	380 V, three-phase, 50 Hz
Speed range	0–1420 r/min

Tab. 2. Technical parameters of the sensor

Parameter	Value
Sensitivity	5100 mV/(m/s ²)
Measurement range	9.8 m/s ²
Frequency range	0.2–500Hz



(a)



(b)



(c)



(d)

Fig. 4. Comprehensive test platform for the rotor-bearing system

DATA DESCRIPTION

The sampling frequency was 100 Hz, and the total number of sampling points was 6,600,000. As summarised in Table 3, we considered three health conditions for the rotor-bearing system: one was the healthy condition, and two represented rotor faults. Three groups of sample data were selected for the working conditions of normal operation, imbalance and misalignment. The total number of samples for all working conditions was 3,300, and the average sample data for each working condition was three equal parts, so the number of data samples for each working condition was 1,100. The sizes of the training, validation and test sets were 2,700, 300 and 300 samples, respectively. In view of the consideration of frequency resolution, when the sampling frequency was 100 Hz, we could have increased the number of sampling points for each sample data. However, it might not be increased blindly as the size of the two-dimensional image converted from GAF would have increased correspondingly, which would seriously reduce the computational efficiency of the deep learning model. For this purpose, the length of each data sample was finally set to 2,000. The time-domain waveform for the sample vibration data is shown in Fig. 5.

Tab. 3. Summary of the three health states of the rotor-bearing system considered in the experiments

Category	Description	Label
1	No fault	H
2	Imbalance	F1
3	Misalignment	F2

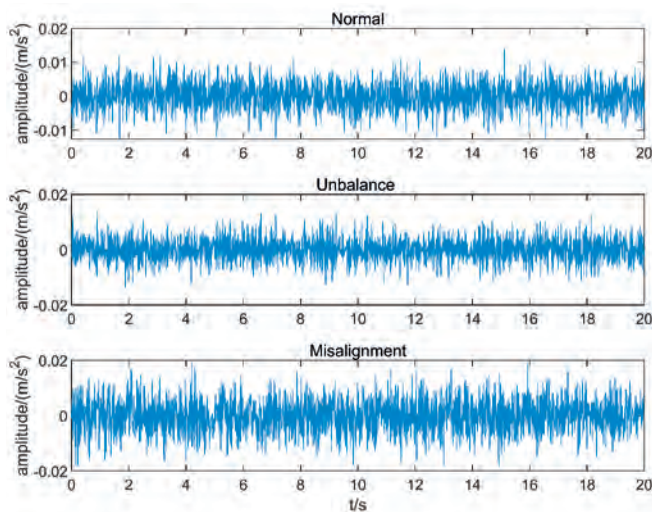


Fig. 5. Time-domain waveform of the sample vibration data under three operating conditions

IMPLEMENTATION

WTD-VMD was performed on the data, which were evenly divided into the previously constructed datasets. Multiple IMFs with limited bandwidth were decomposed by the original signal. The time-domain waveforms for the five-layer IMFs are shown in Figs. 6–8 for the normal, imbalanced and misaligned working conditions. It can be seen from the time-domain waveform that the IMFs were arranged from low to high frequency, and the corresponding features of the original signal that could not be directly found were extracted. Spearman's correlation coefficient was calculated to assess how well each IMF was related to the original signal, for a non-Gaussian and nonlinear original signal. Table 4 gives Spearman's correlation coefficients for the five-layer IMFs under the three working conditions. The optimal IMFs were selected as IMF4 for normal conditions, IMF5 for imbalance, and IMF5 for misalignment, and their frequency spectra were calculated by Fourier transform as shown in Fig. 9. The results for imbalance and misalignment show distinct reflected spectral peaks, which could be regarded as a salient feature of the original signal. The amplitude under imbalance and misalignment conditions was also much larger than under normal operation.

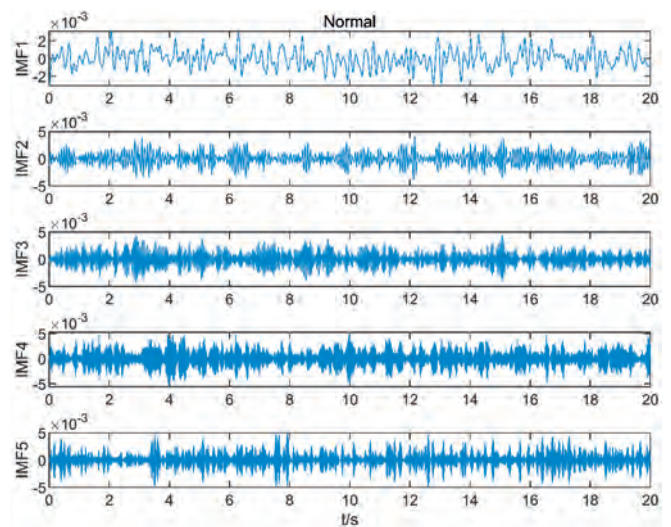


Fig. 6. Time-domain waveforms for the five-layer IMFs under normal conditions

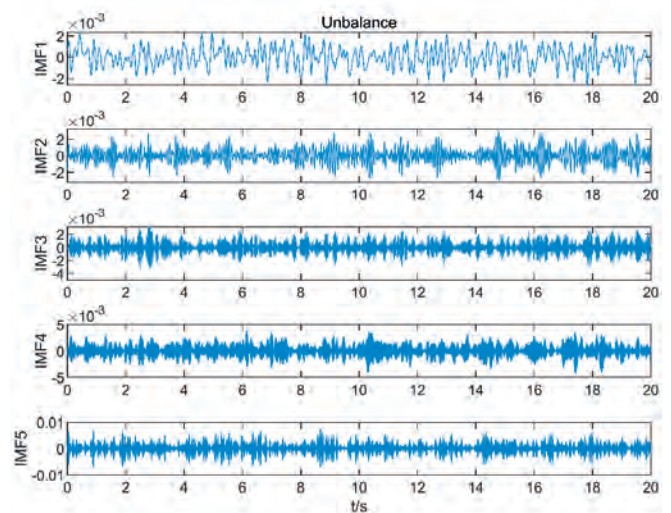


Fig. 7. Time-domain waveforms for the five-layer IMFs under imbalance conditions

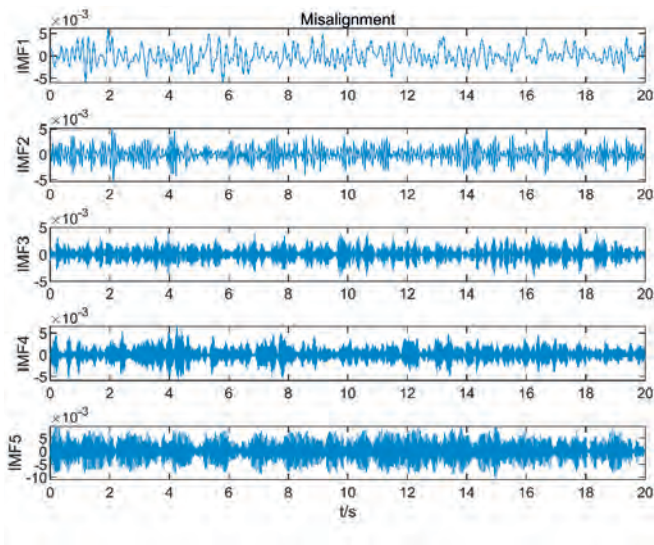


Fig. 8. Time-domain waveforms for the five-layer IMFs under misalignment conditions

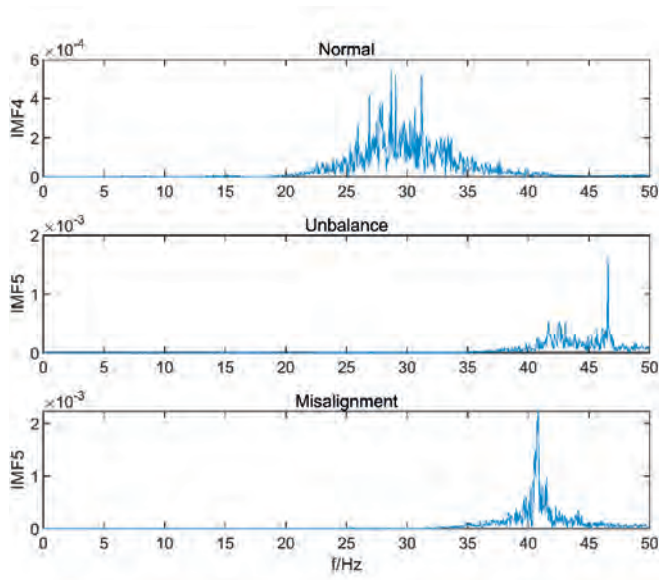


Fig. 9. Frequency spectra for the optimal IMFs under three working conditions

Tab. 4. Spearman's correlation coefficients for five-layer IMFs under three working conditions

	Normal	Imbalance	Misalignment
IMF1	0.332	0.301	0.356
IMF2	0.417	0.341	0.341
IMF3	0.477	0.375	0.337
IMF4	0.573	0.479	0.401
IMF5	0.511	0.716	0.739

A GAF image contains a GASF image and a GADF image. The dimensions of the GAF image were 100×100 in this study, and GAF images of the original signal under the

three working conditions are shown in Fig. 10. The fault features were submerged by the strong background noise, meaning the corresponding working conditions were difficult to distinguish. However, from the GAF images of the optimal IMFs under the three working conditions shown in Fig. 11, it can be seen that the images of the signal processed with WTD-VMD were clearly distinguished compared with the above GAF images. In this process, only the GASF image was considered, since the difference in the training accuracy was not obvious in many experiments when both GAF images were used to transform a one-dimensional time series.

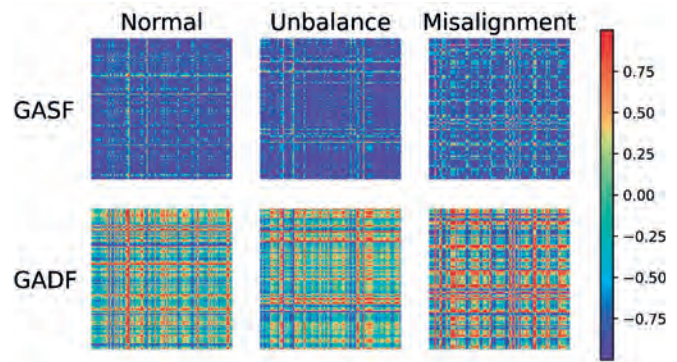


Fig. 10. GAF images of the original signal under three working conditions

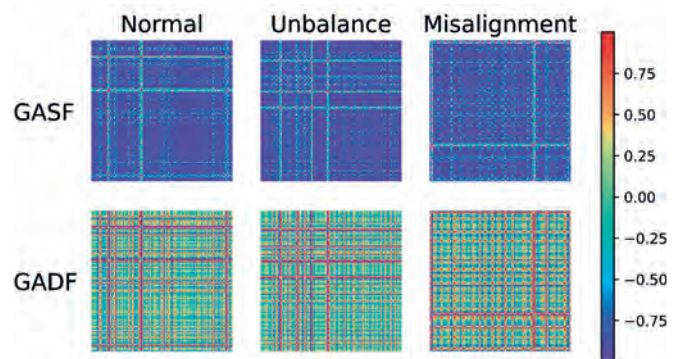


Fig. 11. GAF images of the optimal IMFs under three working conditions

The architecture-related hyperparameters for IDRSN were set as follows in the experiments. In order to demonstrate the training effect of inserting a soft threshold as a nonlinear transformation layer, we used one convolutional layer as the main architecture, with an RSBU between the convolutional layer and the pooling layer. The number of convolutional kernels was 12, and the size of the convolutional kernels was 3×3. The stride was set to one and the padding to one in the convolutional layer. The output of the input layer was passed to the input of convolution layer to calculate the feature map, and a soft threshold in which the output feature map was the same size as the input feature map was inserted as a nonlinear transformation layer. The output of the convolution layer

and nonlinear transformation layer was then processed by batch normalisation, a ReLU activation function and global average pooling, in sequence. The output feature map was flattened and its input was passed to the fully connected layer. Finally, the fault classification results were obtained using a softmax function.

Each batch contained 32 samples, and the training mean square error (MSE) and training accuracy were calculated over 10 epochs. As shown in Fig. 12, the training MSE was reduced from 0.186 to 0.073, and the training accuracy was increased from 59% to 87%. The loss function of the neural network converged to a stable state. It can be seen that the present model had good robustness in terms of dealing with noisy samples. The evaluation results for this model were calculated by substituting the divided test set into the trained model. The test accuracy of fault diagnosis was $85.3\% \pm 1.21\%$ at a 95% confidence interval.

It can be seen from the confusion matrix in Fig. 13 that the test accuracy for misalignment was 100%. This was because that the fault features of misalignment had 2x vibration, and were therefore markedly different from the signal features for normal or imbalanced working conditions. In the test data, the amplitude of vibration caused by misalignment was much greater than that under normal conditions, but was similar to that under imbalanced conditions. However, the fault features of imbalanced operation and signal features of normal conditions were very similar, with 1x vibration, although the amplitude increased under imbalanced conditions. As a consequence, it could be for this reason that fault diagnosis had certain deviation under imbalance, resulting in about 28% of the test sets being classified as normal. Overall, IDRSN has a high accuracy of fault diagnosis under interference from strong background noise, and can be used to carry out fault diagnosis of rotor-bearing systems under actual working conditions.

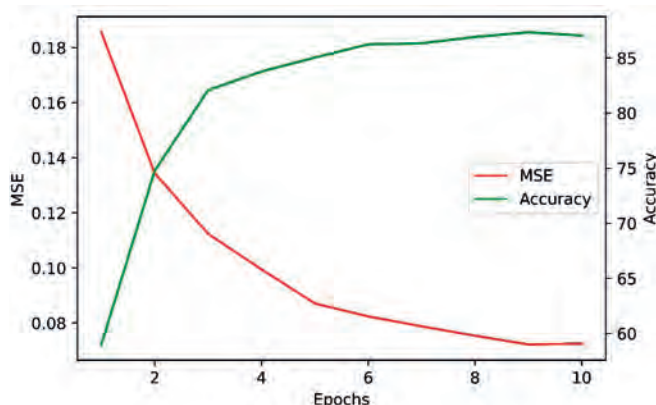


Fig. 12. Changes in MSE and accuracy based on IDRSN

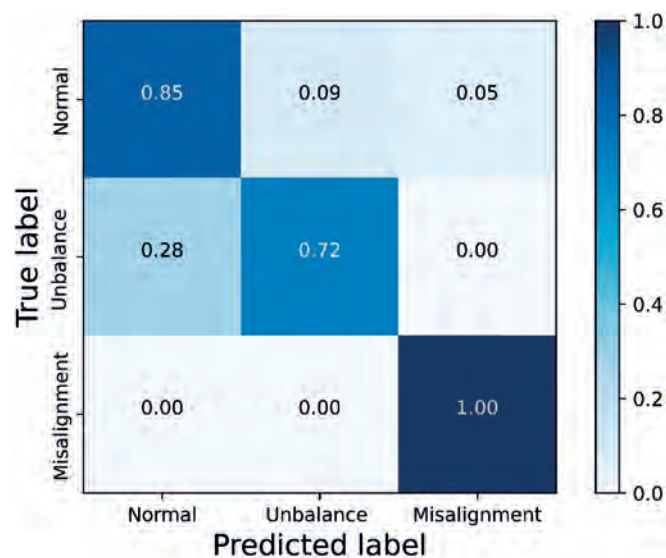


Fig. 13. Confusion matrix for fault diagnosis results

COMPARISON EXPERIMENT

An experiment was carried out to compare the results from using WTD-VMD for feature extraction with those of two other deep learning methods, ConvNet and ResNet. These two deep learning methods were compared with DRSN and were used with and without WTD-VMD, to investigate its effectiveness. The architectures of ConvNet and ResNet are shown in Fig. 2; the convolution layer, pooling layer, activation function and fully connected layer were consistent with those in IDRSN, in order to demonstrate the classification results from using a soft threshold as a nonlinear transformation layer on the same noisy signals. The results for the test accuracy and computational time are shown in Fig. 14.

With regard to the feature extraction methods, it can be seen that for all of the deep learning methods, the test accuracy obtained by substituting datasets processed with WTD-VMD into the model was greater than the test accuracy obtained by directly substituting the datasets into the model. For the same premise condition, the test accuracy based on ConvNet, ResNet and DRSN increased from 51.33% to 62%, 58.3% to 81.33% and 70.99% to 89.67%, respectively. The use of WTD-VMD with these three deep learning methods improved the test accuracy by about 10–23%; however, the use of the feature extraction method had no obvious effect on the computational time. As the complexity of the deep learning architecture increased, the calculation results showed that in ResNet, due to the identity shortcuts that were involved, many identical mappings were performed on this layer when the residual term was zero. This might reduce the computational time when datasets with salient features are substituted as input layers, but for the ConvNet with a classical architecture, its computational time might be mainly affected by batch size.

DRSN achieved a higher test accuracy of fault diagnosis compared with the traditional ConvNet and ResNet when

trained on the same datasets. When all the datasets were used with WTD-VMD, the test accuracy achieved by DRSN improved by 27.67% and 8.34% compared to ConvNet and ResNet, respectively. Furthermore, the deep learning model with a simpler architecture had a lower computational time. When all the datasets were used without WTD-VMD, the computation time for ConvNet was the lowest, at 542 s, and that for ResNet was the second, at 741 s. The computation time for DRSN was the higher, at 756 s. Hence, although the proposed method was better than other methods in terms of efficiency and accuracy, there was no obvious advantage in computation time.

The training errors for ConvNet, ResNet and DRSN are shown in Fig. 15 for the dataset processed with WTD-VMD. The values for DRSN, ResNet and ConvNet at the 10th epoch were 0.0187, 0.0298 and 0.0312 respectively. It can be seen that the training error of DRSN and ResNet decreases faster than that of ConvNet, but that DRSN has the lowest overall training error. Neither over-fitting nor under fitting were observed for IDRSN, indicating its good generalisation ability.

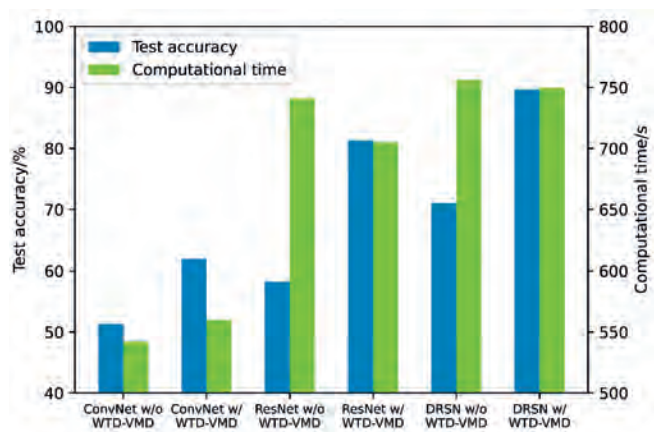


Fig. 14. Comparison of results for different fault diagnosis methods

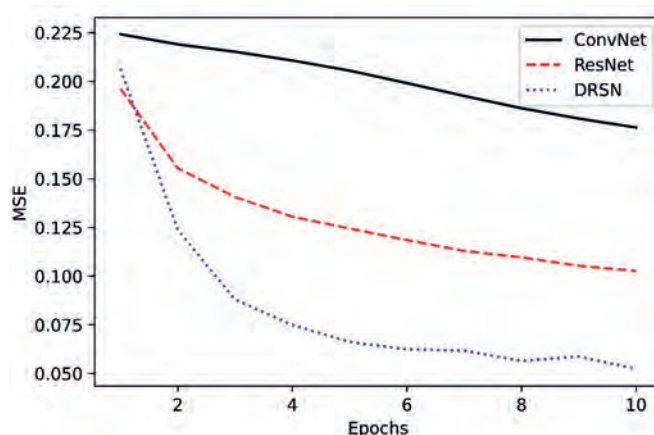


Fig. 15. Comparison of training error for three deep learning methods

CONCLUSION

Imbalance and misalignment are unavoidable in a rotor-bearing system. In this paper, a fault diagnosis method based on IDRSN has been presented with the aim of achieving end-to-end fault diagnosis of a rotor-bearing system. A simulated fault experiment was conducted on a comprehensive test platform of a rotor-bearing system, and the effectiveness of the proposed method under three working conditions (normal operation, imbalance and misalignment) was explored through a simulated fault experiment. The work in this paper can be summarised as follows:

- 1) A comprehensive test platform for a rotor-bearing system was built to simulate these faults, and real vibration signals were collected under corresponding working conditions. A total of 3,300 groups of original data representing different fault modes were collected to provide enough data for the fault diagnosis model.
- 2) WTD-VMD was applied to the real vibration signal data, which were evenly divided into three datasets. The time domain waveforms of IMFs under three working conditions of normal, unbalance and misalignment were presented after filtering and decomposition. Significant differences in corresponding fault modes were seen in the frequency domain waveforms of the IMFs. The optimal IMFs were selected based on Spearman's correlation coefficient and transformed into two-dimensional images via GASF. Datasets for the deep learning models were created based on these 3,300 two-dimensional images.
- 3) An end-to-end multi-fault diagnosis model of a rotor-bearing system was established, which was shown to have good robustness when dealing with noisy samples. The true test accuracy of the present model at a 95% confidence interval may range from 84.09–86.51%, and the values of the test accuracy for normal, imbalanced and misaligned conditions calculated from the confusion matrix were 85%, 72%, and 100%, respectively. The proposed model was found to give good classification results for fault diagnosis under misalignment.
- 4) ConvNet and ResNet were compared with DRSN, with and without WTD-VMD. With respect to the feature extraction methods, we found that the test accuracy when WTD-VMD was included in the model was greater than without WTD-VMD, regardless of the deep learning method used, and WTD-VMD was shown to improve the test accuracy by about 10–23%. The proposed method had a lower training error than ConvNet and ResNet, and the average fault diagnosis accuracy was higher by 27.67% and 8.34%, respectively.

In conclusion, IDRSN has the advantages of high modularity, fast convergence speed, high diagnostic accuracy, and good robustness to noise. Our approach will be of great value in terms of creating engineering applications based on deep learning for fault diagnosis of rotor-bearing systems.

ACKNOWLEDGEMENTS

The authors gratefully acknowledge the National Natural Science Foundation of China (51839005) for funding. They are also grateful to the anonymous reviewers for their criticism, which was helpful in improving this manuscript.

REFERENCES


1. L. Murawski, "Identification of shaft line alignment with insufficient data availability," *Polish Maritime Research*, vol. 16, pp. 35-42, 2009.
2. A. Ursolov, Y. Batrak and W. Tarelko, "Application of the optimization methods to the search of marine propulsion shafting global equilibrium in running condition," *Polish Maritime Research*, vol. 26, pp. 172-180, 2019.
3. E. B. Donald and T. H. Charles, "Fundamentals of rotating machinery diagnostics," American Society of Mechanical Engineers, New York, 2002.
4. J. L. Perez-Ruiz, Y. Tang and I. Loboda, "Aircraft engine gas-path monitoring and diagnostics framework based on a hybrid fault recognition approach," *Aerospace*, vol. 8, 2021.
5. L. Bechou, L. Angrisiani, Y. Ousten, D. Dallet, H. Levi, P. Daponte, and Y. Danto, "Localization of defects in die-attach assembly by continuous wavelet transform using scanning acoustic microscopy," *Microelectronics Reliability*, vol. 39, pp. 1095-1101, 1999.
6. M. E. Moreno-Sánchez, J. A. Villarraga-Ossa and R. Moreno-Sánchez, "Diagnóstico de fallas tempranas de rodamientos en mecanismos susceptibles al desbalanceo y a la desalineación," *Revista UIS Ingenierías*, vol. 18, pp. 187-198, 2019.
7. R. G. Desavale, "Dynamics characteristics and diagnosis of a rotor-bearing's system through a dimensional analysis approach an experimental study," *Journal of Computational and Nonlinear Dynamics*, vol. 14, 2018.
8. H. Talhaoui, A. Menacer, A. Kessal, and A. Tarek, "Experimental diagnosis of broken rotor bars fault in induction machine based on Hilbert and discrete wavelet transforms," *International Journal of Advanced Manufacturing Technology*, vol. 95, pp. 1399-1408, 2018.
9. O. C. Kalay, O. Dogan, C. Yuce, and F. Karpat, "Effects of tooth root cracks on vibration and dynamic transmission error responses of asymmetric gears: A comparative study," *Mechanics Based Design of Structures and Machines*, 2023.
10. J. L. Liu, Z. Gu and S. Y. Liu, "Research on MDO of ship propulsion shafting dynamics considering the coupling effect of a propeller-shafting-hull system," *Polish Maritime Research*, vol. 30, pp. 86-97, 2023.
11. O. Janssens, V. Slavkovikj, B. Vervisch, K. Stockman, M. Loccufier, S. Verstockt, R. Van de Walle, and S. Van Hoecke, "Convolutional neural network based fault detection for rotating machinery," *Journal of Sound and Vibration*, vol. 377, pp. 331-345, 2016.
12. Y. LeCun, Y. Bengio and G. Hinton, "Deep learning," *Nature*, vol. 521, pp. 436-444, 2015.
13. D. Hoang and H. Kang, "Rolling element bearing fault diagnosis using convolutional neural network and vibration image," *Cognitive Systems Research*, vol. 53, pp. 42-50, 2019.
14. K. Bousbai, J. Morales-Sanchez, M. Merah, and J. L. Sancho-Gomez, "Improving hand gestures recognition capabilities by ensembling convolutional networks," *Expert Systems*, vol. 39, 2022.
15. K. He, X. Zhang, S. Ren, and J. Sun, "Deep residual learning for image recognition," in *CVPR*, 2016.
16. M. Shafiq and Z. Q. Gu, "Deep Residual Learning For Image Recognition: A Survey," *Applied Sciences-Basel*, vol. 12, 2022.
17. S. Tang, S. Yuan and Y. Zhu, "Deep learning-based intelligent fault diagnosis methods toward rotating machinery," *IEEE Access*, vol. 8, pp. 9335-9346, 2020.
18. M. Zhao, S. Zhong, X. Fu, B. Tang, and M. Pecht, "Deep residual shrinkage networks for fault diagnosis," *IEEE Transactions on Industrial Informatics*, vol. 16, pp. 4681-4690, 2020.
19. M. Bach-Andersen, B. Romer-Odgaard and O. Winther, "Deep learning for automated drivetrain fault detection," *Wind Energy*, vol. 21, pp. 29-41, 2018-01-01 2018.
20. P. Kumar and A. S. Hati, "Transfer learning-based deep CNN model for multiple faults detection in SCIM," *Neural Computing & Applications*, vol. 33, pp. 15851-15862, 2021.
21. Y. X. Huangfu, E. Seddik, S. Habibi, A. Wassyng, and J. Tjong, "Fault detection and diagnosis of engine spark plugs using deep learning techniques," *SAE International Journal Of Engines*, vol. 15, pp. 515-525, 2022.
22. D. H. Lim and K. S. Kim, "Development of deep learning-based detection technology for vortex-induced vibration of a ship's propeller," *Journal of Sound and Vibration*, vol. 520, p. 116629, 2022.

23. A. Glaeser, V. Selvaraj, S. Lee, Y. Hwang, K. Lee, N. Lee, S. Lee, and S. Min, "Applications of deep learning for fault detection in industrial cold forging," *International Journal Of Production Research*, vol. 59, pp. 4826-4835, 2021.
24. Z. Korczewski and K. Marszałkowski, "Energy analysis of propulsion shaft fatigue process in rotating mechanical system Part I: Testing significance of influence of shaft material fatigue excitation parameters," *Polish Maritime Research*, vol. 25, pp. 211-217, 2018.
25. D. L. Donoho, "De-noising by soft-thresholding," *IEEE Transactions on Information Theory*, vol. 41, pp. 613-627, 1995.
26. K. Dragomiretskiy and D. Zosso, "Variational mode decomposition," *IEEE Transactions on Signal Processing*, vol. 62, pp. 531-544, 2014.
27. Z. Wang and T. Oates, "Imaging time-series to improve classification and imputation," in *IJCAI*, 2015

PRACTICAL FINITE-TIME EVENT-TRIGGERED CONTROL OF UNDERACTUATED SURFACE VESSELS IN PRESENCE OF FALSE DATA INJECTION ATTACKS

Liping Chen*

Poland

Minghua Sun 

College of Navigation, Jimei University, China

Wang Li

Department of Youth League Committee, China

* Corresponding author: lpchen@jmu.edu.cn (Liping Chen)

ABSTRACT

The results of studies on a trajectory-tracking problem affected by false data injection attacks (FDIAs) and internal and external uncertainties are presented in this paper. In view of the FDIAs experienced by the system, we compensate for the serious navigation deviation caused by malicious attacks by designing an online approximator. Next, we study the internal and external uncertainties introduced by environmental factors, system parameter fluctuations, or sensor errors, and we design adaptive laws for these uncertainties to approximate their upper bounds. To further enhance the response velocity and stability of the system, we introduce finite-time technology to ensure that the unmanned underactuated surface vessels (USVs) reach the predetermined trajectory-tracking target within finite time. To further reduce the update frequency of the controller, we introduced event-triggered control (ETC) technology. This saves the system's communication resources and optimizes the system. Through Lyapunov stability theory, a strict and complete stability analysis is provided for the control scheme. Finally, the effectiveness of the control scheme is verified using two sets of simulations.

Keywords: Unmanned underactuated surface vessels; False data injection attacks; Internal and external uncertainty; Finite-time control; Event-triggered control

INTRODUCTION

In recent years, unmanned underactuated surface vessels (USVs) have received widespread attention due to the continuous development of the maritime economy [1]. Unmanned USVs lack lateral drive, which requires researchers to consider more aspects when they design control schemes [2]. We are currently in the information age, and unmanned USVs are also susceptible to cyber-attacks. In particular, false data injection attacks (FDIAs) can cause serious navigation deviations in USVs [3]. Therefore, a more complete control scheme must be designed to deal with the above challenges.

In practice, USVs are inevitably affected by external interference. Under the constraints of external interference, feedback linearization is the most commonly used design method [4]. This method makes the problem simple by introducing appropriate feedback to linearize some parts of or the entire nonlinear system. However, although nonlinear problems can be transformed into linear problems through this method, complex mathematical transformations may be required to achieve this transformation. To avoid similar problems, the authors of [5] automatically adjusted the parameters to respond to environmental changes by introducing adaptive technology. This approach caused the control design to no longer be dependent on an accurate

system model. However, adaptive controllers may overreact to noise or brief perturbations, resulting in unnecessary controller adjustments. To further optimize control, the authors of [6], [7] introduced a disturbance observer (DO) to estimate and compensate for external disturbances in real time. Although the perturbation observer does not completely rely on an accurate system model, it requires some prior knowledge of the model. Therefore, usually, the DO will combine adaptive neural networks (NNs), fuzzy control, and other methods to design the control scheme. The authors of [1] further introduced a finite-time disturbance observer (FTDO) to compensate for external interference. The FTDO can complete disturbance estimation within finite time, which makes its response to disturbances faster than that of the traditional DO.

Due to the modelling technology and the complex structure of the USV itself, the USV mathematical model has unmodelled dynamics. These uncertain dynamics caused by model parameter perturbations, unmodelled dynamics, etc., are called internal uncertainties. The authors of [8] designed a control scheme by combining model predictive control (MPC) and online parameter estimation technology. When system parameters change or there is a disturbance, this scheme uses online estimated parameters to update the model, thereby adapting to the uncertain dynamics of the system to a certain extent [9]. However, MPC needs to solve an optimization problem at each control step. For a system with multiple constraints, the computational complexity will increase dramatically. In addition, the performance of MPC is highly dependent on the accuracy of the model used. If the model deviates significantly from the real system, it may not achieve the desired performance [10]. The authors of [11], [12] used fuzzy and neural networks, respectively, to reconstruct the uncertain dynamics of the system. However, they also face the same problem as MPC, that is, the computing requirements of the system can be high. The authors of [13], [14] used the output feedback design method to estimate the unmeasured state within the system. Compared with NNs, state observers provide a structured approach for estimating unmeasured states. The design logic and principles are usually clear and explainable. The NNs are often regarded as 'black box' models, and their inner workings are difficult to explain. However, the performance of state observers is often highly dependent on accurate knowledge of the system model. If the system model is inaccurate or contains significant modelling errors, the performance of the observer may be severely affected.

In practice, to ensure the safety of the USVs, trajectory tracking needs to be completed within finite time. This may be difficult to achieve with traditional control strategies. Unlike traditional asymptotic stability control strategies, finite time control (FTC) strategies ensure stability and a given tracking performance within a predetermined time. The authors of [15]–[17] designed a finite-time trajectory-tracking control scheme. They reduced possible instability or undesirable behaviour during the transition by reducing the transition time of the system from the initial state to the

desired state. The authors of [1], [18] further introduced FTDO based on [15]–[17], which further improved the steady-state performance of the system. The control signal updates of most of the above control schemes are based on predetermined, fixed time intervals, without considering the system status or external events. Event-triggered control (ETC) only updates control inputs when certain events or conditions are met, rather than at fixed time intervals. Compared with fixed time intervals, communication bandwidth can be saved and energy consumption can be reduced [19], [20]. The authors of [19] designed a model-based time-triggered control scheme. The authors of [20] further considered actuator faults and designed an adaptive Proportional-integral-derivative (PID) fault-tolerant control scheme based on ETC. However, none of the above literature considers the potential impact of the network environment on the USV system.

The authors of [21] developed a predictive compensator based on event-triggered model predictive control. This strategy can mitigate the effects of external interference and input restrictions under cyberattacks such as denial of service (DoS) attacks. The integration of a model predictive controller with a nonlinear disturbance observer in this strategy enables the precise estimation of and compensation for disturbances. In addition, the predictive compensator effectively reduces the impact of cyberattacks, while the event-triggering mechanism saves computing resources. The authors of [22] discussed the security control of multiple autonomous ground vehicles when they faced DoS network attacks and proposed a distributed security formation control algorithm. The algorithm optimizes communication resources using a model-based dynamic event-triggering mechanism and a positive minimum inter-event time. The authors of [23] studied the adaptive event-triggered path tracking control of a USV based on double-layer virtual ship guidance under spoofing attacks. They introduced an adaptive virtual ship model for smooth path generation and a robust adaptive control algorithm to compensate for spoofing attacks. This method combines event-triggering rules with adaptive compensation technology to improve the accuracy and stability of the closed-loop control system. These studies provide innovative solutions for USV security against cybersecurity threats. The above literature did not consider FDIAs.

In the current network security environment, USVs face the threat of multiple network attacks. FDIAs represent a particularly serious threat. This attack disrupts the normal operation of the ship by injecting false or misleading information into the system.

PROBLEM FORMULATION AND PRELIMINARIES

In this paper, we use a mathematical model of USVs with three degrees of freedom. The model contains information such as the USV's mass, displacement, and yaw moment. The specific form is as follows [24] [25]:

$$\begin{cases} \dot{x} = u \cos(\varphi) - v \sin(\varphi) \\ \dot{y} = u \sin(\varphi) + v \cos(\varphi) \\ \dot{\varphi} = r \end{cases} \quad (1)$$

$$\begin{cases} \dot{u} = \frac{1}{m_u} [\tau_u^f + f_u(V) + d_u] \\ \dot{v} = \frac{1}{m_v} [f_v(V) + d_v] \\ \dot{r} = \frac{1}{m_r} [\tau_r^f + f_r(V) + d_r] \end{cases} \quad (2)$$

$$\begin{cases} f_u(V) = (m_v v r - Y_r r^2 + X_u u + X_{u|v|} |u| |v|) \\ f_v(V) = (Y_v v + Y_{v|v|} |v| |v| + Y_{v|r} |r| |v| + Y_r r - m_u u r + Y_{v|v|} |v| |r| + Y_{v|r} |r| |r|) \\ f_r(V) = [(m_u - m_v) u v + Y_r u r + N_v v + N_r r + N_{v|v|} |v| |v| + N_{v|r} |v| |r| + N_{r|v|} |v| |r| + N_{r|r} |r| |r|] \end{cases} \quad (3)$$

where x , y , and φ represent the position and heading angle of the USV in the geodetic coordinate system, respectively. u , v , and r represent the velocity of the USV in different directions, respectively. $f_u(V)$, $f_v(V)$, and $f_r(V)$ represent nonlinear dynamics. m_i ($i = u, v, r$) represents inertial masses. d_u , d_v , and d_r represent external interference items. τ_u^f and τ_r^f are the control inputs disturbed by the FDIAs. The mathematical expressions for these variables are as follows [26]:

$$\begin{cases} \tau_u^f = \tau_u + \xi_u \\ \tau_r^f = \tau_r + \xi_r \end{cases} \quad (4)$$

where ξ_u and ξ_r are the FDIAs experienced by the system.

Remark 1: The physical equipment and controllers of autonomous unmanned vessels are often connected to each other through networks. This connection method makes the system vulnerable to cyberattacks. The focus of this article is to explore a specific form of attack related to Eq. (3), namely additive FDIAs. The core principle of this attack is that the attacker maliciously injects false signals into the communication link between the controller and the actuator, thereby affecting or destroying the normal operation of the system. Such attacks can have serious negative impacts on the safety and performance of autonomous unmanned vessels.

The assumptions and required lemmas in this study are as follows:

Assumption 1 [25]: The $f_i(V)$, $i = (u, v, r)$, are unknown. Interference items outside the system, that is, external interference d_i , $i = (u, v, r)$, are unknown and bounded. That is, there are unknown positive constants η_i , such that d_i satisfies $|d_i| \leq \eta_i$.

Assumption 2: The sway velocity v is passively bounded.

Lemma 1 [27]: Assume that there is a positive definite Lyapunov function $V(x) : \Omega_0 \rightarrow R$ and any scalars $a > 0$, $b > 0$, and $0 < \kappa < 1$, so that the inequality $\dot{V}(x) + aV(x) + bV^\kappa(x) \leq 0$ holds; then, the system is stable in finite time, and its adjustment time satisfies

$$T \leq \frac{1}{a(1-\kappa)} \ln \frac{aV^{1-\kappa}(x_0) + b}{b} \quad (4)$$

where $V(x_0)$ is the initial value of $V(x)$.

Lemma 2 [28] [29]: For any $\lambda > 0$ and $x \in R$, the following relationship is satisfied:

$$0 < |x| - x \tanh\left(\frac{x}{\lambda}\right) \leq 0.2785\lambda \quad (5)$$

CONTROL DESIGN AND STABILITY ANALYSIS

DESIGN OF VIRTUAL CONTROL LAWS

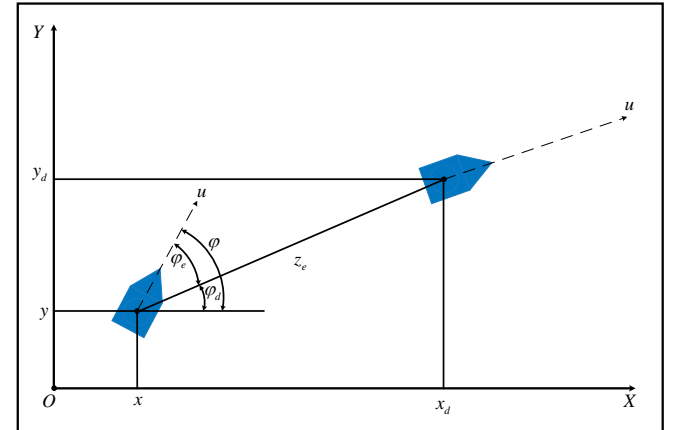


Fig. 1. General framework of USV trajectory-tracking control

The tracking error is defined as follows:

$$\begin{bmatrix} x_e \\ y_e \\ \varphi_e \end{bmatrix} = J^T(\varphi) \begin{bmatrix} x - x_d \\ y - y_d \\ \varphi - \varphi_d \end{bmatrix} \quad (6)$$

$$J^T(\varphi) = \begin{bmatrix} \cos \varphi & \sin \varphi & 0 \\ -\sin \varphi & \cos \varphi & 0 \\ 0 & 0 & 1 \end{bmatrix} \quad (7)$$

where x_e is the lateral error, y_e is the longitudinal error, φ_e is the heading angle error, and $z_e = \sqrt{x_e^2 + y_e^2}$ [23]. $J^{-1}(\varphi)$ is a rotation matrix, and $J^T(\varphi) = J^{-1}(\varphi)$. x_d , y_d , and φ_d are the reference position and reference heading angle, respectively. α_u and α_r are virtual control variables designed later. The specific form of the reference heading is as follows:

$$\varphi_d = \begin{cases} \arctan\left(\frac{\dot{y}_d}{\dot{x}_d}\right), & z_e = 0 \\ 0.5[1 - \text{sgn}(x_e)]\text{sgn}(y_e) + \arctan\left(\frac{y_e}{x_e}\right), & \text{other} \end{cases} \quad (8)$$

Then, we can obtain the new kinematic error equation as follows:

$$\begin{cases} \dot{x}_e = z_e \cos \varphi_d \\ \dot{y}_e = z_e \sin \varphi_d \\ \dot{\varphi}_e = \varphi - \varphi_d \end{cases} \quad (9)$$

The Lyapunov function is defined as follows:

$$H_1 = \frac{1}{2} z_e^2 + \frac{1}{2} \varphi_e^2 \quad (10)$$

By deriving Eq. (10), we can obtain

$$\begin{aligned} \dot{H}_1 &= z_e \dot{z}_e + \varphi_e \dot{\varphi}_e = x_e \dot{x}_e + y_e \dot{y}_e + \varphi_e \dot{\varphi}_e \\ &= z_e [\cos \varphi_d (\dot{x} - \dot{x}_d) + \sin \varphi_d (\dot{y} - \dot{y}_d)] + \varphi_e (r - \dot{\varphi}_d) \\ &= z_e [u_e \cos \varphi_e - v \sin \varphi_e + \alpha_u \cos \varphi_e - \dot{x}_d \cos \varphi_d - \dot{y}_d \sin \varphi_d] + \varphi_e (r - \dot{\varphi}_d) \end{aligned} \quad (11)$$

According to Eq. (11), the virtual control variables are designed as follows:

$$\begin{cases} \alpha_u = \frac{1}{\cos \varphi_e} [\eta_{11} z_e + \eta_{12} \text{sig}^\nu(z_e) + \dot{x}_d \cos \varphi_d + \dot{y}_d \sin \varphi_d + v \sin \varphi_e] \\ \alpha_r = -\eta_{21} \varphi_e - \eta_{22} \text{sig}^\nu(\varphi_e) + \dot{\varphi}_d \end{cases} \quad (12)$$

where η_{11} , η_{12} , η_{21} , η_{22} , and ν are positive definite parameters. $\text{sig}^\nu(\cdot) = |\cdot|^\nu \text{sgn}(\cdot)$, where $\text{sgn}(\cdot)$ is the sign function.

SURGE AND YAW ADAPTIVE CONTROL LAWS DESIGN

To avoid the derivation of the virtual controls α_u and α_r , we introduce the following filter:

$$\begin{cases} \kappa_u \dot{\beta}_u + \beta_u = \alpha_u \\ \kappa_r \dot{\beta}_r + \beta_r = \alpha_r \end{cases} \quad (13)$$

where κ_u and κ_r are positive definite parameters.

According to Eq. (13), the filter error is defined as follows:

$$\begin{cases} e_u^f = \beta_u - \alpha_u \\ e_r^f = \beta_r - \alpha_r \end{cases} \quad (14)$$

By deriving Eq. (14), we can obtain

$$\begin{cases} \dot{e}_u^f = \dot{\beta}_u - \dot{\alpha}_u \\ \dot{e}_r^f = \dot{\beta}_r - \dot{\alpha}_r \end{cases} \quad (15)$$

Substituting Eq. (12) into Eq. (15), we can obtain

$$\begin{cases} \dot{e}_u^f = \dot{\beta}_u - \dot{\alpha}_u = -\frac{e_u}{\kappa_u} + \chi_u \\ \dot{e}_r^f = \dot{\beta}_r - \dot{\alpha}_r = -\frac{e_r}{\kappa_r} + \chi_r \end{cases} \quad (16)$$

where χ_u and χ_r are continuous bounded functions, and the maximum values are P_u and P_r .

The velocity tracking error is defined as follows:

$$\begin{cases} u_e = u - \beta_u \\ r_e = r - \beta_r \end{cases} \quad (17)$$

By taking the time derivative of Eq. (17) and substituting Eqs. (2) and (3) into it, we can obtain

$$\begin{cases} m_u \dot{u}_e = \tau_u + \Theta_u + \xi_{d_u} - m_u \dot{\beta}_u \\ m_r \dot{r}_e = \tau_r + \Theta_r + \xi_{d_r} - m_r \dot{\beta}_r \end{cases} \quad (18)$$

where $\xi_{d_u} = \xi_u + \bar{d}_u$, $\xi_{d_r} = \xi_r + \bar{d}_r$, $\Theta_u = \bar{f}_u(V)$, and $\Theta_r = \bar{f}_r(V)$. \bar{d}_u , \bar{d}_r , $\bar{f}_u(V)$, and $\bar{f}_r(V)$ are the upper bounds of d_u , d_r , $f_u(V)$, and $f_r(V)$, respectively.

The design control law and adaptive law are as follows:

$$\begin{cases} \tau_u = -\eta_{31}u_e - \eta_{32}\text{sig}^\nu(u_e) - \hat{\Theta}_u - \hat{\xi}_{d_u} - |z_e \cos \varphi_e| + m_u \dot{\beta}_u \\ \dot{\hat{\Theta}}_u = \mu_u \left[\tanh\left(\frac{u_e}{\delta_{g_u}}\right) u_e - g_u \hat{\Theta}_u \right] \\ \dot{\hat{\xi}}_{d_u} = \varepsilon_u \left[\tanh\left(\frac{u_e}{\delta_{\phi_u}}\right) u_e - \phi_u \hat{\xi}_{d_u} \right] \\ \tau_r = -\eta_{41}r_e - \eta_{42}\text{sig}^\nu(r_e) - \hat{\Theta}_r - \hat{\xi}_{d_r} - \varphi_e + m_r \dot{\beta}_r \\ \dot{\hat{\Theta}}_r = \mu_r \left[\tanh\left(\frac{r_e}{\delta_{g_r}}\right) r_e - g_r \hat{\Theta}_r \right] \\ \dot{\hat{\xi}}_{d_r} = \varepsilon_r \left[\tanh\left(\frac{r_e}{\delta_{\phi_r}}\right) r_e - \phi_r \hat{\xi}_{d_r} \right] \end{cases} \quad (19)$$

where $\eta_{31}, \eta_{32}, \mu_u, g_u, \delta_{g_u}, \varepsilon_u, \phi_u, \delta_{\phi_u}, \eta_{41}, \eta_{42}, \mu_r, g_r, \delta_{g_r}, \varepsilon_r, \phi_r, \delta_{\phi_r}$ are positive definite parameters. $\hat{\Theta}_u, \hat{\xi}_{d_u}$, and $\hat{\xi}_{d_r}$ are the estimated values of Θ_u, ξ_{d_u} , and ξ_{d_r} , respectively.

Define the measurement error as

$$\begin{cases} e_u(t) = L_u(t) - \tau_u(t), t \in [t_k, t_{k+1}) \\ e_r(t) = L_r(t) - \tau_r(t), t \in [t_k, t_{k+1}) \end{cases} \quad (20)$$

where t is the trigger time interval, $\tau_u(t)$ and $\tau_r(t)$ are the values of the controller at the previous starting time, and $\tau_u(t)$ and $\tau_r(t)$ will start at the trigger time t_k and will be maintained at a constant value by the zero-order holder until the trigger time t_{k+1} is updated.

The design ETC conditions are as follows:

$$\begin{cases} \tau_u(t) = L_u(t_k), \forall t \in [t_k, t_{k+1}) \\ t_{k+1} = \inf \{t \in R \mid |e_u(t)| \geq \eta_u\} \end{cases} \quad (21)$$

$$\begin{cases} \tau_r(t) = L_r(t_k), \forall t \in [t_k, t_{k+1}) \\ t_{k+1} = \inf \{t \in R \mid |e_r(t)| \geq \eta_r\} \end{cases} \quad (22)$$

where η_u and η_r are design parameters greater than 0. When the trigger condition is violated, the update time of the controller is marked as t_{k+1} , and the control signal of the controller is simultaneously updated as $\omega_u(t_{k+1})$ as the control input of the system.

STABILITY ANALYSIS

Select the following Lyapunov function for the closed-loop system:

$$\begin{aligned} H = & H_1 + \frac{m_u}{2} u_e^2 + \frac{m_r}{2} r_e^2 + \frac{1}{2} (e_u^f)^2 + \frac{1}{2} (e_r^f)^2 + \frac{1}{2\mu_u} \tilde{\Theta}_u^2 + \\ & + \frac{1}{2\mu_r} \tilde{\Theta}_r^2 + \frac{1}{2\varepsilon_u} \tilde{\xi}_{d_u}^2 + \frac{1}{2\varepsilon_r} \tilde{\xi}_{d_r}^2 \end{aligned} \quad (23)$$

where $\tilde{\Theta}_u, \tilde{\Theta}_r, \tilde{\xi}_{d_u}$, and $\tilde{\xi}_{d_r}$ are the estimation errors of $\Theta_u, \Theta_r, \xi_{d_u}$, and ξ_{d_r} , respectively.

By deriving Eq. (23) and substituting Eq.(19) into it, we can obtain

$$\begin{aligned} \dot{H} = & \dot{H}_1 + m_u u_e \dot{u}_e + m_r r_e \dot{r}_e + e_u^f \dot{e}_u^f + e_r^f \dot{e}_r^f - \frac{1}{\mu_u} \tilde{\Theta}_u \dot{\hat{\Theta}}_u - \frac{1}{\mu_r} \tilde{\Theta}_r \dot{\hat{\Theta}}_r - \frac{1}{\varepsilon_u} \tilde{\xi}_{d_u} \dot{\hat{\xi}}_{d_u} - \frac{1}{\varepsilon_r} \tilde{\xi}_{d_r} \dot{\hat{\xi}}_{d_r} \\ & - \eta_{11} z_e^2 - \eta_{12} |z_e|^{\nu+1} \text{sgn}(z_e) + z_e u_e \cos \varphi_e - \eta_{21} \varphi_e^2 - \eta_{22} |\varphi_e|^{\nu+1} \text{sgn}(\varphi_e) + \varphi_e r_e \\ & + u_e [-\eta_{31} u_e - \eta_{32} |u_e|^\nu \text{sgn}(u_e) - |z_e \cos \varphi_e| + \hat{\Theta}_u + \hat{\xi}_{d_u}] + r_e [-\eta_{41} r_e - \eta_{42} |r_e|^\nu \text{sgn}(r_e) - \varphi_e + \hat{\Theta}_r + \hat{\xi}_{d_r}] \\ & - \tilde{\Theta}_u \left[\tanh\left(\frac{u_e}{\delta_{g_u}}\right) u_e - g_u \hat{\Theta}_u \right] - \tilde{\Theta}_r \left[\tanh\left(\frac{r_e}{\delta_{g_r}}\right) r_e - g_r \hat{\Theta}_r \right] \\ & - \tilde{\xi}_{d_u} \left[\tanh\left(\frac{u_e}{\delta_{\phi_u}}\right) u_e - \phi_u \hat{\xi}_{d_u} \right] - \tilde{\xi}_{d_r} \left[\tanh\left(\frac{r_e}{\delta_{\phi_r}}\right) r_e - \phi_r \hat{\xi}_{d_r} \right] \\ & - \frac{(e_u^f)^2}{\kappa_u} + e_u^f P_u - \frac{(e_r^f)^2}{\kappa_r} + e_r^f P_r \end{aligned} \quad (24)$$

According to Lemma 2, Eq. (24) can become

$$\begin{aligned} \dot{H} \leq & -\eta_{11} z_e^2 - \eta_{12} |z_e|^{\nu+1} \text{sgn}(z_e) - \eta_{21} \varphi_e^2 - \eta_{22} |\varphi_e|^{\nu+1} \text{sgn}(\varphi_e) \\ & - \eta_{31} u_e^2 - \eta_{32} |u_e|^{\nu+1} \text{sgn}(u_e) - \eta_{41} r_e^2 - \eta_{42} |r_e|^{\nu+1} \text{sgn}(r_e) \\ & + 0.2785 \delta_{g_u} \tilde{\Theta}_u + g_u \tilde{\Theta}_u (\Theta_u - \tilde{\Theta}_u) + 0.2785 \delta_{g_r} \tilde{\Theta}_r + g_r \tilde{\Theta}_r (\Theta_r - \tilde{\Theta}_r) \\ & + 0.2785 \delta_{\phi_u} \tilde{\xi}_{d_u} + \phi_u \tilde{\xi}_{d_u} (\xi_{d_u} - \tilde{\xi}_{d_u}) + 0.2785 \delta_{\phi_r} \tilde{\xi}_{d_r} + \phi_r \tilde{\xi}_{d_r} (\xi_{d_r} - \tilde{\xi}_{d_r}) \\ & - \frac{(e_u^f)^2}{\kappa_u} + e_u^f P_u - \frac{(e_r^f)^2}{\kappa_r} + e_r^f P_r \end{aligned} \quad (25)$$

According to Young's inequality, Eq. (25) can become

$$\begin{aligned} \dot{H} \leq & -\eta_{11} z_e^2 - \eta_{12} |z_e|^{\nu+1} - \eta_{21} \varphi_e^2 - \eta_{22} |\varphi_e|^{\nu+1} - \eta_{31} u_e^2 - \eta_{32} |u_e|^{\nu+1} - \eta_{41} r_e^2 - \eta_{42} |r_e|^{\nu+1} \\ & - \frac{g_u}{2} \tilde{\Theta}_u^2 + \frac{g_u (\Theta_u + 0.2785 \delta_{g_u} g_u^{-1})^2}{2} - \frac{g_r}{2} \tilde{\Theta}_r^2 + \frac{g_r (\Theta_r + 0.2785 \delta_{g_r} g_r^{-1})^2}{2} \\ & - \frac{\phi_u}{2} \tilde{\xi}_{d_u}^2 + \frac{\phi_u (\xi_{d_u} + 0.2785 \delta_{\phi_u} \phi_u^{-1})^2}{2} - \frac{\phi_r}{2} \tilde{\xi}_{d_r}^2 + \frac{\phi_r (\xi_{d_r} + 0.2785 \delta_{\phi_r} \phi_r^{-1})^2}{2} \\ & - \omega_u (e_u^f)^2 - \omega_r (e_r^f)^2 \end{aligned} \quad (26)$$

where $\omega_u = \frac{1}{\kappa_u} - \frac{1}{2} P_u^2$ and $\omega_r = \frac{1}{\kappa_r} - \frac{1}{2} P_r^2$.

By further simplifying Eq. (26), we can obtain

$$\begin{aligned} \dot{H} \leq & -\eta_{11}z_e^2 - \eta_{12}|z_e|^{\nu+1} - \eta_{21}\varphi_e^2 - \eta_{22}|\varphi_e|^{\nu+1} - \eta_{31}u_e^2 - \eta_{32}|u_e|^{\nu+1} - \eta_{41}r_e^2 - \eta_{42}|r_e|^{\nu+1} \\ & - \frac{\vartheta_u}{4}\tilde{\Theta}_u^2 - \frac{\vartheta_r}{4}\tilde{\Theta}_r^2 - \frac{\vartheta_u}{2(\nu+1)}|\tilde{\Theta}_u|^{\nu+1} - \frac{\vartheta_r}{2(\nu+1)}|\tilde{\Theta}_r|^{\nu+1} + \frac{(1-\nu)(\vartheta_u + \vartheta_r)}{4(\nu+1)} \\ & - \frac{\phi_u}{4}\tilde{\xi}_{d_u}^2 - \frac{\phi_r}{4}\tilde{\xi}_{d_r}^2 - \frac{\phi_u}{2(\nu+1)}|\tilde{\xi}_{d_u}|^{\nu+1} - \frac{\phi_r}{2(\nu+1)}|\tilde{\xi}_{d_r}|^{\nu+1} + \frac{(1-\nu)(\phi_u + \phi_r)}{4(\nu+1)} \\ & - \frac{\omega_u}{2}(e_u^f)^2 - \frac{\omega_r}{2}(e_r^f)^2 - \frac{\omega_u}{\nu+1}|e_u^f|^{\nu+1} - \frac{\omega_r}{\nu+1}|e_r^f|^{\nu+1} + \frac{(1-\nu)(\omega_u + \omega_r)}{2(\nu+1)} \\ & + \frac{\vartheta_u(\Theta_u + 0.2785\delta_{\vartheta_u}\vartheta_u^{-1})^2}{2} + \frac{\vartheta_r(\Theta_r + 0.2785\delta_{\vartheta_r}\vartheta_r^{-1})^2}{2} \\ & + \frac{\phi_u(\xi_{d_u} + 0.2785\delta_{\phi_u}\phi_u^{-1})^2}{2} + \frac{\phi_r(\xi_{d_r} + 0.2785\delta_{\phi_r}\phi_r^{-1})^2}{2} \\ = & \nu_1 V - \nu_2 V^{\frac{\nu+1}{2}} + \Omega \end{aligned} \quad (27)$$

where

$$\begin{aligned} \nu_1 = & \min \left\{ 2\eta_{11}, 2\eta_{21}, 2\eta_{31}, 2\eta_{41}, \frac{\vartheta_u}{2}, \frac{\vartheta_r}{2}, \frac{\phi_u}{2}, \frac{\phi_r}{2}, \omega_u, \omega_r \right\}, \\ \nu_2 = & 2^{\frac{\nu+1}{2}} \left\{ \eta_{12}, \eta_{22}, \eta_{32}, \eta_{42}, \frac{\vartheta_u}{2(\nu+1)}, \frac{\vartheta_r}{2(\nu+1)}, \frac{\phi_u}{2(\nu+1)}, \frac{\phi_r}{2(\nu+1)}, \frac{\omega_u}{\nu+1}, \frac{\omega_r}{\nu+1} \right\}, \\ \Omega = & \frac{(1-\nu)(\vartheta_u + \vartheta_r)}{4(\nu+1)} + \frac{(1-\nu)(\phi_u + \phi_r)}{4(\nu+1)} + \frac{(1-\nu)(\omega_u + \omega_r)}{2(\nu+1)} + \frac{\vartheta_u(\Theta_u + 0.2785\delta_{\vartheta_u}\vartheta_u^{-1})^2}{2} \\ & + \frac{\vartheta_r(\Theta_r + 0.2785\delta_{\vartheta_r}\vartheta_r^{-1})^2}{2} + \frac{\phi_u(\xi_{d_u} + 0.2785\delta_{\phi_u}\phi_u^{-1})^2}{2} + \frac{\phi_r(\xi_{d_r} + 0.2785\delta_{\phi_r}\phi_r^{-1})^2}{2} \end{aligned}$$

According to Eq. (27), we can obtain

$$\dot{H} \leq -\nu_1 H - (1-t)\nu_1 H - \nu_2 H^{\frac{\nu+1}{2}} + \Omega \quad (28)$$

where $t = \min\{t_1, t_2\}$ ($0 < t < 1$).

$$\begin{aligned} \text{If } H > \frac{\Omega}{\nu_1}, \text{ then} \\ \dot{H} \leq & -(1-t)\nu_1 H - \nu_2 H^{\frac{\nu+1}{2}} \end{aligned} \quad (29)$$

According to Lemma 1, the system will stabilize to area $\Omega_L = \left\{ L : L \leq \frac{\Omega}{\nu_1} \right\}$ within finite time, and the stabilization

time is as follows:

$$T \leq \frac{4}{(1-t)\nu_1} \ln \left[\frac{(1-t)\nu_1 H^{\frac{1-\nu}{2}}(0) + \nu_2}{\nu_2} \right] \quad (30)$$

From Eq. (20), we can obtain

$$\begin{aligned} \left| \frac{d}{dt} e_u \right| &= \frac{d}{dt} (e_u * e_u) = \text{sgn}(e_u) \dot{e}_u \leq |\dot{L}_u(t)| \\ \left| \frac{d}{dt} e_r \right| &= \frac{d}{dt} (e_r * e_r) = \text{sgn}(e_r) \dot{e}_r \leq |\dot{L}_r(t)| \end{aligned} \quad (31)$$

Since the \dot{L}_i ($i = u, r$) are smoothly differentiable

functions, \dot{L}_i is a continuous function. Since all its variables

are globally bounded, $\lambda_i > 0$ makes $|\dot{L}_i| \leq \lambda_i$. When $t = t_k$

, $e_i(t_k) = 0$ and $\lim_{t \rightarrow t_k} e_i(t) = \eta_i$. Therefore, there is a time

interval t_k^* that satisfies $t^* \geq \frac{\eta_i}{\lambda_i}$. In summary, Zeno's

behaviour will not occur.

SIMULATION

In the simulation stage, the Cybership 2 ship model of the Norwegian University of Science and Technology was selected as the controlled object, and its parameters are detailed in [30]. To verify the effectiveness of the designed finite-time trajectory-tracking control scheme, the time-varying disturbance given in Eq. (32) is selected to simulate the external uncertain interference in actual navigation:

$$\begin{cases} d_u = [1 + 0.5 \sin(0.2t) + 0.2 \cos(0.5t)] \\ d_v = [1 + 0.3 \sin(0.2t) + 0.3 \cos(0.2t)] \\ d_r = [1 + 0.4 \sin(0.3t) + 0.2 \cos(0.3t)] \end{cases} \quad (32)$$

The system's FDIA signals are set as follows:

$$\begin{cases} \xi_u = 0.2 + 0.2 \sin(0.2t) \\ \xi_r = 0.15 + 0.3 \cos(0.1t) \end{cases} \quad (33)$$

The control parameters are detailed in Table 1.

Tab. 1. Controller parameters

$\eta_{11} = 0.3$	$\eta_{12} = 0.1$	$\eta_{21} = 0.3$	$\eta_{22} = 0.1$	$\nu = 0.5$	$\kappa_u = 0.01$	$\kappa_r = 0.1$
$\kappa_r = 0.01$	$\eta_{31} = 0.3$	$\eta_{32} = 0.5$	$\mu_u = 1$	$\vartheta_u = 0.01$	$\delta_{\vartheta_u} = 0.03$	$\varepsilon_u = 1$
$\phi_u = 0.02$	$\delta_{\phi_u} = 0.02$	$\eta_{41} = 0.5$	$\eta_{42} = 0.3$	$\mu_r = 1.5$	$\vartheta_r = 0.01$	$\delta_{\vartheta_r} = 0.02$
$\varepsilon_r = 1$	$\phi_r = 0.01$	$\delta_{\phi_r} = 0.02$	$\eta_u = 0.02$	$\eta_r = 0.3$		

To carry out the quantitative and qualitative analysis of the control scheme designed in this article, we introduce the integrated absolute error (IAE) and mean integrated absolute control (MIAC) in Eq. (35) to evaluate the steady-state performance and energy consumption performance. The evaluation results are shown in Tables 2 and 3:

$$\begin{cases} \text{IAE} = \int_0^{t_f} |v_e| dt, v = x, y \\ \text{MIAC} = \frac{1}{t_f} \int_0^{t_f} |\tau_i(t)| dt, i = u, r \end{cases} \quad (35)$$

Simulation experiment 1

In simulation experiment 1, we set the simulation time to 200 s and the step size to 0.01.

The circular reference trajectory is as follows:

$$\begin{cases} x_d = 50 \sin(0.01\pi t) \\ y_d = 50 - 50 \cos(0.01\pi t) \end{cases} \quad (34)$$

Tab. 2. Performance index comparison of the control schemes for simulation 1

		ETC scheme	Continuous scheme	The scheme in [25]
IAE	x_e	10.23	10.15	11.37
	y_e	9.52	9.26	10.29
MIAC	τ_u	1.36	1.41	1.39
	τ_r	1.12	1.33	1.28

The simulation results of this study are shown in Figures 2–10. Figures 2 and 3 show the effects of three different control schemes for completing tracking tasks. They show that each control scheme successfully completed the established tracking task within a limited time, confirming the effectiveness of the control scheme.

Figure 4 shows the trend of the system velocity with time under these three control schemes. The results show that as time progresses, the system velocity under all control schemes gradually tends toward a bounded stable state.

The time course of the systematic error is shown in Figures 5 and 6. These curves clearly show the performance comparison under different control schemes. The continuous control scheme designed in this article shows the best effect in terms of the control performance, followed by the ETC scheme designed in this article. In contrast, the control effects of these two schemes are better than the control scheme proposed in [25].

Figure 7 shows the duration curve of the system control input. It can be observed from the figure that as time goes by, the control inputs of the three control schemes stabilize within a relatively small interval. This shows the stability and reliability of the control scheme. Figures 7 and 10 further demonstrate the advantages of the ETC control scheme in terms of the controller update frequency compared to the other two continuous control schemes. In the ETC control scheme, the controller is updated only 2611 times and 986 times. For both continuous control schemes, the number of controller updates is 20,000 times. This means that the ETC scheme can achieve effective control with a lower update frequency, thereby more effectively solving the communication resource

limitation problem. In addition, according to the comparison of the performance indicators in Table 2, it can be concluded that the IAE value is the smallest in the continuous control scheme designed in this paper, followed by the ETC scheme and finally the scheme in [25]. The MIAC value is the smallest for the ETC scheme, followed by the scheme in [25] and finally the ETC scheme. This means that the tracking accuracy of the two control schemes is significantly improved compared to the scheme in [25]. However, the energy consumption of the continuous control scheme designed in this article is slightly higher. The ETC control scheme has significant improvements in terms of both the tracking accuracy and energy consumption.

Figures 8 and 9 show the approximation effect of the approximator on FDIAs, external disturbances, and dynamic uncertainties in the system. These plots show that the upper bounds of all uncertainties are effectively estimated, thereby enhancing the robustness of the control scheme.

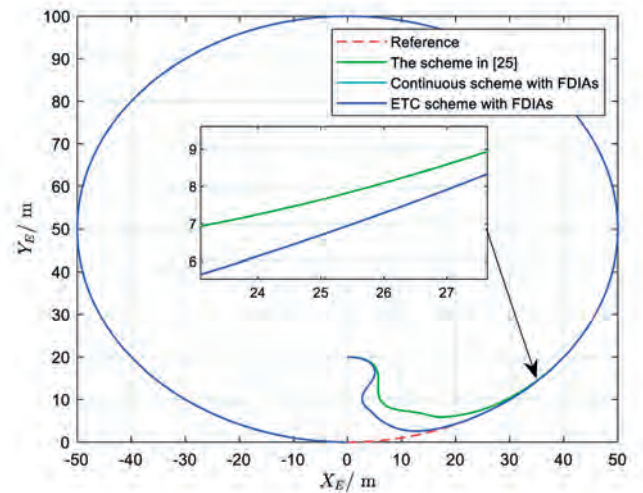


Fig. 2 Actual and reference trajectories in the (x, y) plane

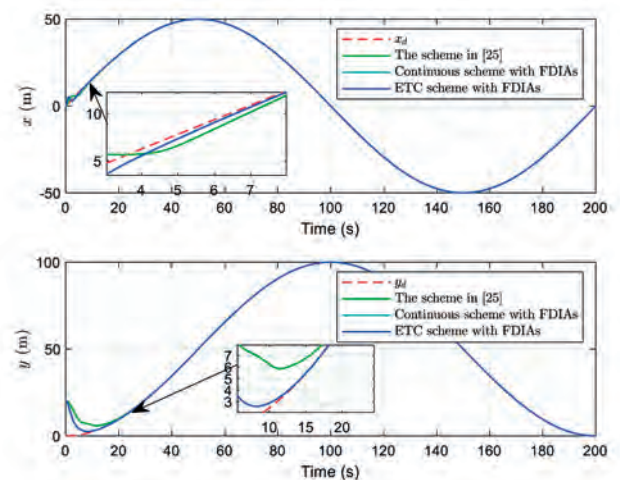


Fig. 3. Actual and reference positions

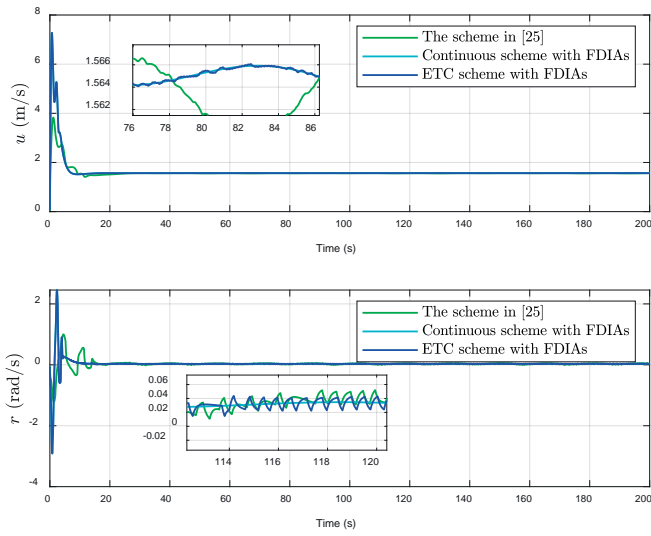


Fig. 4. Vessel velocity duration curve

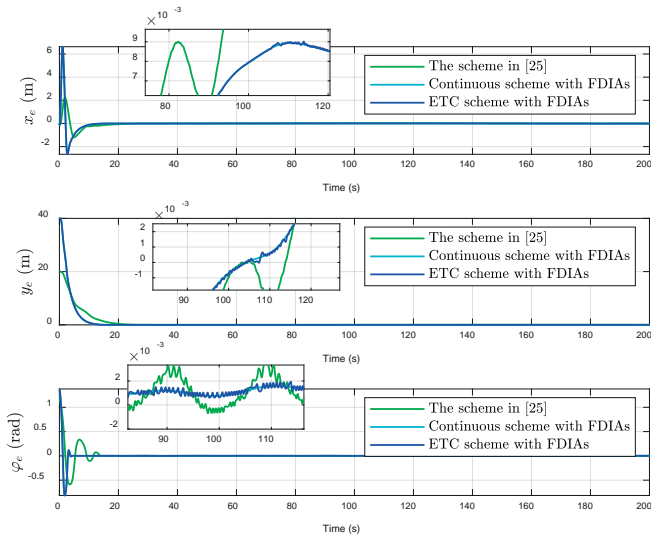


Fig. 5. Time evolution of the attitude errors

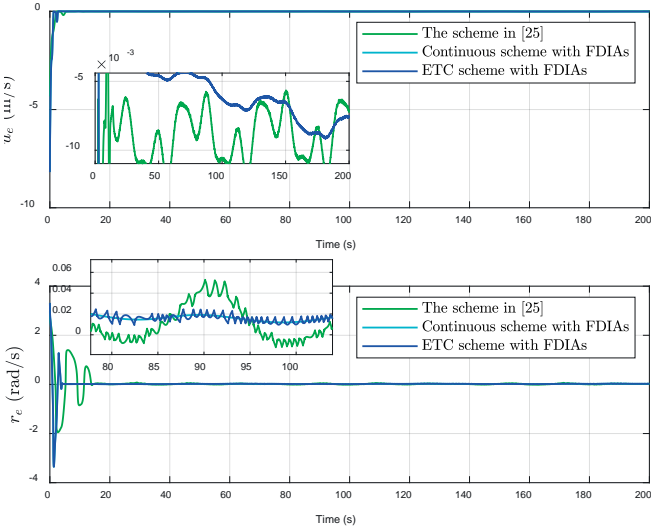


Fig. 6. Time evolution of the velocity errors

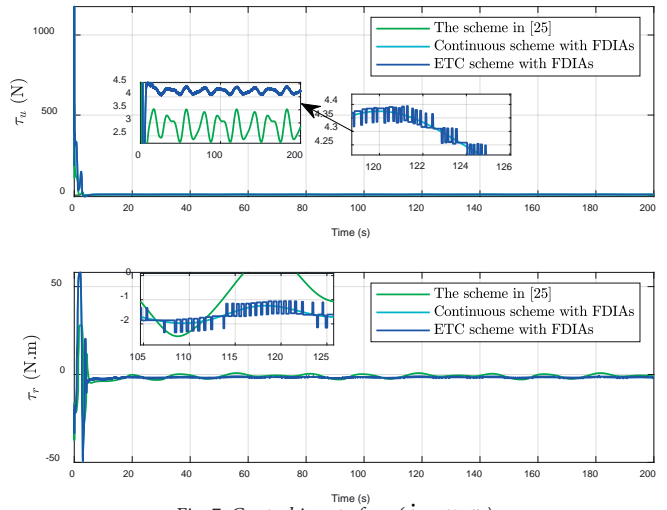


Fig. 7. Control input of τ_i ($i = u, r$)

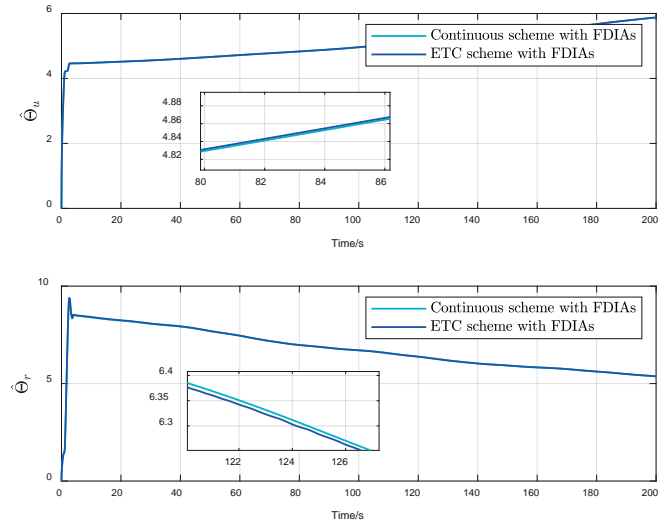


Fig. 8. Estimated values of Θ_u and Θ_r

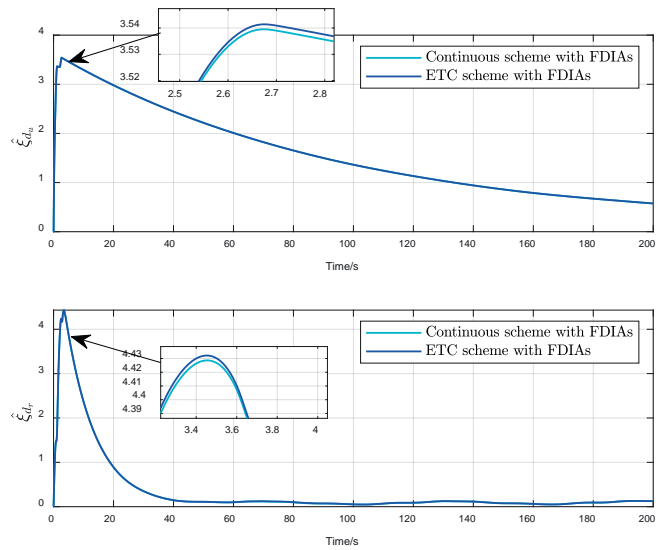


Fig. 9. Estimated values of ξ_{d_u} and ξ_{d_r}

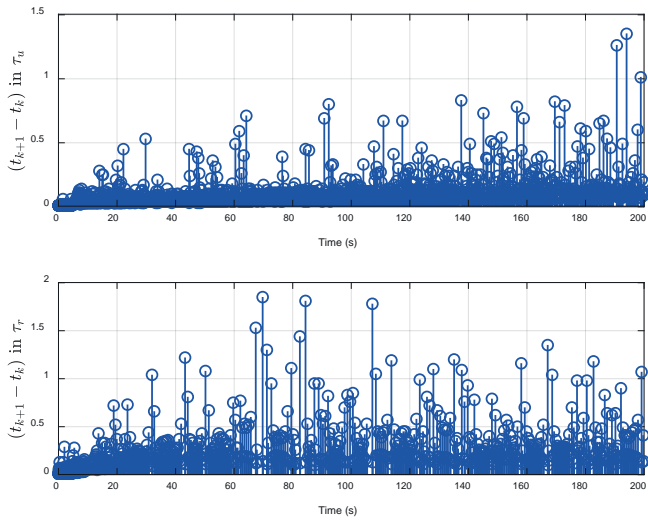


Fig. 10. Time evolution of the inter-event time

Simulation experiment 2

In simulation experiment 2, we set the simulation time to 100 s and the step size to 0.01.

The reference trajectory is as follows:

$$\begin{cases} x_d = 10 \sin(0.02\pi t) \\ y_d = 6 \sin(0.04\pi t) \end{cases} \quad (34)$$

Tab. 3 Performance index comparison of the control schemes for simulation 2

		ETC scheme	Continuous scheme	The scheme in [25]
IAE	x_e	11.15	11.02	12.21
	y_e	10.35	10.02	11.31
MIAC	τ_u	1.45	1.52	1.49
	τ_r	1.31	1.38	1.35

The simulation results are shown in Figures 11–20. Figures 11 and 12 show the tracking effects of the three control schemes on the reference trajectory. They all completed the tracking task excellently. However, the control scheme designed in this article can track the reference trajectory more quickly. Figure 13 shows the velocity changes of the three control schemes. They all tend to be bounded over time. Figures 14 and 15 show the tracking error of the system. The tracking accuracy of the control scheme designed in this paper is significantly higher than that of the control scheme in [25]. By analyzing the performance indicators in Table 2, we can conclude that the continuous control method designed in this article has the highest tracking accuracy, followed by the ETC scheme designed in this article. The method in [25] is slightly inferior in terms of tracking progress. From the perspective of energy consumption, the ETC method

is the most energy-saving, followed by the control scheme in [25] and finally the continuous control scheme designed in this paper. Although the continuous control scheme has the highest control accuracy, it is accompanied by high energy consumption. The ETC method takes into account the advantages of lower energy consumption and higher tracking accuracy.

According to Figures 16 and 19, it can be concluded that the update frequency of the ETC scheme controller has been greatly reduced. In the continuous control scheme and the control scheme in [25], the number of controller updates is 10,000, while in the ETC scheme, it is only 603 and 607. Figure 17 shows the adaptive curve of the system dynamic uncertainty. Figure 18 shows the approximation effect of the system on the composite uncertainty dynamics composed of external disturbances and FDIAs. They are all effectively estimated.

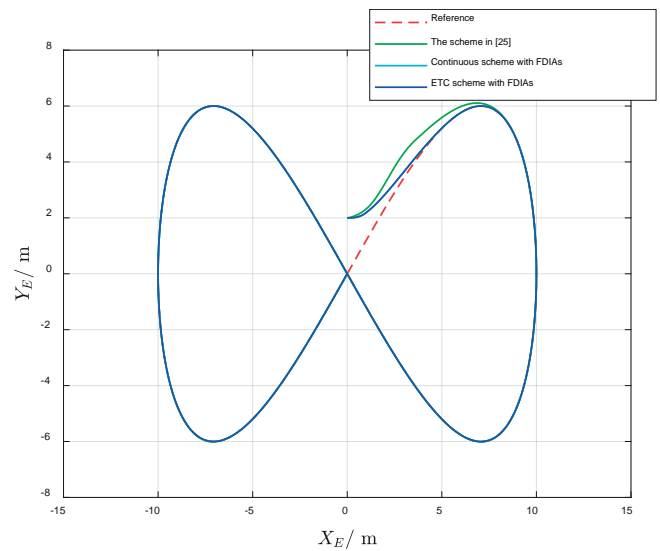


Fig. 11. Actual and reference trajectories in the (x, y) plane

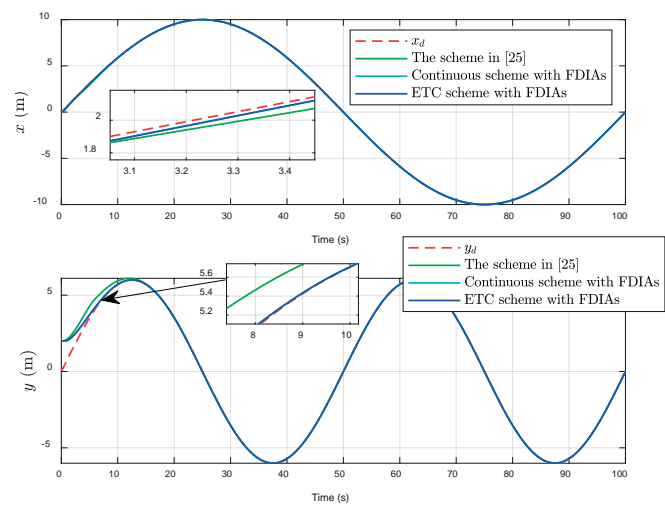


Fig. 12. Actual and reference positions

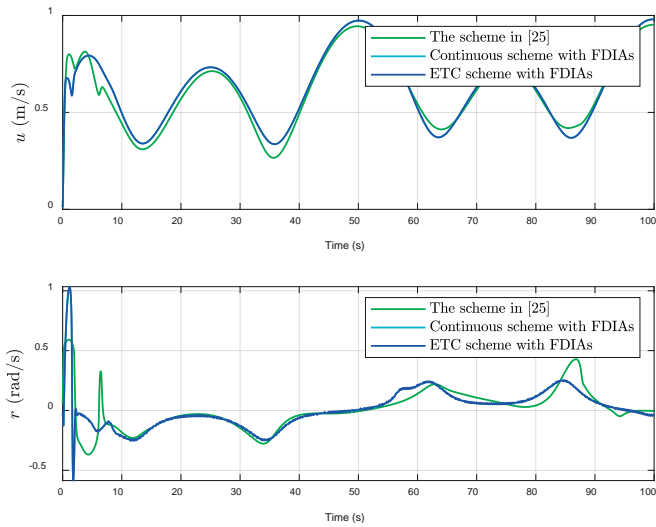


Fig. 13. Vessel velocity duration curve

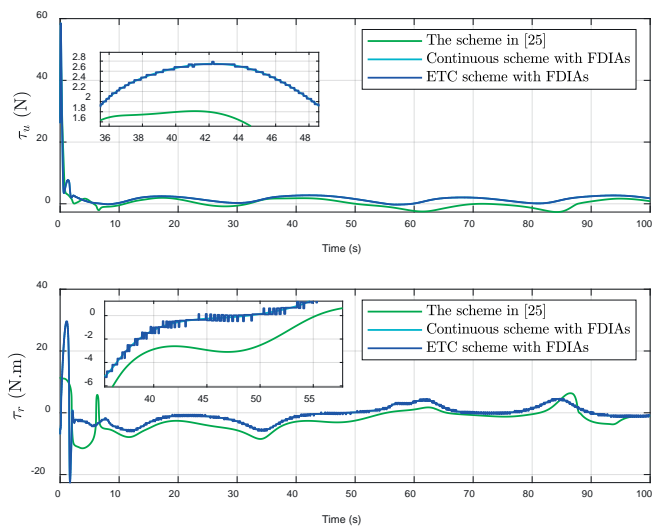


Fig. 16. Control input of τ_i ($i = u, r$)

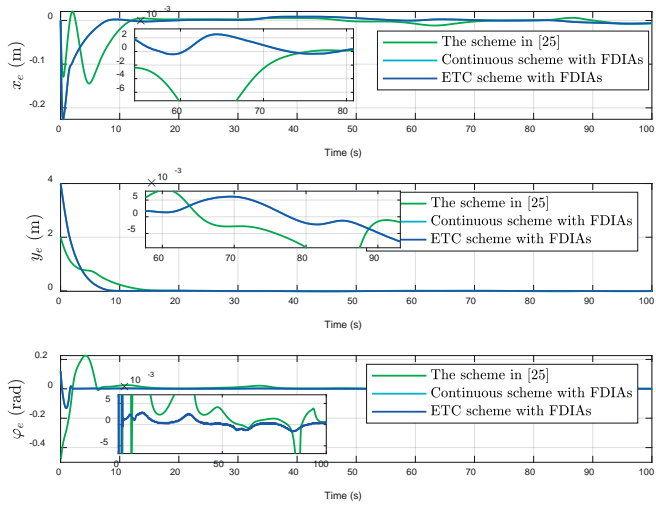


Fig. 14. Time evolution of the attitude errors

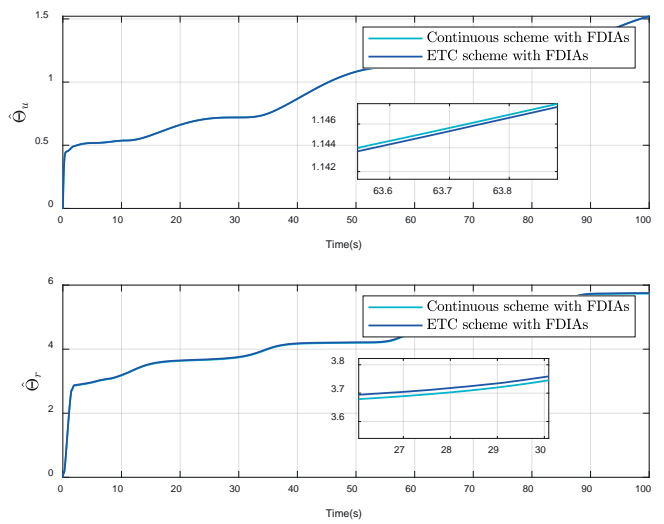


Fig. 17. Estimated values of Θ_u and Θ_r

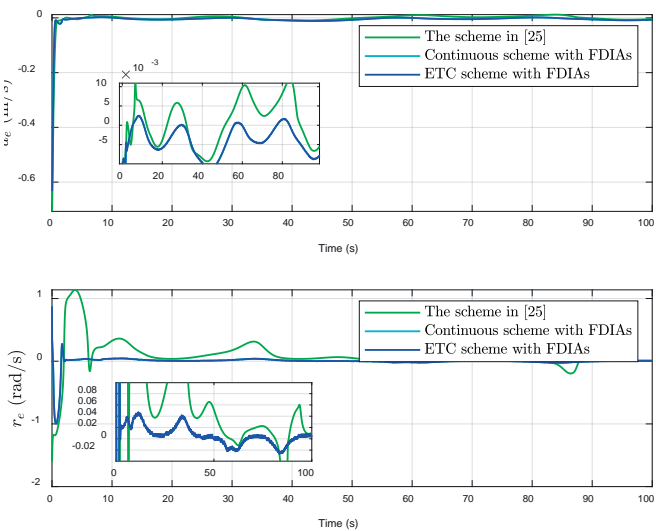


Fig. 15. Time evolution of the velocity errors

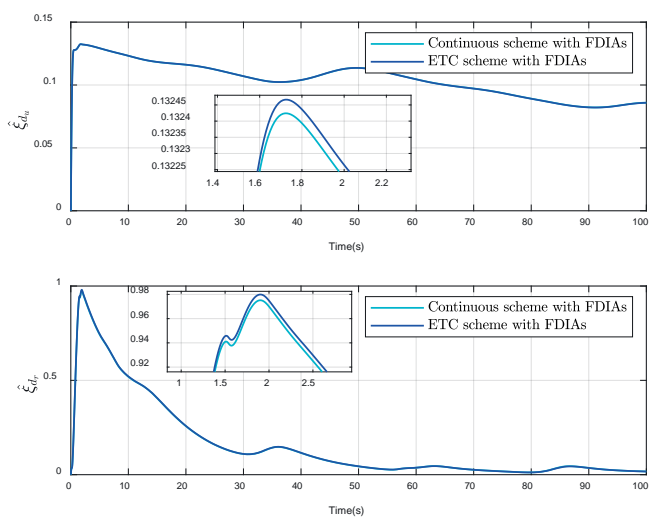


Fig. 18. Estimated values of ξ_{d_u} and ξ_{d_r}

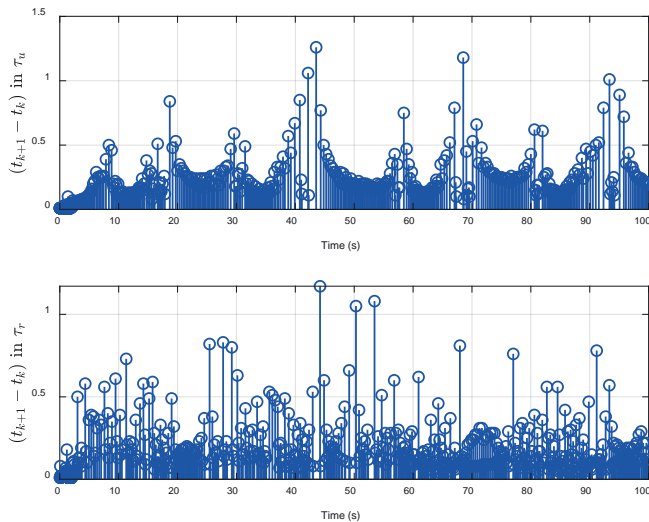


Fig. 19. Time evolution of the inter-event time

CONCLUSION

This paper studies the USV trajectory-tracking control problem constrained by FDIAs and internal and external uncertainties. Uncertain dynamics, including FDIAs, are compensated through the design of online approximators. At the same time, to optimize the tracking performance of the system, we also introduced FTC and ETC technologies. They improve the steady-state performance of the system and save the communication resources of the system. They ensure that the system can still complete control tasks with high precision under the constraints of limited communication resources. The main contributions of this article are as follows:

(1) This paper solves the trajectory-tracking control problem of USVs under the influence of FDIAs for the first time. Compared with [1], [2], this method can effectively cope with and resist the adverse effects of FDIAs, ensuring that USVs can still accurately track the predetermined trajectory when they are attacked.

(2) This paper incorporates FTC technology into the design process of the control scheme. Compared with [8], [13], this scheme ensures that USVs can quickly adjust when they face emergencies, thereby meeting the need for rapid response.

(3) This paper organically combines FTC technology and ETC technology. Compared with [15], [16], this scheme provides the system with rapid response capabilities for emergencies and external disturbances. The ETC mechanism ensures that control is only performed at critical moments while also greatly reducing the computing and communication requirements, making the control system more energy-saving and efficient.

Overall, our research provides an efficient and stable trajectory-tracking control scheme for USVs disturbed by FDIAs and internal and external uncertainties, providing new ideas for research and practical applications in this field.

However, the types of attacks covered in this study are limited to FDIAs targeting actuators. In the future, we hope to expand the attack objects to the output of the system and

introduce more attack types, such as deception attacks and denial of service attacks.

FUNDING

This work was supported by the Education and Research Project for Middle and Young Teachers in Fujian Province (No. JAT210241).

REFERENCES

1. S. L. Yu, J. S. Lu, G. B. Zhu and S. J. Yang, 'Event-triggered finite-time tracking control of underactuated MSVs based on neural network disturbance observer', *Ocean Engineering*, 2022, doi: 10.1016/j.oceaneng.2022.111169.
2. X. F. Meng, G. C. Zhang and Q. Zhang, 'Event-triggered trajectory tracking control of underactuated surface vessels with performance-improving mechanisms under input saturation and actuator faults', *Transactions of the Institute of Measurement and Control*, 2023, doi: 10.1177/01423312231187008.
3. Z. H. Yu and W. L. Chin, 'Blind false data injection attack using PCA approximation method in smart grid', *IEEE Transactions on Smart Grid*, vol. 6, no. 3, pp. 1219–1226, 2015, doi: 10.1109/TSG.2014.2382714.
4. Q. T. Yin, Y. X. Bian, J. Du, W. Zhao and S. B. Yang, 'Dual backstepping variable structure switching control of bounded uncertain nonlinear system', *International Journal of Systems Science*, vol. 53, no. 11, pp. 2341–2357, 2022, doi: 10.1080/00207721.2022.2051094.
5. R. Rout, R. X. Cui and W. S. Yan, 'Sideslip-compensated guidance-based adaptive neural control of marine surface vessels', *IEEE Transactions on Cybernetics*, vol. 52, no. 5, pp. 2860–2871, 2022, doi: 10.1109/TCYB.2020.3023162.
6. D. Menges and A. Rasheed, 'An environmental disturbance observer framework for autonomous surface vessels', *Ocean Engineering*, vol. 285, 2023, doi: 10.1016/j.oceaneng.2023.115412.
7. C. Zhang and S. H. Yu, 'Disturbance observer-based prescribed performance super-twisting sliding mode control for autonomous surface vessels', *ISA Transactions*, vol. 135, pp. 13–22, 2023, doi: 10.1016/j.isatra.2022.09.025.
8. X. W. Wang, J. Liu, H. J. Peng, X. W. Qie, X. D. Zhao and C. Lu, 'A simultaneous planning and control method integrating APF and MPC to solve autonomous navigation for USVs in unknown environments', *Journal of Intelligent & Robotic Systems*, vol. 105, no. 2, 2022, doi: 10.1007/s10846-022-01663-8.

9. X. Han and X. K. Zhang, 'Tracking control of ship at sea based on MPC with virtual ship bunch under Frenet frame', *Ocean Engineering*, 2022, doi: 10.1016/j.oceaneng.2022.110737.
10. W. R. Wang, J. H. Yan, H. Wang, H. L. Ge, Z. Y. Zhu and G. J. Yang, 'Adaptive MPC trajectory tracking for AUV based on Laguerre function', *Ocean Engineering*, 2022, doi: 10.1016/j.oceaneng.2022.111870.
11. E. Tatlicioglu, B. M. Yilmaz, A. Savran and M. Alci, 'Adaptive fuzzy logic with self-adjusting membership functions based tracking control of surface vessels', *Ocean Engineering*, 2022, doi: 10.1016/j.oceaneng.2022.111129.
12. X. F. Meng, G. C. Zhang and Q. Zhang, 'Robust adaptive neural network integrated fault-tolerant control for underactuated surface vessels with finite-time convergence and event-triggered inputs', *Mathematical Biosciences and Engineering*, vol. 20, no. 2, pp. 2131–2156, 2023, doi: 10.3934/mbe.2023099.
13. Y. Fang, E. Zergeroglu, M. S. de. Queiroz and D. M. Dawson, 'Global output feedback control of dynamically positioned surface vessels: an adaptive control approach. Mechatronics', *Mechatronics*, vol. 14, no. 4, pp. 341–356, 2004, doi: 10.1016/S0957-4158(03)00064-3.
14. G. B. Zhu, Y. Ma, Z. X. Li, R. Malekian and Sotelo M, 'Adaptive neural output feedback control for MSVs with predefined performance', *IEEE Transactions on Vehicular Technology*, vol. 70, no. 4 pp. 2994–3006, 2021, doi: 10.1109/TVT.2021.3063687.
15. G. B. Zhu, Y. Ma and S. L. Hu, 'Single-parameter-learning-based finite-time tracking control of underactuated MSVs under input saturation', *Control Engineering Practice*, 2020, doi: 10.1016/j.conengprac.2020.104652.
16. Y. L. Yu, C. Guo and T. S. Li, 'Finite-time LOS path following of unmanned surface vessels with time-varying sideslip angles and input saturation', *IEEE-ASME Transactions on Mechatronics*, vol. 27, no. 1, pp. 463–474, 2022, doi: 10.1109/TMECH.2021.3066211.
17. M. Van, V. T. Do, M. O. Khyam and Do XP, 'Tracking control of uncertain surface vessels with global finite-time convergence', *Ocean Engineering*, 2021, doi: 10.1016/j.oceaneng.2021.109974.
18. X. F. Meng, G. C. Zhang and B. Han, 'Fault-tolerant control of underactuated MSVs based on neural finite-time disturbance observer: An Event-triggered Mechanism', *Journal of the Franklin Institute*, 2024, doi: 10.1016/j.jfranklin.2024.01.004.
19. Y. J. Deng, X. K. Zhang, N. Im, G. Q. Zhang and Q. Zhang, 'Model-based event-triggered tracking control of underactuated surface vessels with minimum learning parameters', *IEEE Transactions on Neural Networks and Learning Systems*, vol. 31, no. 10, pp. 4001–4014, 2020, doi: 10.1109/TNNLS.2019.2951709.
20. G. B. Zhu, Y. Ma and S. L. Hu, 'Event-triggered adaptive PID fault-tolerant control of underactuated ASVs under saturation constraint', *IEEE Transactions on Systems Man Cybernetics-Systems*, vol. 53, no. 8, pp. 4922–4933, 2023, doi: 10.1109/TSMC.2023.3256538.
21. N. Feng, D. F. Wu, H. L. Yu, A. S. Yamashita and Y. Q. Huang, 'Predictive compensator based event-triggered model predictive control with nonlinear disturbance observer for unmanned surface vehicle under cyber-attacks', *Ocean Engineering*, vol. 259, 2022, doi: 10.1016/j.oceaneng.2022.111868.
22. Y. X. Zheng, L. Zhang, B. Huang and Y. M. Su, 'Distributed secure formation control for autonomous surface vessels by performance adjustable event-triggered mechanism', *International Journal of Robust and Nonlinear Control*, vol. 33, no. 14, pp. 8490–8507, 2023, doi: 10.1002/rnc.6832.
23. G. Q. Zhang, X. J. Dong, Q. H. Shan and W. D. Zhang, 'Event-triggered robust adaptive control for unmanned surface vehicle in presence of deception attacks', *Proceedings of the Institution of Mechanical Engineers Part I-Journal of Systems and Control Engineering*, vol. 237, no. 7, pp. 1266–1280, 2023, doi: 10.1177/09596518231153437.
24. T. I. Fossen, *Handbook of marine craft hydrodynamics and motion control*, 2011.
25. Y. Ma, G. B. Zhu and Z. X. Li, 'Error-driven-based nonlinear feedback recursive design for adaptive NN trajectory tracking control of surface ships with input saturation', *IEEE Intelligent Transportation Systems Magazine*, 2019, vol. 11, no. 2, pp. 17–28, doi: 10.1109/MITS.2019.2903517.
26. K. X. Huang, C. J. Zhou, Y. Q. Qin and W. X. Tu, 'A game-theoretic approach to cross-layer security decision-making in industrial cyber-physical systems', *IEEE Transactions on Industrial Electronics*, vol. 67, no. 2, pp. 2371–2379, 2020, doi: 10.1109/TIE.2019.2907451.
27. S. H. Yu, X. H. Yu, B. Shirinzadeh and Z. H. Man, 'Continuous finite time control for robotic manipulators with terminal sliding mode', *Automatica*, vol. 41, no. 11, pp. 1957–1964, 2005, doi: 10.1016/j.automatica.2005.07.001.
28. M. M. Polycarpou, 'Stable adaptive neural control scheme for nonlinear systems', *IEEE Transactions on Automatic Control*, vol. 41, no. 3, pp. 447–451, 1996, doi: 10.1109/9.486648.

29. X. F. Meng, G. C. Zhang, Q. Zhang and B. Han, 'Event-triggered adaptive command-filtered trajectory tracking control for underactuated surface vessels based on multivariate finite-time disturbance observer under actuator faults and input saturation', *Transactions of the Institute of Measurement and Control*, 2024, doi: 10.1177/01423312231195657.
30. R. Skjetne, T. I. Fossen and P. V. Kokotovic, 'Adaptive maneuvering, with experiments, for a model ship in a marine control laboratory', *Automatica*, vol. 41, no. 2, pp. 289–298, 2005, doi: 10.1016/j.automatica.2004.10.006.

ENVIRONMENTAL MARINE DEGRADATION OF PLA/WOOD COMPOSITE AS AN ALTERNATIVE SUSTAINABLE BOATBUILDING MATERIAL

Selin Barış Çamlı ¹

Gokdeniz Naser ² *

Ayberk Sözen ²

¹ Dokuz Eylül University Graduate School of Natural and Applied Sciences, İzmir, Turkey

² Dokuz Eylül University Institute of Marine Sciences and Technology, İzmir, Turkey

* Corresponding author: gokdeniz.naser@deu.edu.tr (Gokdeniz Naser)

ABSTRACT

*In this study, which can be considered a contribution to the global effort to produce sustainable materials and to search new manufacturing methods for the boatbuilding industry, the performance of a 3D printable polylactic acid and recycled wood (PLAW) composite was investigated under the simulated operational conditions of a boat. The wood used in the composite was yellow pine (*Pinus sylvestris*), a local wood widely used in boat building and 8% by weight in the composite. For the study, tensile and compressive strength tests were performed in both atmospheric and post-aging conditions, using composite samples produced by the additive manufacturing method. The durations of the accelerated aging before the experiments were one, two and four weeks. During these aging periods, water spraying, a salty fog environment and a drying cycle were applied at elevated temperatures and at equal time intervals, daily. The effect of wood additive on the composite and the joining efficiency of the components were also examined with scanning and optical microscopes. The performance of the obtained composite and the effects of aging on performance were measured using two different thermal analyses: differential scanning calorimetry and thermogravimetric analysis. From the results obtained, it can be seen that PLAW composite can be used in the manufacture of structural elements subjected to relatively low loads in boats. It is an option that will provide integrity in the future interior design of wooden boats.*

Keywords: Fused Filament Fabrication (FFF); Additive Manufacturing; Wooden boat building; PLA and recycled wood (PLAW) composite; Environmental marine degradation; Yellow pine (*Pinus sylvestris*)

INTRODUCTION

From the first day that humans started using water for transportation (up until about a hundred years ago), wood has been the primary material used to build small marine craft. Although this natural material has now been replaced by steel in large ships, it has maintained its competitiveness in the construction of recreational marine craft through the continual development of woodworking technologies [1]. Different seas, different needs, and different trees enable the traditions of boatbuilding, which have been enriched by the experiences transferred from the master to the apprentice

over the accumulation of centuries, continuing in every corner of the world. Structural wood elements, which have a good 'strength/weight' ratio, are resistant to fatigue loads and shock, as well as being easily repairable, easy to obtain and easy to handle, while being comfortable to work on. Wood is indispensable for those who are especially fond of its naturalness and warmth and reflects the interaction between Man and the forests of the earth.

Although the effects of sea salt in retarding wood decay have been known for centuries, the degradation effects of water and salt in the marine environment on wood material have not been adequately studied. It is known that environmental

factors, such as humidity and moisture distribution, affect the hardness and strength of wood products. For more successful wooden hull designs, it is thought that it is essential to know the time-dependent changes in a tree's qualities, which are exposed to the effects of salt water from the atmosphere and the sea [2].

The yellow pine tree (*Pinus sylvestris*) grows in many parts of the world. They are common in the northern regions of Russia, most of Europe, and Anatolia's northern mountains. Since they have 'pile' roots, they are resistant to storms. The leaves of yellow pines are shorter than those of the other pines, depending on their family. In addition, their cones are small, short, and point downwards. Their pointed peaks exceed 40 m. The tree's name comes from the yellow fox colour of the trunk's bark [3]. This tree was chosen in this study because it is widely used in the structural elements of boats due to its resistance to the marine environment and its cost-effectiveness, compared to commonly used maritime woods, such as teak [4].

'Gulet' type wooden sailing boats are widespread, especially in the Bodrum region of Turkey (Fig. 1). The boatyards in this region are highly competent and specialise in manufacturing gulets, based on a long-standing tradition. The dimensions of these boats are usually between 10-50 m long and their freeboard is very high. They give a sense of safety to their passengers because of their stability.

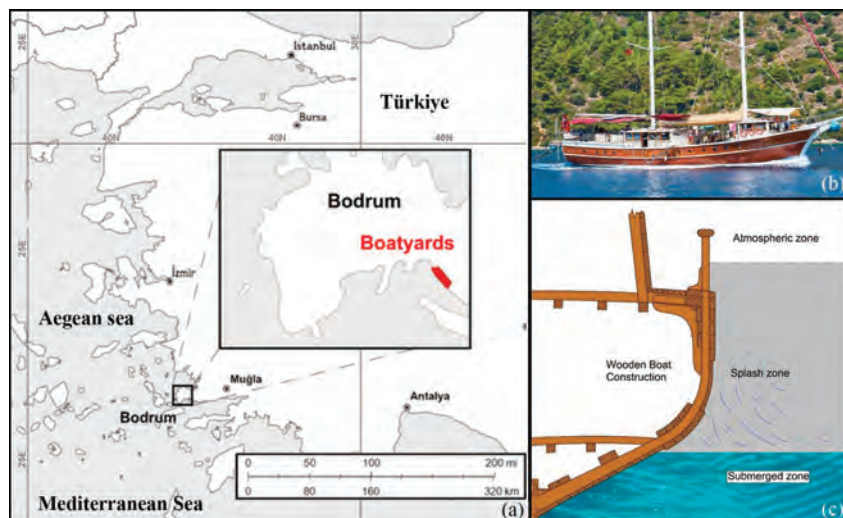


Fig. 1. (a) The wooden boat building zone in Turkey, (b) typical gulet type of boat (b),(c) degradation zones of a wooden boat (c).

In today's wooden boat industry, a significant amount of wood is used to build these boats. The increasing demand for boats (and, therefore, trees) has raised sustainability concerns. This is evident when considering the teak wood used in floor coverings. Due to excessive consumption, teak trees have decreased rapidly in recent years. The high eco-cost of tropical forest deforestation, due to teak logging and long transportation distances, makes this tropical timber less sustainable than timber from more local sources. The industry has turned to synthetic teak and petroleum-derived thermoset plastics, to combat this situation. These materials

have a longer service life and lower maintenance costs but the recycling of these materials is highly problematic. Considering recycling concerns, thermoset petroleum-based polymers were not considered as an alternative sustainable material in this study.

Poly(lactic acid) (PLA) is a biodegradable thermoplastic [5], which has become a widespread alternative to petroleum-derived products, but there are increasing environmental concerns [6]. PLA is polyester produced by the fermentation of a carbohydrate source, such as corn starch or sugar cane, under controlled conditions. Using the fused filament fabrication (FFF) method with 3D printers, this thermoplastic makes the creation of rapid prototypes and complex geometries for engineering applications possible [7].

There are certain limitations in 3D printing technologies, in terms of materials, processes, and performance [8]. Research into naturally derived and renewable polymers, instead of petroleum-based polymers, with a sustainable environment-oriented approach has attracted a great amount of attention [9]. Bio-composite filaments made of natural fibre-reinforced materials, such as wood shavings, hemp or flax fibre, are frequently used to improve composite material properties [10]. PLA with a wood reinforcement (PLAW) composite can be considered as a reasonable alternative to solid wood in complex interior architecture products with improved mechanical properties because handcrafted

wood carvings and furniture are costly and unsustainable [11]. The PLAW composite used in 3D printers has emerged as an economically and environmentally sustainable option for manufacturers [12]. However, the need for more extensive research on the behaviour of this material is also emphasised in the literature [13].

In addition, working with complex hull forms in classical wooden boat production is very challenging, and time and energy consuming; it requires a lot of dexterity [14]. It is clear that the additive manufacturing technique will be extremely useful in the production of boats, phasing out the difficulties created by the high angle curvatures in hull geometry. Thus, boat forms with better hydrodynamic performance will be easily

accessible. Despite the mentioned benefits, the use of additive manufacturing technologies in the boat building industry has not yet become as widespread as in the automotive and aviation industries [15].

Wood-plastic composites, based on heat-treated wood and polypropylene, are also more resistant to UV radiation, which is an essential factor in long-term performance in an open environment [15]. The choice of wood species in such a composite is critical to its resistance to environmental marine degradation [17]. In addition, it is undeniable that mechanical properties will be improved if the surface treatment is applied between the matrix and the fibres [18]. The changes in printing parameters, such as printing temperature, infill rate, and

printing speed, significantly influence the performance in different environments. For this reason, it is necessary to carry out a parameter optimisation study before the manufacturing process [19].

On the other hand, the performance of petrol-derived thermoplastics in a corrosive environment is found to be relatively high compared to biodegradables. The mechanism of the degradation of thermoplastics exhibits complexity and needs to be fully understood [20].

It should be emphasised that the marine environment is highly corrosive and abrasive. Seawater contains an average of 3.5% salt in different forms, depending on the geography and ocean systems [21]. This corrosive environment reaches its maximum in the 'splash zone', as seen in Fig. 3. These regions get wetted by the waves and are then dried and cooled during the day [22]. In this study, an air conditioning cabinet was used to simulate the conditions in the related zones. In addition, marine fouling and boring organisms can degrade the materials by coating them.

PLAW composite degradation severity depends on factors such as the environment, the presence of microorganisms, and the type of components of the composite. Studies have shown that both of the components of the composite could be very sensitive to marine environmental agents as a result of this effect [21]; the emergence of fibre and microplastic pollution will be inevitable.

In order for PLAW composite to be considered as a sustainable material, its components must also be sustainable. Although PLA is derived from sustainable plant sources, the other component, wood, should only be expected to be in the form of waste [23]. The amount of energy needed in the production of PLAW composites with 3D printing technology, and the amount of energy required to produce an equivalent product from solid wood, will also give an idea of which option is more sustainable [24]. In this context, it is important to perform life cycle analyses to compare the environmental impacts of the options.

As the wood fibre ration in the composite increases up to a certain value, it is expected that the mechanical performance of the composite will also increase. However, if this ratio is above a certain value, the composite starts to lose its mechanical performance and printability, together with its toughness. For short fibre-reinforced polymer composites to be used with the FFF technique, the fibre ratio should not generally exceed 20% by weight. The weight ratio varies, according to the matrix and its rheology [25].

In this study, A PLAW composite was designed using PLA and 8% recycled yellow pine macro-particles; test samples were then 3D printed with the FFF technique. In order to appreciate the marine environment's effects on the composite's mechanical performance, accelerated ageing conditioning was applied before tensile and compressive testing was performed. Thermal analyses were also carried out, to better understand the behaviour of the material. The composite material's performance under the mentioned loads was compared with those of the same solid wood.

The potential use of the proposed sustainable composite is suggested in the conclusion.

MATERIALS AND METHODS

PLAW COMPOSITE

The Natureworks' 'Biopolymer 4043D' PLA product was chosen as the matrix of the PLAW composite. This product was primarily designed for filament production in 3D printing. The density of the PLA was $1.24 \times 10^{-3} \text{ kg.m}^{-3}$, the melting temperature was 154°C , and the melt flow rate was $2 \times 10^{-2} \text{ kg.s}^{-1}$.

PLAW composite was reinforced with 8% recycled yellow pine, by weight. This optimal ratio was determined by considering the studies in the literature and additional testing by the authors [26].

As the reinforcement, yellow pine sawdust was obtained from the waste of a wooden boat manufacturing workshop's horizontal saw on the Bodrum Peninsula (Turkey). The wood fibres were sieved through a $5 \times 10^{-4} \text{ m}$ aperture. The wood fibres had an average density of 420 kg.m^{-3} , a diameter between 2×10^{-8} and $5 \times 10^{-7} \text{ mm}$ and a length between 5×10^{-2} and 2 mm . No surface treatment was performed on the wood fibres. The relative moisture of the wood was measured as 12% and it was dried in an oven at a constant temperature.

In Fig. 2, 10 cm long benchmark samples represent the quality of the printing of the PLAW composite using the equipment stated for this study.



Fig. 2. Benchmark samples made by additive manufacturing using PLAW composite

FILAMENT PRODUCTION

PLAW composite pellets were used to produce the filament of $1.75 \pm 0.1225 \text{ mm}$ in a 20 mm twin screw extruder at 205°C and with a screw speed of 230 rpm, while the maximum operating temperature of the setup was 210°C . Water and air cooling was used during the process (Fig. 3). A roundness ratio with an error rate of 8% was found to be acceptable.

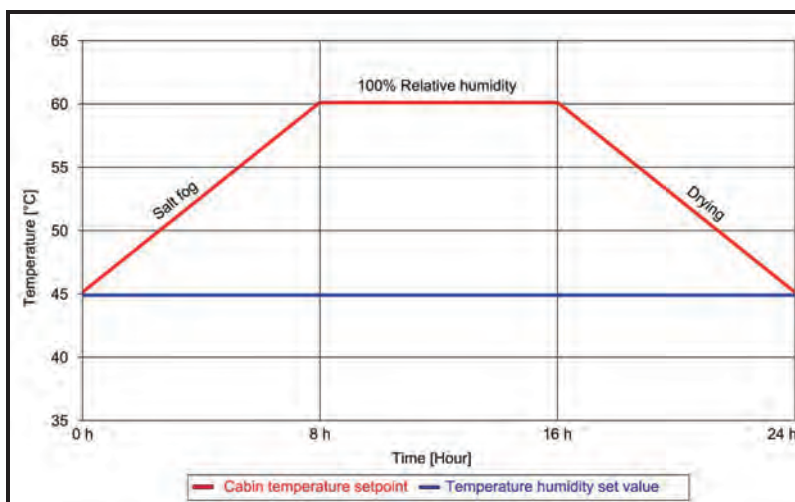


Fig. 3. Temperature and humidity values of the ageing cabinet for 1 day

5 nm gold.

CHARACTERISATION

Optical microscopy

Optical microscope measurements were made using a Bresser BioScience Trino Microscope, to measure fibre lengths and diameters.

Scanning electron microscope (SEM)

Microstructure analyses were performed on a Zeiss Sigma500 FESEM, using the SE2 detector. Specimen imaging of the tensile test cracks was performed at different magnifications, as seen in the line scale in Fig. 8, under 1.5-3.0 kV EHT. Before placement in the microscope chamber, the samples were fixed on aluminium stubs with double-sided carbon tape and sputter coated with

SPECIMEN PRODUCTION

Tensile and compression test specimens were produced using a Creality brand and Cr-200b model FFF 3D printer. The printing temperature was set to 208 °C, while the printing speed was $5 \times 10^{-2} \text{ m.s}^{-1}$. The layer thickness was determined as 12 mm. The raft was used to adhere the products to the heated glass tray during printing. A nozzle width of 6 mm was chosen for production, after experiencing clogging of the 4 mm diameter nozzle. The solid wood and PLAW composite specimen geometries were as shown in Fig. 5. For the compression tests, a 30 x 20 x 20 mm rectangular prism was used. Solid wood samples were prepared by using a CNC router.

ACCELERATED AGING

A standard CC1000ip weathering chamber from the Ascott company (shown in Fig. 6) was used for accelerated ageing, in accordance with ISO 9227 (2017). The device was programmed for three testing durations (one, two and four weeks). During these aging periods, water spraying, a salty fog environment and drying cycle were applied at elevated temperatures and at equal time intervals, daily.

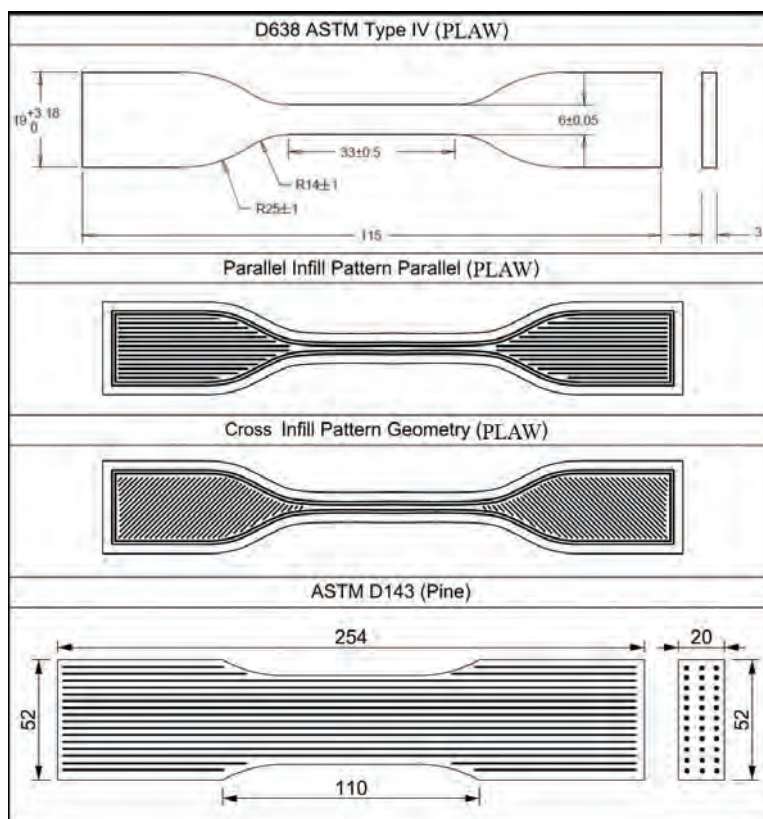


Fig. 5. The geometry of the specimens for tensile testing



Fig. 4. PLAW composite and wood samples in the ageing cabinet

Differential scanning calorimetry (DSC)

Differential Scanning Calorimetry (DSC) analysis was used to determine the glass transition temperature and melting temperature, to analyse the effect of wood reinforcement on thermal properties by comparing them to PLA using a Perkin Elmer Diamond brand DSC. The materials were heated to 300 °C.

Thermogravimetric analysis (TGA)

Thermogravimetric analysis (TGA) was used to investigate thermal resistance and analyse the effect of wood reinforcement on endurance, by comparing it to PLA using a Perkin Elmer Diamond brand TGA. The materials were heated to 850 °C.

RESULTS AND DISCUSSION

According to the results of the tensile and compression testing of PLAW composite and solid wood, there is a significant difference between the strength values. Printing directions and fibre orientation have a significant effect on the strength of the composite. In addition, it was seen that aging has a remarkable degradation effect in both directions. After one month of aging, tensile values of 39% for the 0° orientation and 40% for the 45° orientation were observed. On the other hand, there was a 15% and 33% decrease in compressive values, respectively (Table 1). Materials produced with a parallel fill geometry (0° orientation) show better strength in the tensile direction. Samples with a cross-fill geometry (45° orientation) are preferred when the force loading is not known exactly; they give the material an isotropic structure.

For solid wood samples cut parallel to the loading directions, the tensile strength of 85 MPa (in the control group) decreased to 56 MPa (-34%) at the end of one-month of accelerated ageing. As for the compression test, this value dropped from 59 MPa to 32 MPa (-46%) (Table 1). In addition, colour changes were observed on the surface of the aged samples.

Standard deviations of the test values were found to be relatively high in the mechanical tests. One of the most important reasons for this is that the filament diameter cannot be captured very accurately in the extrusion process,

causing production errors in the filament roundness. Printing errors decrease the overall performance. For this reason, using a water cooling device instead of air cooling in filament production will reduce production errors [27].

From the DSC analysis, when the PLA was reinforced with wood, it was observed that the glass transition temperature increased from 59.83 to 62.37 °C, while the melting temperature decreased from 152.29 to 146.68 °C. As for the TGA analysis, it was seen that the PLA lost its mass significantly at 326.62 °C, while PLAW composites lost their thermal stability at 323.42 °C. It is logical for PLAW composite to have lower thermal properties than PLA because of the reinforcement process of PLA, where the material was extruded twice, which reduces the mechanical performance of the material. Better performance would be achieved if reinforcement and filament production were performed in the same extruder at the same time (Fig. 6).

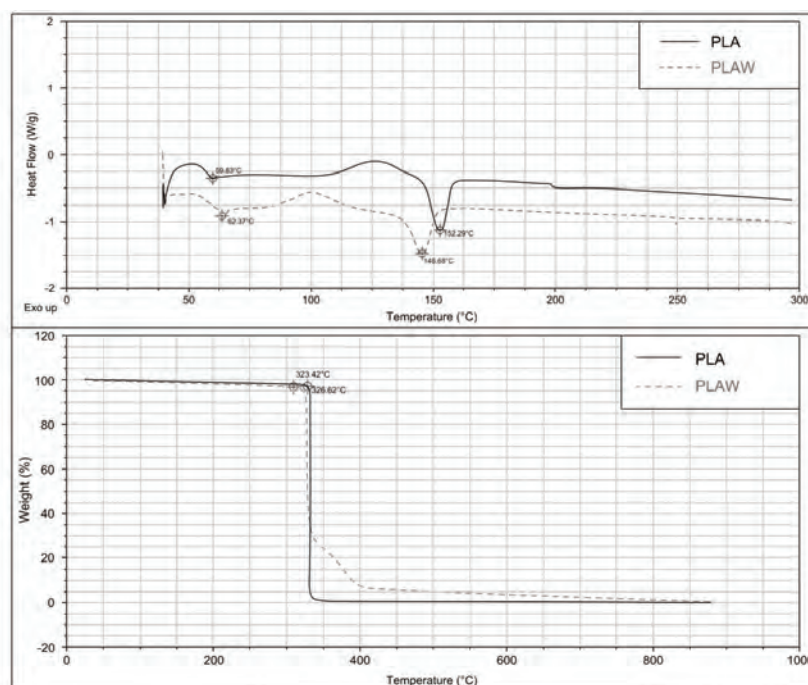


Fig. 6. DSC and TGA analysis of PLAW composite

Table 1. Aging results

Materials	Tests	Orientation	Strength (MPa)			
			Control	One week*	Two week*	One month*
PLAW	Tensile	0°	21	20 (-5%)	19 (-10%)	15 (-39%)
		45°	23	21 (-9%)	20 (-14%)	14 (-40%)
	Compressive	0°	19	18 (-5%)	17 (-11%)	16 (-15%)
		45°	13	13 (-2%)	11 (-16%)	10 (-33%)
Solid Wood	Tensile	0°	85	71 (-16%)	65 (-23%)	56 (-34%)
	Compressive	0°	59	53 (-10%)	40 (-33%)	32 (-46%)

* Values in parentheses are degradation ratios relative to the control samples

SEM images show that parallel printed layers are very rigid as lamina but their adhesion performance was detected as being weak when in line with the thickness. Laminate performance was found insufficient. Also, different combinations of printing parameters, such as printing temperature, speed and layer thickness, could have an effect on the results.

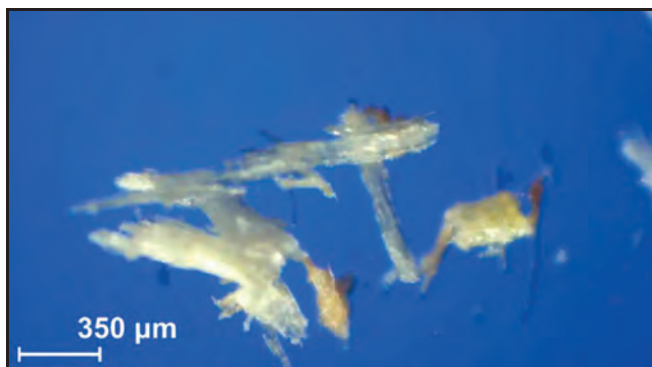


Fig. 7. Image of yellow pine sawdust in an optical microscope

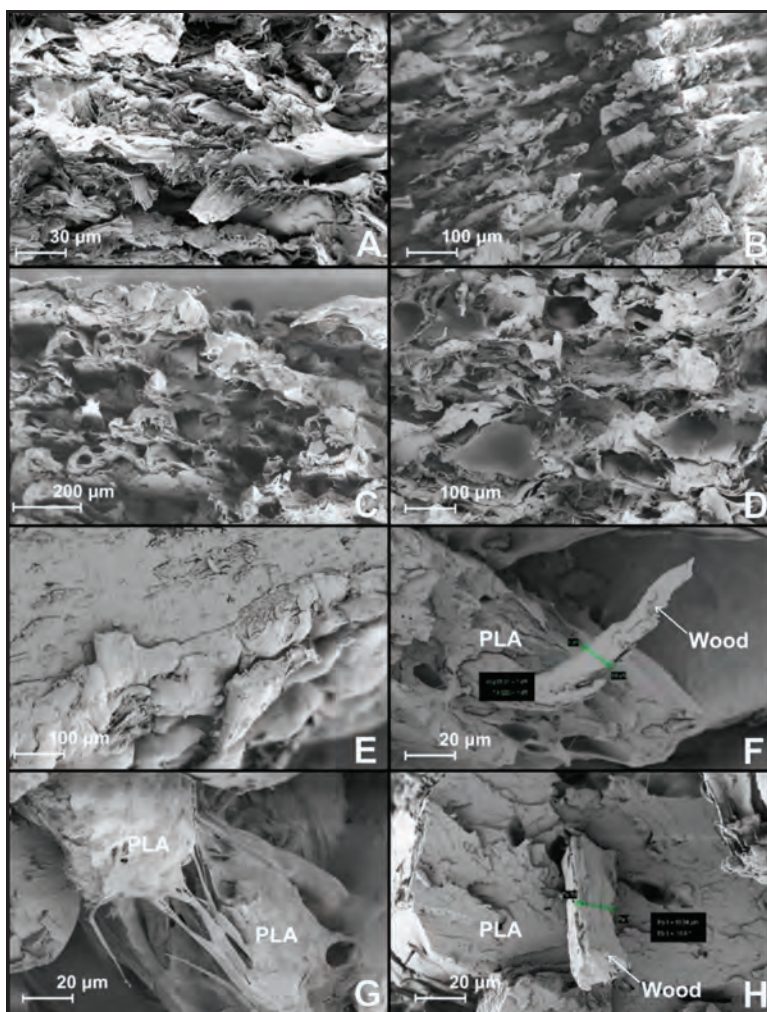


Fig. 8. SEM images of PLAW composites according to printing directions and ageing period. A: parallel, control, B: cross, control, C: parallel, first week, D: cross, first week, E: parallel, second week, F: cross, second week, G: parallel, one month, H: cross, one month

As for ageing performance, the PLAW composite degraded more than solid wood because of the PLA's biodegradable component. In addition, since the PLAW composite contains only 8% wood by weight, the composite tends to behave more like PLA [28]. In almost all cases, from the 2nd week, the degradation is more noticeable. The degradation of solid wood develops rapidly and suddenly, just as described in the literature [29,30] (Table 1).

CONCLUSIONS

In this study, the strength and environmental degradation of a PLAW composite material (which can be an alternative for solid wood elements that do not operate under heavy loads in boatbuilding) was studied in marine conditions. The proposed new material is sustainable because it is obtained from natural resources and waste; the proposed production method, additive manufacturing, is an option which allows designers to work freely. From tensile and compression testing, image analyses and thermal analyses, it has been revealed that PLAW composite is rapidly degraded by the marine environment and yet it can find specific uses, such as the production of decorative objects.

ACKNOWLEDGEMENTS

The authors would like to thank Defne Öztürk from IBGEM (the Izmir Biomedicine and Genome Center Electron Microscopy Core facility) for providing the related infrastructure and expertise during the SEM analysis.

REFERENCES

1. Y. Praharsi, M. A. Jami, G. Suhardjito, and H. M. Wee. "Modeling a traditional fishing boat building in East Java, Indonesia." *Ocean Engineering*. 189, 2019, doi: 10.1016/j.oceaneng.2019.106234.
2. K. Kránitz, W. Sonderegger, C. T. Bues, and P. Niemz. "Effects of aging on wood: a literature review." *Wood Science and Technology*. 50 (1), 2016, 7–22, doi: 10.1007/s00226-015-0766-0.
3. F. E. Bendourou, G. Suresh, M. A. Laadila, P. Kumar, T. Rouissi, G. S. Dhillon, K. Zied, S. K. Brar, and R. Galvez. "Feasibility of the use of different types of enzymatically treated cellulosic fibres for polylactic acid (PLA) recycling." *Waste Management*. 121, 2021, 237–247, doi: 10.1016/j.wasman.2020.11.058.

4. T. N. Maraseni, S. Phimmavong, R. J. Keenan, V. Vongkhamsao, G. Cockfield, and H. Smith. "Financial returns for different actors in a teak timber value chain in Paklay District, Lao PDR." *Land Use Policy*. 75, 2018, 145–154, doi: 10.1016/J.LANDUSEPOL.2018.03.037.
5. C. Xu, C. Sun, H. Wan, H. Tan, J. Zhao, and Y. Zhang. "Microstructure and physical properties of poly(lactic acid)/polycaprolactone/rice straw lightweight bio-composite foams for wall insulation." *Construction and Building Materials*. Vol. 354, 2022, 129216, doi: 10.1016/j.conbuildmat.2022.129216.
6. C. M. Chan, S. Pratt, P. Halley, D. Richardson, A. Werker, B. Laycock, and L. J. Vandí. "Mechanical and physical stability of polyhydroxyalkanoate (PHA)-based wood plastic composites (WPCs) under natural weathering." *Polymer Testing*. 73, 2019, 214–221, doi: 10.1016/J.POLYMERTESTING.2018.11.028.
7. S. Kumar, R. Singh, T. P. Singh, and A. Batish. "PLA Composite Matrix as Functional Prototypes for Four Dimensional Applications." *Encyclopedia of Materials: Composites*. 2019, 1091–1100, doi: 10.1016/B978-0-12-803581-8.11595-4.
8. J. Tian, R. Zhang, Y. Wu, and P. Xue. "Additive manufacturing of wood flour/polyhydroxyalkanoates (PHA) fully bio-based composites based on micro-screw extrusion system." *Materials and Design*. 199, 2021, doi: 10.1016/j.matdes.2020.109418.
9. J. Liu, L. Sun, W. Xu, Q. Wang, S. Yu, and J. Sun. "Current advances and future perspectives of 3D printing natural-derived biopolymers." *Carbohydrate Polymers*. 207, 2019, 297–316, doi: 10.1016/J.CARBPOL.2018.11.077.
10. N. Degiuli, A. Farkas, I. Martić, I. Zeman, V. Ruggiero, and V. Vasiljević. "Numerical and experimental assessment of the total resistance of a yacht." *Brodogradnja*. 72 (3), 2021, 61–80, doi: 10.21278/brod72305.
11. N. P. Nhung, N. M. Chi, P. Q. Thu, B. H. Thuong, D. Ban, and B. Dell. "Market and policy setting for the trade in *Dalbergia tonkinensis*, a rare and valuable rosewood, in Vietnam." *Trees, Forests and People*. 1, 2021, 100002, doi: 10.1016/J.TFP.2020.100002.
12. A. Duigou, D. Correa, M. Ueda, R. Matsuzaki, and M. Castro. "A review of 3D and 4D printing of natural fibre biocomposites." In *Materials and Design*. 194, 2020, doi: 10.1016/j.matdes.2020.108911.
13. J. Antonio Travieso-Rodriguez, M. D. Zandi, R. Jerez-Mesa, and J. Lluma-Fuentes. "Fatigue behaviour of PLA-wood composite manufactured by fused filament fabrication." *Journal of Materials Research and Technology*. 9 (4), 2020, 8507–8516, doi: 10.1016/j.jmrt.2020.06.003.
14. R. Pommier, G. Grimaud, M. Prinçaud, N. Perry, and G. Sonnemann. "Comparative environmental life cycle assessment of materials in wooden boat ecodesign." *International Journal of Life Cycle Assessment*. 21 (2), 2016, 265–275, doi: 10.1007/s11367-015-1009-1.
15. Ş. O. Taş and B. Şener. "The Use of Additive Manufacturing in Maritime Industry." *International Journal of Engineering Trends and Technology*. 67(6), 2019, 47–51, doi: 10.14445/22315381/ijett-v67i6p209.
16. A. Joseph Arockiam, K. Subramanian, R. G. Padmanabhan, R. Selvaraj, D. K. Bagal, and S. Rajesh. "A review on PLA with different fillers used as a filament in 3D printing." *Materials Today: Proceedings*. 2021, doi: 10.1016/J.MATPR.2021.09.413.
17. A. Vedrtam, S. Kumar, and S. Chaturvedi. "Experimental study on mechanical behaviour, biodegradability, and resistance to natural weathering and ultraviolet radiation of wood-plastic composites." *Composites Part B: Engineering*. 176, 2019, 107282, doi: 10.1016/J.COMPOSITESB.2019.107282.
18. M. Kariz, M. Sernek, M. Obućina, and M. K. Kuzman. "Effect of wood content in FDM filament on properties of 3D printed parts." *Materials Today Communications*. 14, 2018, 135–140, doi: 10.1016/j.mtcomm.2017.12.016.
19. X. Wang, F. Sotoudehniakarani, Z. Yu, J. J. Morrell, J. Cappellazzi, and A. G. McDonald. "Evaluation of corrugated cardboard biochar as reinforcing fibre on properties, biodegradability and weatherability of wood-plastic composites." *Polymer Degradation and Stability*. 168, 2019, 108955, doi: 10.1016/J.POLYMDEGRADSTAB.2019.108955.
20. K. C. Hung, Y. L. Chen, and J. H. Wu. "Natural weathering properties of acetylated bamboo plastic composites." *Polymer Degradation and Stability*. 97 (9), 2012, 1680–1685, doi: 10.1016/J.POLYMDEGRADSTAB.2012.06.016.
21. G. T. Kirker, C. Brischke, L. Passarini, and S. L. Zelinka. "Salt damage in wood: Controlled laboratory exposures and mechanical property measurements." *Wood and Fibre Science* 52 (1), 2020, 44–52, doi: 10.22382/wfs-2020-005.
22. Z. Cui, X. Li, K. Xiao, and C. Dong. "Atmospheric corrosion of field-exposed AZ31 magnesium in a tropical marine environment." *Corrosion Science* 76, 2013, 243–256, doi: 10.1016/j.corsci.2013.06.047.
23. M. Ouda, Y. Ibrahim, P. Kallem, B. Govindan, F. Banat, and S. W. Hasan. "Highly permeable, environmentally-friendly, antifouling polylactic acid-hydroxyapatite/polydopamine (PLA-HAp/PDA) ultrafiltration membranes." *Journal of Cleaner Production*. 330, 2022, doi: 10.1016/j.jclepro.2021.129871.

24. M. Hetzer and D. De Kee. "Wood/polymer/nanoclay composites, environmentally friendly sustainable technology: A review." In *Chemical Engineering Research and Design*. 86 (10), 2008, 1083–1093, doi: 10.1016/j.cherd.2008.05.003.
25. M. A. Jenkins, R. N. Klein, and V. L. Mcdaniel. "Yellow pine regeneration as a function of fire severity and post-burn stand structure in the southern Appalachian Mountains." *Forest Ecology and Management*. 262 (4), 2021, 681–691, doi: 10.1016/J.FORECO.2011.05.001.
26. M. A. Binhussain and M. M. El-Tonsy. "Palm leaf and plastic waste wood composite for out-door structures." *Construction and Building Materials*. 47, 2013, 1431–1435, doi: 10.1016/j.conbuildmat.2013.06.031.
27. M. Fernandez-Vicente, W. Calle, S. Ferrandiz, and A. Conejero. "Effect of Infill Parameters on Tensile Mechanical Behaviour in Desktop 3D Printing." *3D Printing and Additive Manufacturing*. 3 (3), 2016, 183–192, doi: 10.1089/3dp.2015.0036.
28. E. Castro-Aguirre, F. Iñiguez-Franco, H. Samsudin, X. Fang, and R. Auras. "Poly(lactic acid)—Mass production, processing, industrial applications, and end of life." In *Advanced Drug Delivery Reviews*. 107, 2016, 333–366, doi: 10.1016/j.addr.2016.03.010.
29. A. Klüppel and C. Mai. "Effect of seawater wetting on the weathering of wood." *European Journal of Wood and Wood Products*. 76 (3), 2018, 1029–1035, doi: 10.1007/s00107-017-1268-6.
30. D. Deb and J. M. Jafferson. "Natural fibres reinforced FDM 3D printing filaments." *Materials Today: Proceedings*. 46, 2021, 1308–1318, doi: 10.1016/j.matpr.2021.02.397.

BLOCKCHAIN-ENABLED TRANSFER LEARNING FOR VULNERABILITY DETECTION AND MITIGATION IN MARITIME LOGISTICS

Chandra Priya J ¹

Krzysztof Rudzki ²

Thanh Tuan Le ³

Hoang Phuong Nguyen⁴

Naruphun Chotechuang⁵

Nguyen Dang Khoa Pham ^{6*}

¹ Department of Computer Science and Engineering, Department of Mechanical Engineering, Mepco Schenk Engineering College, Sivakasi, India.

² Faculty of Marine Engineering, Gdynia Maritime University, Gdansk, Poland

³ Institute of Engineering, HUTECH University, Ho Chi Minh City, Viet Nam

⁴ Academy of Politics Region II, Ho Chi Minh City, Viet Nam, Viet Nam

⁵ Faculty of International Maritime Studies, Kasetsart University, Sri Racha Campus, Chonburi, Thailand

⁶ PATET Research Group, Ho Chi Minh City University of Transport, Ho Chi Minh City, Viet Nam

* Corresponding author: khoapnd@ut.edu.vn (Nguyen Dang Khoa Pham)

ABSTRACT

With the increasing demand for efficient maritime logistic management, industries are striving to develop automation software. However, collecting data for analytics from diverse sources like shipping routes, weather conditions, historical incidents, and cargo specifications has become a challenging task in the distribution environment. This challenge gives rise to the possibility of faulty products and traditional testing techniques fall short of achieving optimal performance. To address this issue, we propose a novel decentralised software system based on Transfer Learning and blockchain technology named as BETL (Blockchain -Enabled Transfer Learning). Our proposed system aims to automatically detect and prevent vulnerabilities in maritime operational data by harnessing the power of transfer learning and smart contract-driven blockchain. The vulnerability detection process is automated and does not rely on manually written rules. We introduce a non-vulnerability score range map for the effective classification of operational factors. Additionally, to ensure efficient storage over the blockchain, we integrate an InterPlanetary File System (IPFS). To demonstrate the effectiveness of transfer learning and blockchain integration for secure logistic management, we conduct a testbed-based experiment. The results show that this approach can achieve high precision (98.00%), detection rate (98.98%), accuracy (97.90%), and F-score (98.98), which highlights its benefits in enhancing the safety and reliability of maritime logistics processes. Additionally, the computational time of BETL (the proposed approach) was improved by 18.9% compared to standard transfer learning.

Keywords: Logistic management, Blockchain, Transfer Learning, Marine ecosystem, Vulnerability detection

INTRODUCTION

In recent years, maritime-related issues have been paid much attention since maritime has been known to play an important role in developing the economy [1]–[4]. However, maritime activities, including shipping and port activities, have a large number of disadvantages, such as high pollutant emissions (including ship and port activities), low operational efficiency, high-cost logistical activities, high fuel consumption, maritime safety... etc. [5]–[11]. Containerisation has played a crucial role in

accelerating global trade and establishing extensive global supply chains, contributing significantly to economic globalisation in the 20th century [12][13]. However, progress in container shipping has not kept up with the rapid advancements in international trade and supply chains [14][15]. Businesses now demand more timely and transparent deliveries with enhanced traceability, which traditional container shipping struggles to meet [16][17]. The movement of containers involves complex bilateral interactions among various entities in the logistics ecosystem, resulting in delays, inefficiencies, and susceptibility to fraud

[18][19]. Paper-based processes and numerous permissions and transactions further contribute to inefficiencies towards hard evidence of its effectiveness [20]. As a result, there is a need for innovative solutions to address these vulnerabilities in maritime logistics [21]. To tackle these challenges, this manuscript introduces a groundbreaking solution: Blockchain-Enabled Transfer Learning. By leveraging the transparency and immutability of blockchain and the analytical capabilities of AI, the proposed system aims to detect and mitigate vulnerabilities in real time, enhancing the security and reliability of the logistics ecosystem [22][23]. The integration of blockchain and Transfer Learning introduces a decentralised architecture with smart contracts, automating trust and collaboration among multiple stakeholders in the logistics chain [24]. A comprehensive testbed-based experiment validates the efficacy of the solution, fortifying the logistics industry against vulnerabilities and disruptions, while improving global maritime trade security and efficiency [25][26].

In traditional maritime logistics, the seamless coordination among diverse entities relies on efficient communication and monitoring within a shared workspace [27]. As cargo is transported by ship from one port to another, several pieces of documentation must also be moved and verified by multiple parties such as bill of lading, packing lists, certificates of origin, commercial invoices, and export licenses [28]. In addition, a vessel's crew, who are not necessarily nationals of the flag state, needs to manage, verify, and validate seafaring crew certificates in compliance with global regulations such as the IMO's International Convention on Standards of Training, Certification and Watchkeeping for Seafarers (STCW) and the Convention on Safety of Life at Sea (SOLAS) [29][30]. However, in a remote working environment, ensuring seamless synchronisation becomes more challenging, leading to potential code errors, oversights, and mistakes [31]. Blockchain adoption in the maritime supply chain for containerised international trade faces several barriers [32][33]. These barriers include a lack of support from influential stakeholders and a lack of government regulations [34]. The key stakeholders in this adoption process are container lines, ports, beneficial cargo owners, freight forwarders/third-party logistics, and customs authorities [35][34]. Additionally, there are non-technical barriers such as resistance to change and a lack of awareness and understanding that should not be underestimated [36]. To successfully implement blockchain in the shipping industry, certain design principles should be considered, including immutability, decentralisation, security, privacy, compatibility, scalability, inclusiveness, and territoriality [37][38]. The implementation phase can be influenced by different approaches, which can affect the likelihood of adoption by industry stakeholders [39]. Actually, intelligent methods such as machine learning and artificial intelligence, which could be successfully applied to many fields such as waste and energy management, optimization, planning, prediction, and error detection aiming to generate a powerful collaboration [40]–[44], could have the potential to revolutionise the maritime sector through improved efficiency, safety, and environmental sustainability [45]–[47].

Secure supply chain management methods (to protect blockchain from attack) can be achieved through the implementation of blockchain technology. Blockchain provides decentralised and

immutable data storage, enabling trust and transparency in supply chain networks [48][49]. By using blockchain, a digital log of all propagating information can be maintained, allowing for the validation of official updates and the rejection of potentially malicious payloads [50][51]. Additionally, the use of attribute-based access control models, in combination with blockchain, can enable decentralised, fine-grained, and dynamic access control management in supply chain systems, ensuring data privacy and network scalability [52]. The integration of blockchain with supply chain management also helps minimise the interference of middleman attacks and allows the discarding of forged products, thereby maintaining integrity and authentication throughout the supply chain. To summarise the state-of-the-art literature, the problem scenarios are listed below.

Over-centralisation: Consider S as the comprehensive set encompassing all entities actively engaged in maritime logistics, C is the set of all communication channels between the entities in S , and R is the set of all associated risks. The problem of centralised maritime logistics is the minimisation of the following expression:

$$f(S, C, R) = \sum (r * p(r)) \quad (1)$$

where $p(r)$ is the probability of risk r occurring.

Data Security in remote workplace: Let G be the probability of a collaborative effort being successful, D is the distance between the collaborating entities and H is the disparity in hardware and software accessibility between remote and in-office workers. Then, the problem of the probability of a collaborative effort can be modelled as follows:

$$P = f(D, H) \quad (2)$$

where f is a function that maps the distance and disparity to the probability of collaboration, and D and H are continuous variables that represent the distance between the collaborating entities and the disparity in software accessibility, respectively. The statistical analysis for the estimating function f has the inferences that G decreases as D increases and as H increases.

Data sharing dilemma: Maritime supply chain stakeholders are concerned with sharing key business information, such as customer, supplier, and freight data. This is because many forwarders and intermediaries benefit from information asymmetry, which could impede widespread adoption. If we let T be the time it takes to complete a task, then it can be modelled as follows:

$$T = g(H) \quad (3)$$

where g is a function that maps the disparity to the time taken to complete a task. The problem is that T is directly proportional to H .

RELATED WORKS

The use of electronic bills of ladings has been shown to enhance the efficiency of shipping operations, ship finance, and marine

insurance. In contrast, Papathanasiou et al. [52] proposed that the shipping industry could derive advantages from blockchain technology in areas such as document exchanges, optimising container utilisation, intelligent transportation, and precise container weighing. Hamidi et al. [53] and Zhong et al. [54] suggested that the adoption and effective use of blockchain by container lines could contribute to reducing price competition between them. Furthermore, Hasan et al. [55] demonstrated a smart-contract solution involving smart containers equipped with Internet of Things (IoT) sensors to efficiently manage shipments. They showcased how blockchain enables real-time tracking of items like vaccines, including monitoring temperature, humidity, and air pressure. In their conceptual study, Lambourdiere and Corbin [56] proposed that blockchain can have a positive impact on information exchange, supply chain coordination, visibility, and performance within maritime supply chains.

Taking a sustainability perspective, Jović et al. [57] conducted a literature review and categorised the benefits of blockchain in maritime supply chains into economic, social, and environmental advantages. Meanwhile, Li et al. [58] explored pilot applications in maritime supply chains and identified significant benefits from blockchain, including expediting processes, reducing costs related to documentation, ensuring secure records for food safety, enabling real-time tracking, facilitating efficient coordination across various modes of transport, and improving compliance with shipment regulations and marine insurance requirements. Lastly, Munim et al. [59] conducted a review of blockchain literature in a maritime context, revealing 17 potential uses of blockchain technology. The state-of-the-art studies focused on the risk analysis of blockchain-integrated systems (BISs) in container shipping. However, it failed to capture the full range of risks and uncertainties associated with other aspects of maritime logistics services [60][61]. The study does not provide a comprehensive analysis of the potential mitigation strategies or recommendations for managing the

identified risks in container shipping BISs. In general, the cause and effect of malicious software is presented in Fig. 1.

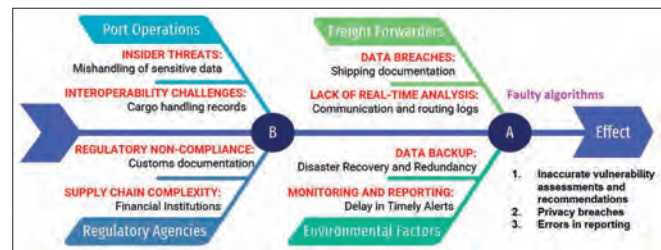


Fig. 1. Cause and effect of malicious software

BLOCKCHAIN-ENABLED TRANSFER LEARNING (BETL): GENERIC ARCHITECTURE

The proposed architecture ensures efficient and accurate vulnerability detection, security, scalability, trust, transparency, and reliability in a multiparty maritime logistics ecosystem [62] [63]. The overall system is divided into two parts: a transfer learning (TL) model that predicts software vulnerabilities, and a blockchain-based system that ensures security, trust, and transparency [64] [65]. InterPlanetary File System (IPFS) is integrated to improve the scalability and efficiency of data storage. The TL model is trained on a large dataset of software vulnerabilities to learn the patterns of vulnerabilities. The model can then be used to predict vulnerabilities in new software. The blockchain-based system uses a distributed ledger to store vulnerability information. This ensures that the information is secure, transparent, and tamper resistant. An IPFS peer-to-peer file storage system is used for scalable and efficient storage. The BETL architecture assumes a multiparty ecosystem, as shown in Fig. 2. The distinctive roles of various stakeholders include the following.

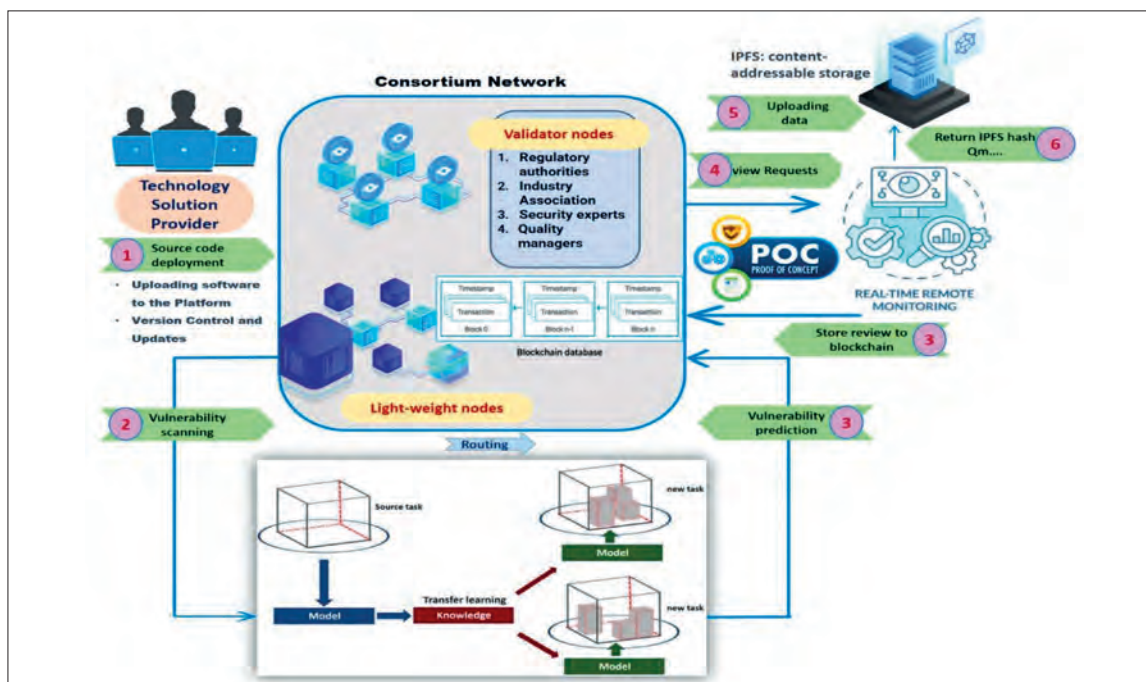


Fig. 2. BETL system architecture

Technology Solution Provider (TSP): The TSP is an authenticated entity in the logistics ecosystem with a unique identifier. It is responsible for writing code, following the requirements of the assigned module. The choice of programming languages depends on the requirements and varies widely based on the application. The TSP is provided with login credentials to access the code submission platform and has the privilege of performing unit testing. It is assumed that the TSP submits its code over a secure network in a remote scenario.

Consortium Network: We opted for a consortium blockchain as it balances the security of a private blockchain and the flexibility of a public blockchain. The network is formed and operated by a group of trusted entities, regulatory authorities, industry associations, security experts, and quality managers. This ensures that the blockchain is highly secure and resistant to attack. *Validator nodes* are responsible for reaching a consensus on the order of transactions and ensuring that no unauthorised changes are made to the blockchain. They do this by using a voting mechanism to approve new blocks of transactions. *Lightweight nodes* can participate in the network by reading the blockchain and querying information. However, they cannot participate in the consensus process.

InterPlanetary File System: An IPFS private network provides secure and decentralised storage and access to data about the supply chain. This can help to improve the efficiency of learning models by reducing the need to transfer data between different systems.

ARCHITECTURAL DESIGN

The BETL architecture consists of three main components: a vulnerability scanner, a blockchain-based decentralised infrastructure, and a private IPFS network shared by the validators. There are four major entities including technology solution providers, validator nodes, lightweight nodes, and IPFS storage architecture. Data and information exchanged among entities are stored on the blockchain as immutable transactions. A smart contract deployed on the blockchain governs the interactions and automates various functionalities. The core functionalities of the proposed architecture are twofold:

- **Transfer Learning-based source code vulnerability scanning:** This component uses artificial intelligence to identify vulnerabilities in the source code.
- **Blockchain-based decentralisation for vulnerability prevention:** This component uses the blockchain to store information about vulnerabilities and to prevent vulnerabilities from being exploited.

TRANSFER LEARNING-BASED VULNERABILITY SCANNING

During the outsourcing of the development process, developers may purposefully or inadvertently make certain mistakes that could result in a vulnerable application. Traditional vulnerability detection in software testing requires human intervention, making it time-consuming.

There is also the possibility of human error in the reviewing process. In such a scenario, transfer learning can greatly help reduce this risk-oriented human intervention in the testing process of vulnerabilities. In the proposed system, a transfer learning model is trained on a dataset of 20,724 source code files from the six most common languages (C, C++, Python, Java, Ruby, and C#). The dataset is categorised into vulnerable and non-vulnerable codes, based on vulnerability thresholds. The National Institute of Standards and Technology (NIST) categorises the level of severity as low, medium, or high. In this work, we propose a non-vulnerability score range mapping with a reverse threshold manner to that of the NIST standard. This is mainly for the following reasons:

- The transfer learning model performs learning for a non-vulnerability score, i.e. the prediction score tells us how well the source code is written.
- Software Development LifeCycle (SDLC) is concerned with ensuring error-free code at the production level. Having a non-vulnerability score, rather than a vulnerability score, for mapping the category range is more intuitive for the lead developer to make better decisions.

We mapped the non-vulnerability score range with the category of secureness of source code files, as shown in Table 2. This mapping can be customised, according to the requirements and policies of the organisation, and is controlled by the blockchain validator nodes. Once source codes are uploaded, the smart contract invokes the transfer learning model to check for vulnerability. The model predicts the non-vulnerability score for the source code and the score is mapped to the secureness category. The lead developer can then take appropriate action, based on the secureness category of the source code. This transfer learning-based vulnerability detection system can help to improve the efficiency and accuracy of vulnerability detection in maritime logistics. It can also help to reduce the risk of human error in the reviewing process. Table 2 summarises the differences between AI-based and transfer learning-based vulnerability detection.

Tab. 1. AI-based learning versus transfer learning

Feature	AI-based learning	Transfer learning
Model training $F: Z \rightarrow \mathbb{R}^d$ $Z \subseteq \mathbb{R}^d$, $d \gg \#$ vulnerabilities	$\{(z_i, y_i)\}_{i=1}^n$ where $z_i \in Z$ is the i^{th} vulnerability and is its label. AI requires n to be high	Let Z_s and Z_t be the source and target domains, respectively. Let f_s be a pre-trained model on source domain Z_s . TL leverage f_s to reduce training time
Accuracy	$Accuracy(f) = \frac{\sum_{x \in Z} I(f(x) = y)}{ Z }$ where $I(x)$ is an indicator function	$Accuracy(f_t) = \frac{\sum_{z_i \in Z_t} I(f_t(z_i) = y_i)}{ Z_t }$ f_t is a model learned on Z_s by leveraging knowledge from f_s . $f_t(z_i)$ is the prediction of the model for the vulnerability z_i
Scalability	$T = a \times D^b$ where T is the training time, D is the dataset size with a and b as constants	$T = a \times S^b + c \times T^d$ where T is the fine-tuning time with S and T as the source and target dataset size involving the constants a, b, c , and d
Cost-effectiveness	Can be expensive to develop and deploy	Can be more cost-effective than AI-based vulnerability detection

BLOCKCHAIN-BASED DECENTRALISATION FOR VULNERABILITY PREVENTION

The blockchain-based decentralised system for prevention consists of a smart contract that acts as the core logic unit of the system [66][67]. The smart contract is used to automate certain tasks on the blockchain, such as testing code for vulnerabilities and storing the results of the testing securely. When a developer uploads code for testing, the smart contract invokes a transfer learning to test the code for vulnerabilities. The neural network is trained on a dataset of known vulnerabilities, so that it can identify vulnerabilities in new code [68][69]. If the model detects vulnerability in the code, the smart contract stores the vulnerability information in the blockchain. The smart contract also stores the results of the testing, which indicates whether the code is vulnerable or not. If the code passes the test, the smart contract stores the results of the testing in the blockchain and stores the source code file in IPFS. IPFS is a distributed file storage system that makes it difficult to modify or delete files.

The access control mechanism of the smart contract ensures that only authorised users can access the data stored in the blockchain. This helps to protect the confidentiality and integrity of the data. The blockchain-based decentralised system for prevention provides several benefits, including:

Automated testing: The smart contract can automate the process of testing code for vulnerabilities. This can help to save time and improve the efficiency of the testing process.

Secure storage: The blockchain is a secure and tamper-proof distributed ledger. This helps to ensure that the data stored in the blockchain is protected from unauthorised access and modification.

Traceability: The blockchain provides a tamper-proof record of all changes to the data stored in the blockchain. This helps to ensure that the data is always accurate and reliable.

Pseudo-transparency: The blockchain is a pseudo-transparent ledger that is accessible to everyone. This helps to ensure that the testing process is transparent and accountable.

IPFS STORAGE FOR ANALYTICS

The IPFS 'DHT' is a Distributed Hash Table used to store the hashes of all the files that are stored in the Kademlia overlay network. N is the set of nodes in the IPFS DHT network [70]. Each node $n \in N$ maintains a routing table T_n that stores the location of other nodes in the network. The routing table is a hash table that maps the hashes of the nodes to the addresses of the nodes. To search for a file, a node n sends a query q to the DHT. The query is a hash of the file that is being searched for. The query is routed to the nodes that store the hash of the file. The routing table is a distributed hash table, so the query is routed to the nodes that are most likely to store the hash of the file. When a file is stored in the DHT, it is split into blocks and distributed to multiple nodes. The blocks of a file are replicated using a hash function to multiple nodes to ensure availability. The hash function is used to generate a unique identifier for each block. The blocks are then replicated to nodes that have the same hash identifier. The fault tolerance of the IPFS DHT

network is achieved through replication. The internal working of IPFS can be represented by the following functions:

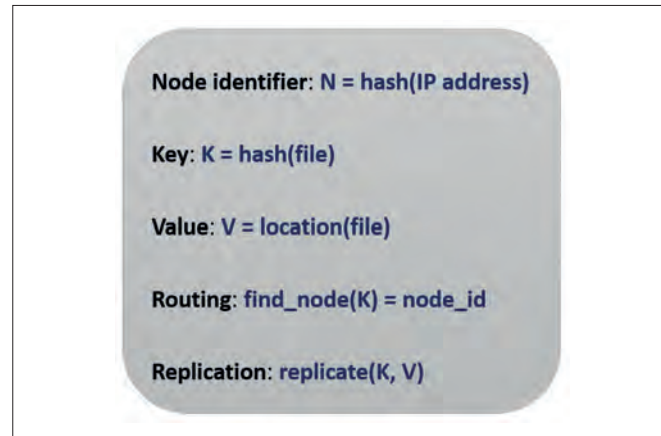


Fig. 3. IPFS-DHT network parameters

Content Publishing:

1. The blockchain validator imports the content into its local IPFS private network and assigns it a unique content identifier (CID).
2. The IPFS instance performs a DHT traversal to locate the closest peers to the CID by XORing the distance of the Peer ID from the SHA256 hash of the CID.
3. The IPFS instance stores the peer record with the closest peers.

Content Retrieval:

1. The requester performs opportunistic Bitswap requests to already connected peers for the CID.
2. If the requester does not find the content, the DHT performs a multi-round iterative lookup to resolve a CID to a peer's Multi-addresses as a traversal, to find a provider record storing the peer.
3. The requester connects to the peer and fetches the content that maps CID using Bitswap.

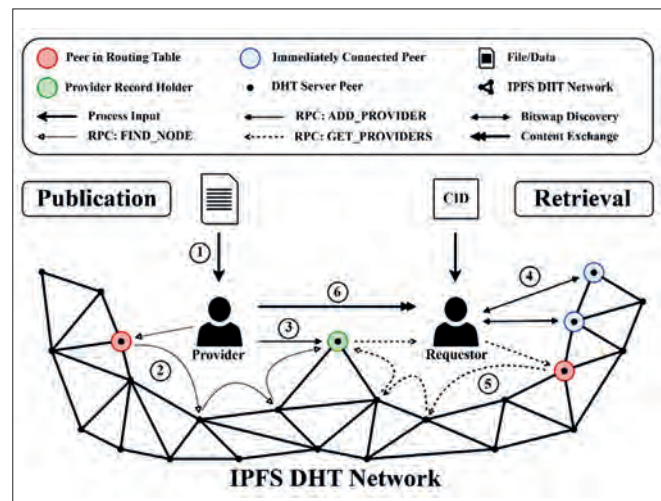


Fig. 4. Content publication and retrieval in IPFS

EXPERIMENTAL SETUP

We conducted experiments on a testbed that integrated transfer learning, blockchain, smart contracts, and private IPFS. The testbed consisted of 8 nodes, which simulated 2 blockchain validators, 4 lightweight nodes, and 2 technological solution providers with the specified system configuration.

Transfer learning environment: A gated recurrent units (GRU) model was used to extract features from the source code to learn long-term dependencies, which is important for source code analysis. We selected the Robustly Optimised BERT Approach (RoBERTa) model with AdamW optimiser, to classify the features extracted by the GRU model and for pre-training, to detect code vulnerabilities. The base model was instantiated using ResNet architectures to extract features from the ISO image and learn deep features. We also employed convolutional neural networks (CNN) to classify the features extracted by the ResNet model and identify vulnerabilities in the ISO image. It was important to freeze the layers from the pre-trained model because we did not want the weights in those layers to be re-initialised. We performed experiments on three sets of datasets containing vulnerable and non-vulnerable C and C++ functions. The first three datasets (LibPNG, PidGIN, and VLC) were collected from publicly available resources. They contained a total of 118 vulnerable and 15,318 non-vulnerable source code files. To address the class imbalance problem, the researchers also included 5,200 vulnerable sample C/C++ files from the Draper Vulnerability Detection in Source Code (VDISC) dataset. The collected files were split into a 9:5:5 ratio to get the training, validation, and test sets. The resulting dataset consisted of 9817, 5453, and 5453 source files for the training, validation, and test sets, respectively.

Tab. 2. Technology stack

Software / Hardware	Version
Platform/OS	Ubuntu 18.04.6 LTS
Processor	Intel Core i7-9700K, frequency 3.6 GHz, maximum turbo frequency 4.90 GHz, 8 CPU cores, 8 threads
System architecture	64-bit operating system and processor
Memory (RAM)	16 GB
Framework	Ganache, Truffle, Plasma, Pre-trained model: RoBERTa,
Ganache	2.5.4 Lightweight Ethereum blockchain network
Node.js	16.15.0 JavaScript runtime environment for building blockchain network
Truffle	5.5.16 Framework for writing and deploying smart contracts
Web3.js	1.7.3 JavaScript library for interacting with the Ethereum blockchain
IPFS	0.13.0 Distributed peer-to-peer file system for storing data
IPFS HTTP Client	53.0.1 JavaScript library for interacting with IPFS
Smart contract	Solidity v0.8.21

Blockchain-based decentralised environment: An Ethereum client was locally instantiated by deploying ganache-cli and with JSON RPC live at port 8545. Ganache enabled the upload of smart contracts onto Ethereum and launched custom-built DApp. The Truffle framework hosted the DApps with a nested chain structure that had contract codes, migrations, and truffle.js. Web3.js facilitated interaction between smart contracts and the blockchain [71]. The Metamask extension was used for browser support. The plasma contract was designed to track and archive only final on-chain proofs, to counteract multiple exits at an indistinguishable range. The contract maintained a list of exitable maps that were updated on the issue of each on-chain proof and the transaction hosted at Ethereum [72]. A plasma contract called main_chain was deployed to the Ethereum core. MainChain.sol had functions to generate Merkle proof of the issued transactions, validate the signature from the physical nodes, and handle submitted blocks. The child_chain console managed transactions and blocks that were posted when an event was triggered in the main_chain. The child chain contract hosted an RPC server on an 8546 port, that smoothed client interfacing. A Python-based wrapper was scripted for client applications, to wrap with child_chain RPC API.

RESULTS AND DISCUSSION

The development environment was set up in accordance with the technical details listed in Table 2. We evaluated the performance of RoBERT on GRU architecture using different epochs and model sizes. The experiments were conducted on a training set of 9817 source code files and a validation set of 5453 source code files. The model sizes were 8, 32, 64, 128, 256, and 512. The model performance was evaluated on a test set of 5453 source code files. We observed that the accuracy of the models increased linearly with the number of epochs. The accuracy results on the training, validation, and test sets with RoBERTa, for an epoch of 10 and 30, are shown in Fig. 5 and Fig. 6, respectively. GRU with RoBERTa with a model size of 512 achieved a test accuracy of 98% and 97% for an epoch of 10 and 30, respectively. The training accuracy increased with the model size, as larger models can make more complex adjustments to fit the training data. However, this can lead to overfitting, where the model becomes too attuned to the training data and does not generalise new data well. Our findings suggest that the optimal model size for avoiding overfitting is 280. This is the size where the validation accuracy, which measures the model's ability to generalise new data, is highest. The testing accuracy, which measures the model's performance on unseen data, is highest at a model size of 515. This suggests that a model size of 515 strikes a good balance between fitting the training data and generalising it to new data. Model sizes of 10 and 80 show signs of overfitting, as the training accuracy is much higher than the validation accuracy. This is because these models are too complex and have memorised the training data too well. Model sizes 415 and 515 show signs of underfitting, as the training accuracy is much lower than the validation accuracy. This is because these models are not complex enough to capture the inherent complexity of the data.

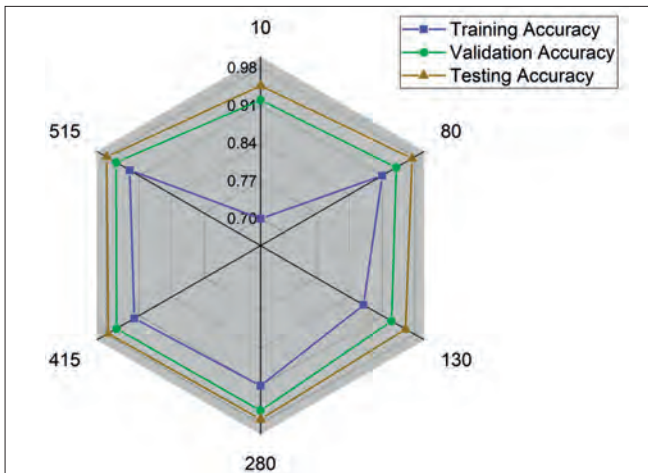


Fig. 5. Accuracy for RoBERTa with 10 epochs on different model sizes

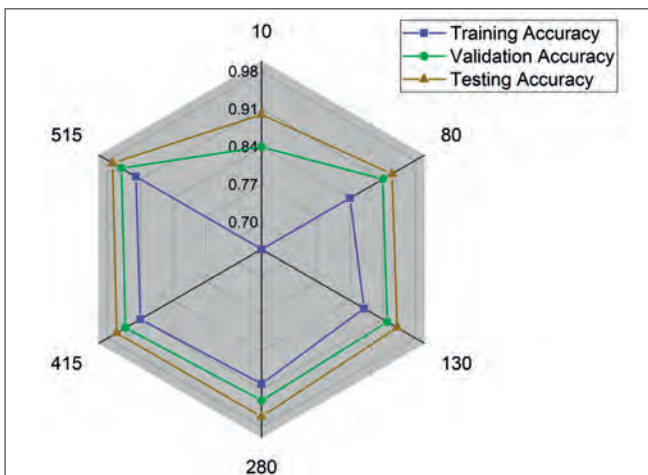


Fig. 6. Accuracy for RoBERTa with 30 epochs on different model sizes

Table 3 shows the performance of the proposed BETL method on two vulnerability datasets: LibPNG and PidGIN. The performance metrics are precision, detection rate, accuracy, and F-score. The results show that BETL on LibPNG has a slightly higher precision and accuracy than on PidGIN. However, the proposed method on PidGIN has a higher detection rate, while BETL on LibPNG is better at avoiding false positives. The computation time of BETL on LibPNG is slightly higher than PidGIN on BETL.

Tab.3. Performance Analysis of Vulnerability Datasets for Proposed BETL method

Measures	LibPNG	PidGIN
Precision	98.99	97.97
Detection Rate	98.98	97.68
Accuracy	97.98	97.12
F-score	98.98	99.02
Computation Time (s)	51.89	49.64

The training loss is the loss that is calculated on the training data, while the validation loss is the loss that is calculated on the validation data. The validation loss is a more accurate measure of the model's performance on unseen data. The results show

that the training loss decreases as the model size increases. This is because larger models are able to learn more complex patterns in the data. However, the validation loss does not decrease at the same rate. This suggests that the models are overfitting the training data. The best model size is the one that has the lowest validation loss. In this case, the best model size is 415. This model has a validation loss of 0.0125, as shown in Fig. 7, which is the lowest of all the models. The training loss is always lower than the validation loss. This is because the training loss is calculated on the data that the model has already seen, while the validation loss is calculated on the data that the model has not seen before. The training loss decreases more rapidly than the validation loss, as the model size increases. This is because larger models are able to learn more complex patterns in the data, but they are also more likely to overfit the training data. The validation loss eventually plateaus as the model size increases. This suggests that there is a limit to the amount of improvement that can be achieved by simply increasing the model size.

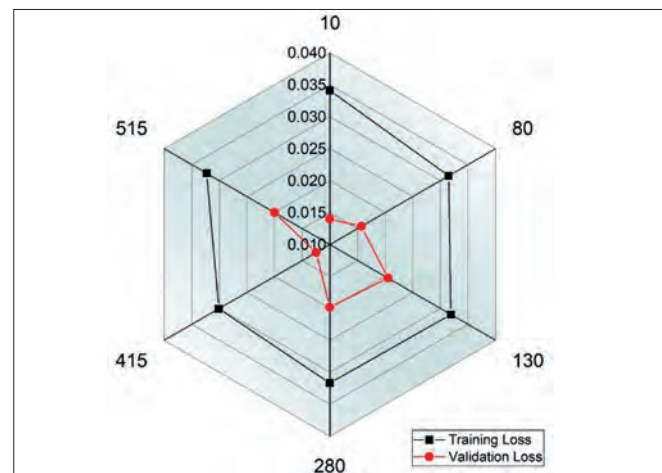


Fig. 7. Loss in RoBERTa pre-training on different model sizes

The training loss decreases as the number of epochs increases for all CNN architectures. This is because the model is able to learn the features of the data better as it is trained for more epochs. The validation accuracy increases as the number of epochs increases for all CNN architectures. This is because the model is able to generalise unseen data better as it is trained for more epochs. ResNet-50 has the lowest training loss and highest validation accuracy for all numbers of epochs. This is because ResNet-50 has more layers and parameters than the other CNN architectures, which allows it to learn more complex features of the data. The difference in training loss and validation accuracy decreases as the number of epochs increases. This is because the model becomes more confident in its predictions as it is trained for more epochs. ResNet-18 has the lowest number of parameters, followed by ResNet-34, ResNet-50, ResNet-101, and ResNet-152. This is because ResNet-18 has the fewest layers. The training time increases as the number of epochs and the number of parameters increases, as depicted in Fig. 8. This is because the model must do more computations to train for more epochs and with more parameters. It is inferred that the ResNet-50 architecture is the best choice since we are dealing with only limited ISO images that require high accuracy.

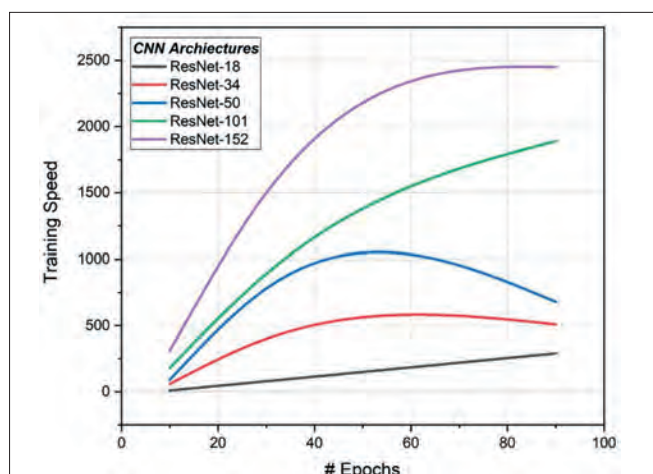


Fig. 8. Model training speed on different epochs

CONCLUSION

We propose a novel BETL system for optimising maritime logistics by harnessing the transparency and immutability of blockchain and the analytical capabilities of transfer learning. We developed a non-vulnerability score range map for the effective classification of operational factors. To ensure efficient storage over the blockchain, we seamlessly integrated IPFS with the blockchain and conducted a testbed-based experiment to demonstrate the effectiveness of BETL for secure logistic management. The results of the experiment show that BETL can achieve high precision (98%), detection rate (98.98%), accuracy (97.9%), and F-score (98.98). This highlights the benefits of BETL in enhancing the safety and reliability of maritime logistics processes. Additionally, the computational time of BETL was improved by 18.9%, compared to standard transfer learning. Beyond its present application, BETL has the potential to extend its utility to other areas of maritime logistics, such as port operations and cargo management. Furthermore, we envision enhancing the usability by incorporating a user-friendly graphical interface for a seamless experience.

REFERENCES

1. A. T. Hoang *et al.*, "Technological solutions for boosting hydrogen role in decarbonization strategies and net-zero goals of world shipping: Challenges and perspectives," *Renew. Sustain. Energy Rev.*, vol. 188, p. 113790, Dec. 2023, doi: 10.1016/j.rser.2023.113790.
2. S. C. Nita and A. Hrebenciuc, "The Importance of Maritime Transport for Economic Growth in the European Union: A Panel Data Analysis," *Sustainability*, vol. 13, no. 14, p. 7961, 2021.
3. S. Gómez, A. Carreño, and J. Lloret, "Cultural heritage and environmental ethical values in governance models: Conflicts between recreational fisheries and other maritime activities in Mediterranean marine protected areas," *Mar. Policy*, vol. 129, p. 104529, 2021.
4. A. Vineetha Harish, K. Tam, and K. Jones, "BridgeInsight: An asset profiler for penetration testing in a heterogeneous maritime bridge environment," *Marit. Technol. Res.*, vol. 6, no. 1, p. 266818, Sep. 2024, doi: 10.33175/mtr.2024.266818.
5. N. Agarwala and C. Saengsupavanich, "Oceanic Environmental Impact in Seaports," *Oceans*, vol. 4, no. 4, pp. 360–380, Nov. 2023, doi: 10.3390/oceans4040025.
6. A. T. Hoang *et al.*, "Energy-related approach for reduction of CO2 emissions: A critical strategy on the port-to-ship pathway," *J. Clean. Prod.*, vol. 355, p. 131772, Jun. 2022, doi: 10.1016/j.jclepro.2022.131772.
7. S. Vakili, A. I. Ölçer, A. Schönborn, F. Ballini, and A. T. Hoang, "Energy-related clean and green framework for shipbuilding community towards zero-emissions: A strategic analysis from concept to case study," *Int. J. Energy Res.*, vol. 46, no. 14, pp. 20624–20649, Nov. 2022, doi: 10.1002/er.7649.
8. F. A. Barata, "High cost of logistics and solutions," in *17th International Symposium on Management (INSYMA 2020)*, 2020, pp. 407–410.
9. A. T. Hoang, V. D. Tran, V. H. Dong, and A. T. Le, "An experimental analysis on physical properties and spray characteristics of an ultrasound-assisted emulsion of ultra-low-sulphur diesel and Jatropa-based biodiesel," *J. Mar. Eng. Technol.*, vol. 21, no. 2, pp. 73–81, Mar. 2022, doi: 10.1080/20464177.2019.1595355.
10. L. Bilgili and V. Şahin, "Emission and environmental cost estimation of ferries operating in Lake Van," *Marit. Technol. Res.*, vol. 5, no. 3, p. 262215, Feb. 2023, doi: 10.33175/mtr.2023.262215.
11. V. V. Pham and A. T. Hoang, "Technological perspective for reducing emissions from marine engines," *Int. J. Adv. Sci. Eng. Inf. Technol.*, vol. 9, no. 6, pp. 1989–2000, 2019, doi: 10.18517/ijaseit.9.6.10429.
12. D. M. Bernhofen, Z. El-Sahli, and R. Kneller, "Estimating the effects of the container revolution on world trade," *J. Int. Econ.*, vol. 98, pp. 36–50, Jan. 2016, doi: 10.1016/j.jinteco.2015.09.001.
13. V. D. Bui and H. P. Nguyen, "Role of Inland Container Depot System in Developing the Sustainable Transport System," *Int. J. Knowledge-Based Dev.*, vol. 12, no. 3/4, p. 1, 2022, doi: 10.1504/IJKBD.2022.10053121.
14. T. T. Le *et al.*, "Management strategy for seaports aspiring to green logistical goals of IMO: Technology and policy solutions," *Polish Marit. Res.*, vol. 30, no. 2, pp. 165–187, 2023, doi: 10.2478/pomr-2023-0031.

15. J. Mangan and C. Lalwani, *Global logistics and supply chain management*. John Wiley & Sons, 2016.
16. Y. Shou, M. Kang, and Y. W. Park, "A Systematic Literature Review of Supply Chain Integration," in *Supply Chain Integration for Sustainable Advantages*, Singapore: Springer Singapore, 2022, pp. 9–29. doi: 10.1007/978-981-16-9332-8_2.
17. M. D. Nguyen, K. T. Yeon, K. Rudzki, H. P. Nguyen, and N. D. K. Pham, "Strategies For Developing Logistics Centres: Technological Trends and Policy Implications," *Polish Marit. Res.*, vol. 30, no. 4, pp. 129–147, 2023, doi: 10.2478/pomr-2023-0066.
18. Y. Zhou, Y. S. Soh, H. S. Loh, and K. F. Yuen, "The key challenges and critical success factors of blockchain implementation: Policy implications for Singapore's maritime industry," *Mar. Policy*, vol. 122, p. 104265, Dec. 2020, doi: 10.1016/j.marpol.2020.104265.
19. V. Isaienko, M. Hryhorak, D. Bugayko, and Z. Zamiar, "Ecosystem Approach to the Formation of Goods Express Delivery Supply Chains in Aviation Logistics," *Logist. Transp.*, vol. 45, no. 1–2, pp. 19–42, 2020.
20. N. Wagner and B. Wiśnicki, "Application of Blockchain Technology in Maritime Logistics," *DIEM Dubrovnik Int. Econ. Meet.*, vol. 4, no. 1, pp. 155–164, 2019.
21. V. Yalama, O. Yakovleva, V. Trandafilov, and M. Khmelniuk, "Future Sustainable Maritime Sector: Fishing Carriers and their Adoption to the Environmental Regulations. Part I," *Polish Marit. Res.*, vol. 29, no. 3, pp. 69–77, Sep. 2022, doi: 10.2478/pomr-2022-0027.
22. H. Fajri, H. Fakhurroja, and M. Lubis, "Social Media Analysis on Aquaculture SupplyChain Management: A Case Study on Freshwater Lobsters," in *2022 International Conference Advancement in Data Science, E-learning and Information Systems (ICADEIS)*, Nov. 2022, pp. 01–06. doi: 10.1109/ICADEIS56544.2022.10037283.
23. N. D. K. Pham, G. H. Dinh, H. T. Pham, J. Kozak, and H. P. Nguyen, "Role of Green Logistics in the Construction of Sustainable Supply Chains," *Polish Marit. Res.*, vol. 30, no. 3, pp. 191–211, Sep. 2023, doi: 10.2478/pomr-2023-0052.
24. S. Wang, L. Ouyang, Y. Yuan, X. Ni, X. Han, and F.-Y. Wang, "Blockchain-Enabled Smart Contracts: Architecture, Applications, and Future Trends," *IEEE Trans. Syst. Man, Cybern. Syst.*, vol. 49, no. 11, pp. 2266–2277, Nov. 2019, doi: 10.1109/TSMC.2019.2895123.
25. H. P. Nguyen, P. Q. P. Nguyen, and V. D. Bui, "Applications of Big Data Analytics in Traffic Management in Intelligent Transportation Systems," *Int. J. Informatics Vis.*, vol. 6, no. 1–2, pp. 177–187, 2022.
26. H. P. Nguyen, P. Q. P. Nguyen, and T. P. Nguyen, "Green Port Strategies in Developed Coastal Countries as Useful Lessons for the Path of Sustainable Development: A case study in Vietnam," *Int. J. Renew. Energy Dev.*, vol. 11, no. 4, pp. 950–962, Nov. 2022, doi: 10.14710/ijred.2022.46539.
27. M. Lind et al., "The future of shipping: Collaboration through digital data sharing," in *Maritime informatics*, Springer, 2020, pp. 137–149.
28. T. Jensen, J. Hedman, and S. Henningsson, "How TradeLens Delivers Business Value With Blockchain Technology," *MIS Q. Exec.*, vol. 18, no. 4, pp. 221–243, Dec. 2019, doi: 10.17705/2msqe.00018.
29. M. E. Manuel and R. Baumler, "The Evolution of Seafarer Education and Training in International Law," 2020, pp. 471–494. doi: 10.1007/978-3-030-31749-2_22.
30. J. Choi, S. Lee, and S. Kim, "Improving the current regulatory issues concerning training ships for maritime institutions: The South Korean case," *Asian J. Shipp. Logist.*, vol. 38, no. 3, pp. 125–134, Sep. 2022, doi: 10.1016/j.ajsl.2022.02.001.
31. S. S. Norman and M. R. Othman, "Reviving the Klang Valley Economy During Pandemic Through Digitalisation of the Maritime Logistics Industry," *J. Marit. Logist.*, vol. 1, no. 2, pp. 40–55, Apr. 2022, doi: 10.46754/jml.2021.12.003.
32. A. Noor, "Adoption of Blockchain Technology Facilitates a Competitive Edge for Logistic Service Providers," *Sustainability*, vol. 14, no. 23, p. 15543, Nov. 2022, doi: 10.3390/su142315543.
33. E. Surucu-Balci, Ç. Iris, and G. Balci, "Digital information in maritime supply chains with blockchain and cloud platforms: Supply chain capabilities, barriers, and research opportunities," *Technol. Forecast. Soc. Change*, vol. 198, p. 122978, Jan. 2024, doi: 10.1016/j.techfore.2023.122978.
34. G. Balci and E. Surucu-Balci, "Blockchain adoption in the maritime supply chain: Examining barriers and salient stakeholders in containerized international trade," *Transp. Res. Part E Logist. Transp. Rev.*, vol. 156, p. 102539, Dec. 2021, doi: 10.1016/j.tre.2021.102539.
35. H. Pyykkö, J. Kuusijärvi, B. Silverajan, and V. Hinkka, "The Cyber Threat Preparedness in the Maritime Logistics Industry," *Proc. 8th Transp. Res. Arena TRA 2020*, 2020.
36. P. Howson, "Building trust and equity in marine conservation and fisheries supply chain management with blockchain," *Mar. Policy*, vol. 115, p. 103873, May 2020, doi: 10.1016/j.marpol.2020.103873.
37. D. Ivanov and A. Dolgui, "Viability of intertwined supply networks: extending the supply chain resilience angles

- towards survivability. A position paper motivated by COVID-19 outbreak,” *Int. J. Prod. Res.*, vol. 58, no. 10, pp. 2904–2915, May 2020, doi: 10.1080/00207543.2020.1750727.
38. F. Lorenz-Meyer and V. Santos, “Blockchain in the shipping industry: A proposal for the use of blockchain for SMEs in the maritime industry,” *Procedia Comput. Sci.*, vol. 219, pp. 807–814, 2023.
 39. S. Saberi, M. Kouhizadeh, J. Sarkis, and L. Shen, “Blockchain technology and its relationships to sustainable supply chain management,” *Int. J. Prod. Res.*, vol. 57, no. 7, pp. 2117–2135, Apr. 2019, doi: 10.1080/00207543.2018.1533261.
 40. P. Sharma *et al.*, “Comparative evaluation of AI-based intelligent GEP and ANFIS models in prediction of thermophysical properties of Fe₃O₄-coated MWCNT hybrid nanofluids for potential application in energy systems,” *Int. J. Energy Res.*, vol. 46, no. 13, pp. 19242–19257, Oct. 2022, doi: 10.1002/er.8010.
 41. Y. Shen, N. Zhao, M. Xia, and X. Du, “A Deep Q-Learning Network for Ship Stowage Planning Problem,” *Polish Marit. Res.*, vol. 24, no. s3, pp. 102–109, Nov. 2017, doi: 10.1515/pomr-2017-0111.
 42. Q. Shi, Y. Hu, and G. Yan, “Fault Diagnosis of ME Marine Diesel Engine Fuel Injector with Novel IRCMDE Method,” *Polish Marit. Res.*, vol. 30, no. 3, pp. 96–110, Sep. 2023, doi: 10.2478/pomr-2023-0043.
 43. Z. Said *et al.*, “Intelligent approaches for sustainable management and valorisation of food waste,” *Bioresour. Technol.*, vol. 377, p. 128952, Jun. 2023, doi: 10.1016/j.biortech.2023.128952.
 44. V. G. Nguyen *et al.*, “An extensive investigation on leveraging machine learning techniques for high-precision predictive modeling of CO₂ emission,” *Energy Sources, Part A Recover. Util. Environ. Eff.*, vol. 45, no. 3, pp. 9149–9177, Aug. 2023, doi: 10.1080/15567036.2023.2231898.
 45. W. Tarelko and K. Rudzki, “Applying artificial neural networks for modelling ship speed and fuel consumption,” *Neural Comput. Appl.*, vol. 32, no. 23, pp. 17379–17395, Dec. 2020, doi: 10.1007/s00521-020-05111-2.
 46. K. Rudzki and W. Tarelko, “A decision-making system supporting selection of commanded outputs for a ship’s propulsion system with a controllable pitch propeller,” *Ocean Eng.*, vol. 126, pp. 254–264, Nov. 2016, doi: 10.1016/j.oceaneng.2016.09.018.
 47. T. Kowalewski, A. Podsiadło, and W. Tarelko, “Application of fuzzy inference to assessment of degree of hazard to ship power plant operator,” *Polish Marit. Res.*, vol. 14, no. 3, pp. 7–14, Jul. 2007, doi: 10.2478/v10012-007-0012-2.
 48. A. Sarfaraz, R. K. Chakraborty, and D. L. Essam, “AccessChain: An access control framework to protect data access in blockchain enabled supply chain,” *Futur. Gener. Comput. Syst.*, vol. 148, pp. 380–394, Nov. 2023, doi: 10.1016/j.future.2023.06.009.
 49. P. Centobelli, R. Cerchione, P. Del Vecchio, E. Oropallo, and G. Secundo, “Blockchain technology for bridging trust, traceability and transparency in circular supply chain,” *Inf. Manag.*, vol. 59, no. 7, p. 103508, Nov. 2022, doi: 10.1016/j.im.2021.103508.
 50. M. Kandpal, C. Das, C. Misra, A. K. Sahoo, J. Singh, and R. K. Barik, “Blockchain assisted Supply Chain Management System for Secure Data Management,” in *2022 International Conference on Advancements in Smart, Secure and Intelligent Computing (ASSIC)*, Nov. 2022, pp. 1–6. doi: 10.1109/ASSIC55218.2022.10088404.
 51. A. S. M. S. Hosen *et al.*, “Blockchain-based transaction validation protocol for a secure distributed IoT network,” *IEEE Access*, vol. 8, pp. 117266–117277, 2020.
 52. J. Liu, G. Yeoh, L. Gao, S. Gao, and O. Ngwenyama, “Designing a Secure Blockchain-Based Supply Chain Management Framework,” *J. Comput. Inf. Syst.*, vol. 63, no. 3, pp. 592–607, May 2023, doi: 10.1080/08874417.2022.2089774.
 53. S. M. M. Hamidi, S. F. Hoseini, H. Gholami, and M. Kananizadeh, “Blockchain Capabilities to Improve the Productivity of Maritime Logistics Processes: Review, Taxonomy, Open Challenges and Future Trends,” *J. Inf. Technol. Manag.*, vol. 14, no. Special Issue: The business value of Blockchain, challenges, and perspectives., pp. 144–170, 2022.
 54. H. Zhong, F. Zhang, and Y. Gu, “A Stackelberg game based two-stage framework to make decisions of freight rate for container shipping lines in the emerging blockchain-based market,” *Transp. Res. Part E Logist. Transp. Rev.*, vol. 149, p. 102303, May 2021, doi: 10.1016/j.tre.2021.102303.
 55. H. Hasan, E. AlHadhrani, A. AlDhaheri, K. Salah, and R. Jayaraman, “Smart contract-based approach for efficient shipment management,” *Comput. Ind. Eng.*, vol. 136, pp. 149–159, Oct. 2019, doi: 10.1016/j.cie.2019.07.022.
 56. E. Lambourdiere and E. Corbin, “Blockchain and maritime supply-chain performance: dynamic capabilities perspective,” *Worldw. Hosp. Tour. Themes*, vol. 12, no. 1, pp. 24–34, Jan. 2020, doi: 10.1108/WHATT-10-2019-0069.
 57. M. Jović, E. Tijan, D. Žgaljić, and S. Aksentijević, “Improving Maritime Transport Sustainability Using Blockchain-Based Information Exchange,” *Sustainability*, vol. 12, no. 21, p. 8866, Oct. 2020, doi: 10.3390/su12218866.
 58. L. Li and H. Zhou, “A survey of blockchain with applications in maritime and shipping industry,” *Inf. Syst. E-bus. Manag.*,

- vol. 19, no. 3, pp. 789–807, Sep. 2021, doi: 10.1007/s10257-020-00480-6.
59. Z. H. Munim, O. Duru, and E. Hirata, “Rise, Fall, and Recovery of Blockchains in the Maritime Technology Space,” *J. Mar. Sci. Eng.*, vol. 9, no. 3, p. 266, Mar. 2021, doi: 10.3390/jmse9030266.
 60. S. Nguyen, p. Shu-Ling Chen, and Y. Du, “Risk assessment of maritime container shipping blockchain-integrated systems: An analysis of multi-event scenarios,” *Transp. Res. Part E Logist. Transp. Rev.*, vol. 163, p. 102764, Jul. 2022, doi: 10.1016/j.tre.2022.102764.
 61. D. Kim, C. Lee, S. Park, and S. Lim, “Potential Liability Issues of AI-Based Embedded Software in Maritime Autonomous Surface Ships for Maritime Safety in the Korean Maritime Industry,” *J. Mar. Sci. Eng.*, vol. 10, no. 4, p. 498, Apr. 2022, doi: 10.3390/jmse10040498.
 62. K. H. Kwak, J. T. Kong, S. I. Cho, H. T. Phuong, and G. Y. Gim, “A study on the design of efficient private blockchain,” *Comput. Sci. Appl. Informatics* 5, pp. 93–121, 2019.
 63. U. Majeed, L. U. Khan, I. Yaqoob, S. M. A. Kazmi, K. Salah, and C. S. Hong, “Blockchain for IoT-based smart cities: Recent advances, requirements, and future challenges,” *J. Netw. Comput. Appl.*, vol. 181, p. 103007, 2021.
 64. S. Tanwar, Q. Bhatia, P. Patel, A. Kumari, P. K. Singh, and W.-C. Hong, “Machine learning adoption in blockchain-based smart applications: The challenges, and a way forward,” *IEEE Access*, vol. 8, pp. 474–488, 2019.
 65. M. Shafay, R. W. Ahmad, K. Salah, I. Yaqoob, R. Jayaraman, and M. Omar, “Blockchain for deep learning: review and open challenges,” *Cluster Comput.*, vol. 26, no. 1, pp. 197–221, 2023.
 66. R. Xu, Y. Chen, and E. Blasch, “Decentralized access control for IoT based on blockchain and smart contract,” *Model. Des. Secur. Internet Things*, pp. 505–528, 2020.
 67. R. Xu, Y. Chen, and E. Blasch, “Decentralized Access Control for IoT Based on Blockchain and Smart Contract,” in *Modeling and Design of Secure Internet of Things*, Wiley, 2020, pp. 505–528. doi: 10.1002/9781119593386.ch22.
 68. G. Lin, S. Wen, Q.-L. Han, J. Zhang, and Y. Xiang, “Software vulnerability detection using deep neural networks: a survey,” *Proc. IEEE*, vol. 108, no. 10, pp. 1825–1848, 2020.
 69. B. S. Egala, A. K. Pradhan, V. Badarla, and S. P. Mohanty, “iBlock: An Intelligent Decentralised Blockchain-based Pandemic Detection and Assisting System,” *J. Signal Process. Syst.*, vol. 94, no. 6, pp. 595–608, Jun. 2022, doi: 10.1007/s11265-021-01704-9.
 70. D. Trautwein *et al.*, “Design and evaluation of IPFS,” in *Proceedings of the ACM SIGCOMM 2022 Conference*, Aug. 2022, pp. 739–752. doi: 10.1145/3544216.3544232.
 71. S. K. Panda and S. C. Satapathy, “An investigation into smart contract deployment on Ethereum platform using Web3.js and solidity using blockchain,” in *Data Engineering and Intelligent Computing: Proceedings of ICICC 2020*, 2021, pp. 549–561.
 72. G. D’ANGELO and p. F. COSTA, “Ethereum blockchain as a decentralized and autonomous key server: storing and extracting public keys through smart contracts,” 2017.


APPROXIMATE ESTIMATION OF MAN-DAY IN SHIP BLOCK PRODUCTION: A TWO-STAGE STOCHASTIC PROGRAM

Yusuf Genç 

Fatsa Vocational Higher School, Vessel Construction Program, Ordu University, Fatsa/Ordu, Turkiye, Turkey

Mustafa Kafali* 

Naval Architecture and Maritime Faculty, Izmir Katip Celebi University, Cigli/Izmir, Turkiye, Turkey,

Uğur Buğra Çelebi 

Naval Architecture and Marine Engineering Department of Yildiz Technical University, Besiktas/İstanbul, Turkiye, Turkey,

* Corresponding author: mustafakafali@outlook.com (Mustafa Kafali)

ABSTRACT

It is critical to estimate the workforce requirements for the production of blocks in shipbuilding. In this study, the number of workforce (man-day) required for the production of a passenger ship's double bottom block was estimated. Initially, the production of the block was observed, and the average working performance of the mounting, welding, and grinding workers was recorded. Block drawings were examined and the work required was calculated. The amount of work increased, depending on any revisions required due to incorrect or incomplete designs. The average working performance of an employee is uncertain due to environmental factors, including the weather and working conditions, as well as health (both physical and mental). A two-stage stochastic programming model with recourse was established to estimate man-day required and a Sample Average Approximation (SAA) technique was used to obtain a near-optimum solution. The results of the study were compared with shipyard records and an agreement of approximately 90% was achieved.

Keywords: Shipbuilding; Block Production; Planning; Stochastic Modelling

INTRODUCTION

Shipbuilding comprises many complex activities which are carried out concurrently and necessitate systematic engineering [1,2]. These activities include steel hull manufacturing, pipe fitting, painting, machinery, and wiring. One of the initial phases of shipbuilding (after design), includes cutting the sheets. Following that, blocks are manufactured by welding the parts in a certain order [3,4]. After the blocks are transferred to the building berth, mounting and welding are completed, respectively. Thus, the hull structure of a ship is produced [5]. Poor decisions in process planning can lead to delays in delivery and, therefore, major cost overruns

[6,7]. A production planning system that accurately reflects the production environment can ensure a high on-time performance and improve competitiveness [8,9]. Workforce planning, especially in the block manufacturing phase, is one of the major concerns of shipyards. Efforts to establish efficient production planning continue to improve the shipbuilding process. On the other hand, it is considered that planning in shipbuilding mostly depends on the experience of the staff [10]. There is a lack of academic studies on shipbuilding planning and increasing efficiency [8,11]. Predicting the required labour force (the objective of this study) would be very useful for proper planning. This may also provide a positive contribution to delivery performance and cost. On-time delivery is very

important for ship-owners and is essential for a shipyard if it is to receive new ship orders [12-14].

A literature review revealed that improving block production and planning in a shipyard, the transportation of blocks, spatial planning, mounting and welding processes on the building berth, reducing duration, automatic process planning in mounting operations, and man-hour estimations have been examined by various studies. Lei et al. [15] proposed a mounting sequence planning method based on reasoning. In the study, the mounting sequence was optimised with geometric constraints and the fuzzy method. Porath et al. [16] developed a measurement-supported mounting method to shorten the mounting time. In order to determine the capacity requirement in the preproduction of a block, Kafalı et al. [17] examined the process from a stochastic perspective. Kang et al. [6] presented a block mounting sequence planning method by emphasising the optimum mounting time and welding deformations. Urbanski et al. [18] investigated the technological usefulness of panel line on the basis of welding technologies. Jeong et al. [19] created a new spatial layout planning model for large blocks based on the greedy algorithm. Afzalirad and Rezaeian [20] developed a new resource-constrained parallel machine planning model for a block mounting scheduling problem. Wang et al. [21] proposed a scheduling model for panel line, including a rolling horizon and rescheduling, by considering many uncertain factors. Yuguang et al. [22] developed a hull assembly line balancing model based on the particle swarm optimisation algorithm. A method for planning the assembly of ship hulls that focuses on a welding sequence was developed by Iwankowicz [23]. In this study, an intelligent hybrid sequencing method was obtained, using fuzzy clustering, case-based reasoning and evolutionary optimization to determine the optimal assembly order. Kwon and Lee [24] focused on spatial planning based on the assembly of blocks. A mixed integer programming model and a two-stage heuristic algorithm was developed. Hadjina et al. [25] presented a new methodology based on the simulation of the robotic profile production line. By applying lean manufacturing to the panel line, Oliveira and Gordo [26] obtained substantial savings in both time and costs. Hur et al. [27] presented a man-hours estimation system, in terms of certain shipbuilding activities. Hu et al. [28] developed a heuristic hybrid algorithm for the block-building area, which is accepted as being an important bottleneck in the shipbuilding process. Zheng et al. [29] developed a spatial scheduling system by using the greedy search algorithm with the help of data obtained from a large ship. Liu et al. [30] applied discrete event simulation by modelling the stochastic events for dynamic spatial scheduling. Wahidi et al. [31] achieved a significant gain, in terms of man-hours, with the robot welding technology applied to the double bottom block. Liu and Jiang [32] proposed three different models utilising simple linear regression, multiple linear regression, and an artificial neural network, to estimate man-hour. They concluded that the artificial neural network model provides more accurate and reliable results.

Based on the above-mentioned studies, it can be said that there is not enough academic study regarding the estimation of the workforce required in ship block production. The usual practice in shipyards is to use data from previously built ships to estimate the operating time or the expected number of working hours for a given sub-process. Similarly, it can be argued that production costs can be calculated using the same approach. However, this is not a systematic practice. There are techniques for man-hour estimation in many sectors [33,34] and new methods can be applied for a more realistic approach in shipyards. On the other hand, Kafalı et al. [17] conducted an analysis of the workforce, specifically focusing on preproduction workstations. They developed a two-stage stochastic program to determine workforce requirements. They mentioned that the model they presented could be used to optimise the workforce and enhance the production process in shipbuilding. Additionally, they suggested the need for a more comprehensive model that encompasses other production phases in ship block production. In this study, we address this issue by expanding on the previous study and incorporating all production phases involved in the production of a passenger ship's double bottom block; grinding activity is included in the model, to obtain more realistic results. Moreover, the solution of the stochastic program is compared with real data and the results are validated.

The remaining sections of this paper are organised as follows. First, general information about block production and a description of the problem are presented in the introduction. In the methodology section, the mathematical model is introduced, the steps of the solution method are explained, and a case study for a double bottom block is then presented. This is followed by the results and a discussion section. Finally, the conclusions are presented.

ACTIVITIES IN THE PRODUCTION OF SHIP BLOCKS

The block production process starts with the transport of plates and sections from the stockyard to the production area. The shot-blasted and priming-painted plates are prepared for CNC cutting, based on the design department's data. After the marking and cutting process, the pre-production phase starts with the related parts [35].

Blocks are manufactured by joining the plates and profiles. The first step in the joining process is the mounting of the parts by spot-welding. Mounting is crucial for the healthy continuation of the welding and grinding processes. After that, the full welding process is performed by an appropriate welding method, where gas metal arc welding is generally preferred. Then, grinding is performed on the welds where necessary. In this process, the grinding wheel, in which the abrasive grains are held together, is used to remove tiny chips from the welds. Examples of these three processes and the main titles of the products obtained during the block manufacturing process are shown in Fig. 1 and Table 1 [36].



Fig. 1. Block production activities

Tab. 1. Interim products and definitions

Interim product	Description	Construction view
C, small group	Constructions made by welding separate components.	
D, module	Combination of C and C.	
E, panel	Combination of large plates.	
F, profiled panel	Combination of profiles and panel.	
G, sub block	Combination of F and D.	
H, bent panel	Combination of large plates by bending.	
K, block	Combination of F and G.	

The bottom structure forms a flange of the hull girder. Therefore, the bottom structure is important, in terms of longitudinal strength. While contributing significantly to the strength, it distributes the local loading during docking. In addition, the bottom structure of a ship has to withstand bending stresses as well as water pressure. Single and double bottom structures are the two different forms of bottom structures. Moreover, longitudinal or transverse framing is applied to bottom structures [35]. A longitudinally framed double bottom block is examined in this study.

DEFINITION OF THE PROBLEM

Shipbuilding is a labour-intensive production process but it is hard to determine the exact workforce required in production processes. Revisions due to incorrect or incomplete designs, customer demands, and the reworking of defective manufacturing may occur. Besides this, the performance of employees is variable [37].

This study aims to calculate the workforce required in the C, D, E, F, G, H, and K production phases of a double bottom block belonging to a passenger ship. For this purpose, the average working performance of mounting, welding, and grinding workers was determined by conducting field observations. All the drawings of the block were examined and the amount of work required for mounting, welding, and grinding each interim product was calculated, and yet the work to be done, depending on revisions and errors, increases and becomes variable. Working conditions and the weather, as well as the mental and physical health of an employee, cause the average working performance of a worker to fluctuate. Various measures are taken to prevent possible delays in the production process due to the increased workload and varying worker performance. For example, the production process can be compensated for by shifting workers from another compartment to the disrupted one. However, the cost of newly added workers would be higher than that of those already employed because the required tools and equipment should be moved to the relevant compartment; adaptation to the new work area would be required.

Considering the aforementioned situations, a mathematical model (called a 'two-stage stochastic recourse model') was created to calculate the man-day for mounting, welding, and grinding activities, to prevent unexpected cost increases and delays. It is difficult to obtain real solutions to two-stage mathematical models and, thus, the Sample Average Approximation (SAA) technique was used in the solution of the model. Two stochastic situations were defined when creating the scenarios to be used in the solution. The first is the increase in workload, due to revisions and the rectification of defective manufacturing, and the second is the average performance of the workers. The increase in workload was followed up by the planning department of the shipyard. Accordingly, a 1-2%, 5-10%, 10-15%, and 15-20% range of increase in the E-F, C-D, G-H, and K production phases was observed, respectively. The examinations made in the production area show that the average worker's performance

can change randomly within the range of $\pm 10\%$. Monte Carlo sampling was applied for the generation of scenarios for the SAA solution method, in which the increased workload rates and the changes in performance were both considered. In stochastic mathematical models, where scenarios are expressed with a continuous or discrete distribution, the SAA technique provides convenience in the approximate solution of the problem [38].

The mathematical model is defined based on cost minimisation in worker wages. Therefore, the objective function would aim to calculate the workforce requirement that gives the minimum cost through the constraints relevant to the target. The duration of an activity is given by Eq. (1) [17].

$$d = \frac{L}{P \times R} \quad (1)$$

where d is duration [day]; L is the amount of work [unit]; P is the average performance [unit/(man-day)]; and R is the number of workers [man].

Here, multiplying the number of workers by the duration gives the workforce required or, in other words, the number of man-days needed to complete the work. In this case, Eq. (1) turns into the Eq. (2):

$$d \times R = \frac{L}{P} \quad (2)$$

Accordingly, the expression used becomes a parameter that includes the number of workers and time, becoming the decision variable used in the model.

METHODOLOGY

MATHEMATICAL MODEL

Stochastic programming encompasses the mathematical modelling to be used to make decisions under uncertainty [39]. The general form of the two-stage stochastic programming model with recourse is as follows [40].

$$\begin{aligned} \min z &= c^T x + E_{\xi}[\min_{y(\omega)} q(\omega)^T y(\omega)] \\ \text{s.t.} \quad & Ax = b, \\ & T(\omega)x + Wy(\omega) = h(\omega), \\ & x \geq 0, y(\omega) \geq 0, \end{aligned} \quad (3)$$

where x is the first-stage decision vector; y is the second-stage decision vector; ω is the stochastic event; A is the first-stage matrix; b represents the first-stage right-hand side values; T is the technology matrix; h represents the second-stage right-hand side values; and W is the recourse matrix. In this study, the decision vectors consist of the workforce (i.e. man-day), which are the product of the duration and the number

of workers. Moreover, the objective function represents the total workforce cost. Accordingly, the following two-stage stochastic programming model with recourse was developed to forecast the required man-day for mounting, welding, and grinding activities at each production phase of the double bottom block.

$$\begin{aligned} \min z = & \left(c_1^M \cdot (dR_1^{(Y,M)}) + c_1^W \cdot (dR_1^{(Y,W)}) + i \cdot c_1^G \cdot (dR_1^{(Y,G)}) \right. \\ & \left. + \sum_{s=1}^S \mathcal{P}_s \left(c_2^M \cdot (dR_{2,s}^{(Y,M)}) + c_2^W \cdot (dR_{2,s}^{(Y,W)}) + i \cdot c_2^G \cdot (dR_{2,s}^{(Y,G)}) \right) \right) \\ \text{s.t.} \quad & i \cdot P_s^{(Y,Z)} \cdot (dR_1^{(Y,Z)} + dR_{2,s}^{(Y,Z)}) \geq i \cdot L_s^{(Y,Z)}; \forall s = 1, \dots, S; \\ & \forall Y \in \{C, D, E, F, H, G, K\}; \forall Z \in \{M, W, G\} \\ & \text{If } Y = \{E\} \wedge Z = \{G\} \text{ Then } i = 0 \text{ else } i = 1 \\ & \text{all decision variables} \geq 0 \text{ and are integers} \end{aligned} \quad (4)$$

where c_1^M is the daily cost of a mounting worker, c_1^W is the daily cost of a welder, c_1^G is the daily cost of a grinding worker, c_2^M is the daily cost of an additional mounting worker, c_2^W is the daily cost of an additional welder, and c_2^G is the daily cost of an additional grinder. These are the constant parameters of the objective function. \mathcal{P}_s is the probability of scenario s . Within each independent sample, the probabilities of the scenarios are considered to be equal.

The other letters used in the model can be defined as follows: d represents duration; P , R , and L are the worker performance, number of workers, and amount of work, respectively; Y (written as a superscript) indicates the production phases (i.e. C , D , E , F , H , G , and K); and Z (written as a superscript) shows the activities (i.e. Mounting (M), Welding (W), and Grinding (G)). For example, $dR_1^{(C,M)}$ stands for the amount of mounting workforce allocated to the production phase C at the first stage. Also, $dR_{2,s}^{(C,M)}$ stands for the amount of additional mounting workforce for production phase C if scenario s occurs. Furthermore, $P_s^{(D,W)}$ is the welder performance at the production phase D in scenario s and $L_s^{(D,G)}$ is the grinding work to be completed at the production phase D in scenario s . It was accepted that the daily costs of the mounting worker, welder, and grinder are constant.

In Eq. (4), 'minz' is the objective function representing the total labour cost. This objective function consists of two parts: the first stage and the second stage. The first stage is deterministic, while the second stage is stochastic.

In the first stage of the objective function, the daily cost of a mounting worker was multiplied by the total workforce for the mounting, the daily cost of a welder was multiplied by the total workforce for the welding, and the daily cost of a grinder was multiplied by the total workforce for the grinding.

In the second stage of the objective function, recourse costs were calculated. It is assumed that the costs of the additional workers are constant. At this stage, the daily cost of the additional mounting worker was multiplied by the mounting workforce shortage, the daily cost of the additional welder was multiplied by the welding workforce shortage, and the daily cost of the additional grinder was multiplied by the grinding workforce shortage.

Similar to the objective function, the decision variables were also divided into two parts, reflecting the decisions made before and after the realisation of an uncertain event, such as work amounts and worker performance fluctuations. $dR_1^{(Y,Z)}$ represents the first stage decision variable, which shows the amount of the workforce. In the same manner, $dR_{2,s}^{(Y,Z)}$ is the second stage decision variable, showing the amount of workforce after the realisation of an uncertain event for the relevant scenario.

Constraint equations provide the completion of scenario-based work amounts. To do so, the calculated workforce amount was multiplied by the scenario-based performance. Since there is no grinding activity in 'production phase E ', grinding is not included in this phase.

STEPS OF THE SAMPLE AVERAGE APPROXIMATION (SAA) TECHNIQUE

The SAA technique is used to solve the two-stage stochastic recourse model. This method allows us to deal with the problem in a smaller size and facilitate the solution. A sample of N scenarios ($\xi^1, \xi^2, \dots, \xi^N$) is generated for the random vector ξ . Then, the expected value function $\mathbb{E}[Q(x, \xi)]$ is calculated with the sample function $N^{-1} \sum_{n=1}^N Q(x, \xi^n)$. The steps of the SAA technique can be summarised as follows [41].

There are $M(m = 1, 2, \dots, M)$ independent random samples with N_m scenarios (N : sample size). A sufficiently large reference sample is chosen: ($N' \gg N$). Here, the scenarios consist of combinations of the amount of work, revision status, and worker performance. The scenario table contains the final values for the amount of work and performance.

Step 1: This practice has eight different parameter sets. Therefore, the solution is performed for sixty different independent samples m . For each independent sample m , the following model is solved by any deterministic optimisation algorithm. In Eq. (5), \hat{v}_N^m stands for minz, as seen in Eq. (4), and so it refers to the total workforce cost.

$$\hat{v}_N^m = \min_{x \in X} \left\{ c^T x + \frac{1}{N_m} \sum_{n=1}^{N_m} Q(x, \xi_n^m) \right\} \quad (5)$$

The SAA problem's optimum value is shown by \hat{v}_N^m . Thus, it is possible to determine the optimum solution for each m ($\hat{x}_N^m, \dots, \hat{x}_N^M$) and objective function value ($\hat{v}_N^m, \dots, \hat{v}_N^M$).

Step 2: The average of the optimal objective function values determined in the first stage () is calculated. This computation is also applied to eight different parameter sets.

$$\bar{v}_N^M := \frac{1}{M} \sum_{m=1}^M \hat{v}_N^m \quad (6)$$

\bar{v}_N^M is an unbiased estimator for $\mathbb{E}[v_N]$ and a statistical lower limit for the optimum value of the true problem v^* . A variance estimator for \bar{v}_N^M is determined by Eq. (7). With

this calculation, the average deviation of the objective function values from the average objective function is obtained.

$$S_{\bar{v}_N}^2 := \frac{1}{M(M-1)} \sum_{m=1}^M (\hat{v}_N^m - \bar{v}_N^M)^2 \quad (7)$$

Step 3: For each independent random sample with a reference sample size N' , the true objective function value estimate is determined by resolving the following formulation, using the best solutions from step 1.

$$\hat{g}_{N'}(\hat{x}_N^m) := c^T \hat{x}_N^m + \frac{1}{N'} \sum_{n=1}^{N'} Q(\hat{x}_N^m, \xi^n), \quad m = 1, 2, \dots, M \quad (8)$$

The statistical upper bound for the optimum value of the true problem \bar{v}^* is determined by Eq. (8) and the variance estimator of this value is calculated as follows:

$$S_{\hat{g}_{N'}(\hat{x}_N^m)}^2 := \frac{1}{N'(N'-1)} \sum_{n=1}^{N'} [c^T \hat{x}_N^m + Q(\hat{x}_N^m, \xi^n) - \hat{g}_{N'}(\hat{x}_N^m)]^2, \quad m = 1, 2, \dots, M \quad (9)$$

The average of the upper bound values, determined according to Eq. (8), can be calculated and the arithmetic average of the true objective function values (calculated for independent values of m for each parameter set) can be observed.

$$\bar{g}_{N'}^M := \frac{1}{M} \sum_{m=1}^M \hat{g}_{N'}(\hat{x}_N^m), \quad m = 1, 2, \dots, M \quad (10)$$

Also, the average of the variances calculated by Eq. (9) can be determined. With Eq. (11), the average deviation of the true objective function values is obtained from the average true objective function.

$$\bar{S}_{\hat{g}_{N'}^M}^2 := \frac{1}{M} \sum_{m=1}^M S_{\hat{g}_{N'}(\hat{x}_N^m)}^2 \quad (11)$$

Step 4: Eq. (12) is used to determine the optimal gap of the \hat{x}_N^m solution. When this value approaches zero, it indicates convergence to the optimum solution.

$$gap_{N,M,N'}(\hat{x}_N^m) = \hat{g}_{N'}(\hat{x}_N^m) - \bar{v}_N^M \quad (12)$$

The estimated variance of the optimal gap of the related solution obtained by Eq. (11) is calculated as follows:

$$S_{gap}^2(\hat{x}_N^m) = S_{\hat{g}_{N'}(\hat{x}_N^m)}^2 + S_{\bar{v}_N^M}^2 \quad (13)$$

Also, the average of the optimal gap values is calculated by Eq. (14). This value shows the average of the optimal gap values obtained from each parameter set.

$$\overline{gap}_{N,M,N'} := \frac{1}{M} \sum_{m=1}^M gap_{N,M,N'}(\hat{x}_N^m) \quad (14)$$

The average of the optimal gap and its variance are used in the calculation of confidence interval values. Accordingly, the average of the variances of the optimal gaps is found from:

$$\bar{S}_{gap}^2 := \frac{1}{M} \sum_{m=1}^M S_{gap}^2(\hat{x}_N^m) \quad (15)$$

The confidence interval for the average of the optimal gap is calculated [42]. By using this equation, it can be seen whether the average gap values are within the confidence interval boundaries.

$$\overline{gap}_{N,M,N'} \pm t_{(\alpha/2), (M-1)} \left(\frac{\bar{S}_{gap}^2}{\sqrt{M}} \right) \quad (16)$$

CASE STUDY: MAN-DAY PREDICTION FOR PASSENGER SHIP DOUBLE BOTTOM BLOCK PRODUCTION

The flow chart of the implementation can be seen in Fig. 2. Accordingly, to initiate the process, our first imperative was to gather the essential data necessary for our analysis. This involved conducting field research, where we observed and documented worker performance and activities within the production. The next crucial step was the development of a mathematical model designed to represent the problem we were addressing. This model was crafted in detail, incorporating various variables to accurately simulate the real-world situation. Additionally, numerous scenarios were created and then the model was solved with SAA.

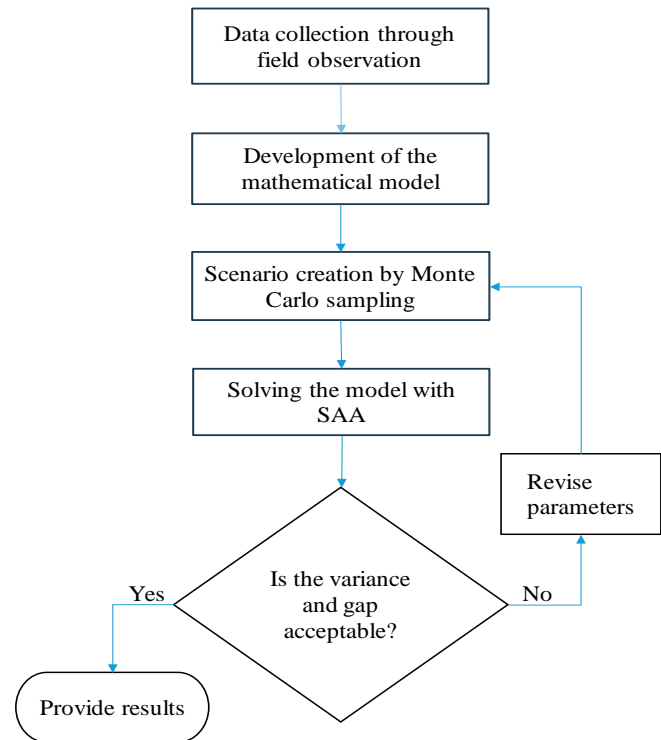


Fig. 2. The flow chart of the implementation

In the case study, eight different forms were solved (Table 2). N indicates the number of scenarios in the independent sample selected from the reference sample, M is the number

of independently determined samples, and N' is the total number of scenarios in the reference sample, respectively.

Tab. 2. Parameters and values used in the application.

Set No		Parameter set values							
		1	2	3	4	5	6	7	8
Parameters	N	20	200	20	200	20	200	20	200
	M	5	5	10	10	5	5	10	10
	N'	2000	2000	2000	2000	10000	10000	10000	10000

Firstly, the amount of work and performance scenarios were generated for $N' = 2000$ and $N' = 10000$. N s for each different m were obtained by applying the Monte Carlo sampling method. However, the scenarios for all forms are not shown here, due to space limitations. A portion of the amount of work and performance scenarios produced for $m = 1$, $N = 20$ in set no. 1 is shown in Table 3 and Table 4, as examples. The costs are taken as $c_1^M = 1080$, $c_1^W = 540$, $c_1^G = 540$, $c_2^M = 1300$, $c_2^W = 650$, and $c_2^G = 650$ currency units.

Tab. 3. Amount of work (labour) scenarios for $m=1$, $N=20$ in set no. 1

n	$L^{(C,M)}$	$L^{(C,W)}$	$L^{(C,G)}$	$L^{(D,M)}$	$L^{(D,W)}$	$L^{(D,G)}$	$L^{(E,M)}$	$L^{(E,W)}$	$L^{(E,G)}$	$L^{(F,M)}$	$L^{(F,W)}$	$L^{(F,G)}$	$L^{(H,M)}$	$L^{(H,W)}$	$L^{(H,G)}$	$L^{(G,M)}$	$L^{(G,W)}$	$L^{(G,G)}$	$L^{(K,M)}$	$L^{(K,W)}$	$L^{(K,G)}$
1	1382	407	402	455	153	138	367	147	1485	520	519	842	249	243	1768	560	460	1869	560	460	
2	1362	406	409	465	151	139	367	147	1484	520	521	812	249	245	1842	556	444	1810	563	462	
..	
..	
19	1353	406	404	459	149	138	365	147	1488	520	522	829	246	246	1796	569	449	1799	561	460	
20	1379	417	415	454	154	136	368	147	1486	523	522	839	243	244	1833	560	446	1822	580	464	

Tab. 4. Performance scenarios for $m=1$, $N=20$ in set no. 1

n	$\hat{p}^{(C,M)}$	$\hat{p}^{(C,W)}$	$\hat{p}^{(C,G)}$	$\hat{p}^{(D,M)}$	$\hat{p}^{(D,W)}$	$\hat{p}^{(D,G)}$	$\hat{p}^{(E,M)}$	$\hat{p}^{(E,W)}$	$\hat{p}^{(E,G)}$	$\hat{p}^{(F,W)}$	$\hat{p}^{(F,G)}$	$\hat{p}^{(H,M)}$	$\hat{p}^{(H,W)}$	$\hat{p}^{(H,G)}$	$\hat{p}^{(G,M)}$	$\hat{p}^{(G,W)}$	$\hat{p}^{(G,G)}$	$\hat{p}^{(K,M)}$	$\hat{p}^{(K,W)}$	$\hat{p}^{(K,G)}$
1	208	92	106	173	69	60	309	692	193	735	153	195	106	159	143	86	66	67	37	35
2	227	95	99	147	58	66	340	756	205	783	152	188	115	161	144	75	65	66	37	33
⋮	⋮	⋮	⋮	⋮	⋮	⋮	⋮	⋮	⋮	⋮	⋮	⋮	⋮	⋮	⋮	⋮	⋮	⋮	⋮	⋮
⋮	⋮	⋮	⋮	⋮	⋮	⋮	⋮	⋮	⋮	⋮	⋮	⋮	⋮	⋮	⋮	⋮	⋮	⋮	⋮	⋮
19	225	91	100	161	68	69	324	777	182	695	171	177	119	155	139	85	68	65	41	34
20	227	89	116	157	68	67	327	752	185	762	161	186	117	140	153	87	62	59	39	33

Tab. 5. The calculated decision variable values for set no. 4

$dR_1^{(C,M)}$	$dR_1^{(D,M)}$	$dR_1^{(E,M)}$	$dR_1^{(F,M)}$	$dR_1^{(H,M)}$	$dR_1^{(G,M)}$	$dR_1^{(K,M)}$	$dR_1^{(C,W)}$	$dR_1^{(D,W)}$	$dR_1^{(E,W)}$	$dR_1^{(F,W)}$	$dR_1^{(H,W)}$	$dR_1^{(G,W)}$	$dR_1^{(K,W)}$	$dR_1^{(C,G)}$	$dR_1^{(D,G)}$	$dR_1^{(F,G)}$	$dR_1^{(H,G)}$	$dR_1^{(G,G)}$	$dR_1^{(K,G)}$
7	3	2	7	5	15-16	18	6	3	1	1	4	17	22-23	7	4	7	6	27	36

The decision variables and related objective function values are calculated by using Eq. (5) and are given in Tables 5 and 6. Table 5 presents the 20 different decision variables computed for each independent sample in set no 4, where only the workforce values observed for $dR_1^{(G,M)}$ and $dR_1^{(K,W)}$ differ between 15-16 and 22-23, respectively. The other values are identical, e.g. all ten values for $dR_1^{(C,M)} = 7$; $dR_1^{(D,M)} = 3$... The first column in Table 6 shows the number of independent samples. Column 2 shows the objective function values and column 3 displays the true objective function value estimation calculated by Eq. (8). The variance estimator of these values is calculated by Eq. (9) and shown in column 4. The gap values calculated by Eq. (12) are presented in column 5 and the gap variances calculated by Eq. (13) are in column 6.

Tab. 6. The calculated values for set no. 4

m	\hat{v}_N^m	$\hat{g}_{N'}(\hat{x}_N^m)$	$S_{\hat{g}_{N'}(\hat{x}_N^m)}^2$	gap	variance
1	150747	150940	5044	46.5	12548
2	151204	150906	5212	13.2	12716
3	150502	150906	5212	13.2	12716
4	150922	150906	5212	13.2	12716
5	151305	150906	5212	13.2	12716
6	150955	150907	4947	14.2	12451
7	150600	150906	5212	13.2	12716
8	151208	150906	5212	13.2	12716
9	150723	150906	5212	13.2	12716
10	150766	150906	5212	13.2	12716

RESULTS AND DISCUSSION

There are many factors that cause uncertainties in the shipbuilding process. With stochastic programming models, approximate estimations can be achieved for workforce requirements under uncertainty. In this study, a two-stage stochastic mathematical model was created to predict the mounting, welding, and grinding workforce required for double bottom block production phases. The SAA method was used to obtain the approximate solution of this model, where the amount of work and average worker performance are uncertain. The problem was solved for eight different parameter sets and boundary values for all of the solutions are shown in Table 7. While the objective function values, which are calculated using the reference sample, are upper bounds, the objective function values obtained from the other scenarios are lower bounds.

Tab. 8. The best results obtained by SAA.

Set no	$dR_1^{(C,M)}$	$dR_1^{(D,M)}$	$dR_1^{(E,M)}$	$dR_1^{(F,M)}$	$dR_1^{(H,M)}$	$dR_1^{(G,M)}$	$dR_1^{(K,M)}$	$dR_1^{(C,W)}$	$dR_1^{(D,W)}$	$dR_1^{(E,W)}$	$dR_1^{(F,W)}$	$dR_1^{(H,W)}$	$dR_1^{(G,W)}$	$dR_1^{(K,W)}$	$dR_1^{(C,G)}$	$dR_1^{(D,G)}$	$dR_1^{(E,G)}$	$dR_1^{(H,G)}$	$dR_1^{(C,G)}$	$dR_1^{(K,G)}$	Objective
1	7	3	2	7	5	15	19	6	3	1	1	4	17	22	7	4	7	5	27	36	149425
2	7	3	2	7	5	15	18	6	3	1	1	4	17	23	7	4	7	6	27	36	150785
3	7	3	2	7	5	16	18	6	3	1	1	4	17	23	7	4	7	5	27	36	150187
4	7	3	2	7	5	15	18	6	3	1	1	4	17	23	7	4	7	6	27	36	150502
5	7	4	2	7	5	15	18	6	3	1	1	4	17	23	7	4	7	6	27	36	148972
6	7	3	2	7	5	15	18	6	3	1	1	4	17	23	7	4	7	6	27	36	150612
7	7	3	2	7	5	15	18	6	3	1	1	4	17	23	7	4	7	6	28	35	149615
8	7	3	2	7	5	15	18	6	3	1	1	4	17	23	7	4	7	6	27	36	150395

Tab. 7. Statistical values obtained by SAA.

Set no	Lower bound		Upper bound	
	\bar{v}_N^M	$S_{\bar{v}_N^M}^2$	$\bar{g}_{N'}^M$	$\bar{S}_{\bar{g}_{N'}^M}^2$
1	150618	219605	151064	4796
2	151009	11260	150906	5212
3	151100	56030	150991	4874
4	150893	7505	150910	5169
5	150625	253556	151013	1008
6	150860	9207	150904	1022
7	151099	47511	151085	919
8	150902	8064	150904	1022

In Table 7, the second and third columns represent the lower bounds. Accordingly, the mean objective values calculated by Eq. (6) are found in column two and their mean variances, calculated by Eq. (7), are found in column three. The fourth and fifth columns show the upper bounds. The mean value of the upper bound values calculated by Eq. (10) is indicated in column four and the mean variances calculated by Eq. (11) are presented in column five.

In Table 8, columns 2-21 show the best values of the decision variables obtained for each parameter set. The 22nd column indicates the best objective function values.

In Table 9, the second and third columns show the gap values calculated by Eq. (14) and their mean variances calculated by Eq. (15), respectively. The fourth column indicates the ratio of the mean gap value to the lower bound of the objective function. Columns 5-7 show the 90% confidence interval calculated by Eq. (16) for the gap values.

Tab. 9. Optimal gap and 90% confidence interval calculations

Set no	Average values		$\frac{gap_{N,M,N'}}{\bar{v}_N^M}$	90% confidence interval of gap		
	$\overline{gap}_{N,M,N'}$	\bar{S}_{gap}^2		min	max	max-min
1	446	224401	0.296	-5.6	897.8	903.3
2	-103	16471	-0.070	-225.4	19.3	244.7
3	-109	60903	-0.070	-251.8	34.3	286.1
4	17	12673	0.011	-48.7	81.9	130.5
5	388	254564	0.257	-93.5	868.6	962.1
6	44	10229	0.029	-52.5	140.4	192.9
7	-14	48431	-0.010	-141.2	114.0	255.1
8	2	9086	0.002	-52.9	57.6	110.5

The best objective function values are shown in Fig. 3. These values were obtained from the eight different parameter sets solved.

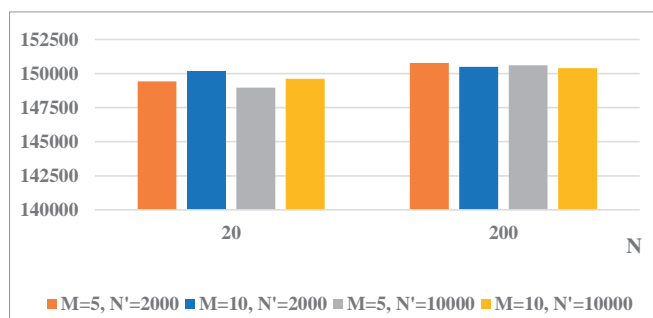


Fig. 3. Best objective function values

The best objective value is obtained from the eighth parameter set (i.e. $N = 200$, $M = 10$, $N' = 10000$) as 150395 currency units. Among the sets 1, 3, 5, and 7 (i.e. scenarios with $N = 20$), the third parameter set gives the best objective

value of 148972 currency units. For each set, M different gap values were calculated. After that, the average gap for each different set was determined as an absolute value (Fig. 4), where the vertical axis is logarithmic.

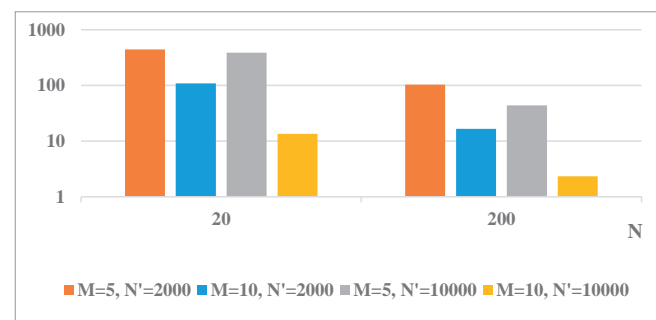


Fig. 4. Average gap values

It can be seen that increasing the number of scenarios from 20 to 200 for $M = 5$ and $N' = 2000$ reduces the average gap from 446.094 to 103.030. It is also understood that increasing the value of $N' = 2000$ to $N' = 10000$ also helped to reduce the gap. For instance, while the mean gap for set 2 is calculated as 103.030, this value is 43.948 for set 6. Provided that $N = 200$, and $N' = 10000$ remain constant, it is observed that increasing the number of independent samples from 5 to 10 reduced the average gap from 43.948 to 2.348. The upper and lower bounds, which are calculated using the reference sample and selected scenarios, respectively, are shown in Fig. 5.

It can be seen that increasing the number of scenarios from 20 to 200 makes the lower and upper bounds more stable. Besides, increasing M and N does not have a significant effect on the stability of the lower and upper bound values.

Fig. 6 presents the 90% confidence interval and average gaps and shows that increasing N rather than M is more effective in reducing the confidence interval. Also, increasing N' has little effect on reducing the confidence interval.

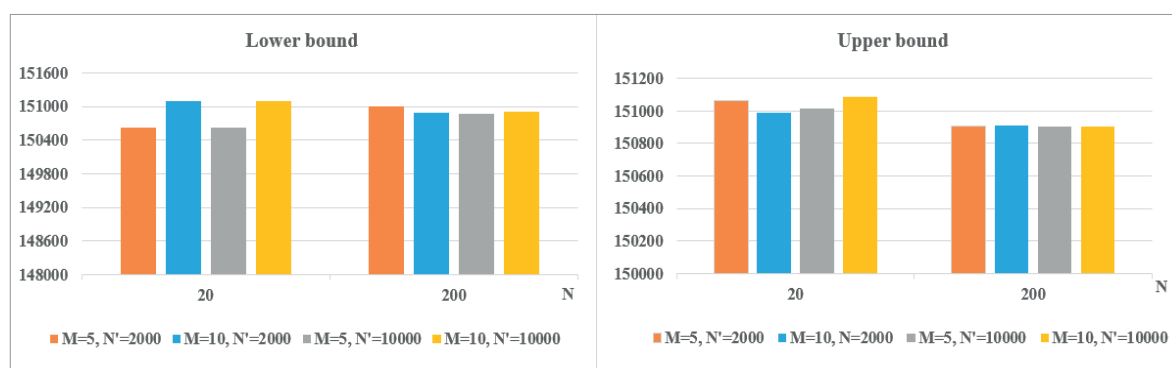


Fig. 5. Change in lower and upper bounds

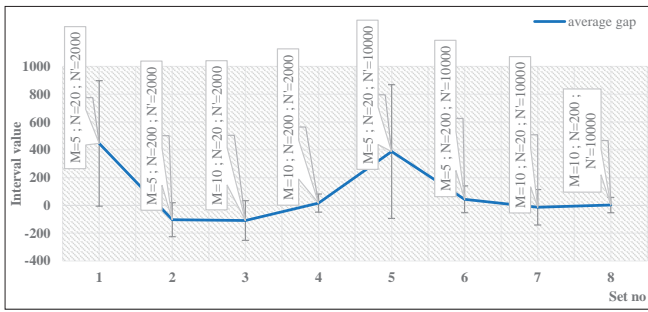


Fig. 6. Average gap values and 90% confidence interval

Average gap variances are shown in Fig. 7, whose vertical axis is logarithmic. Choosing $N = 200$, instead of 20, significantly reduces the mean gap variance and increasing M and N' are less effective in decreasing the variance.

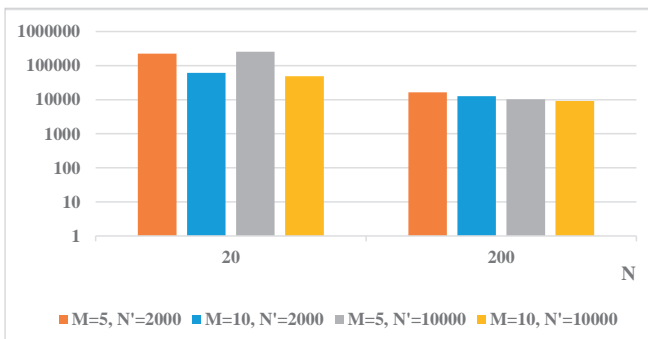


Fig. 7. Average gap variance values

Generally speaking, it was observed that, rather than enlarging the reference sample N' , increasing the number of selected scenarios N and independent samples M makes the objective function results more balanced and may improve the solution. Increasing the number of selected scenarios is important, in terms of decreasing the gap and variance. This means that the average gap is reduced as well. Therefore, the most effective parameter for decreasing the gap and variance is N .

The comparison of the developed model results with the actual shipyard records is shown in Table 10. As 'production phase E' does not involve any grinding activities, grinding is excluded from this phase, leaving twenty decision variables. Here, the model data calculated for each production phase is compared with the shipyard data. The results coincide at the 90% level. The observed difference between the shipyard data and the developed model results is attributed to the reliance on certain assumptions and simplifications during the analysis.

CONCLUSIONS

In labour-intensive production, such as the shipbuilding industry, it is very difficult to improve the process due to low automation, the mental status of the employees, etc. The goal of this study is to estimate the workforce (man-day) required and its cost for mounting, welding, and grinding activities in the production of a double bottom block of 38820 kg belonging to a passenger ship. A two-stage stochastic program with recourse was developed. Eight different parameter sets were configured and the SAA method was used to solve the model. The results indicate a certain level of agreement with the shipyard records.

Data from field observations reveal that worker performance is variable in character. Similarly, it has been realised that the amount of work may change due to reasons such as revision, customer amendment requests, or the need for reworking due to faulty production. So, the amount of work and average worker performance are uncertain factors. On the other hand, since the parameters have a great effect on the results, it is important to use the suitable most appropriate parameter set.

In order to reduce the gap and variance, increasing N greatly improves the results, while increasing M and N' provide partial improvement. Besides this, it was also concluded that increasing M and N has a positive effect on reducing the confidence interval. When the solutions of all parameter sets are examined, it can be seen that the minimum gap is obtained from the eighth parameter set (i.e. $N' = 10000$,

Tab. 10. Comparison of the results with the shipyard

Product	Mounting (man-day)		Ratio	Welding (man-day)		Ratio	Grinding (man-day)		Ratio
	Model (M)	Shipyard (S)		Model (M)	Shipyard (S)		Model (M)	Shipyard (S)	
C	7	8	0.88	6	7	0.86	7	9	0.78
D	3	5	0.60	3	4	0.75	4	5	0.80
E	2	2	1.00	1	1	1.00	-	-	-
F	7	6	1.17	1	1	1.00	7	8	0.88
H	5	5	1.00	4	5	0.80	6	7	0.86
G	15	17	0.88	17	19	0.89	27	28	0.96
K	18	20	0.90	23	25	0.92	36	39	0.92
Total	57	63	0.90	55	62	0.89	87	96	0.91

$N = 200$, and $M = 10$); whereas, the minimum objective is obtained in the fifth set. The reason for the minimum gap can be interpreted as the upper and lower bounds being quite close to each other. In this context, $L^{C,M}$, $L^{D,M}$, $L^{E,M}$, $L^{F,M}$, $L^{H,M}$, $L^{G,M}$, and $L^{K,M}$ production phases in the mounting area require 7, 3, 2, 7, 5, 15, and 18 man-day, respectively; $L^{C,W}$, $L^{D,W}$, $L^{E,W}$, $L^{F,W}$, $L^{H,W}$, $L^{G,W}$, and $L^{K,W}$ production phases in the welding area require 6, 3, 1, 1, 4, 17, and 23 man-day; and $L^{C,G}$, $L^{D,G}$, $L^{E,G}$, $L^{H,G}$, $L^{G,G}$, and $L^{K,G}$ production phases in the grinding area require 7, 4, 7, 6, 27, and 36 man-day. As a result, the total labour cost for this block was estimated to be 150395 currency units.

One of the prerequisites for utilising the established model is the execution of a production control system in the shipyard, to continually measure current performance. The implementation of such innovations in a shipyard faces employee resistance and organisational, economic, and technical challenges. However, these challenges can be overcome by emphasising the contribution of this cultural change to the planning of the production process. Another requirement is software which is capable of determining the length of the joint interface for calculating the amount of work, thereby speeding up the process; otherwise, it may take a long time.

In a future study, other shipbuilding processes, such as preparation activities (cutting, marking, etc.) of plates and profiles, outfitting, etc., may be included in the model. Moreover, transforming the model into a practically usable software-supported tool that can be employed by shipyards for the estimation of man-day needed for a specific activity (e.g. a block or a whole ship) is thought. Actual performance and work amount (workload) serve as data input for the software tool to predict the required workforce.

REFERENCES

1. Y. Guo, H. Wang, X. Liang, and H. Yi, "A quantitative evaluation method for the effect of construction process on shipbuilding quality," *Ocean Engineering*, vol. 169, pp. 484-491, 2018, doi.org/10.1016/j.oceaneng.2018.09.046.
2. H. Wang, Y. Guo, X. Liang, and H. Yi, "A function-oriented quality control method for shipbuilding," *Ships and Offshore Structures*, vol. 14, no. 2, pp. 220-228, 2019, doi.org/10.1080/17445302.2018.1493910.
3. H. Kim, J. Kang, and S. Park, "Scheduling of shipyard block assembly process using constraint satisfaction problem," *Asia Pacific Management Review*, vol. 7, no. 1, pp. 119-138, 2002.
4. J. Li, M. Sun, D. Han, J. Wang, X. Mao, and X. Wu, "A knowledge discovery and reuse method for time estimation in ship block manufacturing planning using DEA," *Advanced Engineering Informatics*, vol. 39, pp. 25-40, 2019, doi.org/10.1016/j.aei.2018.11.005.
5. J. Park, D. Lee, and J. Zhu, "An integrated approach for ship block manufacturing process performance evaluation: case from Korea shipbuilding company," *International Journal of Production Economics*, vol. 156, pp. 214-222, 2014, doi.org/10.1016/j.ijpe.2014.06.012.
6. M. Kang, J. Seo, and H. Chung, "Ship block assembly sequence planning considering productivity and welding deformation," *International Journal of Naval Architecture and Ocean Engineering*, vol. 10, pp. 450-457, 2018, doi.org/10.1016/j.ijnaoe.2017.09.005.
7. H. Kim, S. S. Lee, J. H. Park, and J. G. Lee, "A model for simulation-based shipbuilding system in a shipyard manufacturing process," *International Journal of Computer Integrated Manufacturing*, vol. 18, no. 6, pp. 427-441, 2005, doi:10.1080/09511920500064789.
8. J. M. Lee, Y. K. Jeong, and J. H. Woo, "Development of an evaluation framework of production planning for the shipbuilding industry," *International Journal of Computer Integrated Manufacturing*, vol. 31, no. 99, pp. 831-847, 2018, doi.org/10.1080/0951192X.2018.1449968.
9. A. Türk, S. Gürgen, M. Özkök, and İ. Altın, "A comprehensive investigation into the performance of genetic algorithm for effective shipyard topological layout," *Proceedings of the Institution of Mechanical Engineers Part M-Journal of Engineering for the Maritime Environment*, vol. 236, no. 3, pp. 726-740, 2022, doi.org/10.1177/147509022110620.
10. B. Lujibenkov, B. Blagojević, J. Bašić, and M. Bašić, "Procedure for reconstruction of gajeta hull form using photogrammetric measurement method," *Brodogradnja*, vol. 73, no. 2, pp. 139-151, 2022, doi.org/10.21278/brod73208.
11. Y. J. Song, J. H. Woo, and J. G. Shin, "Research on systematization and advancement of shipbuilding production management for flexible and agile response for high value offshore platform," *International Journal of Naval Architecture and Ocean Engineering*, vol. 3, no. 3, pp. 181-192, 2011, doi.org/10.2478/IJNAOE-2013-0061.
12. I. H. Hwang, Y. Kim, D. K. Lee, and J. G. Shin, "Automation of block assignment planning using a diagram-based scenario modelling method," *International Journal of Naval Architecture and Ocean Engineering*, vol. 6, no. 1, pp. 162-174, 2014, doi.org/10.2478/IJNAOE-2013-0170.
13. M. Kafalı and M. Özkök, "Evaluation of shipyard selection criteria for ship owners using a fuzzy technique," *Journal of Marine Engineering & Technology*, vol. 14, no. 3, pp. 146-158, 2015, doi.org/10.1080/20464177.2015.1118787.

14. U. Bilen and Ş. Helvacıoğlu, "Data driven performance evaluation in shipbuilding," *Brodogradnja*, vol. 71, no. 4, pp. 39-51, 2020, doi.org/10.21278/brod71403.
15. L. Lei, L. Di, W. Pengyu, and Z. Honggen, "Research on hull assembly planning based on rule reasoning" *Materials Science and Engineering*, vol. 751, pp. 1-7, 2020, doi:10.1088/1757-899X/751/1/012084.
16. M. de C. Porath, R. Simoni, R. de A. Nunes, and A. Bertoldi, "Feasibility of measurement-assisted assembly of ship hull blocks," *Marine System & Ocean Technology*, vol. 14, pp. 23-33, 2019, doi.org/10.1007/s40868-018-00053-w.
17. M. Kafalı, N. Aydın, Y. Genç, and U. B. Çelebi, "A two-stage stochastic model for workforce capacity requirement in shipbuilding," *Journal of Marine Engineering & Technology*, vol. 21, no. 3, pp. 146-158, 2022, doi.org/10.1080/20464177.2019.1704977.
18. T. Urbanski, T. Graczyk, M. Taraska, and R. R. Iwankowicz, "Assessment of technological usefulness of panel production line in shipbuilding process," *Polish Maritime Research*, vol. 25, pp. 134-144, 2018, doi:10.2478/pomr-2018-0034.
19. Y. K. Jeong, S. Ju, H. Shen, D. K. Lee, J. G. Shin, and C. Ryu, "An analysis of shipyard spatial arrangement planning problems and a spatial arrangement algorithm considering free space and unplaced block," *The International Journal of Advanced Manufacturing Technology*, vol. 95, pp. 4307-4325, 2018, doi:10.1007/s00170-017-1525-1.
20. M. Afzalirad and J. Rezaeian, "Resource-constrained unrelated parallel machine scheduling problem with sequence dependent setup times, precedence constraints and machine eligibility restrictions," *Computers & Industrial Engineering*, vol. 98, pp. 40-52, 2016, doi.org/10.1016/j.cie.2016.05.020.
21. C. Wang, P. Mao, Y. Mao, and J. G. Shin, "Research on scheduling an optimisation under uncertain conditions in panel block production line in shipbuilding," *International Journal of Naval Architecture and Ocean Engineering*, vol. 8, pp. 398-408, 2016, doi.org/10.1016/j.ijnaoe.2016.03.009.
22. Z. Yuguang, A. Bo, and Z. Yong, "A PSO algorithm for multi-objective hull assembly line balancing using the stratified optimisation strategy," *Computers & Industrial Engineering*, vol. 98, pp. 53-62, 2016, doi.org/10.1016/j.cie.2016.05.026.
23. R. R. Iwankowicz, "A multi-case-base assembly management method for the shipbuilding industry," *Polish Maritime Research*, vol. 28, no. 2, pp. 27-35, 2021, doi:10.2478/pomr-2021-0018.
24. B. Kwon and G. M. Lee, "Spatial scheduling for large assembly blocks in shipbuilding," *Computers & Industrial Engineering*, vol. 89, pp. 203-212, 2015, doi.org/10.1016/j.cie.2015.04.036.
25. M. Hadjina, N. Fafandjel and T. Matulja, "Shipbuilding production process design methodology using computer simulation," *Brodogradnja*, vol. 6, no. 2, pp. 77-91, 2015.
26. A. Oliveire and J. M. Gordo, "Lean tools applied to a shipbuilding panel line assembling process," *Brodogradnja*, vol. 69, no. 4, pp. 53-64, 2018, doi.org/10.21278/brod6944.
27. M. Hur, S. K. Lee, B. Kim, S. Cho, D. Lee, and D. Lee, "A study on the man-hour prediction system for shipbuilding," *Journal of Intelligent Manufacturing*, vol. 26, no. 6, pp. 1267-1279, 2015, doi:10.1007/s10845-013-0858-3.
28. S. Hu, T. Liu, S. Wang, Y. Kao, and X. Sun, "A hybrid heuristic algorithm for shipbuilding construction space scheduling problem," *Discrete Dynamics in Nature and Society*, vol. 2015, no.7, pp. 1-6, 2015, doi:10.1155/2015/841637.
29. J. Zheng, Z. Jiang, and Q. Chen, "Block spatial scheduling modelling and application in shipbuilding," *International Journal of Production Research*, vol. 50, no. 10, pp. 2744-2756, 2012, doi.org/10.1080/00207543.2011.588629.
30. Z. Liu, D. K. H. Chua, and K. H. Wee, "A simulation model for spatial scheduling for dynamic block assembly in shipbuilding," *Journal of Engineering, Project, and Production Management*, vol. 1, no. 1, pp. 3-12, 2011, doi:10.32738/JEPPM.201107.0002.
31. S. I. Wahidi, S. Oterkus, and E. Oterkus, "Simulation of a ship's block panel assembly process: optimising production processes and cost through welding robots," *Journal of Marine Science and Engineering*, vol. 11, no. 8, pp. 1506-1522, 2023, doi.org/10.3390/jmse11081506.
32. B. Liu and Z. H. Jiang, "The man-hour estimation models & its comparison of interim products assembly for shipbuilding," *International Journal of Operations Research*, vol. 2, no. 1, pp. 9-14, 2005.
33. Y. Imai, Y. Ohta, and H. Suzuki, "A man-hour estimation tool focused on graphical user interface," *Lecture Notes of Software Engineering*, vol. 4, no. 3, pp. 175-178, 2016, doi: 10.18178/lmse.2016.4.3.245.
34. S. A. Seyfi, İ. Yanıkoğlu, and G. Yılmaz, "Multi-stage scenario-based stochastic programming for managing lot sizing and workforce scheduling at Vestel," *Annals of Operations Research*, Published online, 2023, doi.org/10.1007/s10479-023-05741-4.

35. D. J. Eyres and G. J. Bruce, *Ship Construction*, Seventh Edition, Butterworth-Heinemann: Oxford, UK, 2012.
36. M. Kafalı, Y. Ünsan, and M. Özkök, "A production planning and control methodology for shipyards," (In Turkish) *Journal of ETA Maritime Science*, vol. 6, no. 1, pp. 47-59, 2018, doi.org/10.5505/jems.2018.02986.
37. F. Dong, H. Parvin, M. P. V. Oyen, and D. J. Singer, "Innovative ship block assembly production control using a flexible curved block job shop," *Journal of Ship Production*, vol. 25, no. 4, pp. 206-213, 2009, doi:10.5957/jsp.2009.25.4.206.
38. M. Branda, "Sample approximation technique for mixed-integer stochastic programming problems with several change constraints," *Operation Research Letters*, vol. 40, pp. 207-211, 2012, doi.org/10.1016/j.orl.2012.01.002.
39. S. W. Wallace and W. T. Ziemba, (Eds.), *Applications of stochastic programming*, 1st ed., MPS SIAM- Series in Optimisation Number 5, 2005.
40. J. R. Birge and F. Louveaux, "Introduction to Stochastic Programming", 2nd Edition, Springer, New York, 2011.
41. S. Ahmed and A. Shapiro, 2002. "The sample average approximation method for stochastic programs with integer recourse", [Optimisation Online], 2002, <http://www.optimisation-online.org>.
42. B. Ayvaz, B. Bolat, and N. Aydin, "Stochastic reverse logistics network design for waste of electrical and electronic equipment," *Resources, Conservation and Recycling*, vol. 104, pp. 391–404, 2015, doi.org/10.1016/j.resconrec.2015.07.006.